

STUDY OF HYBRID PEROVSKITE BASED THIN FILMS
FOR FIELD EFFECT TRANSISTOR AND UV
PHOTODIODE APPLICATIONS

YASHOTHA SUBRAMANIAM

FACULTY OF SCIENCE
UNIVERSITI MALAYA
KUALA LUMPUR

2023

**STUDY OF HYBRID PEROVSKITE BASED THIN
FILMS FOR FIELD EFFECT TRANSISTOR AND UV
PHOTODIODE APPLICATIONS**

YASHOTHA SUBRAMANIAM

**THESIS SUBMITTED IN FULFILMENT OF THE
REQUIREMENTS FOR THE DEGREE OF DOCTOR OF
PHILOSOPHY**

**FACULTY OF SCIENCE
UNIVERSITI MALAYA
KUALA LUMPUR**

2023

UNIVERSITI MALAYA
ORIGINAL LITERARY WORK DECLARATION

Name of Candidate: **YASHOTHA SUBRAMANIAM**

Matric No: **17201915/1**

Name of Degree: **DOCTOR OF PHILOSOPHY**

Title of Thesis ("this Work"):

**STUDY OF HYBRID PEROVSKITE BASED THIN FILMS FOR FIELD
EFFECT TRANSISTOR AND UV PHOTODIODE APPLICATIONS**

Field of Study: **EXPERIMENTAL PHYSICS**

I do solemnly and sincerely declare that:

- (1) I am the sole author/writer of this Work;
- (2) This Work is original;
- (3) Any use of any work in which copyright exists was done by way of fair dealing and for permitted purposes and any excerpt or extract from, or reference to or reproduction of any copyright work has been disclosed expressly and sufficiently and the title of the Work and its authorship have been acknowledged in this Work;
- (4) I do not have any actual knowledge nor do I ought reasonably to know that the making of this work constitutes an infringement of any copyright work;
- (5) I hereby assign all and every rights in the copyright to this Work to the University of Malaya ("UM"), who henceforth shall be owner of the copyright in this Work and that any reproduction or use in any form or by any means whatsoever is prohibited without the written consent of UM having been first had and obtained;
- (6) I am fully aware that if in the course of making this Work I have infringed any copyright whether intentionally or otherwise, I may be subject to legal action or any other action as may be determined by UM.

Candidate's Signature

Date: **22/8/2023**

Subscribed and solemnly declared,

Witness's Signature

Date: **22/8/2023**

Name:

Designation:

STUDY OF HYBRID PEROVSKITE BASED THIN FILMS FOR FIELD EFFECT TRANSISTOR AND UV PHOTODIODE APPLICATIONS

ABSTRACT

Recent developments in the field of electronics involving three-dimensional (3D) organic-inorganic hybrid perovskites have sparked the discovery of two-dimensional (2D) and one-dimensional (1D) materials. The introduction of bigger organic amine groups into the perovskite structure results in low-dimensional perovskites having enormous potential for creating high-stability perovskite photovoltaics and optoelectronics. The morphology issues greatly limit charge transport in the thin film. Primarily, this study uses solution processing techniques to investigate the potential application of low dimensional perovskite as an active layer in field-effect transistors (FET). Adding Nafion as a surface modification to the top of the indium tin oxide (ITO) electrode has demonstrated that charge injection can be improved. A thin layer of spin-coated Nafion deposited between the ITO and the perovskite active layer reduces the injection barrier by altering the ITO's effective work function from 4.40 eV to 4.90 eV. Subsequently, poly (9-vinylcarbazole) PVK blended into a one-dimensional Propylammonium lead bromide (PAPbBr₃) precursor solution. The blended PVK induced preferential vertically orientated nanopillars as revealed by synchrotron-based two-dimensional grazing incident X-ray diffraction. This simultaneously reduced the grain boundaries and improved pin-hole free films. As a result, maximum hole mobility of 0.012 cm²/Vs was achieved. Additionally, it was discovered that adding PVK to pristine PAPbBr₃ reduced the hysteresis voltage from 4V to 0.95 V (in PAPbBr₃: the PVK-25% device). This research indicated that the performance of FETs depends on the injection barrier and the perovskite nanopillar microstructure. The next phase of this thesis assessed the applicability of low-dimensional perovskite, 2D layered phenethylammonium lead

bromide ($\text{PEA}_2\text{PbBr}_4$) as an active layer in a self-powered ultra-violet (UV) photodiode. The PEDOT: PSS was chosen to serve as the hole transport layer, while the PCBM material was chosen as the electron transporting hole blocking layer. The moisture-sensitive PEDOT: PSS, on the other hand, led to inadequate surface coverage and the deterioration of perovskite material. This, in turn, led to a decrease in the device's performance and instability. A significant increase in photocurrent and stability was observed when a hydrophobic Nafion layer was added on top of the PEDOT: PSS and perovskite interface. At 0 V bias, the best $\text{PEA}_2\text{PbBr}_4$ film-based device had a high photocurrent of 0.34 mA/cm^2 and a fast response time of $15.6 \text{ }\mu\text{s}$. The improved device's responsivity and detectivity were estimated to be 25 mA/W and $2.54 \times 10^{11} \text{ Jones}$, respectively. Field-emission scanning electron microscopy and energy dispersive x-ray spectroscopy have proven that the increased surface coverage is directly responsible for better device performance. Moreover, owing to the hydrophobic nature of the Nafion layer, the $\text{PEA}_2\text{PbBr}_4$ films and devices based on Nafion-coated PEDOT: PSS exhibited superior UV light stability than those without the Nafion layer. Thus, high-performing devices were successfully fabricated using highly repeatable, solution-processed, and cost-effective methods.

Keywords: Low dimensional perovskite, FET, solution-processed, self-powered, UV photodiode.

KAJIAN HYBRID PEROVSKITE BERDASARKAN FILM UNTUK FIELD – EFFECT TRANSISTOR DAN UV FOTODIOD

ABSTRAK

Perkembangan terkini dalam bidang elektronik yang berasaskan tiga dimensi (3D) perovskites hibrid organik-bukan organik telah mendorong penemuan baru bahan dua dimensi (2D) dan satu dimensi (1D). Pengenalan kumpulan amina organik yang lebih besar ke dalam struktur perovskite menghasilkan perovskites dimensi rendah, yang mempunyai potensi besar untuk menghasilkan peranti optoelektronik perovskite dengan kestabilan tinggi. Walau bagaimanapun, pengangkutan cas dalam filem nipis dihindari oleh kecacatan morfologi dan ketidakcocokan tahap tenaga pada perovskite dimensi rendah yang mempunyai jalur valens maksimum (VBM) yang dalam. Terutama, kajian ini menggunakan teknik proses larutan untuk menyiasat potensi penggunaan perovskite dimensi rendah sebagai lapisan aktif dalam transistor kesan medan (FET). Penambahan Nafion sebagai pengubahsuaian permukaan elektrod Indium Tin Oksida (ITO) telah menunjukkan bahawa suntikan cas dapat ditingkatkan. Lapisan nipis Nafion bersalut putar yang tersimpan di antara ITO, dan lapisan aktif perovskite mengurangkan penghalang suntikan dengan mengubah fungsi kerja berkesan ITO dari 4.40eV menjadi 4.90eV. Selepas itu, poly (9-vinylcarbazole) PVK digabungkan menjadi larutan prekursor Propylammonium plumbum bromida (PAPbBr₃) satu dimensi. PVK yang diadun mendorong nanopillar berorientasikan menegak seperti yang dinyatakan oleh difraksi sinar-X kejadian ragut dua dimensi berasaskan sinkron. Ini secara serentak mengurangkan batas butiran dan memperbaiki filem bebas kecacatan. Hasilnya, mobiliti lohong maksimum 0.012cm² / Vs dicapai. Selain itu, didapati bahawa menambahkan PVK ke dalam larutan PAPbBr₃ mengurangkan voltan histeresis dari 4V hingga 0.95V (peranti di PAPbBr₃:PVK-25%). Hasil penyelidikan ini menunjukkan bahawa prestasi FET bergantung pada penghalang suntikan dan struktur mikro nanopillar perovskite. Fasa

seterusnya tesis ini menilai kebolehlaksanaan perovskite dimensi rendah, 2D berlapis phenethylammonium plumbum bromida ($\text{PEA}_2\text{PbBr}_4$) sebagai lapisan aktif dalam fotodetektor ultra-ungu berkuasa sendiri (UV). PEDOT: PSS dipilih untuk berfungsi sebagai lapisan pengangkutan lohong, sementara bahan PCBM dipilih sebagai lapisan penyekat lohong dan pengangkut elektron. PEDOT: PSS sensitif kelembapan dan menyebabkan liputan permukaan yang tidak mencukupi dan kemerosotan bahan perovskite. Seterusnya, menyebabkan penurunan prestasi dan ketidakstabilan peranti. Peningkatan ketara dalam arusfoto dan kestabilan diperhatikan apabila lapisan Nafion hidrofobik ditambahkan di antara PEDOT: PSS dan perovskite. Pada bias 0 V, peranti berasaskan filem $\text{PEA}_2\text{PbBr}_4$ mempunyai arusfoto yang tinggi $0.34\text{mA}/\text{cm}^2$ dan masa tindak balas pantas $15,6\mu\text{s}$. Tindak balas dan pengesanan peranti yang ditingkatkan masing-masing dianggarkan $25\text{mA}/\text{W}$ dan $2.54 \times 10^{11}\text{Jones}$. Mikroskopi elektron pengimbasan medan dan spektroskopi sinar-x penyebaran tenaga telah membuktikan bahawa peningkatan liputan permukaan bertanggungjawab secara langsung untuk prestasi peranti yang lebih baik. Lebih-lebih lagi, kerana sifat hidrofobik lapisan Nafion, filem $\text{PEA}_2\text{PbBr}_4$, dan peranti berdasarkan PEDOT: PSS bersalut Nafion menunjukkan kestabilan cahaya UV yang unggul daripada yang tanpa lapisan Nafion. Oleh itu, peranti berprestasi tinggi berjaya dibuat dengan menggunakan teknik proses larutan dan menjimatkan kos.

Keywords: Perovskite berdimensi rendah, FET, teknik proses larutan, dikuasakan sendiri, fotodiod UV.

ACKNOWLEDGEMENTS

My special gratitude goes out to my supervisor, Associate Professor Dr. Woon Kai Lin, for the trust he placed in me, the direction he provided, and the fruitful conversations we had that assisted me in overcoming the difficult circumstances I had while working on my PhD. This research endeavor never would have been a reality if it had not been for Dr. Woon's insightful guidance and unwavering support.

Without the help of several individuals at the Low Dimensional Materials Research Center (LDMRC), my thesis would not have been completed. I want to express my sincere gratitude to Dr. Wah Seng, Mr. Sufian, Ms. Hannan, Ms. Adilah, Dr. Arif, Ms. Syaza, Mr. Fadlan, and Mr. Amirul.

Additionally, I'd like to express my gratitude to Ms. Hanan Alzahrani, a dear friend and ally who has been there for me during our time at Universiti Malaya. My thanks also go to the laboratory's administrative and research staff. Their assistance in the laboratory makes my research process run more smoothly.

Most importantly, I am indebted and forever grateful to my spouse, Mr. Dineson for his encouragement, compassionate understanding, and full support during my PhD pursuit. I couldn't have succeeded without his help. I will be eternally grateful to my parents, whose unending love and encouragement have driven me to achieve my goals from a young age onward.

As a final note, I'd want to express my gratitude to everyone who played a role in my research, whether directly or indirectly, and who isn't explicitly mentioned here.

Thank you very much!

TABLE OF CONTENTS

ABSTRACT	III
ABSTRAK	v
ACKNOWLEDGEMENTS	vii
TABLE OF CONTENTS	viii
LIST OF FIGURES	xii
LIST OF TABLES	xxi
LIST OF SYMBOLS AND ABBREVIATIONS	xxii
LIST OF APPENDICES	xxv
CHAPTER 1: INTRODUCTION.....	1
1.1 Introduction	1
1.2 Motivations.....	5
1.2.1 Field-effect transistor (FET).....	5
1.2.2 Photodetector.....	6
1.3 Objectives	8
1.4 Thesis Outline.....	9
CHAPTER 2: LITERATURE REVIEW.....	11
2.1 Introduction	11
2.2 Semiconductor	11
2.3 Semiconductor-Light Interactions	14
2.4 Organic semiconductor (OSC)	17
2.5 Organic-inorganic halide perovskite material	19
2.5.1 Key Characteristics of organic-inorganic halide perovskites.....	23
2.5.1.1 Tunable Light Absorption and Emission	23

2.5.1.2	Charge transport	24
2.5.1.3	Defects and traps	24
2.6	Low-dimensional perovskites	26
2.6.1	Two-dimensional (2D) organic-inorganic hybrid perovskites	28
2.6.2	One-dimensional (1D) organic-inorganic hybrid perovskites	30
2.6.3	Optical and physical properties of low-dimensional halide perovskite ...	32
2.7	Perovskite crystallization	38
2.8	Deposition of Perovskite	41
2.9	Device physics of electronic applications	43
2.9.1	Field Effect Transistor (FET)	43
2.9.2	Basic operating mode	46
2.9.3	Electrical Characterization of FETs	50
2.9.4	Low-dimensional hybrid perovskites-based FETs	53
2.10	Photodetector (PD)	54
2.10.1	Key performance parameters for photodetectors	59
2.10.2	Hole transport layer (HTL)	63
2.10.3	Self-powered Photodetector	65
2.10.4	Low-dimensional hybrid perovskite photodetectors	66
CHAPTER 3: MATERIAL AND METHODS.....		68
3.1	Introduction	68
3.2	Materials	68
3.2.1	Propylammonium lead bromide (PAPbBr ₃)	68
3.2.2	Phenethylammonium Lead Bromide (PEA ₂ PbBr ₄)	68
3.2.3	Sulfonated tetrafluoroethylene-based fluoropolymer-copolymer (Nafion)	69
3.2.4	Poly (N-vinyl carbazole) PVK	69

3.2.5	Polytetrafluoroethylene (PTFE)	70
3.2.6	Poly (3,4-ethylenedioxythiophene):poly(styrene sulfonate) (PEDOT:PSS).....	71
3.2.7	[6,6]-phenyl C61 butyric acid methyl ester (PC ₆₁ BM)	71
3.2.8	ITO and Aluminum Electrode	72
3.3	Experimental procedure.....	73
3.3.1	Substrate Cleaning Procedure	73
3.3.2	Thin film preparation and device fabrication	75
3.4	Thin film characterization	79
3.4.1	Surface Profilometer	79
3.4.2	Contact angle measurement	80
3.4.3	Ultraviolet/visible/infrared (UV/Vis/NIR) Spectrophotometer.....	82
3.4.4	Atomic force microscope (AFM)	84
3.4.5	Field Emission Scanning Electron Microscope (FESEM) and Energy dispersive X-ray (EDX)	85
3.4.6	X-ray diffraction (XRD).....	87
3.4.7	Grazing incidence X-ray diffraction (GIXRD)	89
3.4.8	Ultraviolet photoelectron spectroscopy (UPS).....	92
3.4.9	4-point probe analysis	95
3.5	Measurement of Perovskites-Based Devices.....	98
3.5.1	I-V Characterization of FETs Devices	98
3.5.2	I-V and Characterization of PDs Devices	100
3.6	Summary.....	102

CHAPTER 4: PA: PVK-BASED FIELD-EFFECT TRANSISTOR (FET)	103
4.1 Introduction	103
4.2 Experimental Method	105
4.3 Result and discussion	108
4.3.1 Effect of ITO work function modification on PA-based FET.	108
4.3.2 Effect of PVK blending on PA-based FET	112
4.3.3 Electrical performance of FET based on PAPbBr ₃ -PVK blend system.	119
4.4 Conclusion	127
 CHAPTER 5: PEA₂PBBR₄-BASED SELF-POWERED ULTRA-VIOLET PHOTODIODE 128	
5.1 Introduction	128
5.2 Experiment methods	131
5.3 Result and discussion	132
5.3.1 Effect of Nafion interlayer on PEA ₂ PbBr ₄ morphology	132
5.3.2 Electrical Performance of PEA ₂ PbBr ₄ Photodiode	137
5.3.3 Effect of illumination intensity on the performance of optimized self- powered PEA ₂ PbBr ₄ Photodiode	150
5.4 Conclusion	156
 CHAPTER 6: CONCLUSION AND FUTURE WORKS	157
6.1 Conclusion	157
6.2 Future Works	159
REFERENCES.....	160
LIST OF PUBLICATIONS AND PAPERS PRESENTED	184
APPENDIX	187

LIST OF FIGURES

Figure 1.1:	Organic semiconductor-based applications, (a) Bank notes, (b) Flexible display, (c) Sensors, (d) Bio-electronics, (e) RFID, (f) Thermoelectric (Picture source from: www.azom.com , www.electronicweekly.com , www.chemistryworld.com , arcasystems.com and www.rsc.org).	2
Figure 1.2	National Renewable Energy Laboratory's last updated graph for record cell efficiencies (Dec 2021) from 1991 to 2021, perovskites solar cells compared to their inorganic cell counterparts(NREL, 2021).....	3
Figure 1.3:	Schematic crystal structures of 3D perovskite, 2D perovskite and 1D perovskite[Adopted from (Zhou et al., 2019)].....	4
Figure 1.4:	The total number of publications from the Web of Science-Core Collection with the topic keywords "perovskite" AND "field-effect transistor" OR "photodetector" OR "photodiode".....	5
Figure 1.5:	Health problems caused by over UVA radiation exposure (a) skin cancer, (b) premature ageing, and (c) corneal damage (Picture source from ellayelabanico.com and www.aao.org).....	7
Figure 2.1:	(a) Energy diagram for an intrinsic semiconductor, (b) Energy band diagram of N-type semiconductor, (c) Energy band diagram of P-type semiconductor [Picture source from (Báez-Lópe & Guerrero Castro,2011).....	13
Figure 2.2:	(a) A low-energy photon is transmitted because it cannot transport electrons from the valence band (VB) to the conduction band (CB) across the bandgap, (b) A high-energy photon is absorbed by promoting an electron, (c) An electron and hole relax before recombining and emitting a photon by photoluminescence[Picture source from (Harwell, 2018)].....	14
Figure 2.3:	(a) A semiconductor with a direct bandgap, in which an electron can be easily moved across the bandgap by a photon, (b) Indirect bandgap, in which accelerating an electron from the VBM to the CBM requires absorbing both a photon for energy and a phonon To be absorbed without the participation of a phonon, a photon's energy must be more significant than ΔE_{direct} , (c) comparing the absorption constants of silicon (indirect) and GaAs (direct).[Picture source from (Palik, 2012)].....	16

Figure 2.4:	(a) A C=C double bond's π bond and anti-bond formation. Due to the electrons' average proximity to the carbon atoms, the bonding orbital has a lower energy than the anti-bond, (b) The mechanism by which the bonding separates the energy levels into a HOMO and a LUMO[Picture source from (Harwell, 2018)].....	17
Figure 2.5:	(a) The double and single bonds that make up a conjugated polymer, (b) the formation of electron-conducting cloud, for example, (c) poly-3-hexyl thiophene, (d) polyphenylene vinylene[Picture source from (Labram, 2011)].....	19
Figure 2.6:	Crystal structure of ABX ₃ perovskite with the origin centred at (a) the B site and (b) the A site[Picture source from (Das et al., 2019)].....	20
Figure 2.7	(a) Total DOS and CH ₃ NH ₃ ⁺ , Pb and I partial DOS(Yin et al., 2014) (b) Schematic of APbX ₃ bonding/antibonding orbitals showing valence band(VB) and conduction bands (CB)(Brandt et al., 2015), (c) VBM and CBM electron densities of cubic CH ₃ NH ₃ PbI ₃ [Picture source from (T. Zhao et al., 2016)].....	21
Figure 2.8	Summarises the available amines, metal cations, and anions used in TF calculations. Among the total of 2352 TFs found, 742 (562 organic anions based, 180 halide based) fall within the interval ($0.8 < t < 1$)[Adapted from (Kieslich et al., 2015)].....	22
Figure 2.9:	Diagram of a self-trapped exciton's general configuration (STE). Coordinate Configuration Q. Dependence of self-trapping energy barrier on dimensionless localization parameter λ for 3D, 2D, and 1D materials [Picture source from (Rondiya et al., 2021)].....	25
Figure 2.10:	A comparison of 2D, 1D, and 0D perovskites (the squares, wavy lines, and brown dots stand for BX ₆ octahedral units, bulky organic cations, and small organic cations, respectively)[Picture source from (P. Chen et al., 2018)].....	27
Figure 2.11:	The (RNH ₃) ₂ MX ₄ and (NH ₃ RNH ₃)MX ₄ type structures frequently exhibit two hydrogen-bonding configurations: (a) the bridging halide configuration and (b) the terminal halide configuration[Picture source from (Mitzi et al., 1999)].....	28
Figure 2.12:	The crystal structure of (PEA) ₂ PbBr ₄ , also known as 2-phenylethylammonium lead bromide, exhibits a two-dimensional layered perovskite arrangement [Picture source from (D. Liang et al., 2016)].....	30

Figure 2.13:	(a) A packing diagram for $[\text{CH}_3\text{SC}(\text{NNH}_2)\text{NH}_2]\text{PbI}_5$, displaying the thick bond chains and detailed structure. (b) A diagram of two connected PbI_5 units shows the atoms and ellipses with a 50% chance of occurrence.[Picture source from (Mousdis et al., 1998)].	31
Figure 2.14:	(a) The band energy diagram of $\text{BA}_2\text{MA}_{n-1}\text{PbI}_{3n+1}$ perovskite compounds(D. H. Cao et al., 2015) (b) The band structure of $\text{PEA}_2\text{MA}_{n-1}\text{PbI}_{3n+1}$ perovskite compounds with different n values.[Picture source from (M. Yuan et al., 2016)].	33
Figure 2.15:	Syntheses of Poly(1-phenyl-1-alkyne) Ammonium Salt-Lead Bromide Perovskite Hybrids [Picture source from (Hua et al., 2005)]	35
Figure 2.16:	Schematic diagram of the Wannier excitons and the Frenkel excitonsv[Picture source from (Manser et al., 2016)]	36
Figure 2.17:	Schematic representation of the processes of creation and degradation of MAPbI_3 when exposed to water[Picture source from (Song et al., 2016)]	37
Figure 2.18:	A better level of stability can be achieved in organometal halide perovskites by decreasing their dimensionality[Picture source from (Quan et al., 2016)]	38
Figure 2.19:	Illustrations of classical homogeneous and heterogeneous nucleation in supersaturated thin-film solutions [Picture source from (L. Gao & Yang, 2020)]	39
Figure 2.20:	Temperature-dependent nucleation and development of homogeneous and heterogeneous solution-derived thin films [Picture source from (Bretos et al., 2018)]	40
Figure 2.21:	One-step spin-coating deposition	42
Figure 2.22:	Two-step spin-coating deposition	42
Figure 2.23:	Chemical vapour deposition	43
Figure 2.24:	A thin-film transistor construction schematic shows a channel width, W, and channel length, L. The dashed line represents the flow of charge in the channel.	44
Figure 2.25:	Various FET device geometries (a) bottom-gate, top-contact (BGTC), (b) bottom-gate, bottom-contact (BGBC), and (c) top-gate, bottom-contact (TGBC).	45

Figure 2.26:	Energy level band diagram of an ideal MIS structure for a p-type semiconductor (a) at equilibrium, (b) biased in the accumulation region, (c) biased at the inversion region. (Picture source from Molecular Electronics: From Principles to Practice, 2007)	47
Figure 2.27:	Operation of field-effect transistor. (a) Linear regime. (c) Start of saturation regime at pinch-off, (c) Saturation regime.	49
Figure 2.28:	Typical FET characteristics: (a) output (I_{DS} vs. V_{DS} for different V_{GS} voltages), (b) transfer characteristics (I_{DS} vs. V_{GS} at $V_{DS} = \text{const.}$) transport curves of a p-channel device [Picture source from (Mei, 2018)].	51
Figure 2.29:	The graphical technique for determining Threshold voltage (V_{TH}).....	51
Figure 2.30:	Current modulation ratio determination using a transfer curve.....	52
Figure 2.31:	Radiative (a) generation and (b) recombination mechanisms for an arbitrary semiconductor with an energy band gap of E_g	55
Figure 2.32:	Structure of type of photodetectors. (a) Photodiode, (b) Photoconductor, and (c) Phototransistor.	56
Figure 2.33:	Under the influence of an electric field, photoconductors exhibit carrier trapping and mobility of another type of carrier (electrons are trapped in this illustration).[Inspired from (Konstantatos & Sargent, 2011)].....	57
Figure 2.34:	Rise time (tr rise) and decay time (td decay) of a photodetector with a square-pulse signal [Picture source from (Marshall, 2017)]. ...	61
Figure 2.35:	(a) Mechanisms for dark currents: Injection of charge into the tail states of the Gaussian density of states from interactions (DOS). HEL and EEL stand for the corresponding electron and hole transport layers.[Picture source from (Simone et al., 2020)].	63
Figure 2.36:	Chemical structure of PEDOT: PSS.	65
Figure 3.1:	Chemical structure of Nafion	69
Figure 3.2:	Chemical structure of Poly (N-vinyl carbazole)	70
Figure 3.3:	Chemical structure of PTFE.....	70
Figure 3.4:	Chemical structure of PEDOT: PSS	71
		72

Figure 3.5:	Chemical structure of PCBM	
Figure 3.6:	Geometry design of Pre-patterned ITO substrate of (a) FET (b) Photodetectors.	74
Figure 3.7:	Oxygen plasma parallel plate etcher (Polaron PT7170).	75
Figure 3.8:	(a) Spin-coating process (b) Spin coater (WS-650-23nppm, Laurell Technologies).	76
Figure 3.9:	The fabrication process of (a) FET and (b) Photodetectors.	78
Figure 3.10:	(a) Thermal Evaporation System inside Nitrogen gas-filled glove box, Low Dimensional Material Research Centre (LDMRC), (b) structure diagram of the thermal evaporator.....	79
Figure 3.11:	(a) FET shadow mask and (b) Photodetector shadow mask.....	79
Figure 3.12:	(a) The KLA Tencor P-6 Surface Profiler (b) Thickness measurements using a surface profiler.	80
Figure 3.13:	Diagram of equilibrium for droplets on a surface	81
Figure 3.14:	(a) Contact angle measurement set-up, (b) OneAttension software, (c) Wettability.....	82
Figure 3.15:	(a) Lambda 750 UV-VIS-NIR Spectrometer and (b) the optical path of the UV-VIS-NIR system.....	83
Figure 3.16:	(a) UV-Vis spectra and (a) Tauc plot of perovskite with an estimated optical bandgap of 1.59 eV. [example taken from (LL, 2022)].	84
Figure 3.17:	Schematic diagram of AFM	85
Figure 3.18:	Field Emission Scanning Electron Microscope (FESEM) JEOL JSM-7600F.....	86
Figure 3.19:	(a) A visual representation of Bragg's Law(Bragg, 1913), (b) XRD pattern, (c)Example of experimental X-ray diffraction pattern(Gawlinska et al., 2017).	88
Figure 3.20:	Layout of the BL7.2W: MX beamline(Sripukdee et al., 2018).....	89
Figure 3.21:	Graphical Representation of GIXRD (a) A depiction of high-incidence X-ray diffraction on a thin film. (b) The same evaluation as in (a), but with a small incident angle(Widjonarko, 2016).	90

Figure 3.22:	In three-dimensional reciprocal space, the scattering vector q is composed of in-plane elements (q_x , q_y , or $q_{xy} = \sqrt{q_x^2 + q_y^2}$), as well as an out-of-plane component q_z	91
Figure 3.23:	Valence electrons in UPS are excited by lower energy photons from the deep UV region.....	92
Figure 3.24:	Photoelectric effect measurement of UPS.....	94
Figure 3.25:	An illustration of (a) an atom's outer energy and (b) the UPS spectrum of au.	94
Figure 3.26:	UPS spectra of the (He I) of HDABiI5/FTO for direct determination of (a) work function and (b) valence-band maximum [picture source from (Fabian & Ardo, 2016)]......	95
Figure 3.27:	Diagram illustrating the four-point probe technique.....	96
Figure 3.28:	Schematic diagram of a 4-point probe set-up.	97
Figure 3.29:	Square probe tips on a thin film sample surface.	97
Figure 3.30:	Experimental set-up and device structure of I-V characterization.	99
Figure 3.31:	Typical FET characteristics (a) output (b) transfer curves of the p-type device [Picture source from (Blom, 2020)].	100
Figure 3.32:	Schematic IV set-up measurement.....	101
Figure 3.33:	Optical density filter.....	101
Figure 3.34:	Optical chopper	102
Figure 3.35:	Schematic of response time measurement.	102
Figure 4.1:	The molecular structure of materials used in this research section.....	106
Figure 4.2:	PA and PVK blended solutions in DMF	106
Figure 4.3:	Schematic diagram of Top-gate bottom contact FET	106
Figure 4.4:	Output characteristics of FET using pristine ITO	108
Figure 4.5:	(a) Output characteristics of FET Nafion treated ITO as S/D electrode, (b) Transfer characteristics of FET using pristine ITO and Nafion treated ITO as S/D electrode.	109

Figure 4.6:	(a) UPS spectra at high-energy cut-off (HECO) and (b) low-energy cut-off (LECO) for PAPbBr ₃ /ITO and PAPbBr ₃ /Nafion/ITO.....	111
Figure 4.7:	The energy diagram of the charge injection at the interface between the metal and perovskite, Evac is vacuum level, and Ef is the Fermi level.....	111
Figure 4.8:	Contact angle images (average angle value of four measurements noted in the image) of (a) Pristine (PVK-0%), (b) PVK-16%, and (c) PVK-25% precursor solution, respectively, on Nafion/ITO substrates.	113
Figure 4.9:	Absorption spectra of pristine PAPbBr ₃ and PAPbBr ₃ -PVK blends films.	114
Figure 4.10:	XRD pattern of Pristine PA and PA: PVK blended films.....	115
Figure 4.11:	FESEM images of PAPbBr ₃ -PVK blend films at different ratios: (a) Pristine PAPbBr ₃ (PVK-0%), (b) PVK-16%, (c) PVK-25%.	116
Figure 4.12:	Optical microscope images of spin-coated (a) Pristine (PVK-0%), (b) PVK-16%, and (c) PVK-25% on Nafion/ITO substrates, respectively. (Scale bar= 20μm).....	117
Figure 4.13:	AFM images of PAPbBr ₃ -PVK blend films at different ratios: (a) Pristine PAPbBr ₃ (PVK-0%), (b) PVK-16%, (c) PVK-25%.	117
Figure 4.14:	2D-GIXRD pattern of (a) pristine PAPbBr ₃ , (b) PVK-16% and (c) PVK-25% blends films.	119
Figure 4.15:	(a) Output characteristic of pristine, PVK-16% and PVK-25% blend FET (b) Semi-logarithmic curve of transfer characteristic of pristine, PVK-16% and PVK-25% blend FET, (c) Square root curve of transfer characteristic of pristine, PVK-16% and PVK-25% blend FET.	121
Figure 4.16:	Energy level structure	122
Figure 4.17:	Transfer characteristics of (a) PAPbBr ₃ -PVK 50%, (b) Pristine PVK FET, (c) AFM image of PAPbBr ₃ -PVK 50% blend film..	123
Figure 4.18:	Transfer characteristics of (a) pristine PAPbBr ₃ , (b) PVK-16%, and (c) PVK 25%.	124
Figure 4.19:	Contact angles with water of (a) Pristine (PVK-0%), (b) PVK-16%, and (c) PVK-25%.....	125
Figure 4.20:	Log-scale plot of the extracted field-effect mobility from different pristine PA and PVK blend film based FETs.....	126

Figure 4.21:	Comparison of transfer characteristics of Nafion only FET with optimized PA:PVK 25% FET device in the saturation regime at room temperature.....	127
Figure 5.1:	(a) Chemical structures of Nafion and PEDOT: PSS. Contact angle of DMF/CB solvent containing PEA2PbBr ₄ on top of PEDOT: PSS (b) PEDOT: PSS without Nafion layer (c) PEDOT: PSS/Nafion 1:10 (d) PEDOT: PSS/Nafion 1:4.	134
Figure 5.2:	FESEM top view images (a-c) and mapping images of EDX analysis PEA layer corresponding to bromine and lead mapping on PEDOT: PSS (d-e) without Nafion layer, (f-g) Nafion 1:10 layer, (h-i) Nafion 1:4 layer.	135
Figure 5.3:	XRD spectra of the PEA2PbBr ₄ thin films deposited at the same concentration and speed on PEDOT: PSS without and with the Nafion layer.....	136
Figure 5.4 :	Absorption spectra of the PEA2PbBr ₄ thin films deposited at the same concentration and speed on PEDOT: PSS without and with the Nafion layer.....	137
Figure 5.5:	Thickness of spin-coated PEA2PbBr ₄ layer on PEDOT: PSS/Nafion bilayer with different Nafion dilution concentration.	137
Figure 5.6:	(a) Schematic structure (b) energy level diagram of the photodiodes based on PEA2PbBr ₄	138
Figure 5.7:	J-V curves of the devices under dark without Nafion and with Nafion layer-based photodiode.	139
Figure 5.8:	(a) Current density-voltage curves of the devices (b) time-dependent photocurrent response under periodic illumination of 395 nm UV irradiation (13.5 mW/cm ²) at zero bias.	141
Figure 5.9:	Conductivity of PEDOT: PSS/Nafion bilayer with different Nafion dilution concentrations.....	142
Figure 5.10:	The semi-logarithmic plot of responsivity and detectivity of the optimized device Nafion 1:4 and without Nafion at bias voltage from - 1 to 1 V, under 395 nm UV illumination.	144
Figure 5.11:	(a) On-off cycles of Nafion 1:4 photodiodes under 395 nm LED light (3 mWcm ⁻²) at 100 Hz and (b) at 1000 Hz (c) Singular cycle showing the rise and decay time of the resultant perovskite PD.....	146
Figure 5.12:	Time-dependent photoresponse of (a) Nafion 1:4 photodiode (b) without Nafion photodiode (b) before and after continuous exposure to 395 nm LED light for 15 hrs.	148

Figure 5.13:	(a) Contact angle of water on PEDOT-PSS, Without Nafion, (b) Contact angle of water on PEDOT-PSS, Nafion 1:4.	149
Figure 5.14:	(a) Electron-only device (ITO/LiF/PEDOT:PSS or Nafion/LiF/Al) and (b) Hole-only device (ITO/PEDOT:PSS or PEDOT:PSS/Nafion/Au).....	150
Figure 5.15:	(a) Semi-log J–V curve of photodiode based on Nafion 1:4 HTL under different UV light intensity, (b) The relationship of Jsc and Voc parameters of self-powered Nafion 1:4 based photodiode with various UV light intensity.	152
Figure 5.16:	The relation between (a) photocurrent and light intensity and (b) log of photocurrent vs log of light intensity at different reverse biasing voltages of Nafion 1:4 photodiodes.....	154
Figure 5.17:	(a) Semi-log photosensitivity of self-powered based Nafion 1:4 under different UV light intensity (b) Sensitivity versus light intensity at 0 V bias.	155
Figure 5.18:	The change of responsivity and detectivity of self- powered Nafion 1:4 based photodiode with illumination intensity.	156
Figure 5.19:	ON/OFF switching behavior of Nafion 1:4 photodiode under the influence of various illumination intensities.	157

LIST OF TABLES

Table 1.1:	Classification of ultraviolet (UV) radiation.....	7
Table 3.1:	Details all of the solvents employed in the thesis. They were used in their anhydrous form without any further purification.	73
Table 4.1:	Performance comparison of PAPbBr ₃ FETs based on different PVK blending ratio.....	121
Table 4.2:	Comparison of mobility of low dimensional perovskites based FETs from literature.....	122
Table 5.1:	Performance comparison of PEA ₂ PbBr ₄ UV photodiode devices based on HTL with and without Nafion at 0V bias.....	144
Table 5.2:	Comparison of the characteristic parameters of self-powered photodetectors reported in the literature with that of reported in this work. (Applied voltage = 0 V).....	147

LIST OF SYMBOLS AND ABBREVIATIONS

ω	:	Angular velocity
ϕ	:	Injection barrier
τ_{rise}	:	Rise time
τ_{decay}	:	Fall time
σ	:	conductivity
λ	:	Wavelength
μ	:	Charge carrier mobility
1D	:	One-dimensional
2D	:	Two-dimensional
2θ	:	Diffraction angle
3D	:	Three-dimensional
AFM	:	Atomic force microscopy
Al	:	Aluminium
Au	:	Gold
c	:	speed of light in a vacuum
CB	:	Chlorobenzene
CBM	:	Conduction band maximum
C_i	:	Capacitance per unit area
D	:	Detectivity
DFT	:	Density functional theory
DMF	:	Dimethylformamide
DMSO	:	Dimethyl sulfoxide
DOS	:	Density of states
E_c	:	lowest conduction band edge

EDX	:	Energy dispersive x-ray spectroscopy
E_F	:	Fermi level
E_g	:	Energy Bandgap
EQE	:	External quantum efficiencies
ETL	:	Electron transport layer
E_v	:	Highest edge of the covalent band
f	:	Frequency bandwidth
FESEM	:	Field-emission scanning electron microscopy
FET	:	Field-effect Transistor
FET	:	Field-effect Transistor
GIXRD	:	Grazing-Incidence X-ray diffraction
h	:	Planck's constant
HECO	:	High-energy cut-off
HOMO	:	Highest occupied molecular orbital
HTL	:	Hole transport layer
I_D	:	Drain current
IP	:	Ionization potential
IPA	:	Isopropyl alcohol
ITO	:	Indium Tin Oxide
I-V	:	Current-voltage
J_{dark}	:	Dark current
J_{ph}	:	Photocurrent
$k_B T$:	Thermal energy
LDR	:	Linear dynamic range
LECO	:	Low-energy cut-off
L_{light}	:	Light intensity

LUMO	:	Lowest unoccupied molecular orbital
MIS	:	Metal insulator semiconductor
MOSFETs	:	Metal oxide semiconductor field-effect transistors
OSC	:	Organic semiconductors
PAPbBr ₃	:	Propylammonium lead bromide
PC	:	Photoconductive
PC ₆₁ BM	:	[6,6]-phenyl C61 butyric acid methyl ester
PD	:	Photodiode
PEA ₂ PbBr ₄	:	Phenethylammonium lead bromide
PEDOT: PSS	:	Poly (3,4-ethylene dioxythiophene): poly(styrene sulfonate)
PL	:	Photoluminescence
PTFE	:	Polytetrafluoroethylene
PV	:	Photovoltaic
PVD	:	Physical vapor deposition
PVK	:	Poly (9-vinylcarbazole)
q	:	Elementary charge
R	:	Responsivity
S/D	:	Source and drain electrode
t	:	thickness
UPS	:	Ultraviolet photoelectron spectroscopy
UV	:	Ultra-violet
VBM	:	Valence band maximum
V_{DS}	:	Drain-source voltage
V_{GS}	:	Gate-source Voltage
V_{TH}	:	Threshold voltage
XRD	:	X-ray diffraction

LIST OF APPENDICES

Appendix A: Calculation of lattice parameter from 2θ versus intensity data...	189
Appendix B: Grain size calculation from FESEM images using imageJ.....	190

Universiti Malaya

CHAPTER 1: INTRODUCTION

1.1 Introduction

Since the 1960s, Silicon has been the favoured material choice for semiconductors, making up 95% of the device types available in the market. However, it presented some long-term difficulties. Silicon cannot continue producing gains without the ability to shrink ICs further. Another drawback of silicon solar cells is their manufacturing requires expensive ultra-high-purity Silicon. Also, the carbon monoxide produced by silicon mining and manufacturing can cause environmental damage. The energy demand for silicon became a real obstacle to fulfilling Paris Accords. The importance of silicon technology will continue to grow however other potential technologies which can serve as silicon replacements using organic/hybrid electronics should be considered.

Organic electronics technologies are based on organic semiconductors (OSC) that can be mass-produced cheaply and in large quantities. If these organic semiconductor-based devices can target new applications and products unavailable with conventional inorganic electronics, it can offer a tremendous economic advantage. Since organic semiconductors are produced at low temperatures, they can be deposited onto practically any surface, from the inflexible silicon wafer to the pliable polymer to a person's skin, paper, or clothing. Active electronic anti-counterfeiting and tracking devices incorporated into banknotes are just one example (Figure 1.1a)(Zschieschang et al., 2011). Other examples include flexible and rollable displays(Figure 1.1b), sensors(Figure 1.1c), bio-electronics(Figure 1.1d), radio frequency identification (RFID) tags(Figure 1.1e), thermoelectrics(Figure 1.1f), disposable and wearable electronics, and more (Bandakkanavar, 2017; Baumbauer et al., 2020; C. S. Kim et al., 2018; Steve Kelly, 2013)

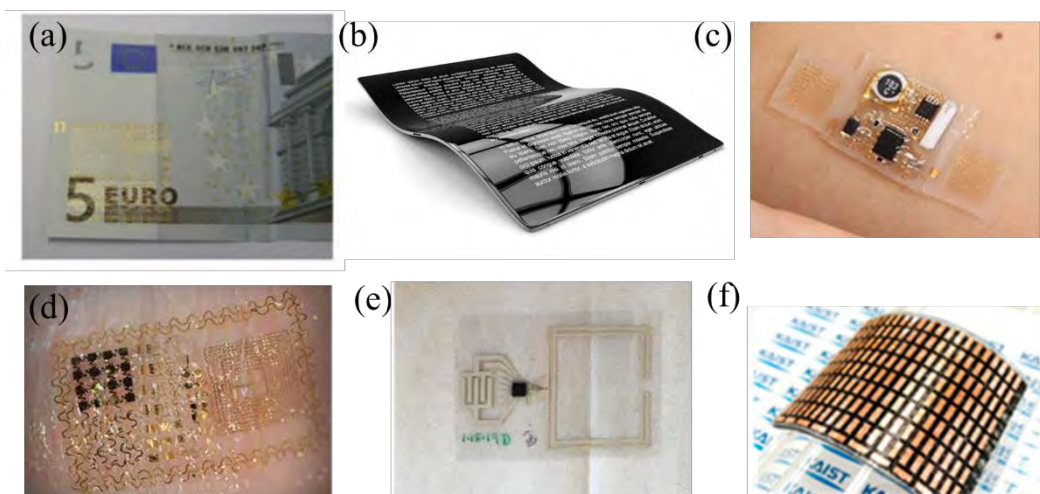


Figure 1.1 Organic semiconductor-based applications, (a) Bank notes, (b) Flexible display, (c) Sensors, (d) Bio-electronics, (e) RFID, (f) Thermoelectric(Picture source from: www.azom.com, www.electronicweekly.com, www.chemistryworld.com, arcasystems.com and www.rsc.org).

While OSC performance continues to improve, a new class of semiconductors called organic-inorganic hybrid perovskites has emerged, intending to combine the best features of both classes while avoiding their drawbacks. Hybrid perovskites are a newly found substance initially used in semiconductor circuits in 2009(Kojima et al., 2009). Hybrid perovskites have demonstrated remarkable optoelectronic properties, such as high light-harvesting capability, light absorption coefficient ($\sim 10^5 \text{ cm}^{-1}$) and high photoluminescence quantum yield (PLQY), narrow-band emission, and low exciton binding energies ($< 50 \text{ meV}$). Moreover, the organic groups of hybrid perovskite materials make them soluble, allowing for easy processing (Im et al., 2012; Pang et al., 2014), while the inorganic interactions aid in optimizing the crystal structure and charge transfer(Antonietta Loi & Hummelen, 2013; Mitzi et al., 1999). Miyasaka and his colleagues were among the first to use solar cells. Created using a dye-sensitized solar cell architecture and with a mesoporous TiO_2 layer on top of the perovskite as an electron collector, they achieved 3.8% power conversion efficiency (PCE) (Kojima et al., 2009).

The PCE of perovskite solar cells has made significant progress from 3.8% to 25.7% (Min et al., 2021) for a single junction and 31.3% (NREL, 2021) for a tandem architecture. Likewise, since their first display in 2014, perovskite light-emitting diodes (LEDs) have seen substantial development. In just a few short years, the perovskite LED industry has seen a rise in external quantum efficiency of more than 20% (Z. K. Tan et al., 2014). Whereas several decades are needed for other types of inorganic solar cells to reach this, most photovoltaic materials never even reach 20% efficiency. Data for certified efficiency records for all perovskite solar cell types are plotted against data for inorganic solar cell types in Figure 1.2, which spans the years 1991 through 2020 (NREL, 2021).

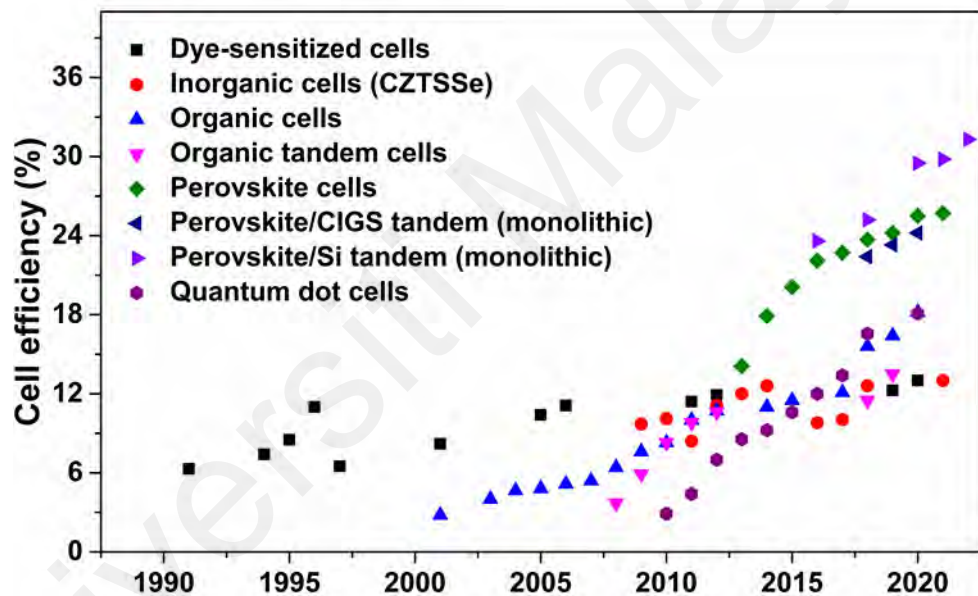


Figure 1.2: National Renewable Energy Laboratory's last updated graph for record cell efficiencies (Dec 2021) from 1991 to 2021, perovskites solar cells compared to their inorganic cell counterparts (Picture source from www.nrel.gov).

On the other hand, low stability towards moisture and temperature is one of the critical difficulties inhibiting the practical implementations of 3D hybrid perovskite-based optoelectronic devices, despite their stunning performance and inexpensive fabrication cost. To overcome these difficulties, low-dimensional perovskites with much-improved stability have been integrated into the active layers of various device designs, demonstrating performance comparable to that of their 3D counterparts.

Low-dimensional perovskites are generally categorized as two-dimensional (2D) and one-dimensional (1D) perovskites. Figure 1.3 demonstrates hybrid perovskites with varied molecular dimensions. Due to quantum size effects, developed low-dimensional hybrid perovskites, such as 2D perovskite nanoplatelets and 1D perovskite nanowires, show unique characteristics to their bulk counterparts.

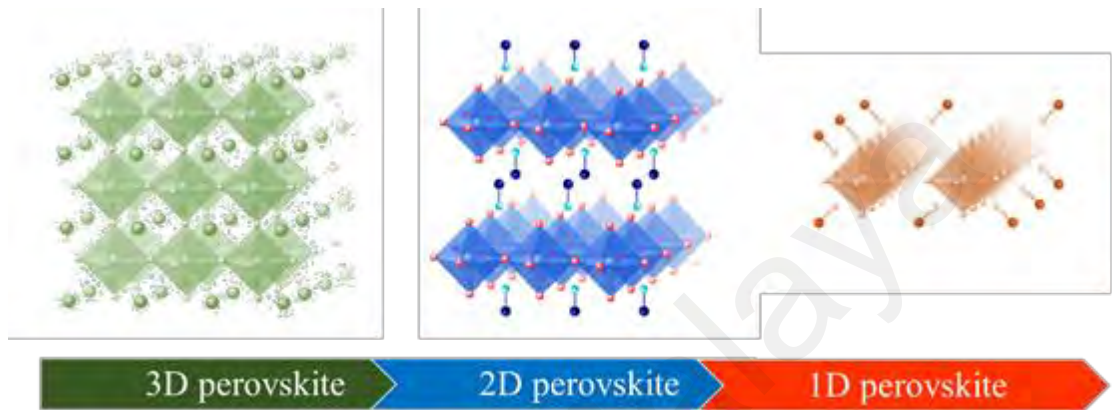


Figure 1.3: Schematic crystal structures of 3D perovskite, 2D perovskite and 1D perovskite[Picture source from (Zhou et al., 2019)].

Despite the intrinsic charge carrier mobilities, research into perovskite-based field-effect transistors and photodetectors has been considerably less intensive. Furthermore, the number of papers containing the keywords "perovskites" AND "Field-effect transistor" OR "photodetector" from the Web of Science-Core Collection climbs to 4000 in the span of five decades beginning in 1970 and continuing through 2020, displayed in Figure 1.4. Nevertheless, research on other optoelectronic devices based on perovskites, such as transistors and photodetectors are motivated and sustained by the high projected charge carrier mobility and the ease of processing employing scalable, cost-efficient manufacturing techniques, as demonstrated for large-area solar cell modules.

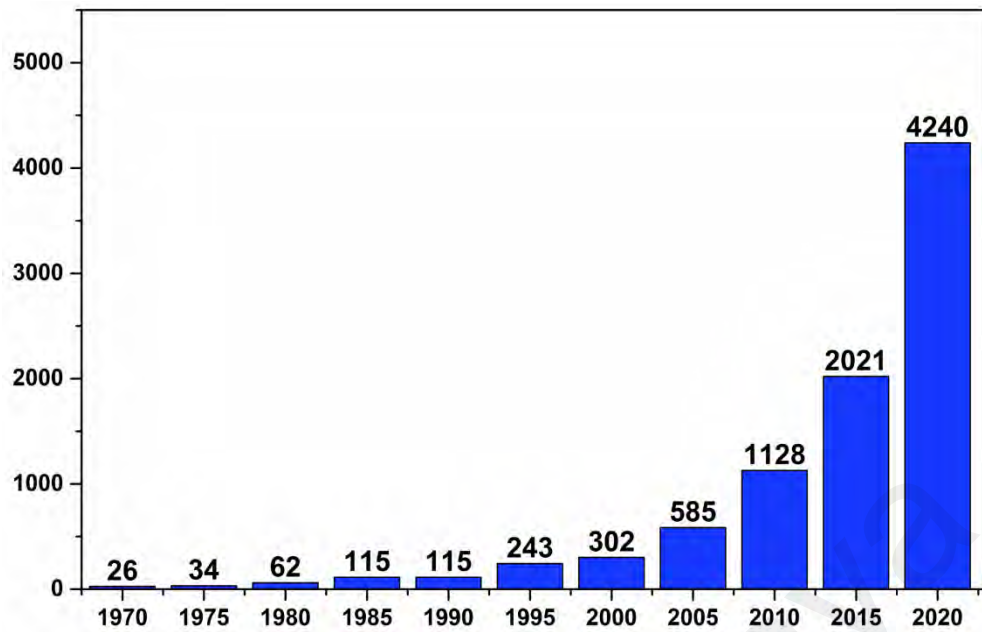


Figure 1.4: The total number of publications from the Web of Science-Core Collection with the topic keywords "perovskite" AND "field-effect transistor" OR "photodetector" OR "photodiode".

1.2 Motivations

1.2.1 Field-effect transistor (FET)

In today's consumer electronics, field effect transistors (FETs) play a crucial role. There are three electrical connections in a FET: the source, the drain, and the gate. In a thin-film FET, the channel is made of a thin film of semiconductor material. A FET operates because the gate terminal regulates the channel resistance between the drain and source terminals (Braga et al., 2018). When a voltage is provided to the gate terminal, the channel resistance of a FET can be adjusted capacitively using the electric field. Low-dimensional perovskites have an advantage over 3D perovskite materials for FETs due to their remarkable crystal growth orientation and facile fabrication method. The replacement of costly semiconductors with these low-dimensional hybrid perovskites will reduce transistor costs due to the inexpensive cost of low-dimensional perovskites compared to standard inorganic semiconductors, for example, single crystal Si.

Nonetheless, there remain challenges in the quest for research and the creation of low-dimensional perovskite transistors and circuits with good performance. Electronic devices, such as transistors, rely on the efficient transport of carriers through the bulk of the material and the charge injection mechanism from the contact electrodes into the active layer. A high potential energy barrier between the contact electrode and the transporting band in the device causes charge injection to be poor, and contact resistance will dominate the operation of the device. However, the band alignment at the interface depends on factors like the electrode work function, interfacial traps or dipoles. Investigating these factors is one of the goals of this thesis; this will be further addressed in Chapter 4.

1.2.2 Photodetector

Ultraviolet (UV) light detection is essential for many scientific and industrial uses, particularly in human health monitoring. UV rays are broken down into the categories shown in Table 1.1 (Monroy et al., 2003). Since UVA radiation (315-400nm) has a longer wavelength, more are reaching Earth's surface. A deeper layer of skin may be breached, resulting in photo-ageing over time. It is well established that too much exposure to UVA radiation can lead to skin cancer, sunburn, premature skin ageing, eye damage, and other serious health problems, as illustrated in Figure 1.5 (Bald et al., 2014; Bouilly-Gauthier et al., 2010; Strickley et al., 2019; S. Q. Wang et al., 2001).

Table 1:1: Classification of ultraviolet (UV) radiation

UVA (320nm-400nm)	Regarding frequency, UVA is the sun's most pervasive and potentially damaging UV light since it may reach deep into the skin (to the dermis).
UVB (280nm-320nm)	A less penetrating kind of ultraviolet radiation than UVA, with a short wavelength to reach more profound than the outermost layer of skin. The Earth's ozone layer blocks some UVB rays, and so can treated glass.
UVC (280nm-100nm)	As the ozone layer absorbs the sun's ultraviolet (UVC) rays, humans are only exposed to UVC through artificial sources like lasers and welding torches.



Figure 1.5: Health problems caused by over UVA radiation exposure (a) skin cancer, (b) premature ageing, and (c) corneal damage (Picture source from ellayelabanico.com and www.aao.org).

Hence, self-powered photodetectors that operate with low power consumption or without any external power source are critical for guaranteeing that UVA illumination intensity levels are below acceptable limits for human beings. Photodetectors, often known as PDs, are light sensors capable of transforming light signals into electrical signals. PD's operation is governed by light absorption, which results in the production of a photocurrent or photovoltage inside the device.

This photocurrent or photovoltage can then be processed by the readout electronics that are typically used. Primarily, there has been a recent interest in producing self-driven or self-powered photodetectors. Self-powered photodetectors can detect incident light at zero bias by employing an internal photovoltaic effect. These photodetectors do not require any additional external power sources. This intriguing function will make devices more trustworthy and suitable for the energy-saving needs of the modern era.

A low-dimensional hybrid perovskite is a suitable approach for UV-A photodetectors attributed to its wide bandgap and strong optical absorption coefficient in the near UV-A range (320 to 400 nm) (Y. Liu et al., 2019; Z. Tan et al., 2016). To that end, this section (**Chapter 5**) of the thesis concentrated on the solution-processed preparation of a self-powered photodiode with a vertical structure optimized for performance in the UVA range. Further, the effects of different light intensities were studied.

1.3 Objectives

This thesis investigated the properties of low-dimensional hybrid perovskites, which refers to Propylammonium lead bromide (PAPbBr_3) and Phenethylammonium Lead Bromide ($\text{PEA}_2\text{PbBr}_4$), by evaluating the performance of fabricated electronic devices, namely FET and photodiode. This research work is aligned with five primary objectives as follows:

- To increase charge injection by modifying the work function of the electrode and increase surface coverage of active layer by incorporating hydrophobic layer.
- To fabricate and enhance mobility of a PAPbBr_3 : PVK blend-based field-effect transistor by reduce the pinholes formed in the perovskite layer by blending polymer through solution processing techniques.

- To fabricate and improve charge transport in self-powered $\text{PEA}_2\text{PbBr}_4$ photodiode by employing interlayer at the hole transport layer and active layer interface.

1.4 Thesis Outline

This thesis consists of six chapters. **Chapter 1** presents a brief introduction to organic-inorganic hybrid perovskite materials. The motivations behind this study and the objectives of this thesis are introduced based on the development of low dimensional inorganic-organic hybrid halide perovskites and the challenges in perovskite field-effect transistor and photodetector applications.

Chapter 2 presents a review of the literature regarding organic-inorganic halide perovskite materials. The working principle of FETs and photodetectors is also described.

Chapter 3 introduces fabrication and characterization methods for developing perovskite-based FETs and photodetectors. The following section of the chapter is devoted to the perovskite thin film morphological and electrical characterization techniques used in this thesis, for example, X-ray diffraction (XRD), Grazing-Incidence X-ray diffraction (GIXRD), optical absorbance spectrum, atomic force microscopy (AFM), Field-emission scanning electron microscopy (FESEM), Ultraviolet photoelectron spectroscopy (UPS), contact angle and current-voltage measurement. The principle, instrumental setup and data collection of each technique are also presented in this chapter.

Chapter 4 covers the work function modification of the ITO electrode by employing an interlayer. The role of PVK on perovskite film quality and, consequently, on the device's performance has been studied. The current-voltage (I-V) characteristic has performed the charge carrier behaviour.

The transfer characteristics and UPS results reveal that reducing the energy barrier at the ITO/perovskite interface improves hole mobility.

Chapter 5 reports on the role of the hydrophobic layer in forming homogeneous and densely packed perovskite films to be deposited over the hole transport layer. Subsequently, the underlying physical phenomena of charge carrier transport in photodiode for improved performance.

Chapter 6 summarizes this thesis with achieved critical findings for the overall study and suggests several ideas for future work in optimizing the performance of low-dimensional hybrid perovskites-based electronic devices.

Universiti Malaysia

CHAPTER 2: LITERATURE REVIEW

2.1 Introduction

This chapter covers the literature review regarding the origin of organic-inorganic hybrid perovskite materials and the theory associated with electronic devices applied during this thesis. The general review concerning perovskite materials in terms of their crystal structure and dimension reduction is discussed in Section 2.4. A review emphasizing perovskite-based organic electronic devices is given in Section 2.5. Finally, the physics underlying the operation of organic electronic devices assessed in this study, namely Field-effect transistor and photodetector, is elaborated in Sections 2.7 and 2.8, respectively.

2.2 Semiconductor

A thorough understanding of a semiconductor's functions is necessary before attempting to comprehend what makes perovskites unique. In every solid, electron occupy quantum states characterized by energy, momentum, and spin. The electrons occupy discrete states that, in bulk, form into bands, with prohibited zones with no available states between the bands. The forbidden area, whose minimal width is referred to as the band gap, is a region in which electronic wave function cannot exist. A semiconductor is a substance in which, at absolute zero, all of the states in one band are completely unoccupied while electrons fill all possible states up to the edge of that band. The valence band is the lower energy, filled band, whereas the conduction band is the higher energy, an unoccupied band (see Figure 2.1). In a typical semiconductor, the Fermi level (E_f) is located precisely in the middle of the band gap. It represents the energy of the highest occupied state at absolute zero (Patterson & Bailey, 2009).

An electron must change momentum to conduct electricity, so the system's net momentum is no longer zero. At absolute zero, this is impossible because all the electrons are in the valence band, where there are no vacant states (because it is filled). As a result, there won't be any conduction at absolute zero. Some electrons are moved into the conduction band when heat is introduced, and there are many possible states for electrical transmission. The efficiency of electrical conduction increases with the number of electrons in the conduction band, and the number of electrons promoted to the valence band is correlated with the thermal energy ($k_B T$) ratio to bandgap (ΔE). Therefore, semiconductors become more conductive as the temperature rises or the bandgap closes. The conduction band electrons and the valence band holes created by them can conduct current in a semiconductor. Holes, the gaps left behind by these processes, function as positively charged quasiparticles. In contrast to metals, where only electrons are the predominant charge carrier, electrons and holes are charge carrier in semiconductor (Kittel, 2004).

In intrinsic semiconductors, the electronic structure of the pure material directly determines the electrical behavior. The semiconductor is considered extrinsic when impurity atoms determine its electrical properties. As shown in Figure 2.1(a), the electron band structure of intrinsic semiconductors is characterized by a filled valence band at 0 K, separated from a conduction band devoid of electrons by a relatively small forbidden band gap, typically less than 2eV. Intrinsic semiconductors have limited usage on their own. They are neither good conductors nor good insulators; their conduction depends significantly on temperature. Foreign compounds or impurities introduced into the crystal can change the material's characteristics. Dopants are another name for these impurities.

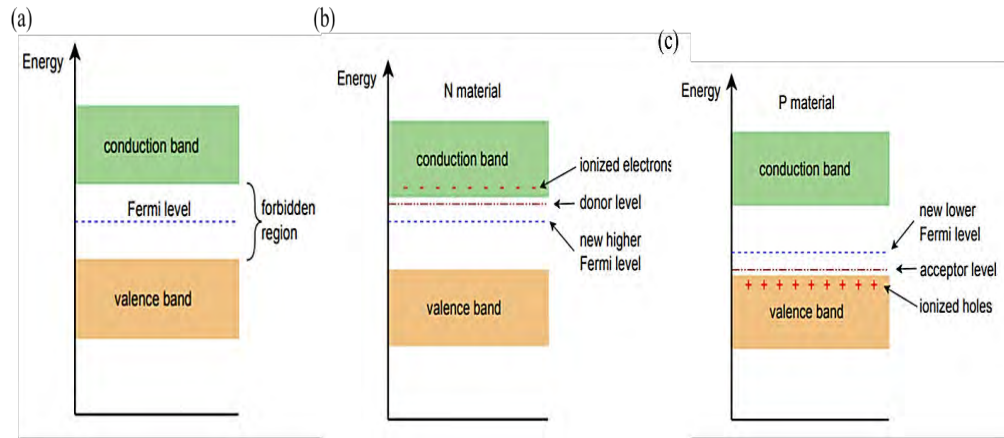


Figure 2.1: (a) Energy diagram for an intrinsic semiconductor, (b) Energy band diagram of N-type semiconductor, (c) Energy band diagram of P-type semiconductor [Picture source from (Báez-López & Guerrero-Castro, 2011)]

An extrinsic semiconductor, or doped material, is a crystal with a dopant added. There are two possible varieties of semiconductors. The first is N-type material, whereas the second is P-type. Adding pentavalent impurities, a dopant with five electrons in its outer shell produces N-type material, producing a donor or additional electron. The donor electrons' energy level lies above the conduction band's lowest point (see Figure 2.1(b)). In other words, the distance between the donor level and the conduction band's maximum is considerably lower than the band gap. Because of this, it is relatively simple for these donor electrons to enter the conduction band, where they can then become free ionized electrons and leave behind ionized holes.

On the other hand, P-type material is produced by the addition of a trivalent impurity, which is an impurity that has three electrons in its outer shell. Thus has a hole, an area where one electron is missing. In this sense, trivalent impurities are sometimes referred to as acceptors. This is demonstrated by the energy band diagram for P-type material, shown in Figure 2.1(c). The valence band now lies closer to the Fermi level (Báez-López & Guerrero-Castro, 2011).

2.3 Semiconductor-Light Interactions

Semiconductors' interactions with light are among their more intriguing characteristics. A low-energy photon cannot be absorbed because it cannot supply the energy necessary to get the electron across the bandgap since they have a large region where electrons are not allowed to enter. Therefore, until the photon energy equals the energy of the bandgap, semiconductors will not absorb any light. The material becomes highly absorbent once the photon energy is more significant than or equal to the bandgap because there are suddenly many states available for the electron to be stimulated into, as depicted in Figure 2.2. The absorbed photon creates a free electron and a hole. In a semiconductor with flat bands, the absorption spectrum would follow a step function, with no absorption below the bandgap and high absorption above the bandgap. In an actual semiconductor, the bands are curved, indicating that the number of absorbable states does not precisely follow a step function. Therefore, the absorption beginning is not entirely vertical, but the concept remains the same. An electron decays to its lowest energy state when driven to a level much above the bandgap.

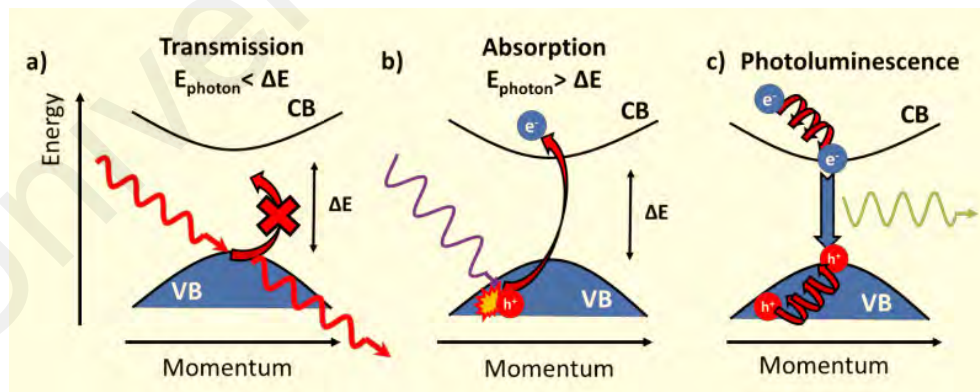


Figure 2.2: (a) A low-energy photon is transmitted because it cannot transport electrons from the valence band (VB) to the conduction band (CB) across the bandgap, (b) A high-energy photon is absorbed by promoting an electron, (c) An electron and hole relax before recombining and emitting a photon by photoluminescence[Picture source from (Harwell, 2018)].

The first step in this process is relaxation, during which the electron rapidly moves among the different states in the conduction band while releasing heat as it does so. This is a highly rapid process; typically, the electron will reach the band edge in less than a picosecond. A similar process happens when a hole is formed in the valence band, but instead of "dropping down" to the conduction band minimum (CBM), holes "bubble up" to the valence band maximum (VBM). When an electron reaches the band edge, it cannot traverse the bandgap by phonon relaxation, and it must decay via photoluminescence (PL).

PL is a slower process in which the electron radiatively recombines with a hole on the opposite side, releasing energy as a photon. Therefore, when more energy than the bandgap is used to excite a semiconductor, the semiconductor will always produce a photon with the same energy as the bandgap and release any surplus energy as waste heat. One would anticipate that the emission spectrum would resemble a delta function in a perfect semiconductor with the bandgap energy at its centre. The structure of the energy bands and interactions with phonons and defect states will all work together to broaden the spectrum in the actual material.

Indirect bandgap semiconductors are a prominent exception to these norms. Figure 2.3(b) depicts the band diagram of semiconducting materials with an indirect bandgap, where the minimum of the conduction band and the maximum of the valence band are not at the same momentum. In order to cross the bandgap, an electron must absorb both a photon and a phonon simultaneously. A phonon is a quasiparticle that is generated when a lattice undergoes vibration. Since this is much less likely than just absorbing in a single photon, an indirect bandgap semiconductor's absorption and emission are much weaker than those of a direct bandgap semiconductor.

Silicon, which has a direct bandgap of 3.3 eV and an indirect bandgap of 1.14 eV, is the most extensively used semiconducting material and a classic example of an indirect bandgap material. Silicon solar cells require a thickness of hundreds of microns, as compared to hundreds of nanometers for direct bandgap materials. Silicon's absorption spectrum shows this effect vividly compared to that of a direct bandgap semiconductor like gallium arsenide (GaAs), as described in Figure 2.3(c). GaAs exhibit a highly distinct absorption step around its bandgap at 900 nm (Palik, 2012), corresponding to direct bandgap absorption. Due to the bandgap's indirect nature, silicon's absorption at its bandgap of 1100 nm occurs more gradually, whereas the absorption at 400 nm corresponds to the direct bandgap.

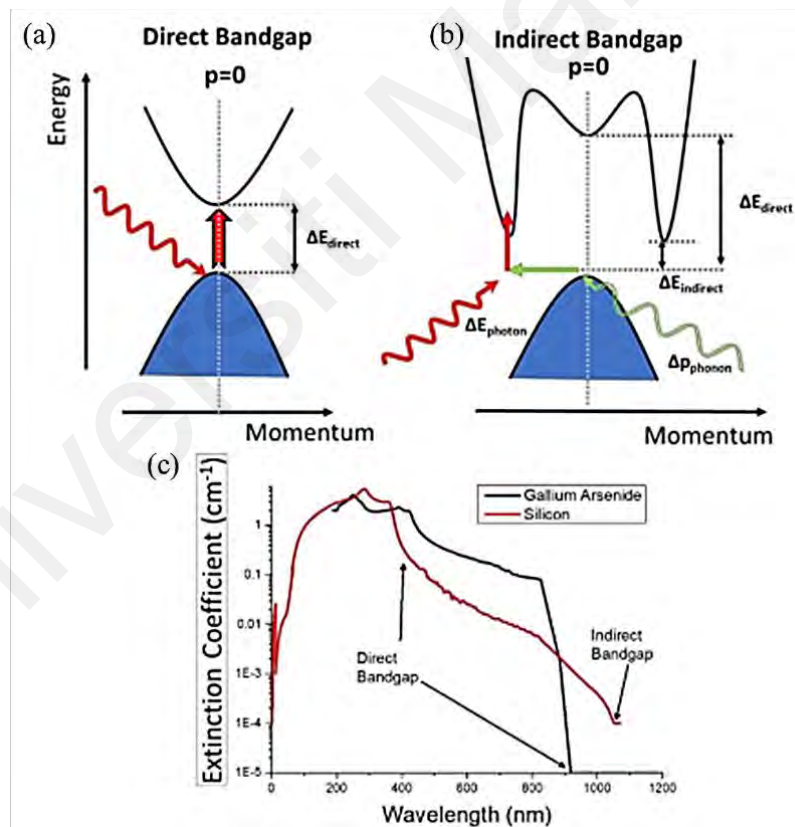


Figure 2.3: (a) A semiconductor with a direct bandgap, in which an electron can be easily moved across the bandgap by a photon, (b) Indirect bandgap, in which accelerating an electron from the VBM to the CBM requires absorbing both a photon for energy and a phonon To be absorbed without the participation of a phonon, a photon's energy must be more significant than ΔE_{direct} , (c) comparing the absorption constants of silicon (indirect) and GaAs (direct).[Picture source from (Palik, 2012)].

2.4 Organic semiconductor (OSC)

Organic semiconductors (OSC) are carbon-based compounds, frequently based on conjugated polymers (Forrest, 2020). OSCs have a direct bandgap. Like inorganics, a linear combination of atomic orbitals generates energy levels. The bands in inorganics, however, derive from the overlap of free electron wave functions with a crystal lattice. In contrast, the bands in OSCs originate from the overlap of p orbitals from π bonds in carbon-carbon double bonds. The energy gap between the lowest unoccupied molecular orbital (LUMO) and the highest occupied molecular orbital (HOMO) is what creates the bandgap(Forrest, 2020).

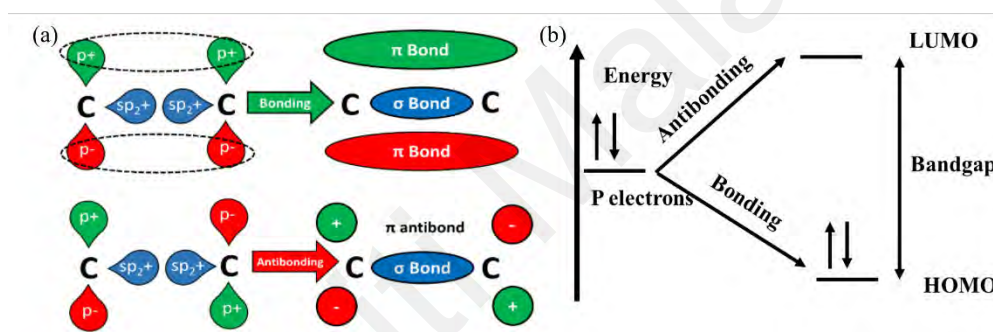


Figure 2.4: (a) A $C=C$ double bond's π bond and anti-bond formation. Due to the electrons' average proximity to the carbon atoms, the bonding orbital has a lower energy than the anti-bond, (b) The mechanism by which the bonding separates the energy levels into a HOMO and a LUMO[Picture source from (Harwell, 2018)].

Two carbon atoms are joined together by a sigma bond and a pi bond to form a double bond. The pi bond comprises two p orbitals that are perpendicular to the bond and have a slight overlap, whereas the sigma bond comprises two sp^2 hybridized orbitals in the plane of the bond. Figure 2.4(a) shows that this weaker bond makes a cloud of electrons above and below the bond. The energy levels of carbon are split into two configurations, which include bonding (constructive interference of wave functions) and antibonding (destructive interference) configurations.

Since the bonding orbitals have lower energies than the electrons in an isolated carbon, they can accept all available electrons to form the HOMO, which is the OSC's version of a valence band. Due to the antibonding orbitals' higher energy than the original carbon, they are left vacant and form the LUMO (equivalent to the conduction band). By altering how efficiently the orbitals in the bond may overlap, the bandgap the difference in energy between the HOMO and LUMO can be changed. On the other hand, an OSC molecule consists of a lengthy chain of carbon atoms with single and double bonds in alternating positions throughout the chain. This is known as a conjugated chain, and in this case, the isolated double bonds will combine to form a single, long, delocalized cloud in which the electrons are free to flow up and down the chain. This particular chain has two accessible electrons for every repeat unit, which indicates that the HOMO level is filled, resulting in the chain acquiring the properties of a semiconductor. The simplest conjugated polymer, polyacetylene, depicted in Figure 2.5, illustrates how this happens.

Closer examination reveals that the overlap between the p orbitals can occur over the single and double bonds. It can be represented as a line of alternating single bonds with a π bond over each double bond. A more accurate representation is that the p orbitals overlap in a chain, creating a single cloud of delocalized charge across which the electrons can freely flow. Consequently, the polymer's conjugated chain can conduct electricity. Polythiophene, polyfluorene, and polyphenylene vinylene are just a few examples of conjugated polymers. These all have unique characteristics that can be further fine-tuned by incorporating other functional groups into the essential backbone.

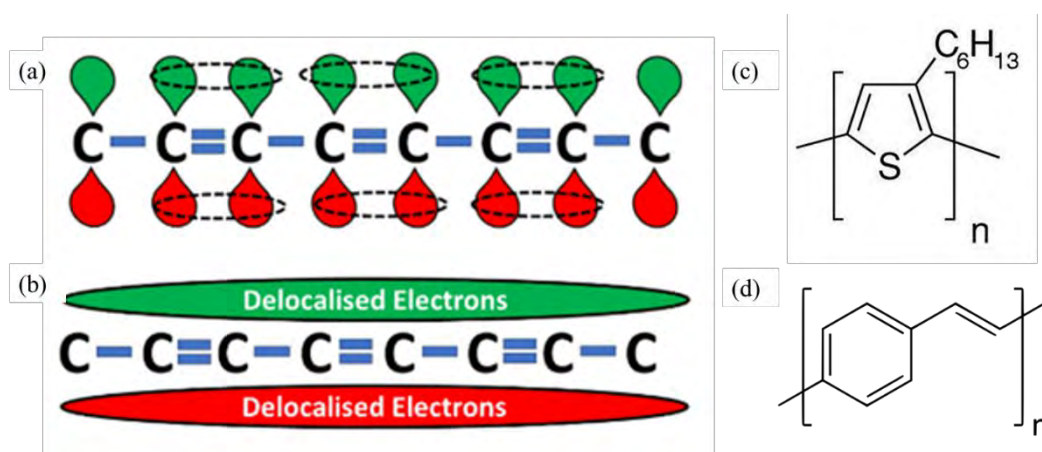


Figure 2.5: (a) The double and single bonds that make up a conjugated polymer, (b) the formation of electron-conducting cloud, for example, (c) poly-3-hexyl thiophene, (d) polyphenylene vinylene[Picture source from (Labram, 2011)].

An essential benefit of this method for fabricating semiconductors is that the OSC can be modified by adding functional groups to render it soluble in common solvents like chloroform. This drastically reduces the complexity of device production by making it possible to print components directly from a solution at low temperatures rather than growing a single crystal. Thus, OSC devices may be far less expensive and more generally applicable than inorganic devices. Lastly, the carbon structure's adaptability allows for a great deal of leeway in molecular design, which means that a material can be fine-tuned to fit the needs of a device perfectly.

2.5 Organic-inorganic halide perovskite material

The name 'perovskite' refers to the Calcium titanate mineral form (CaTiO₃), a mineral discovered by the German mineralogist Gustav Rose in 1839. It was named after the Russian mineralogist Lev Perovski (Sasaki et al., 1987). Since then, the name "perovskite" has broadly referred to a group of compounds that share calcium titanium oxide's crystalline structure. Kojima et al. were the first to successfully demonstrate the use of organometal halide perovskite in solar cells in the year 2009 (Kojima et al., 2009).

Henceforth, these halide perovskite materials with the general formula ABX_3 (where A and B are cations and X is a halide anion) have attracted significant scientific interest in solar cells and other optoelectronic applications. The octahedra (BX_6) in Figure 2.6 represents the characteristic three-dimensional structure of such a crystal. It is possible to create a wide variety of perovskite materials by combining 'A,' 'B,' and 'X' ions. 'A' could be a monovalent organic cation like methylammonium ($CH_3NH_3^+$) or formamidinium ($HC(NH_2)_2^+$) or a metal cation like Cs^+ , whereas 'B' could be a divalent metal ion like Pb^{2+} or Sn^{2+} . These cations have bonded with the halide anion (X), which can be Cl^- , Br^- , or I^- . It's also possible for this anion to form with several halide elements. Many publications have shown that the bandgap can be continuously tuned by integrating two halides (for example, I- and Br-)(Kojima et al., 2009; Noh et al., 2013).

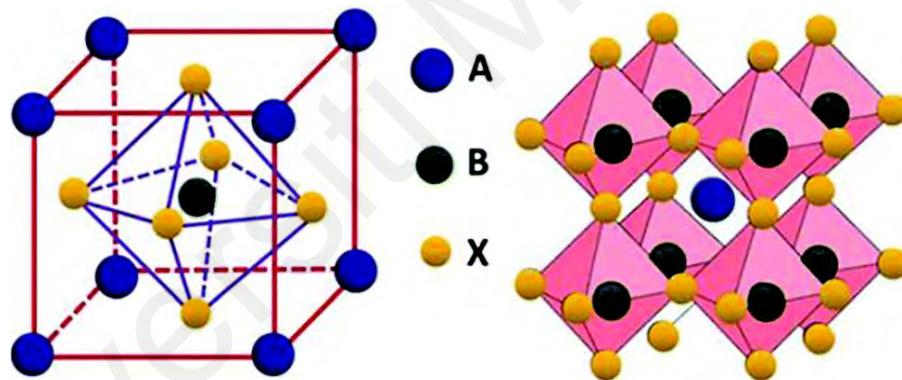


Figure 2.6: Crystal structure of ABX_3 perovskite with the origin centred at (a) the B site and (b) the A site [Picture source from (Das et al., 2019)].

While the A-site cations have a minor impact on the electrical characteristics, they have been proven to directly affect the creation of a close-packed perovskite structure (Borriello et al., 2008). They work to maintain charge neutrality and serve as "fillers" between the layers of inorganic octahedra. When a small cation, such as cesium (Cs^+), methylammonium ($CH_3NH_3^+$ or MA^+), or formamidinium ($HC(NH_2)_2^+$ or FA^+), occupies the A site, 3D symmetry is attained. However, the inclusion of bigger cations can break the 3D cage of octahedra (Boix et al., 2015).

As the name suggests, the B metal cation sites in lead-based halide perovskites are occupied by divalent Pb^{2+} ions, which contribute to creating a lower conduction band. Monovalent halide anions inhabit the X anion sites (I-, Br-, and Cl-), which contribute to the development of the upper valence band (Walsh, 2015). CBM is made up of the $6p$ -orbital of Pb and the $5p$ -orbital of I, whereas the VBM is primarily derived from the $5p$ -orbital of I with a minor contribution from the $6s$ -orbital of Pb (Figure 2.7b) (T. Zhao et al., 2016). For example, the band gap of 1.5 eV forms between the unoccupied Pb p orbital and the occupied I p orbital in the perovskite $\text{CH}_3\text{NH}_3\text{PbI}_3$, where Pb and CH_3NH_3 donate one and two electrons to the three I ions, respectively. While giving one electron to the Pb-I framework, the CH_3NH_3 molecule does not significantly contribute to the band edge (see figure 2.7a) (Yin et al., 2014). Figure 2.7 (c) shows that the $6s$ -orbital of Pb and $5p$ -orbital of I are centred on the atomic nuclei, displaying an ionic bond. The CBM's $6p$ -Pb orbitals and $5p$ -I orbitals are antibonding.

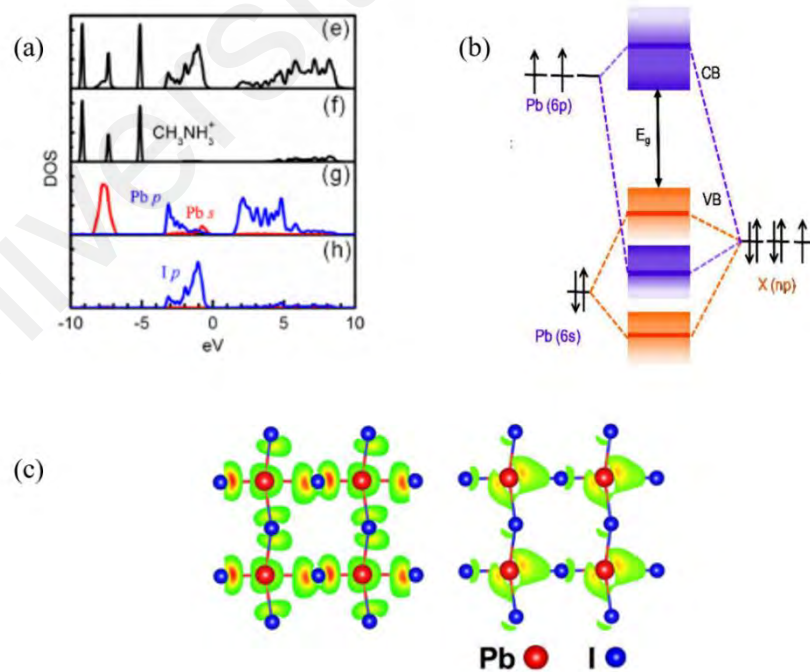


Figure 2.7: (a) Total DOS and CH_3NH_3^+ , Pb and I partial DOS (Yin et al., 2014) (b) Schematic of APbX_3 bonding/antibonding orbitals showing valence band (VB) and conduction bands (CB) (Brandt et al., 2015), (c) VBM and CBM electron densities of cubic $\text{CH}_3\text{NH}_3\text{PbI}_3$ [Picture source from (T. Zhao et al., 2016)].

A tolerance factor (TF) discovered by Goldschmidt is extensively used to forecast the creation of a stable 3D perovskite structure, as stated by the following Equation (H. S. Kim et al., 2014):

$$t = \frac{R_A + R_x}{\sqrt{2}(R_M + R_x)} \quad (2.1)$$

R_A , R_M , and R_X are the ions A, B, and X's respective effective ionic radii. Generally, when $0.8 < t < 1$ and octahedral factor, μ in the range of 0.4–0.9 (Mitzi et al., 1995), it is possible to create perovskites with cubic symmetry. Using this method, G. Kieslich et al. (Figure 2.8) estimated TFs for a collection of 13 protonated amines, 21 divalent metals, and eight anionic species. They proposed the synthesis of nearly 600 novel hybrid perovskites (Kieslich et al., 2015).

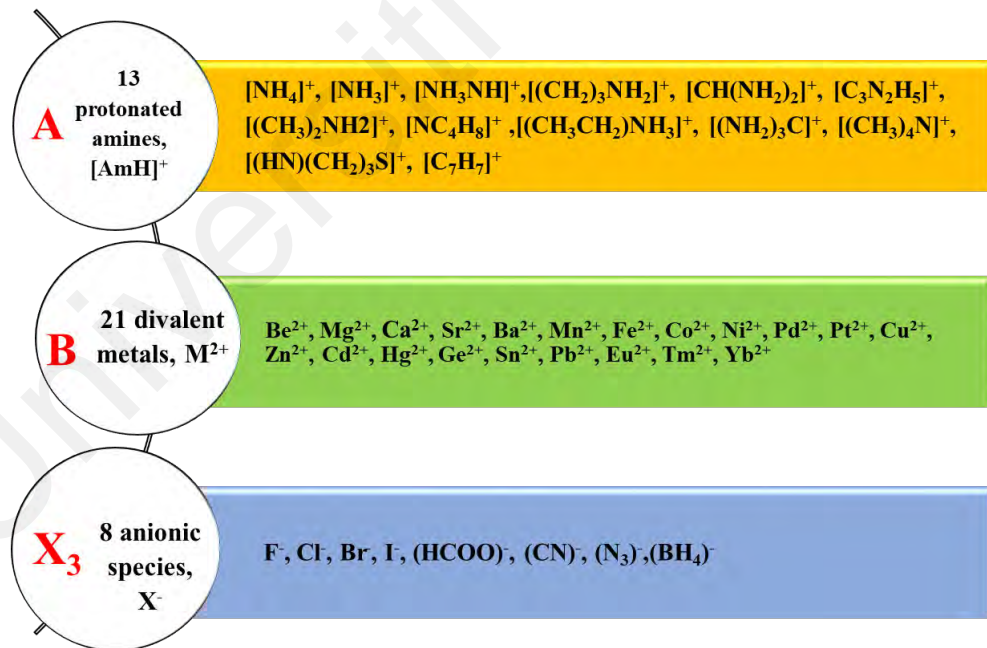


Figure 2.8 summarises the available amines, metal cations, and anions used in TF calculations. Among the total of 2352 TFs found, 742 (562 organic anions based, 180 halide based) fall within the interval ($0.8 < t < 1$).

2.5.1 Key Characteristics of organic-inorganic halide perovskites

2.5.1.1 Tunable Light Absorption and Emission

Most notably, halide perovskites are direct-bandgap semiconductors with very high absorption coefficients in the UV-visible range (up to 10^5 cm^{-1}) (Burschka et al., 2013; M. Liu et al., 2013). Perovskite material's optical-absorption coefficient is highly correlated with its electronic structure. With its high light absorption, perovskite can be used in various optoelectronic devices. Fascinatingly, chemical substitution allows for tuning the bandgap of halide perovskites without significantly altering their essential electrical characteristics. In general, halide perovskite's bandgap and transport properties may be tuned by varying the A site cation, metal cation, and halide anion. However, the easiest way to tune the bandgap of perovskite across the whole UV-visible spectrum is by varying the halide concentration from Cl to Br to I. For instance, it has been found that the bandgaps of $\text{CH}_3\text{NH}_3\text{PbCl}_3$, $\text{CH}_3\text{NH}_3\text{PbBr}_3$, and $\text{CH}_3\text{NH}_3\text{PbI}_3$ are, respectively, 3.1 eV, 2.2 eV, and 1.6 eV. Depending on the halide ions, the bandgap of various mixed halide perovskites ranges from 1.6 eV to 3.1 eV. A change in the cation at the A site will likewise have a very modest impact on the bandgap. Strong photoluminescence (PL) emission is observed in perovskite because of band edge excitonic recombination, which is a consequence of perovskite being a direct bandgap semiconductor. The efficiency with which excitons recombine after being excited by light can differ between halide perovskites. Specifically, iodine-based perovskites ($\text{CH}_3\text{NH}_3\text{PbI}_3$ or CsPbI_3) are well-suited for solar cell and photodetection applications due to their photo-generated solid carrier production and low radiative recombination.

2.5.1.2 Charge transport

An essential feature of any optoelectronic device is its carrier transport. The electronic band structure of semiconductors is intrinsically linked to their capacity to transport charge carriers. The diffusion times are typically linked to the free photo-generated carriers. The average distance an excited carrier travels in a material before recombining is referred to as the diffusion length of that carrier type (Frohna & Stranks, 2019). In a recent study, Dong et al. showed that monocrystalline MAPbI₃ films with diffusion lengths greater than 175 μm under one sun illumination improved carrier mobility (Dong et al., 2015). The high mobility and longer diffusion lengths imply that carriers can move through the film. However, it should be noted that diffusion lengths strongly correlate with film composition and grain size and morphology are sensitive to deposition techniques and processing conditions. While carrier mobilities for single crystal perovskites were more significant than $200\text{ cm}^2\text{V}^{-1}\text{s}^{-1}$, diffusion coefficients and mobilities for polycrystalline perovskites films have been reported to reach $0.05\text{-}0.2\text{ cm}^2\text{s}^{-1}$ and $1\text{-}30\text{ cm}^2\text{V}^{-1}\text{s}^{-1}$, respectively. Carrier lifetimes of perovskite are in range from a few ns to μs (Dequilettes et al., 2019). They depend on composition, morphology, particle size, defects, etc.

2.5.1.3 Defects and traps

The two primary categories of carrier trap states in semiconductors are deep traps and shallow traps. The significant potential for crystal-structure deformation characterizes perovskites, and as a result, trap states are mainly formed near their surfaces and interfaces. Self-trapped excitons, also known as STEs, are excited-state electron-hole pairs (excitons) trapped in the unit cell due to local deformations (Lekina & Shen, 2019). The phenomenon of self-trapped exciton occurs naturally. Excitons may become bonded to the material's impurities or defects, resulting in the formation of trapped excitons.

Creating a halide (cation) dimer molecule inside the ionic lattice is a frequent technique for the hole (electron) self-trapping (S. Kim et al., 2020; R. T. Williams & Song, 1990). For example, the hole in alkali halides forms an X_2^- - dimer by binding together two neighbouring halogen atoms. Figure 2.9 illustrates how carriers can localize into self-trapped states and how the energy of the lattice in the ground and excited changes due to local distortions (shown by coordinate Q).

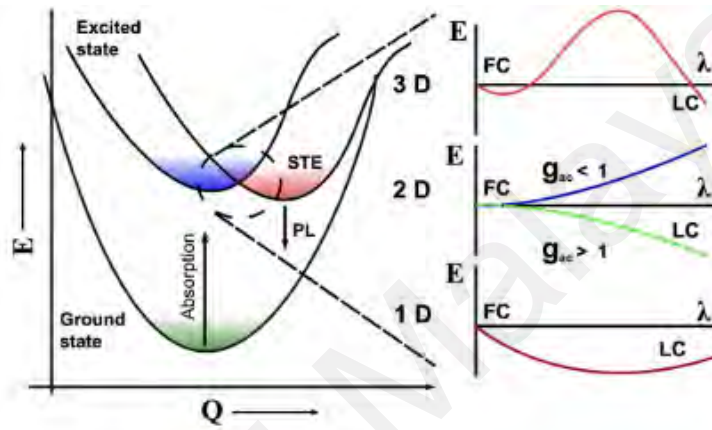


Figure 2.9: Diagram of a self-trapped exciton's general configuration (STE). Coordinate Configuration Q . Dependence of self-trapping energy barrier on dimensionless localization parameter λ for 3D, 2D, and 1D materials [Picture source from (Rondiya et al., 2021)].

Thermally activated atomic vacancies are the most common shallow defects in halide perovskites. When free electrons and holes interact, they have the potential to generate an exciton, which has a high probability of dissociation into its component free electrons and free holes. Excitons can occasionally recombine in one of two ways: either radiatively, which results in photoluminescence, or nonradiatively. Stranks et al found since the electrons and holes spend more time as free charge at higher temperatures and lower excitation fluences than they do bound as excitons, the free electrons are more likely to become trapped at defect sites, leading to nonradiative decay (Stranks et al., 2014). This allows the trap density to vary as a result of temperature.

Shallow defects have a significant impact on perovskite's charge transport capabilities. The bulk trap density for polycrystalline perovskite films was estimated to be 5×10^{14} - $7.5 \times 10^{17} \text{ cm}^{-3}$, while surface trap density was determined to be $\sim 10^{17} \text{ cm}^{-3}$. But it was shown that the trap density in perovskite single crystals could be as low as 10^{10} cm^{-3} . The defects and trap density of perovskite are sensitive to its synthesis method, composition, structure, grain boundaries, etc. Many perovskite optoelectronic devices suffer from defects and trap states.

2.6 Low-dimensional perovskites

Low-dimensional perovskites have been used in the active layers of various device designs, performing on par with their 3D counterparts thanks to their vastly improved stability. These low-dimensional perovskites are typically divided into three categories: two-dimensional (2D), one-dimensional (1D), and zero-dimensional (0D) (see Figure 2.10). Conceptually, low-dimensional perovskites and their derivatives are generated from the parental three-dimensional perovskite. These low-dimensional perovskites are constructed using corner-, edge-, or face-sharing BX_6 octahedra. The 2D layered perovskites, for instance, can be visualized as one-layer thick BX_6 octahedral slices cut from a cubic network of 3D perovskite along various plane directions, such as the orientations $\langle 100 \rangle$, $\langle 110 \rangle$, and $\langle 111 \rangle$. These layered inorganic frameworks can be detached into 1D chained segments or 0D isolated octahedra clusters from $\langle 110 \rangle$ and $\langle 111 \rangle$ orientation, respectively, due to the strong influence of the spatial effect of chosen organic A cations on the deformation of 2D perovskites (P. Chen et al., 2018).

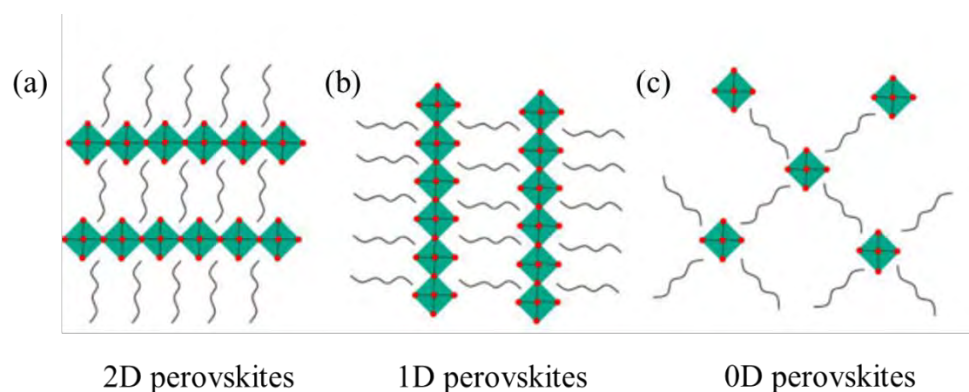


Figure 2.10: A comparison of 2D, 1D, and 0D perovskites (the squares, wavy lines, and brown dots stand for BX_6 octahedral units, bulky organic cations, and small organic cations, respectively)[Picture source from (P. Chen et al., 2018)].

In low-dimensional perovskites, there is no restriction on the length of organic A cations; nevertheless, the diameter of the organic interlayer is restricted because of the area formed by the terminal halides of four near surrounding octahedral. Additionally, using trivalent B cations, severely distorted BX_6 octahedral coordination with the general chemical formula $A_3B_2X_9$ can be formed, which stretches the valence balance rule. The organic A cations used in perovskite compounds need terminal ammonium groups to satisfy the ionic connection between organic and inorganic frameworks. The organic molecule (R) in the majority of known layered perovskites has one or two protonated primary amines attached to its terminal carbon atom, giving rise to the formulae $(RNH_3)_2MX_4$ and $(NH_3RNH_3)MX_4$, respectively (Figure 2.11). In theory, any of the eight halides (i.e., four bridging/four terminal) can form a hydrogen bond with the ammonium head(s) of the organic cations in the holes made by the corner-sharing MX_6 octahedra. Still, the rest of the organic molecule must not interfere with the inorganic M and X cations. Hydrogen bonding can quickly occur with the anionic inorganic substructure in the presence of ammonium cations, hence dictating the orientation of the interlayer organic cations. Therefore, the perovskite structures are ultimately governed by the interplay of the spatial effect, the charge balancing requirement, and the hydrogen bonding (Mitzi, 2001).

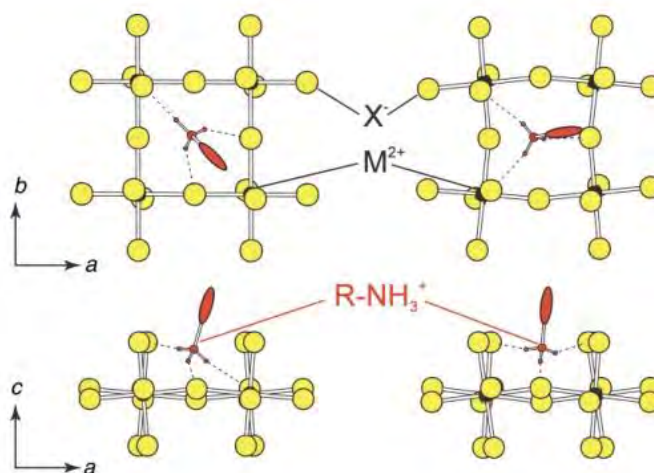


Figure 2.11: The $(\text{RNH}_3)_2\text{MX}_4$ and $(\text{NH}_3\text{RNH}_3)\text{MX}_4$ type structures frequently exhibit two hydrogen-bonding configurations: (a) the bridging halide configuration and (b) the terminal halide configuration [Picture source from (Mitzi et al., 1999)].

2.6.1 Two-dimensional (2D) organic-inorganic hybrid perovskites

The quasi-2D perovskite family adopts the Ruddlesden-Popper crystal structure; a 3D network of corner-sharing BX_6 octahedra layers is restricted between interdigitating bilayers of intercalated bulky alkylammonium cations, creating a hybrid dimensionality between 3D and 2D (D. H. Cao et al., 2015). For this formula for quasi-2D perovskite, n is the number of layers of symmetric corner-sharing octahedra; hence setting $n = \infty$ yields 3D perovskite. Furthermore, the ionic radii and the produced hydrogen bonding of the organic cations used, such as butylammonium cation (BA , $\text{C}_4\text{H}_9\text{NH}_3^+$) (L. Li et al., 2017; Lin et al., 2017; H. Tsai et al., 2016; Z. Wang et al., 2017) and phenethylammonium cation (PEA , $\text{C}_6\text{H}_5\text{C}_2\text{H}_4\text{NH}_3^+$) (Liao et al., 2017; Smith et al., 2014; M. Yuan et al., 2016), determine the distance of the insulating barrier. The conflicting contacts between various organic cations and the shared inorganic frameworks govern the distortion levels of the quasi-2D perovskite crystal structures, which are determined by the differing stereochemical requirements of the used large and small organic cations (Stoumpos et al., 2016).

For example, in the quasi-2D perovskite $\text{BA}_2\text{MA}_2\text{Pb}_3\text{I}_{10}$, the BA and MA cations tend to deform the perovskite structure along the b-axis and the ac-plane, respectively, so that neither is under its ideal spatial arrangement. This means that by adjusting the ratios of the various organic cations, the structural preference of the quasi-2D perovskites can be altered. Quasi-2D perovskites with suitable optoelectronic properties can be easily constructed due to their high structural flexibility, which is enabled by the controlled stacking of layers and the included organic insulating cations. The incorporation of BA cations (20%) into the 3D perovskites led to improved external quantum efficiencies (EQE), further demonstrating the supremacy of this intermediate dimensionality (Xiao et al., 2017).

(a) Phenylethylammonium lead bromide ($\text{PEA}_2\text{PbBr}_4$)

The organic cation known as 2-phenylethylammonium ($\text{C}_6\text{H}_5\text{CH}_2\text{CH}_2\text{NH}^{3+}$, also referred to as PEA or phenethylammonium) is responsible for the formation of 2D layered perovskites denoted as $\text{PEA}_2\text{PbBr}_4$. These perovskites exhibit a crystal structure, as depicted in Figure 2.12, wherein layers of an inorganic semiconductor composed of corner-sharing PbBr_6 octahedra are interleaved with layers of insulating PEA counter cations. The particular organic cation of PEA has been seen to result in the formation of 2D perovskites that exhibit a narrow photoluminescence (PL) peak with a high quantum efficiency. This discovery has facilitated the development of light-emitting diode (LED) devices that can operate at room temperature. Moreover, Bromide-based two-dimensional perovskites have reduced susceptibility to oxidation when exposed to ambient air (Tong, 2020).

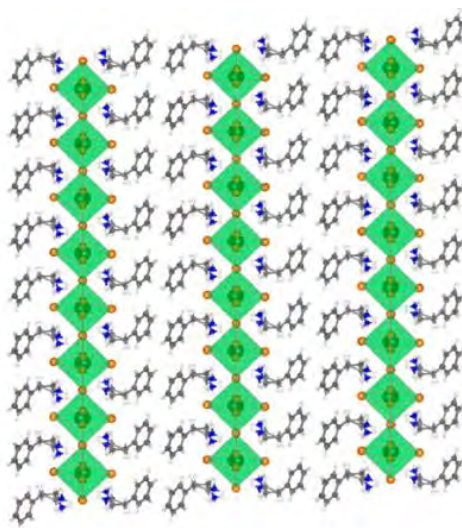


Figure 2.12: The crystal structure of (PEA)₂PbBr₄, also known as 2-phenylethylammonium lead bromide, exhibits a two-dimensional layered perovskite arrangement [Picture source from (D. Liang et al., 2016)].

2.6.2 One-dimensional (1D) organic-inorganic hybrid perovskites

When $m = 1$ (where ‘m’ represents the number of sheets between layers), 1D perovskite frameworks are realized in the family of $\langle 110 \rangle$ orientated perovskites with a generic formula of $A'_2A_mB_mX_{3m+2}$. Incorporating structure-directing iodoformamidinium cation on both sides, the A cation-based dimers consisting of two octahedral BX_6 units are sandwiched, generating infinite chained segments, studying the 1D configuration of $(CH_3SC(=NH_2)NH_2)_3PbI_5$ (Figure 2.13) reveals the importance of the templating influence from specific ammonium cations in this family of compounds (Mousdis et al., 1998). As was previously indicated, the use of cyclohexylammonium cations ($C_6H_{11}NH_3^+$) in perovskites results in a layered structure with the preferred orientation of $\langle 100 \rangle$ (Billing & Lemmerer, 2007, 2009). However, due to the slight change in the structure-directing cations, the dimensionality of these compounds can be lowered from 2D $\langle 100 \rangle$ oriented layers to 1D $\langle 111 \rangle$ oriented chains and 0D $\langle 111 \rangle$ oriented clusters, all by simply shifting the location of the aminomethyl group of isomers.

The $\text{CH}_3\text{NHCH}_2\text{CH}_2\text{NHCH}_3\text{PbBr}_4$ compound also prefers to crystallize in a chain-like shape, thanks to the template effect of the highlighted $\text{CH}_3\text{NH}^+\text{CH}_2\text{CH}_2\text{NH}^+\text{CH}_3$ cations (Z. Yuan et al., 2017). The steric hindrance from larger cross-sectional areas and strengthened hydrogen bonding also classify the Ge-analogues containing guanidinium $\text{C}(\text{NH}_2)_3^+$, trimethylammonium $(\text{CH}_3)_3\text{NH}^+$, and isopropyl ammonium $(\text{CH}_3)_2\text{CHNH}^+$ as 1D perovskites (Stoumpos et al., 2015). From these compounds, it can be deduced that the functional groups in organic cations have a crucial role in determining the perovskite dimensions.

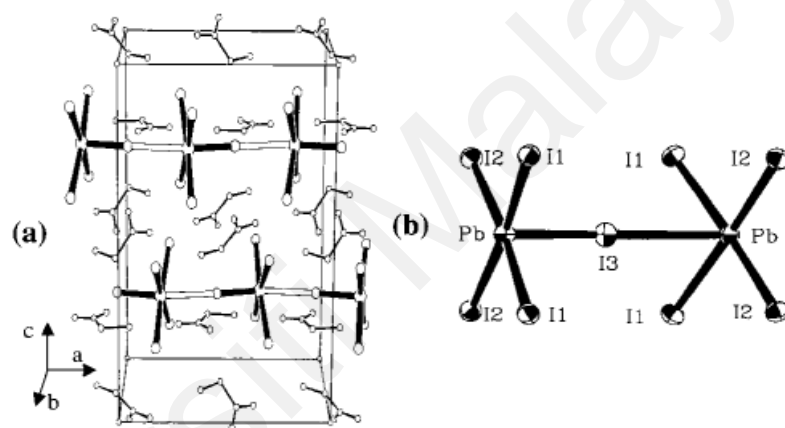


Figure 2.13: (a) A packing diagram for $[\text{CH}_3\text{SC}(\text{NNH}_2)\text{NH}_2]_3\text{PbI}_5$, displaying the thick bond chains and detailed structure. (b) A diagram of two connected PbI_5 units shows the atoms and ellipses with a 50% chance of occurrence. [Picture source from (Mousdis et al., 1998)].

(a) Propyl ammonium lead bromide (PAPbBr_3)

Propylammonium lead bromide, a perovskite with a simple one-dimensional chain structure, is considered a viable candidate among hybrid perovskites. Additionally, it is worth noting that this particular perovskite has significant thermal stability. The compound exhibits a distinct white color and exhibits a broad energy band gap of around 3 eV (Ren et al., 2019). This perovskite has great optoelectronic potential due to its simple structure and large band gap.

The structural stability and optical properties of PAPbBr_3 were examined by Ren and co-workers, the utilization of high-pressure X-ray diffraction and spectroscopic techniques such as Raman, ultraviolet-visible (UV-vis) absorption, and photoluminescence measurements. Sengupta and team. However, there has been limited research conducted on PAPbBr_3 , resulting in a significant gap in our understanding of the correlation between its structure and properties. This scarcity of knowledge poses a substantial constraint on both the scientific investigation and practical utilization of this substance.

2.6.3 Optical and physical properties of low-dimensional halide perovskite

The band gap of semiconductors, defined as the energy needed to excite an electron from its ground state in the valence band (VB) to the conduction band (CB), influences the wavelength range across which the material can absorb light. Pb 6s dominate the valence band maximum of the 3D perovskite $\text{CH}_3\text{NH}_3\text{PbI}$ and I 5p states, whereas the conduction band minimum is primarily due to the Pb 6p state.

The antibonding s-p interaction between the Pb long pair 6s orbital and the I 5p orbital significantly increases the band dispersion in VB, which results in relatively small effective masses for holes. Moreover, a direct band gap resulting from a p-p optical transition is advantageous for the optical absorption properties. Due to the organic cations' primary role as electron donors in these compounds, the organic cations used have specific indirect impacts on the crystal structure, such as dimensional reduction, tilting and deformation of the inorganic framework, and hydrogen bonding. As the perovskite crystal structure is reduced in dimension, the optical band gap increases relative to 3D perovskites. The bandgap is highly influenced by the number of perovskite slabs (n); for substantial values of n, the perovskite moves towards a 3D structure, whereas for larger values of n, the bandgap shrinks and the quantum confinement strength decreases.

For instance, due to weak band dispersion between organic cations and inorganic frameworks, the optical band gaps in the layered $(\text{C}_4\text{H}_9\text{NH}_3)_2(\text{CH}_3\text{NH}_3)_{n-1}\text{PbI}_{3n+1}$ series increase from 1.52 eV ($n = \infty$) to 2.24 eV ($n = 1$) with the decreased thickness of inorganic slabs as shown in Figure 2.14(a) (D. H. Cao et al., 2015; Stoumpos et al., 2016). Similar trends are found in the layered $(\text{C}_6\text{H}_5\text{CH}_2\text{CH}_2\text{NH}_3)_2(\text{CH}_3\text{NH}_3)_{n-1}\text{PbI}_{3n+1}$ series when the highlighted organic cations are substituted. As anticipated, the band gaps of these quasi-2D perovskites grow from 1.57 eV ($n = \infty$) to 2.10 eV ($n = 3$), see Figure 2.14(b) (M. Yuan et al., 2016). In this broad family of low-dimensional perovskites, flexible compositional tailoring can seek functional materials capable of addressing optical band gaps for various optoelectronic applications.

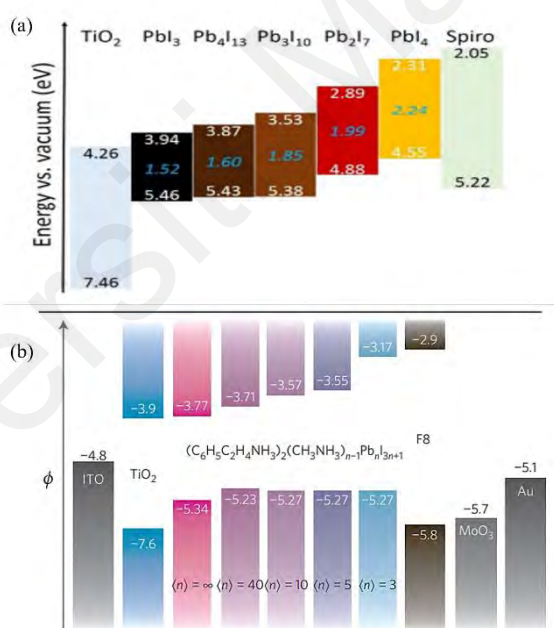


Figure 2.14: (a) The band energy diagram of $\text{BA}_2\text{MA}_{n-1}\text{PbI}_{3n+1}$ perovskite compounds (D. H. Cao et al., 2015) (b) The band structure of $\text{PEA}_2\text{MA}_{n-1}\text{PbI}_{3n+1}$ perovskite compounds with different n values. [Picture source from (M. Yuan et al., 2016)].

Low-dimensional perovskites may contain both inorganic cations and organic molecules of various lengths because they do not have the size mentioned above restriction. This gives them infinite compositional and structural flexibility.

Given the vast number of organic molecules that can be inserted into the inorganic framework, it is conceivable that the library of hybrid low-dimensional perovskites will be even more diverse than all known compounds to date. The inclusion of functional organic molecules, however, is their most appealing property because it not only gives perovskites a lever to regulate their optical and electrical properties but also new properties. One example is the emergence of new luminescence peaks from incorporating optically active organic compounds(Y. Y. Li et al., 2006; Mitzi et al., 1999). For example, a weak emitter polyacetylene emits light with a high photoluminescence quantum yield (PLQY) of 62% at 466 nm when implanted as a spacer within a 2D layered lead bromide perovskite, Figure 2.15(Hua et al., 2005). The improved light absorption of the inorganic framework and the efficient energy transfer to the organic emitter enables this high PLQY.

Other low-dimensional functionalization examples are adding polymerizable organic compounds(Tieke & Chapuis, 1984), organic clusters and zwitterions containing metals(Mercier & Riou, 2004), fullerene derivatives(Kawabata et al., 2009), and photochromic chromophore molecules(El Gemayel et al., 2015; Era & Yamada, 2001).

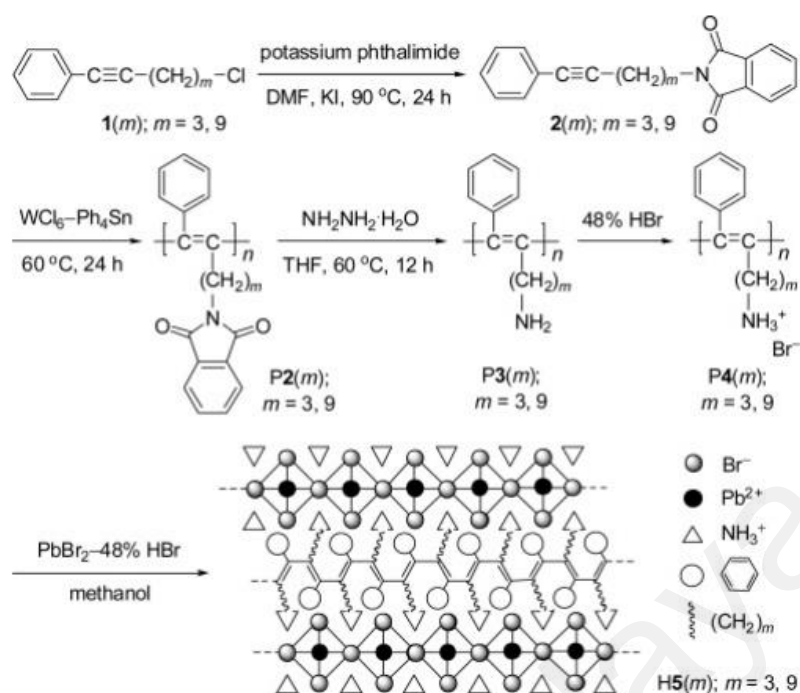


Figure 2.15: Syntheses of Poly(1-phenyl-1-alkyne) Ammonium Salt-Lead Bromide Perovskite Hybrids [Picture source from (Hua et al., 2005)].

The exciton is a fundamental elementary excitation that significantly affects the charge carrier mobility in semiconductors because it is a bound state of an electron and a hole attracted to each other by the electrostatic Coulomb attraction (Q. Zhang et al., 2017). Figure 2.16 illustrates the two broad categories into which excitons fall: Frenkel excitons and Wannier excitons (Manser et al., 2016). Wannier excitons have larger Bohr radii (often 30-100 Å) and lower binding energies (typically 10-30 meV), while Frenkel excitons have much smaller Bohr radii (typically 5-100 Å) and higher binding energies (typically 500-1000 meV) (Agranovich et al., 2011).

At room temperature, excitons tend to dislocate into free carriers when their binding energy is less than the thermal fluctuation energy (around 26 meV) (Saparov & Mitzi, 2016), which can freely diffuse across the host lattices and spread the excitation energy without carrying a net electric charge because of their low binding energies, semiconductors used in solar applications efficiently diffuse charge carriers.

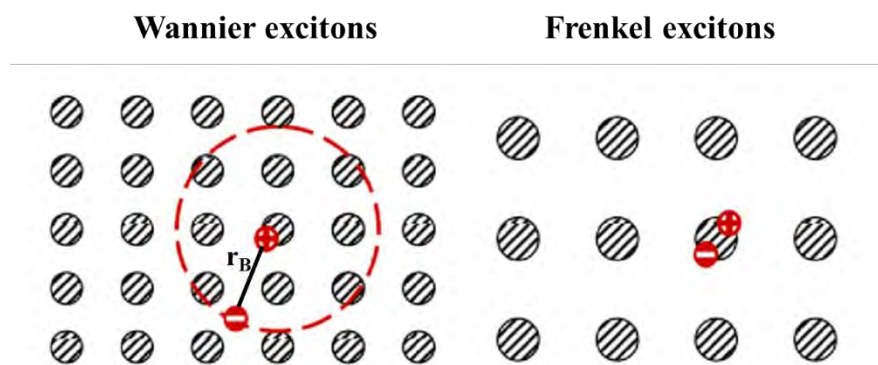


Figure 2.16: Schematic diagram of the Wannier excitons and the Frenkel excitons[Picture source from (Manser et al., 2016)].

Furthermore, prior research has demonstrated that 2D perovskite lattices improve the optical gains of quasi-2D perovskite materials (Milot et al., 2016). It was claimed that incorporating 2D perovskite fragments can efficiently passivate the surface or grain boundaries of the perovskite films, reducing trap-related non-radiative monomolecular recombination and optical losses in quasi-2D perovskites (F. Wang et al., 2016). This passivation effect was also found in quasi-2D perovskites containing di-ammonium cations, including ethane-1,2-diammonium (EDA^{2+} , $^+\text{NH}_3(\text{CH}_2)_2\text{NH}_3^+$) and octane-1,2-diammonium (ODA^{2+} , $^+\text{NH}_3(\text{CH}_2)_8\text{NH}_3^+$) (Lu et al., 2017).

Compared to their 3D counterparts, low-dimensional perovskites are typically more resistant to moisture. Hydrophobic organic linkers used in low-dimensional perovskites shield them from attack by atmospheric moisture (Lermer et al., 2016). According to humidity stability, water molecules would readily enter the structure of perovskite, creating intermediate hydrate products due to their higher polarity, thus deteriorating perovskites (Ansari et al., 2018; Huang et al., 2017; Leijtens et al., 2017). Water's reaction with $\text{CH}_3\text{NH}_3\text{PbI}_3$ can be broken down into multiple phases in a breakdown mechanism that has been proposed (Figure 2.17) (Frost et al., 2014). After a brief period of exposure to moisture, a reversible colourless monohydrate phase of $\text{CH}_3\text{NH}_3\text{PbI}_3 \cdot \text{H}_2\text{O}$ with a chained structure emerges in the early stage (Equation 2.2).

After a prolonged exposure period, an irreversible pale yellowish hydrated phase of 0D $(\text{CH}_3\text{NH}_3)_4\text{PbI}_6 \cdot 2\text{H}_2\text{O}$ forms (Equation 2.3), which further breaks down into solid PbI_2 , volatile $\text{CH}_3\text{NH}_3\text{I}$, and H_2O . (Equation 2.4)(Leguy et al., 2015; Song et al., 2016). The PbI_2 product is only weakly soluble in water, which raises concerns about toxicity(Koushik, Verhees, Kuang, et al., 2017). The water molecules only serve as effective catalysts to start the breakdown.

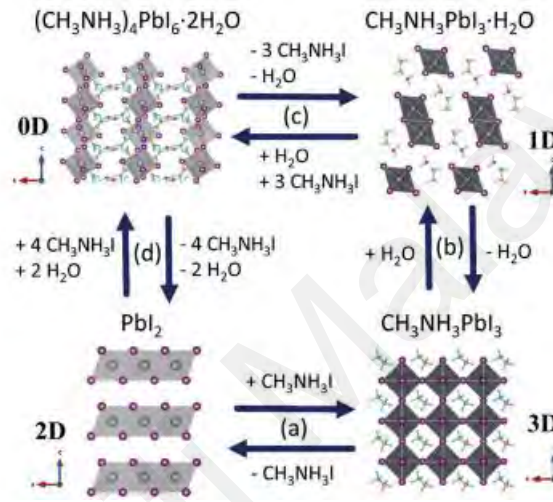
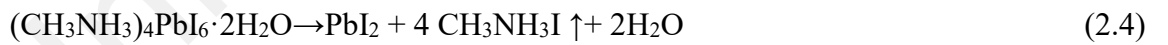
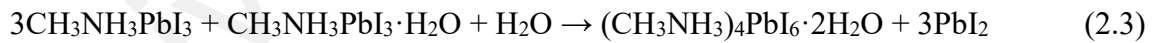
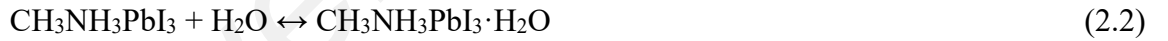


Figure 2.17: Schematic representation of the processes of creation and degradation of MAPbI_3 when exposed to water[Picture source from (Song et al., 2016)].



The van der Waals interaction between the bigger organic amine cations is more significant in the newly created low-dimensional perovskites than in the original 3D perovskites. This explains why the low-dimensional perovskites are more stable in a humid environment(Quan et al., 2016). Density functional theory (DFT) simulations reveal that larger organic groups, such as phenethylamine iodide (PEAI), require more energy (0.36eV higher than MAI) to be removed from hybrid perovskite.

The low-dimensional perovskite materials are stabilized by the hydrophobic nature of most of the bigger organic amine groups, such as PEA(Cohen et al., 2017), n-BA, and iso-BA(Y. Chen et al., 2017), which can shield the hybrid perovskite layers from water. As depicted in Figure 2.18, $n = 1$ refers to a single 2D slab of the perovskite structure, or a monolayer, which is then enclosed by an organic barrier(Quan et al., 2016). Further, evidence demonstrates that water molecules degrade 3D hybrid perovskites layer by layer(Christians et al., 2015). Although water molecules in the highly humid atmosphere have already begun to degrade the exterior perovskite layers of low-dimensional perovskites, the larger organic amine groups will act as waterproof barriers to shield the core perovskite layers from further deterioration.

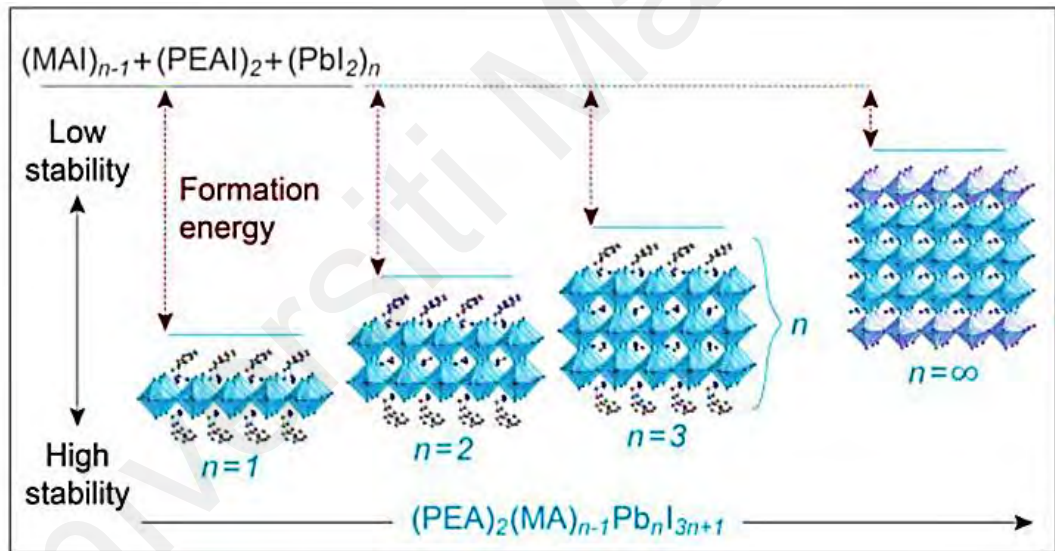


Figure 2.18: A better level of stability can be achieved in organometal halide perovskites by decreasing their dimensionality[Picture source from (Quan et al., 2016)].

2.7 Perovskite crystallization

The defect concentrations in the material and the resulting electrical properties, such as charge transport under working circumstances, are determined by the morphology and microstructure of the perovskite thin film. In polycrystalline perovskite films, the crystals are irregularly oriented, and different faces are exposed to charge extraction layers.

Improved crystal alignment may reduce defect densities in perovskite films and improve interface engineering in the device layouts. In addition, perovskite crystallization is highly dependent on the substrate's interface. Changes in surface roughness have a profound effect on the nucleation and crystallization of perovskite concerning the wetting behaviour of the substrate towards the polar precursor solutions. For this reason, most perovskite crystallization methods are constrained by the nature of the bottom interface.

There is a need to address these constraints before the widespread use of perovskite thin films in various device designs is possible. Particularly crucial to perovskite device commercialization is the up-scaling to modules. There can be either heterogeneous or homogeneous nucleation during the perovskite conversion process, as seen in Figure 2.19 schematic illustrations (Ding et al., 2016; L. L. Gao et al., 2016). The formation of homogeneous nucleation occurs naturally inside the solution and does not require any assistance from external sources. On the other hand, the process of heterogeneous nucleation is facilitated by external sites (for example surface of the substrates or colloidal particle nucleation in solution).

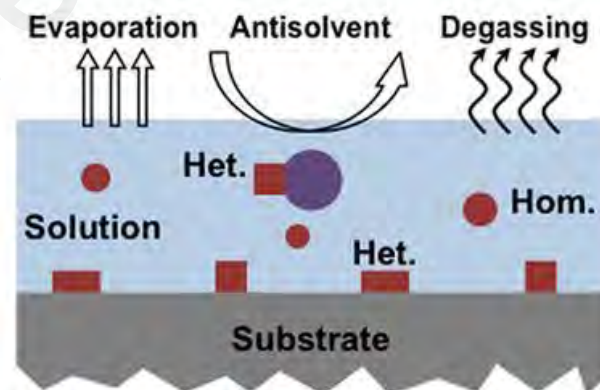


Figure 2.19: Illustrations of classical homogeneous and heterogeneous nucleation in supersaturated thin-film solutions [Picture source from (L. Gao & Yang, 2020)].

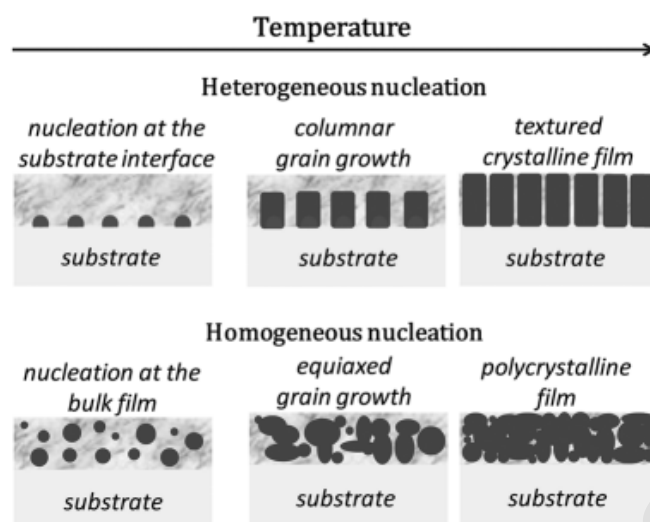


Figure 2.20: Temperature-dependent nucleation and development of homogeneous and heterogeneous solution-derived thin films [Picture source from (Bretos et al., 2018)].

In general, polar solvents like dimethylformamide (DMF), dimethyl sulfoxide (DMSO), and N-methyl-2-pyrrolidone (NMP) can dissolve the inorganic PbI_2 salt. This occurs because the O-donor ligands in the solvent form a strong coordination bond with the Pb atoms in the salt (Davidovich et al., 2009). The organic halide precursor, for example, MAI, dissolves more easily in the solvent and can coordinate to the lead atoms. Due to the possibility that these precursor solutions contain colloidal particles, they are not regarded to be "real" solutions (Yan et al., 2015).

Commonly the complex adducts that make up colloidal particles are of the type $\text{MAI.PbI}_2.x\text{DMF}$ (Wakamiya et al., 2014) or $\text{MAI.PbI}_2.x\text{DMSO}$ (Wu et al., 2014). In addition to acting as heterogeneous nucleation sites, the strong hydrogen bonding between these colloidal particles in solution allows them to self-assemble into bulk structures. As a result, the substrate is most likely to contain a low density of MAPbI_3 nuclei, leading to an excessive increase in size for the few existing nuclei and a lack of uniform coverage after annealing.

Through the modification of the nucleation parameters (such as temperature and interface energy), methods for increasing coverage have had some success, including regulating the solvent evaporation rate(Kang et al., 2014), changing the solvent's characteristics (such as volatility, boiling point, and coordination power)(H.-B. Kim et al., 2014), and enhancing wetting with the substrate (such as interfacial-layer insertion)(J. Wang et al., 2015).

2.8 Deposition of Perovskite

Perovskite thin films are used as active layers in transistors and as light absorbers in photodetectors. The device's effectiveness relies heavily on the caliber of the perovskite film deposition. Consequently, the deposition of high-quality perovskite films has become an appealing research topic. Perovskites can be deposited through different methods, such as solution-processed and physical vapour deposition(B. Jeong et al., 2021; Luo et al., 2017; Shao et al., 2020; S. Yuan et al., 2018). It can be further broken down into one-step, two-step, antisolvent-assisted, and other types of deposition(Giuliano et al., 2021; Shor Peled et al., 2021; B. Zhang et al., 2021).

Perovskite layers were first deposited using the one-step spin-coating deposition process (Figure 2.21). A perovskite precursor can be made by combining all the materials and solvents. Next, the precursor solution is dropped onto the substrate, spin-coated at the right speed and time, and then annealed to obtain the thin film(Cho et al., 2018; F. Zhang et al., 2019). It is important to note that numerous parameters affect the quality of the film, namely substrate temperature, ambient environment, annealing time, and temperature and precursor solution concentration. In addition, the solvents of the perovskite precursor have a considerable impact on the crystallization and morphology of the thin film. The antisolvent-assisted deposition is similar to one-step spin-coating deposition, with the addition of an antisolvent spin-coating.

Washing out the solvents of the perovskite precursor with an antisolvent like chlorobenzene creates a dense, smooth perovskite layer (Gedamu et al., 2018; X. Liu et al., 2020).

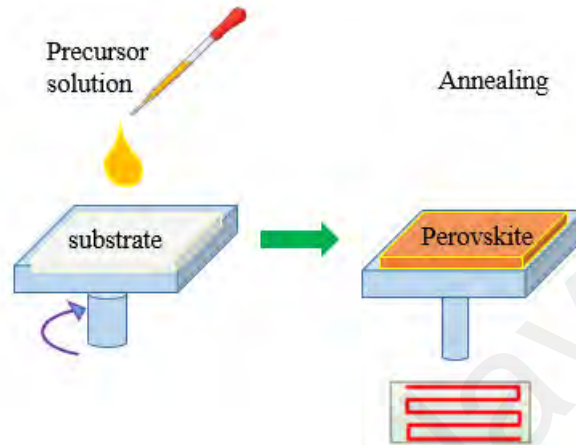


Figure 2.21: One-step spin-coating deposition

Two-step spin-coating deposition (Figure 2.22) is two separate processes, as opposed to just one, like in conventional deposition. The substrate is first spin-coated with a precursor (such as PbBr_2), and then a second precursor is deposited (e.g., $\text{CH}_3\text{NH}_3\text{Br}$). During the depositing of the second precursor, the perovskite layer is formed (D. Liu et al., 2015; Rahaq et al., 2018). Notably, the concentration of the $\text{CH}_3\text{NH}_3\text{Br}$ precursor solution significantly impacts the quality of thin films produced by this approach.

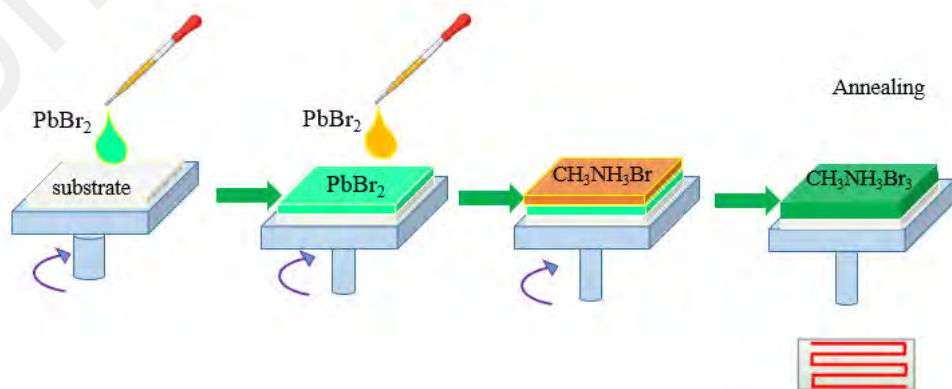


Figure 2.22: Two-step spin-coating deposition

Perovskite thin films can also be grown and deposited using chemical vapour deposition (Figure 2.23). Chemicals are often separated into many evaporation sources before being heated and vaporized in a high-vacuum environment. The evaporated chemicals cause a reaction in the chamber, followed by the deposition of a thin coating of perovskite on the substrate. In order to complete the crystallization of the perovskite thin film, an annealing step is carried out (Waleed et al., 2017). The film quality is high, but the equipment is costly, and the prep work is time-consuming, making this method less attractive.

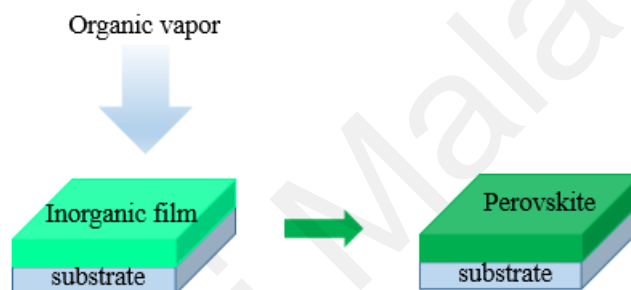


Figure 2.23: Chemical vapour deposition

As a result, perovskite thin film is grown and deposited using a one-step solution deposition technique in the current work. The procedure is straightforward, the cost is low, and the potential for practical use is high, with high-quality, stable film results.

2.9 Device physics of electronic applications

2.9.1 Field Effect Transistor (FET)

In 1925, the field-effect transistor (FET) idea was first described (Lilienfeld, 1930) and first implemented in 1949 (Bardeen & Brattain, 1949; Shockley et al., 1949). Since their invention, FETs and transistors have generally brought about revolutionary change worldwide. A FET has a semiconductor that serves as the active layer, a gate dielectric that separates the gate from the active layer, and three electrodes known as the source (*S*), drain (*D*), and gate (*G*).

A gate dielectric is a material with electrical insulation properties. This stack of materials forms a capacitor, and its presence in the transistor is necessary for its operation. The width of the active layer, represented by the channel width W , and the length of the channel, represented by L , the distance between the metal contacts for the source and drain, are two of the most fundamental aspects of the device. The active layer is in direct contact with the source and drain electrodes, which are responsible for injecting and collecting charges through the channel. Figure 2.24 depicts a thin-film transistor. The source electrode is connected to the ground and can serve as a voltage reference for the gate and drain electrodes. For short, "gate voltage" refers to the potential difference between the gate and the source (V_{GS}). The potential difference between the drain and the source is referred to as the drain-source voltage (V_{DS}) or the drain voltage.

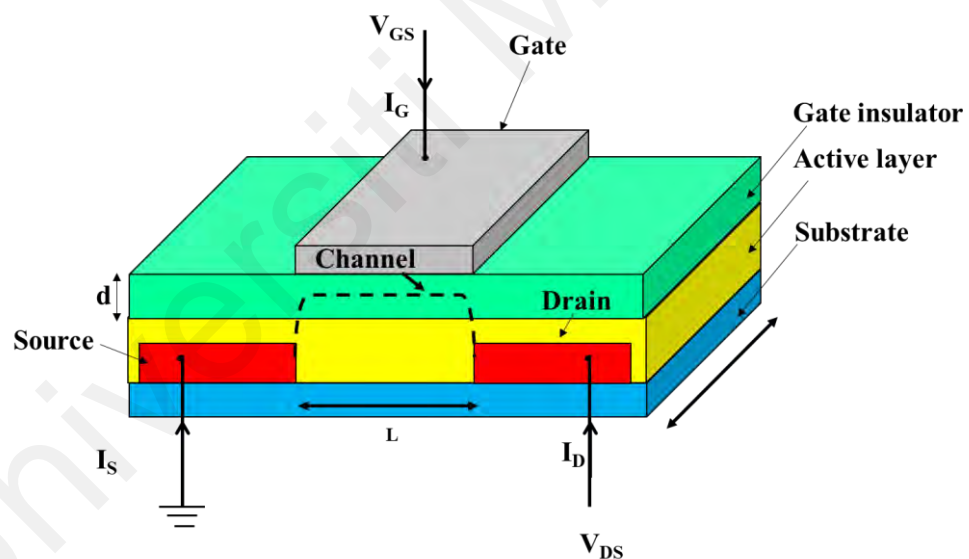


Figure 2.24: A thin-film transistor construction schematic shows a channel width, W , and channel length, L . The dashed line represents the flow of charge in the channel.

There are a few different architectures that can be utilized for FETs, but the three most prevalent ones are bottom-gate, top-contact (BGTC), bottom-gate, bottom-contact (BGBC), and top-gate, bottom-contact (TGBC). Figure 2.25 depicts the various OFET device topologies, which can result in noticeably different OFET behaviour.

Typically, charges are injected at the source electrode, propagate along the semiconductor and dielectric interface (where they create a "channel"), and are then retrieved at the drain electrode. In FETs, the conducting channel forms in the first few molecular layers at the interface between the semiconductor and the insulator (Dinelli et al., 2004; Dodabalapur et al., 1995; Horowitz et al., 1999). This observation can be explained by referring to where the source and drain electrodes are with the interface. Because of the staggered nature of geometries 2.25(a) and 2.25(b), injected charges can travel up to 100nm in a low conductivity layer before entering the channel.

On the contrary, charges with coplanar geometry, Figure 2.25(c) are injected into the high-conducting channel via the interface. The morphology of the critical interface varies depending on the order of layer processing, and the possibility of new trap states being introduced by metals evaporated directly onto the semiconductor. The insulator in top gate devices may serve as a crude encapsulation layer, preventing water and oxygen penetration into the semiconductor and lowering unintentional doping in bulk.

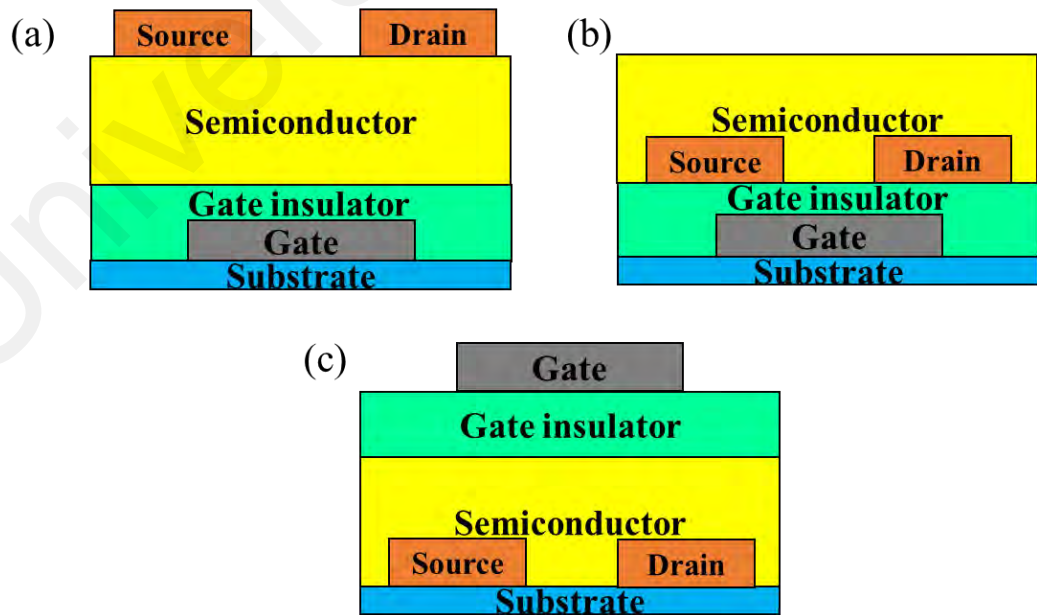


Figure 2.25: Various FET device geometries (a) bottom-gate, top-contact (BGTC), (b) bottom-gate, bottom-contact (BGBC), and (c) top-gate, bottom-contact (TGBC).

2.9.2 Basic operating mode

The FET's on/off states are achieved by producing and removing a sheet of charge at the semiconductor and insulator interface. To further comprehend the operation of a FET with such a structure, it is necessary first to examine its metal insulator semiconductor (MIS) structure. A FET resembles a MIS structure without drain voltage ($V_D = 0$). Figure 2.26 displays the energy level band diagrams of a MIS structure with two distinct modes of operation using a p-type organic semiconductor (Hori, 1997; Petty, 2007). An ideal MIS structure is assumed here, meaning that the insulator does not conduct electricity, and the metal and semiconductor's Fermi levels (E_F) are aligned before contact. Figure 2.26(a) demonstrates no band bending at zero external voltages. E_C is the lowest conduction band edge corresponding to organic semiconductors' lowest-unoccupied molecular orbital (LUMO) level. E_V is the highest edge of the covalent band that fits the highest-occupied molecular orbital (HOMO) level in organic semiconductors. With a negative gate voltage (V_{GS}), the bands invert, and the top of the HOMO level shifts closer to E_F , as shown in Figure 2.26(b). This results in a concentration of holes in the active channel close to the insulator/semiconductor interface. As shown in Figure 2.26(c), the bands bend downward when a positive gate voltage V_{GS} is applied, resulting in a drop in the total number of net charge carriers in the channel until all free carriers have been cleared. At this moment, electrons begin to outnumber holes, and the MIS structure is in the inversion phase.

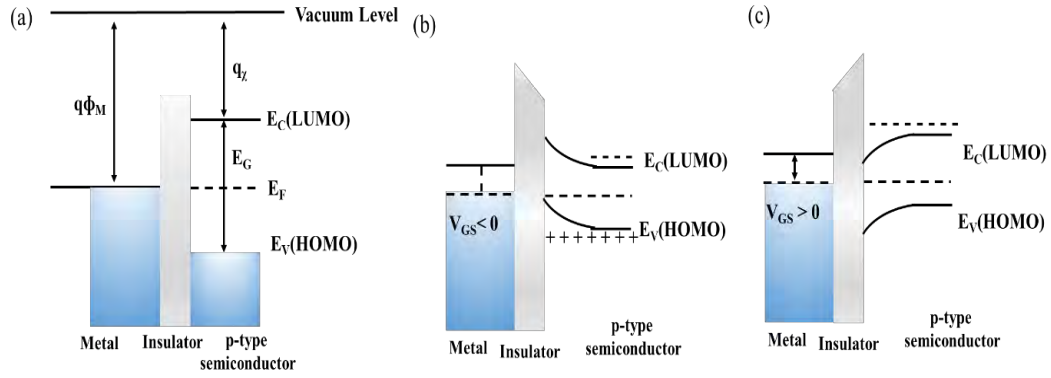


Figure 2.26: Energy level band diagram of an ideal MIS structure for a p-type semiconductor (a) at equilibrium, (b) biased in the accumulation region, (c) biased at the inversion region. (Picture source from Molecular Electronics: From Principles to Practice, 2007).

This subsection discusses p-type semiconductor FET operation, which is representative of the devices explored in this thesis. The behaviour of n-type FETs can be described similarly by inverting the charge carriers' polarity and the applied voltages. While Metal oxide semiconductor field-effect transistors (MOSFETs) function in a depletion or inversion mode, FETs often function in an accumulation state.

When the threshold voltage, or V_{TH} , in a device with a p-type semiconductor is exceeded, the device is said to be off, and drain current, I_D , is highly dependent on the device's size and the base conductivity of the semiconductor material (Figure 2.27a). V_{TH} is the gate electrode voltage needed to initiate the accumulation of the positive majority charge carriers (holes) at the semiconductor-dielectric interface and the subsequent rise in conductivity of the source-drain channel (the region of the semiconductor between the source and drain electrodes). According to Figure 2.27(b), a device operates in the linear regime only if $|V_{GS}| > |V_{TH}|$ and $|V_{DS}| < |V_{GS}|$. In other words, I_D varies linearly with V_{DS} for a fixed V_{GS} , and the channel functions as a resistor. Conversely, if $|V_{GS}| > |V_{TH}|$ and $|V_{DS}| > |V_{GS}|$, the device is saturated, I_D is independent of V_{DS} and remains relatively constant for a given V_{GS} .

When $|V_{DS}| > |V_{GS}|$, positively charged holes are attracted to the drain rather than the gate, and the position of the accumulated charge carriers shifts, creating a region of higher conductivity near the drain and a region of lower conductivity near the source in the channel between the source and drain (Figure 2.27c). This is the physical mechanism by which I_D saturates. As $|V_{DS}|$ continues to increase in the negative direction, the accumulated charge carriers will shift their orientation toward the drain, increasing the total resistance of the channel and, ideally, keeping I_D unchanged.

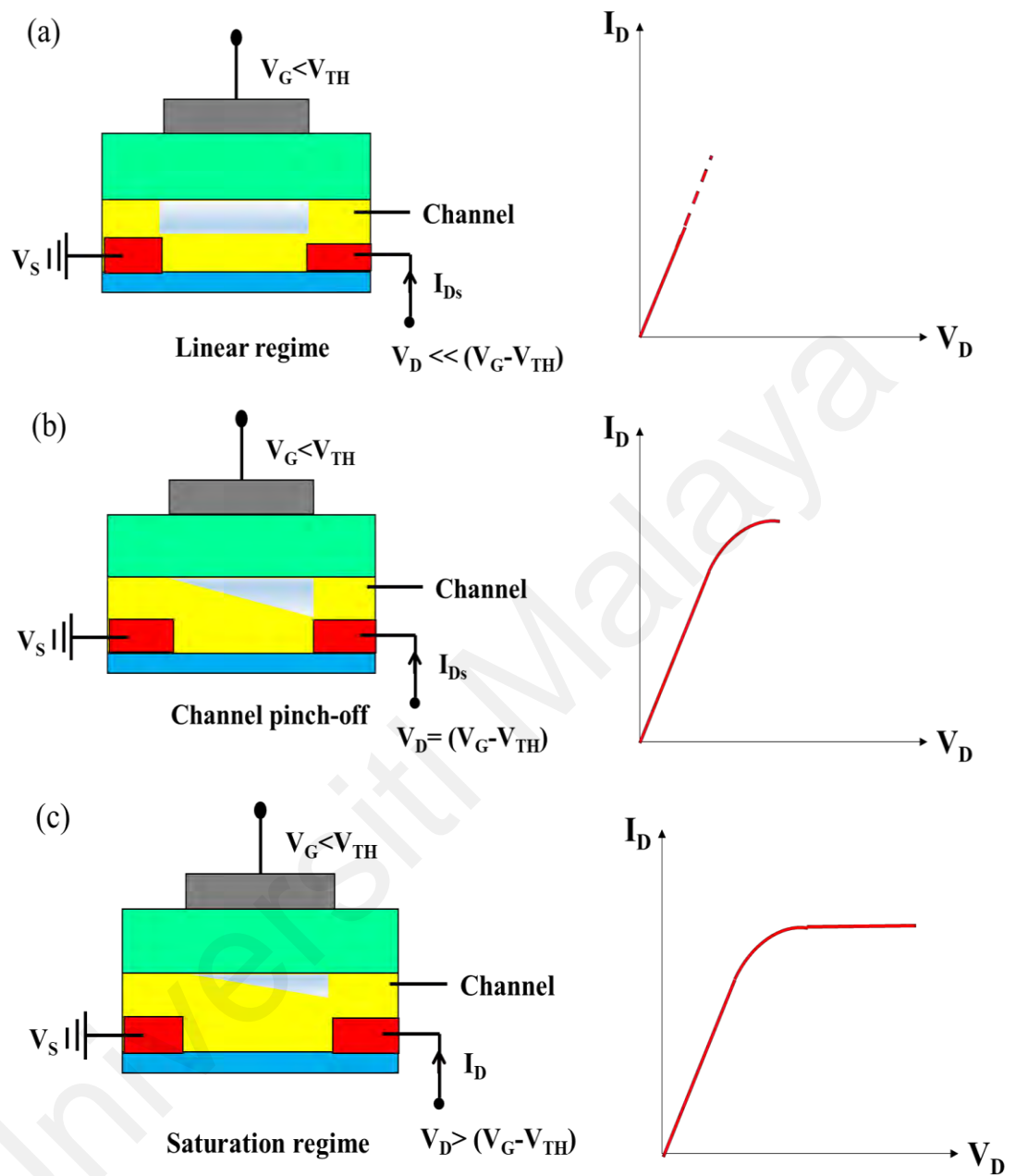


Figure 2.27: Operation of field-effect transistor. (a) Linear regime. (c) Start of saturation regime at pinch-off, (c) Saturation regime.

2.9.3 Electrical Characterization of FETs

(a) *The output characteristics*

Typically, a plot of drain current (I_D) vs. source-drain voltage (V_{DS}) at constant gate-source voltages (V_{GS}) is used to illustrate the current-voltage (IV) operation of a transistor (Figure 2.28a). This aspect of a transistor's performance is its output characteristic. The current behaviour may be broken down into two distinct primary regions: linear growth followed by saturation. For each voltage applied to the gate electrode, the current in the area of low drain voltages is proportional to V_{DS} according to Ohm's law. This area is known as the linear region. When the drain voltage is increased indefinitely, the voltage drop eventually becomes zero. When the drain voltage is close to the gate voltage, a phenomenon known as pinch-off occurs, and from that point on, the channel current is constant regardless of the drain voltage (Klauk, 2006). This region is referred to as the saturation region. The dashed line in Figure 2.28 (a) illustrates the drain voltage at which the current achieves its maximum value (Sze & Ng, 2006).

(b) *The transfer characteristics*

Figure 2.28(b) illustrates a plot of drain I_D vs. gate voltage with a constant drain bias. These transfer characteristics indicate the gate voltage's efficiency may turn the device on or off. If a p-type transistor turns on at $V_G > 0$, it may be because the semiconductor has sufficient impurity dopants to generate a bulk current without a gate voltage (Meijer et al., 2003). In an ideal transistor, no current or a very minimal current would flow between the source and drain electrodes when the gate voltage is less than the threshold voltage (V_{TH}).

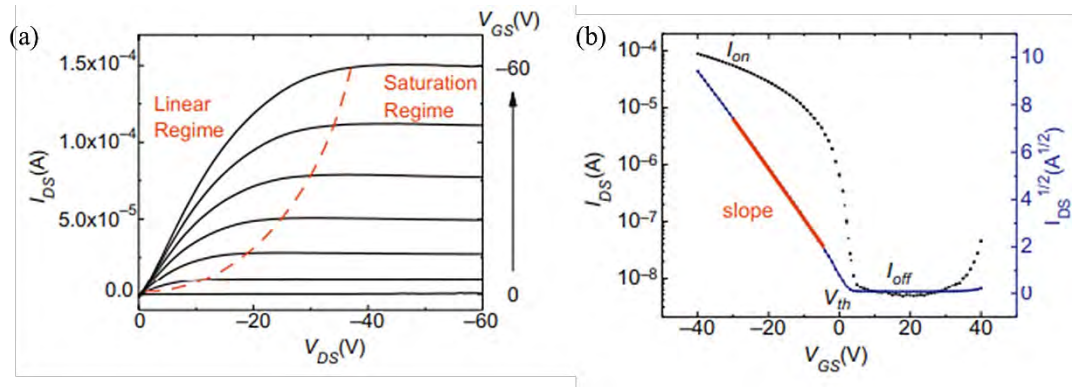


Figure 2.28: Typical FET characteristics: (a) output (I_{DS} vs. V_{DS} for different V_{GS} voltages), (b) transfer characteristics (I_{DS} vs. V_{GS} at $V_{DS} = \text{const.}$) transport curves of a p-channel device [Picture source from (Mei, 2018)].

Charges are transported through the conducting channel from source to drain for gate voltages more significant than this specific threshold voltage. The threshold voltage thus represents the gate voltage that causes the channel to "open". It is common for p-type semiconductor-based FETs to have a negative V_{TH} , with subsequent turn-on being aided by an even more negative V_{GS} . But in cases where an n-type semiconductor is used, V_{TH} is typically positive (Horowitz, 1998; Waldauf et al., 2003). Its value can be estimated by plotting a graph of the square root of I_{DS} against V_{GS} for a fixed V_{DS} (Figure 2.29). A straight line is derived from the linear section of the plot, and its extrapolation with the V_{GS} axis at zero current yields the threshold voltage.

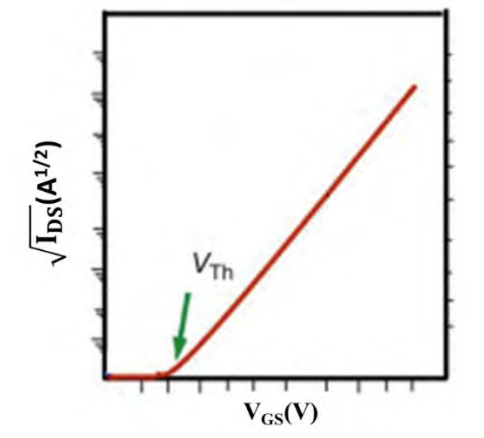


Figure 2.29: The graphical technique for determining Threshold voltage (V_{TH}).

Maximum current and minimum current acquired for the device during the "on" and "off" states, respectively, are represented by the on/off ratio (I_{ON}/I_{OFF}). It is generally preferable to maximize I_{ON}/I_{OFF} , as it is the limiting factor for signal amplification and switching. This value specifies the extent to which a change in V_{GS} for a given V_{DS} can affect the transistor's output current (I_D). As illustrated in Figure 2.30, I_{ON}/I_{OFF} is often determined by selecting V_{DS} so that the device is in the saturation region. Then choose two values of V_{GS} : one where the device is at or near its minimum I_D ("off") and one where it is near its highest I_D ("on").

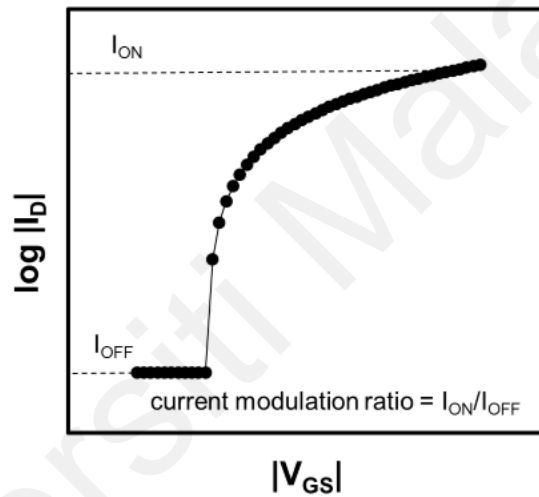


Figure 2.30: Current modulation ratio determination using a transfer curve.

Charge carrier mobility (μ), or mobility, characterizes how quickly charge carriers can travel across a material under the influence of an electric field. Current is proportional to charge carrier mobility and can be calculated in the two operational areas of a FET using formulae available for metal-oxide-semiconductor field-effect transistors (Sze & Ng, 2006). In the linear region where $V_{DS} < (V_{GS} - V_{TH})$, the current can therefore be represented as follows:

$$I_{DS} = \mu_{lin} C_i \frac{W}{L} (V_{GS} - V_{TH}) V_{DS} \quad (2.5)$$

where μ_{lin} and C_i represent the linear region's mobility and the capacitance per unit area of the gate, respectively. As a result of deriving Equation (2.5) as a function of V_{DS} , the mobility in the linear region can be expressed as follows:

$$\mu_{lin} = \frac{\partial I_{DS}}{\partial V_{DS}} \frac{W}{L} \frac{1}{C_i} \frac{1}{V_{GS} - V_{TH}} \quad (2.6)$$

where V_{TH} and $\frac{\partial I_{DS}}{\partial V_{DS}}$ can be driven experimentally.

Specifically, where $V_{DS} > (V_{GS} - V_{TH})$ in the saturation area, the current is defined as:

$$I_{DS} = \mu_{sat} C_i \frac{W}{2L} (V_{GS} - V_{TH})^2 \quad (2.7)$$

The mobility in the saturation region (μ_{sat}) can be expressed by:

$$\mu_{sat} = \frac{I_{DS}}{C_i} \frac{2L}{W} \frac{1}{(V_{GS} - V_{TH})^2} \quad (2.8)$$

2.9.4 Low-dimensional hybrid perovskites-based FETs

Studies on Pb-based perovskite FETs for low-dimensional perovskites are still in their infancy. Li and colleagues published the first study of FETs fabricated from a Pb-based two dimensional perovskite single crystal with pure phase (M.K.Li et al., 2018). The researchers found the unipolar n-type transport behaviour within $(BA)_2(MA)_{n-1}Pb_nI_{3n+1}$. They exhibited the FETs based on a series of high-quality exfoliated 2D perovskites $(BA)_2(MA)_{n-1}Pb_nI_{3n+1}$ with varying n values under different temperatures.

The carrier mobility of a FET is very sensitive to the thickness of an inorganic BX_6^{4-} octahedral layer (with varying n values) at 77K; these values are 2×10^{-3} , 8.3×10^{-2} , and $1.25 \times 10^2 \text{ cm}^2 \text{ V}^{-1} \text{ s}^{-1}$, for $n = 1, 2$, and 3 .

Wang et al. conducted follow-up studies on $(\text{BA})_2\text{PbI}_4$ perovskite FETs and discovered that their in-plane mobility of $8.2 \times 10^{-2} \text{ cm}^2 \text{ V}^{-1} \text{ s}^{-1}$ is more than an order of magnitude higher than their out-of-plane mobility of $4.7 \times 10^{-3} \text{ cm}^2 \text{ V}^{-1} \text{ s}^{-1}$ (K. Wang et al., 2019). The low-dimensional perovskite FETs' potential is enhanced if the anisotropic carrier transport feature is exploited. Zhu et al. further reported a facile and rapid antisolvent crystallization method to synthesize free-standing phenylethyl-ammonium lead halide $(\text{PEA})\text{PbI}_4$ nanosheets with a few-layer thickness, which is a deviation from the standard solution-based process and therefore beneficial to the development of materials and devices (L. Zhu et al., 2018). As a result, the comparable FET has a V_{TH} of 5.19 V and mobility of $1.43 \times 10^{-1} \text{ cm}^2 \text{ V}^{-1} \text{ s}^{-1}$ at ambient temperature.

2.10 Photodetector (PD)

Photodetectors are devices that transform the light signal into an electrical signal. The Equation represents the energy associated with a photon:

$$E_{\text{photon}} = \frac{hc}{\lambda} \quad (2.9)$$

where h is Planck's constant, c is the speed of light in a vacuum, and λ is its wavelength. When a photon hits an electron in the valence band of a semiconductor with energy larger than or equal to the band gap, the bound electron can absorb the photon's energy and jump to the conduction band, creating a vacancy (hole) in the valence band. When a device uses a semiconductor, the electrons and holes in its conduction and valence bands serve as charge carriers and generate current.

But since electrons and holes have opposite electric charges, they are attracted to one another. When an electron-hole pair recombines, the electron moves back to a lower energy state in the valence band, which results in the emission of a photon with the same energy as the band gap. This process is known as recombination. This process, by which photons are produced via the recombination of charge carriers, is known as photoluminescence (or radiative recombination) (Figure 2.31). Photodetectors are designed to minimize the recombination of free charge carriers and generate a current by producing electron-hole pairs. Typically, an applied bias voltage generates an electric field separating these carriers, preventing their instantaneous recombination.

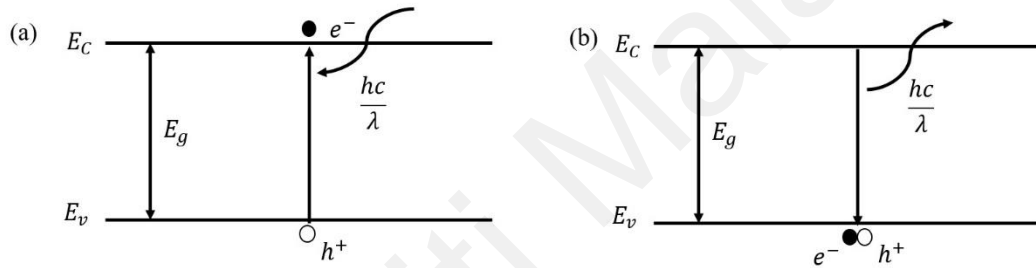


Figure 2.31: Radiative (a) generation and (b) recombination mechanisms for an arbitrary semiconductor with an energy band gap of E_g .

A photodetector's device architecture can be roughly broken down into two categories: vertical, also known as photovoltaic-type (or photodiode), and lateral, also known as photoconductive-type (consisting of metal-semiconductor-metal [MSM] and field-effect transistor [FET] configurations) as shown in Figure 2.32. Compared to the photovoltaic versions, the MSM structure is the easiest to manufacture and produces superior figures of merit (such as responsivity, EQE, and gain). On the other hand, photoconductive detectors have a slow response time and a high dark current. However, photovoltaic-type detectors have a fast response time, a large LDR, low noise, and low dark current. FET-type detectors combine photovoltaic-type and MSM-type properties with balanced performances such as low dark current and excellent responsivity.

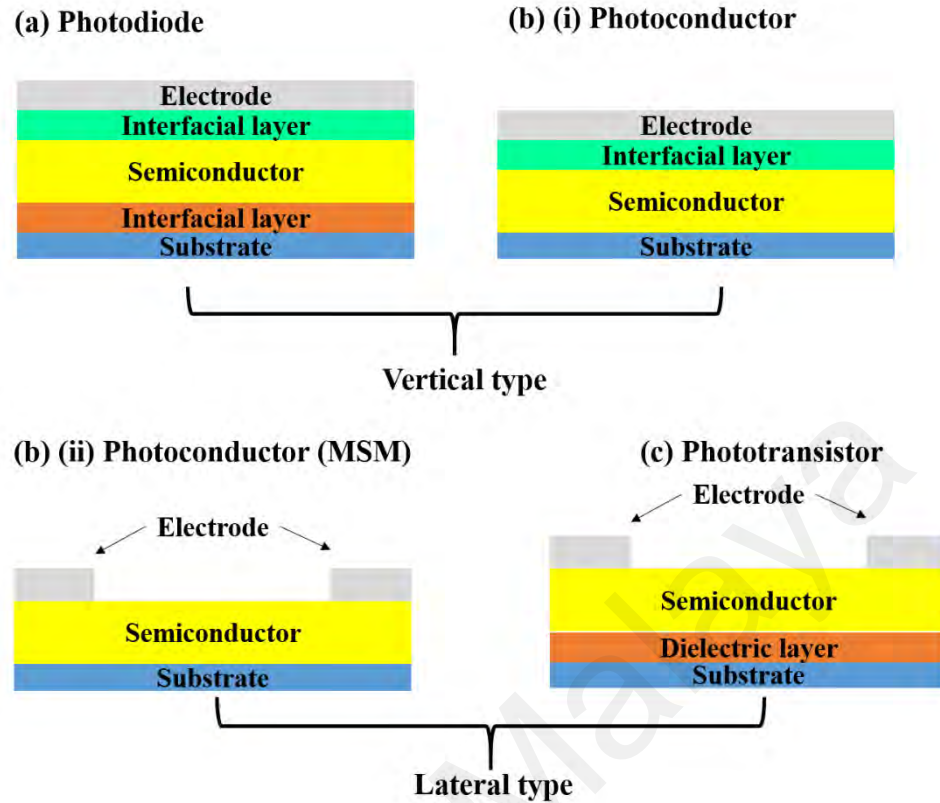


Figure 2.32: Structure of type of photodetectors. (a) Photodiode, (b) Photoconductor, and (c) Phototransistor.

Photoconductors are two-terminal devices that amplify photocurrent intrinsically. The primary driving force behind photoconductors is the photoconductive effect, which relies on the semiconductor's ability to produce extra free carriers (Muñoz et al., 1998). Photoconductors are unipolar because they only conduct single-type carriers (Figure 2.33). In photoconductors, externally provided bias voltage is required to separate photo-generated electron-hole pairs, which typically comprise photoactive materials and two Ohmic contacts. Under a bias voltage, metal contacts inject charge carriers into a semiconductor layer. High gain is possible in photoconductors (Petritz, 1956) because one type of charge carrier (for example, holes) can circulate through an external circuit multiple times before it recombines with its opposite carrier (for example, electrons), which stays trapped in the photoconductor bulk (see Figure 2.33) (Konstantatos & Sargent, 2011).

However, the long carrier lifetime of photoconductors has disadvantages, such as poor response speed. Contrarily, in order to separate photo-generated carrier pairs under reverse bias, photodiodes with structures like p-n, p-i-n, or Schottky junctions primarily rely on a built-in electric field (Konstantatos & Sargent, 2010). Compared to photoconductors, photodiodes have the benefit of having a rapid response speed and a shallow dark current when subjected to reverse bias.

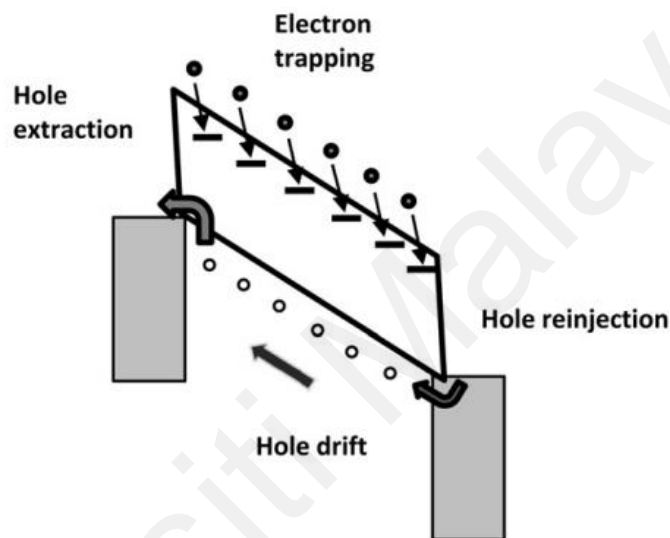


Figure 2.33: Under the influence of an electric field, photoconductors exhibit carrier trapping and mobility of another type of carrier (electrons are trapped in this illustration). [Picture source from (Konstantatos & Sargent, 2011)].

Additionally, photodiodes can operate in the photovoltaic mode without an external energy supply. In the case of phototransistors, varying the gate voltage alters the carrier concentration in the channel. When operating in the depletion regime, phototransistors can produce relatively low dark current, and when illuminated by light, they exhibit significant gains, much like photoconductors.

Generation of efficient free-charge-carrier

The photovoltaic effect allows a photodetector to transform light energy into a usable electrical current. This can be broken down into three phases: charge creation, separation, and transfer. The exciton binding energy is the minimum energy required to split a system of excitons into electrons and holes. Electron-hole pairs with low binding energy (EB) achieve effective free-charge-carrier generation in perovskite photodetectors. Next, the holes in the valence band are created when photons are absorbed, and electrons are driven from the conduction band to the valence band. The band gap refers to the energy difference between the conduction and valence bands. An increase in open-circuit voltage due to a wide band gap can also diminish photocurrent by limiting the efficiency with which electrons may convert the gap into conduction. In contrast, a narrow band gap can result in a high photocurrent, but it will also increase electron energy loss. Consequently, an optimal band gap is anticipated.

Efficient charge separation

The electric fields enable the separation of electrons and holes. However, not every pair of electrons and holes can be separated. Some of them are capable of recombining and releasing energy. The recombination process can take many distinct forms. Spontaneous emission, which results in the release of a photon, is the cause of radiative recombination, also known as band-to-band recombination. Auger recombination allows the energy to be transferred to other charge carriers, and extra energy is lost as heat. The result of the defects in the materials is trap-assisted recombination, also known as Shockley-Read-Hall recombination. The perovskite thin film is doped with defects, which serve as charge traps and recombination sites, before radiating their energy as heat. Therefore, altering the morphology of semiconductor materials can prevent trap-assisted recombination.

Efficient charge transport

Perovskite photodetectors have superior charge transport because of their extended carrier lifetime, long diffusion length, and long drift duration. The drift current is a current induced by the migration of electrons or holes (charge carriers) due to an electric field's application of an electric force to the charge carriers. Mobility is defined as the ratio of the drift velocity to the electric fields, which indicates how quickly a charge carrier may move through a metal or semiconductor with the number of electric fields. Diffusion current is a current that generates in a semiconductor due to the diffusion of charge carriers (holes and electrons), which is brought on by the semiconductor's non-uniform concentration of charged particles. The average distance that charge carriers travel before recombining is the diffusion length. The duration of diffusion relies on the longevity and mobility of the carriers. The moderate mobility and extended carrier lifetimes (100ns to 15s under one-sun conditions) result in a long drift and diffusion length, indicating that perovskite photodetectors have excellent charge transport.

2.10.1 Key performance parameters for photodetectors

(a) Responsivity (R)

Responsivity is the ratio of photocurrent and light intensity. It indicates the sensitivity of the detector to optical signals. The greater the responsivity of photodetectors, the more effectively they respond to an optical signal. The Equation represents responsivity:

$$R = \frac{J_{ph}}{L_{light}} \quad (2.10)$$

where R (mA/W) is responsivity, J_{ph} is photocurrent and L_{light} is the intensity of light.

(b) Detectivity (D^*)

A photodetector's specific detectivity (D^*) describes the ability of the device to detect the lowest light intensity. In general, the Equation of specific detectivity is given as:

$$D^* = \frac{(A \cdot f)^{0.5}}{NEP} \quad (2.11)$$

NEP is an alternative meaning of noise equivalent power that is not normalized to measurement bandwidth (W), A is the sensor's size, and f is the frequency bandwidth (Hz). When shot noise dominates the dark current (at high frequencies and low temperature), detectivity can be described as (Gong et al., 2009):

$$D^* = \frac{R}{\sqrt{2qJ_{dark}}} \quad (2.12)$$

where D^* (Jones = $\text{cm Hz}^{1/2}/\text{W}$) is the detectivity, R (mA/W) is the responsivity, q is the elementary charge (1.6×10^{-19} C), and J_{dark} (mA/cm²) is the dark current.

(c) On/Off ratio

The active layer's photoelectric conversion and charge transport are primarily responsible for the on/off ratio, defined as the ratio of the PD's photocurrent (I_{ph}) to its dark current (I_{dark}). To achieve a higher on-to-off ratio, it is necessary to either increase the photocurrent or reduce the dark current.

(d) Response time

A photodetector's response time measures how quickly it reacts to light that is incident from outside. It is typically identified by the rise time (τ_{rise}) and decay time (τ_{decay}), which are defined as the period it takes for the current to reach 90% of its maximum after being exposed to incident light and the time it takes for the current to reach 10% of its maximum after the incident light has been turned off, respectively as shown in Figure 2.34 (Marshall, 2017).

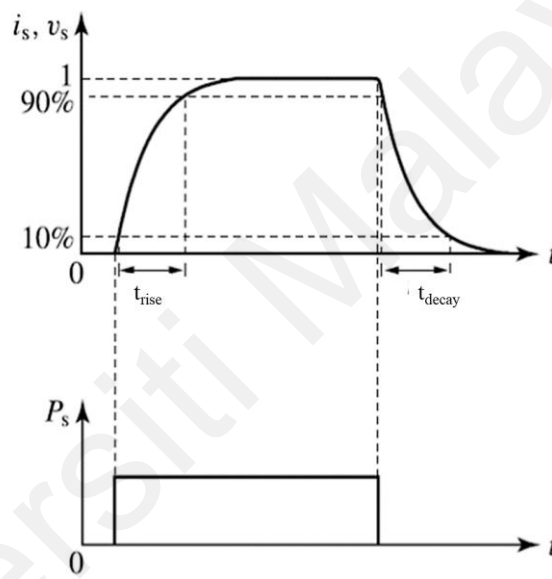


Figure 2.34: Rise time (τ_{rise}) and decay time (τ_{decay}) of a photodetector with a square-pulse signal [Picture source from (Marshall, 2017)].

(e) Dark current density (J_{dark})

In the absence of illumination, a "dark current" is produced when a reverse bias voltage is applied. The negative impact of a high dark current density on photodetector performance can be assessed by its negative effect on many critical measures. First off, sensitivity to low light intensities decreases with high J_{dark} . Additionally, raising the minimum detectable photocurrent limits the linear dynamic range (LDR) or the range of usable light intensities within which the image sensor can function (Jansen-van Vuuren et al., 2016).

Equation (2.12) shows that the specific detectivity D^* declines with increasing dark current densities. In contrast to R , J_{dark} can vary by multiple orders of magnitude depending on the material characteristics and device architecture; hence lowering J_{dark} is crucial for enhancing LDR and D^* in photodetectors (Kielar et al., 2016).

Under a reverse bias voltage, the rate at which charge carriers are injected from the contacts into the semiconductor or thermally generated in the bulk of the active layer is primarily responsible for the intrinsic J_{dark} of the photodetector (i.e., in the absence of pinholes or other extrinsic leakage phenomena). Donor and acceptor energy levels are shown as solid orange lines and dotted black lines, respectively, in Figure 2.35(a). Donor highest occupied molecular orbital (HOMO) and acceptor lowest unoccupied molecular orbital (LUMO) density of states (DOS) are considered to be Gaussian. While holes are injected from the low work function electrode into the tail states of the donor HOMO, electrons are injected from the high work function electrode into energy levels in the tail of the Gaussian DOS of the acceptor LUMO. The charge injection rate is anticipated to be highly dependent on the injection barrier, ϕ_b which is defined as the difference in energy between the donor HOMO and Fermi level of the high work function electrode in the case of holes. For a specifically applied bias, a greater ϕ_b leads to a lower dark current. Considering there are perfect Ohmic contacts and alignment between the acceptor LUMO and the low (high) work function electrode Fermi level (donor HOMO), donor and acceptor materials are in direct contact with both electrodes; thus, the injection-limited J_{dark} should be proportional to the effective band gap E_g . The influential band gap E_g is the energy difference between the donor HOMO and acceptor LUMO of the donor.

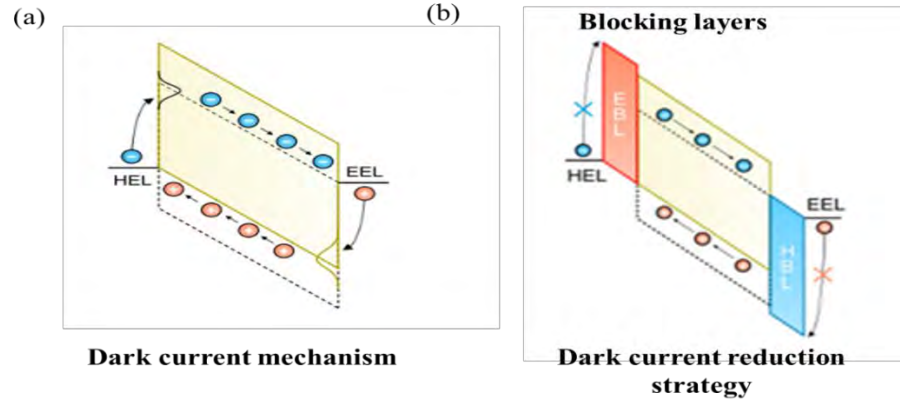


Figure 2.35: (a) Mechanisms for dark currents: Injection of charge into the tail states of the Gaussian density of states from interactions (DOS). HEL and EEL stand for the corresponding electron and hole transport layers.[Picture source from (Simone et al., 2020)].

Enhancing charge selectivity at the contacts is one of the methods that can be utilized to lower J_{dark} . This is achieved by increasing the energy barriers for charge injection under reverse bias while keeping an energy cascade between the active layer and the matching electrodes to ease the extraction of photo-generated carriers. To accomplish this, the photoactive material layer is placed between layers that block electrons (known as EBLs) and layers that block holes (known as HBLs). These include an extra interlayer between the electrode and the photoactive layer, resulting in a higher energetic barrier for charge injection when $E_{LUMO, EBL} > E_{LUMO, acceptor}$ for electrons and $E_{HOMO, HBL} < E_{HOMO, donor}$ for holes. So that the collection of photo-generated carriers is not hampered, it is preferable that $E_{HOMO, EBL} = E_{HOMO, donor}$, and $E_{LUMO, HBL} = E_{LUMO, the acceptor}$.

2.10.2 Hole transport layer (HTL)

An ideal hole transport material candidate inherently has high hole mobility, and energy levels compatible with the perovskite layer are stable in air for long periods and resistant to light and heat degradation. When utilized in p-i-n photodetectors, HTL should also be solution-processed for preparation.

It is crucial to consider the HTLs' low cost and simple preparation for scaled manufacture and further commercial application(J. Chen & Park, 2019; Krishna & Grimsdale, 2017; Urieta-Mora et al., 2018). The most common p-type organic interlayers are the conductive Poly (3,4-ethylene dioxythiophene): poly(styrene sulfonate) (PEDOT: PSS). Figure 2.36 depicts the chemical structure of PEDOT: PSS. The HTL performance of a perovskite photodetector employing PEDOT: PSS is excellent because of the material's transparency and conductivity(Du et al., 2018; Duan et al., 2020). High-quality PEDOT: PSS film can be fabricated using standard solution-based coating techniques. It is dispersible in water and some organic solvents(Groenendaal et al., 2000).

Besides its low price and vital thermal and mechanical flexibility, PEDOT: PSS also has outstanding thermal stability. So, in recent years, PEDOT: PSS has been the go-to material for inverted perovskite solar cells' hole transport layer (HTL)(Y. Yang et al., 2014). The hygroscopic and acidic properties of PEDOT: PSS, however, would have an impact on the stability of the devices. The acidic composition of PEDOT: PSS causes ITO electrode corrosion. In addition, the hygroscopic nature of PEDOT: PSS leads the perovskite absorber layer to decompose by absorbing moisture from the surrounding environment(Hu et al., 2017; Jørgensen et al., 2008; Sun et al., 2015).

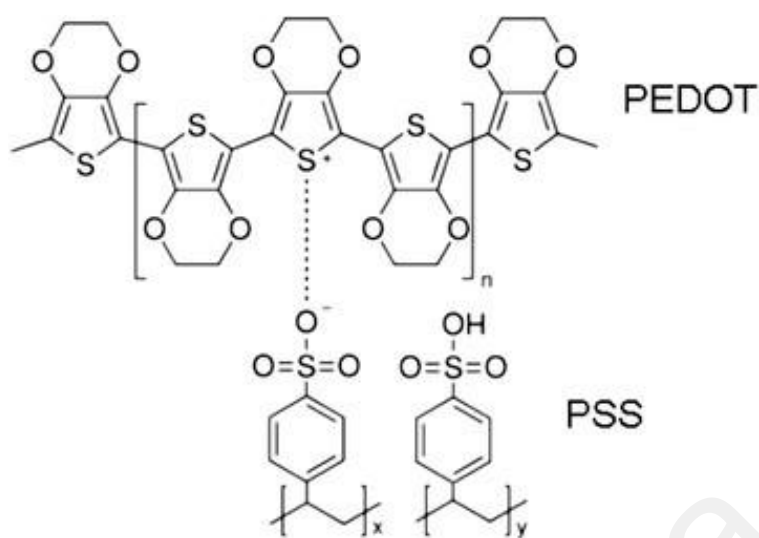


Figure 2.36: Chemical structure of PEDOT: PSS.

Several p-type inorganic compounds, including CuSCN, CuI, and NiO, have been presented as possible alternatives to PEDOT: PSS for strengthening the stability of electronic devices (Christians et al., 2014; Ye et al., 2015; You et al., 2016). However, the performance of the devices is limited by the inorganic materials' low conductivity. Therefore, it is essential to optimize the features of the PEDOT: PSS HTL while constructing devices with long-term stability. It has been demonstrated that optimizing the PEDOT: PSS HTL layer's pH value, hydrophilicity, work function, surface shape, and electrical conductivity can increase the performance and stability of devices (S. Chen et al., 2014; W. H. Chen et al., 2019; Reza et al., 2020; T. C. Tsai et al., 2014).

2.10.3 Self-powered Photodetector

Optoelectronics devices with low power consumption are an active area of study. Typically, conventional photodetectors must be powered by an external energy source; in most cases, the battery is used. In contrast, a future intelligent sensor system cannot use decentralized power sources because (1) the building material used in batteries is anticipated to be highly dangerous to the ecosystem, and (2) the cost of an integrated photodetector network must account for the necessity of battery recycling.

Therefore, photodetectors can be self-sufficient, long-lasting, and require zero maintenance if they either have an internal power source or can harvest energy from their natural environment. This highlights the requirement for efficient photodetectors that function without a bias voltage. Self-powered photodetectors are a novel type of photodetectors that operate without an external power source. Photodetectors are based on the fundamental principle that electrons can change from a lower energy state to a higher energy one when exposed to photonic illumination.

Currently, photovoltaic (PV) and photoconductive (PC) modes are the two primary ways commercial PDs are powered. PC mode detectors determine the presence of light by measuring the resistance shift across a photoactive material while it is illuminated. In contrast, photodiodes of the PV type use the intrinsic electric field in heterojunction or Schottky junctions to isolate photo-generated electron-hole pairs effectively. PV-type photodetectors could be successfully made through doping or simple hybrid material combinations because the necessary built-in electrical fields typically exist in junctions between materials with different work functions.

2.10.4 Low-dimensional hybrid perovskite photodetectors

The tunable perovskites have been employed as the active layers in photodetectors. They have produced good photodetection performance because of the proven benefits of effective light absorption in the broadband range, high photo-generated carrier yield, and high charge mobility. Zhu et al. demonstrated large-scale, regulated crystal formation of the two dimensional halide perovskite $(\text{C}_4\text{H}_9\text{NH}_3)_2\text{PbBr}_4$ precipitated in the presence of potassium ions.

Low dark currents of 1.5×10^{-9} A were observed in the photodetectors fabricated by dropping the $(\text{C}_4\text{H}_9\text{NH}_3)_2\text{PbBr}_4$ nanobelts on the interdigitated Au electrodes, and photocurrents of 8.21×10^{-8} A and 6.76×10^{-8} A were observed in response to light irradiation at 365 nm and 405 nm, respectively, at an applied voltage of 5 V (B. S. Zhu et al., 2018). They found that the pores within the $(\text{C}_4\text{H}_9\text{NH}_3)_2\text{PbBr}_4$ nanobelts could improve light scattering, contributing to the nanobelts' light-harvesting capabilities and, in turn, the photodetection performance, explaining the observed high photocurrent. Because the exciton binding energy is so high (more than ten times the thermal energy at ambient temperature), the photodiode made from the 2D perovskite $(\text{C}_6\text{H}_9\text{C}_2\text{H}_4\text{NH}_3)_2\text{PbI}_4$ described in the literature only showed 10% EQE at a wavelength of 508 nm (Ahmad et al., 2015). The high retrieved photocurrents also indicate that electron/hole transport layers should be implemented. Long-term device stability was significantly enhanced in 2D perovskite-based photodetectors, although their performance is lower than that of 3D analogues.

CHAPTER 3: MATERIAL AND METHODS

3.1 Introduction

This chapter presents the techniques for fabricating perovskite-based FET and photodetector measurement methodology. The first part of this chapter explains the materials and methods used in the fabrication process, including cleaning of ITO substrates, plasma etching, solution preparations, and material deposition methods such as spin coating and physical vapour deposition. Further explanation of perovskite thin film characterization involving UV-Vis Spectroscopy, Contact angle, X-ray Diffraction, Ultraviolet Photoelectron Spectroscopy, and Atomic Force Microscopy are presented in this chapter. The field-effect transistor, photodetector fabrication, and electrical measurement are also described.

3.2 Materials

3.2.1 Propylammonium lead bromide (PAPbBr₃)

PAPbBr₃(CH₃CH₂CH₂NH₃PbBr₃) used in this study was purchased from Xi'an polymer Light Technology Corp. PAPbBr₃ is in off-white colour powder form with molecular weight 507.03g/mol, purity>99%. PAPbBr₃ is an intriguing one-dimensional perovskite due to its single-chain structure, high electron-phonon interaction strength, and promising applications in optoelectronic devices(Saidaminov et al., 2017). However, PAPbBr₃ has not been used as an active component in devices because of its extremely deep VBM (Subramaniam et al., 2021). The deep VBM perovskites used in this study serve as the FET's active layer.

3.2.2 Phenethylammonium Lead Bromide (PEA₂PbBr₄)

PEA₂PbBr₄ (C₆H₅CH₂NH₃)₂PbBr₄), purity >99%, was obtained from Xi'an polymer Light Technology Corp. PEA₂PbBr₄ is an off-white colour powder and has a molecular weight of 743.14g/mol.

The exciton absorption peak of $\text{PEA}_2\text{PbBr}_4$ is close to the ultraviolet region (B. Guo et al., 2020), making it a good choice for an active layer in a UV photodetector.

3.2.3 Sulfonated tetrafluoroethylene-based fluoropolymer-copolymer (Nafion)

Nafion, 5% of the weight of lower aliphatic alcohols and water, was purchased from Sigma Aldrich. Nafion has a hydrophobic fluorocarbon backbone, perfluoro vinyl ether branch, and sulfonic acid end group (Figure 3.1). The hydrophilic sulfonic acid group ($-\text{SO}_3\text{H}$) at the end of this hydrophobic chain conducts holes but blocks electrons (Heitner-Wirguin, 1996). Nafion has been extensively explored as a proton exchange membrane in fuel cells due to its high conductivity and chemical stability.

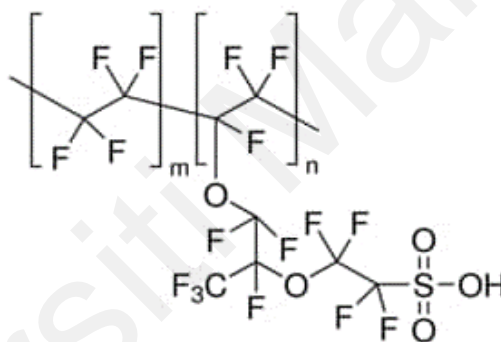


Figure 3.1: Chemical structure of Nafion

3.2.4 Poly (N-vinyl carbazole) PVK

Sigma Aldrich supplied high molecular weight PVK ($M_w = 100\,000$). Given its excellent film-forming properties, high hole transport capacity, and high solubility in DMF, PVK is chosen as the polymer host for the perovskite active layer.

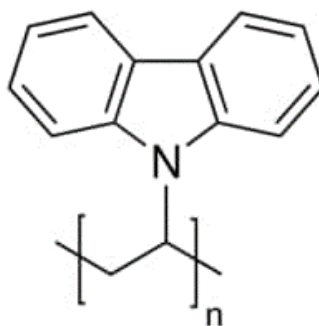


Figure 3.2: Chemical structure of Poly (N-vinyl carbazole)

3.2.5 Polytetrafluoroethylene (PTFE)

PTFE as purchased from Chemours Company and used as received. PTFE is composed of fluorine atoms and possesses a symmetrical chain structure. The chemical structural formula is depicted in Figure 3.3. PTFE exhibits several notable features, including its remarkable temperature resistance ranging from -230 to 260 °C, exceptional heat resistance, favorable chemical stability, and nonhygroscopic nature (Sparnacci et al., 2009; P. Zhao et al., 2018). Consequently, PTFE (Dielectric constant= 2.0) was employed as the dielectric layer in the field-effect transistor.

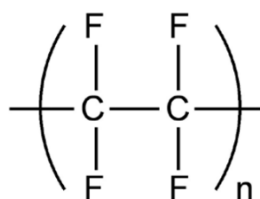


Figure 3.3: Chemical structure of PTFE

3.2.6 Poly (3,4-ethylenedioxythiophene):poly(styrene sulfonate) (PEDOT:PSS)

The water-soluble chemical PEDOT: PSS (Figure 3.4) PH1000 was bought from Heraeus Clevios in a soluble form and filtered using a 0.45 μ m PTFE filter. PEDOT: PSS is a popular HTL material because of its many advantages, including transparency, adaptability, low cost, and ease with which it may be deposited using traditional methods. Here, PEDOT: PSS aqueous dispersion is employed as the HTL in a perovskite photodetector.

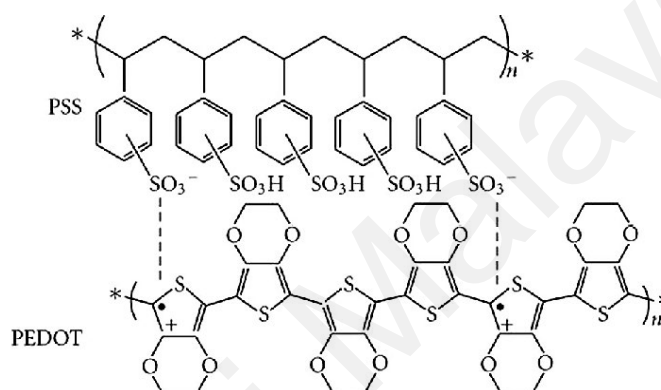


Figure 3.4: Chemical structure of PEDOT: PSS

3.2.7 [6,6]-phenyl C61 butyric acid methyl ester (PC₆₁BM)

PC₆₁BM (purity >99.9%) (Figure 3.5) with a molecular weight of 910.88 g/mol was purchased from Sigma Aldrich. PC₆₁BM has a brown-to-black powder appearance. The PC₆₁BM material was used as the electron transport layer (ETL) for a low-cost and time-efficient procedure in photodetectors.

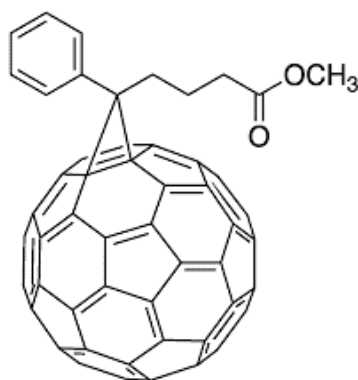
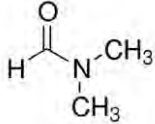
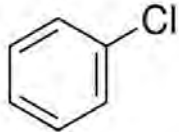
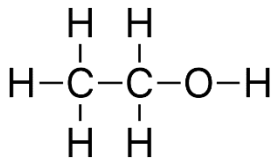
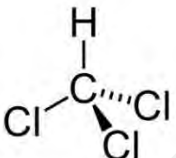


Figure 3.5: Chemical structure of PCBM

3.2.8 ITO and Aluminum Electrode

Electrodes play a crucial role in the production of semiconductor devices. Whether the metal-semiconductor interface is rectifying or ohmic is determined by the work function of the metallic electrode and the VBM-CBM energy levels of semiconductor materials. Aluminum (Al) was supplied by Sigma Aldrich in the form of a meter-long length of wire, and it has a purity rating of 99.999 percent metal. Al has a boiling point of 2460°C and a melting point of 660°C. With a work function of 4.4 eV, Al was used as an electrode in this research for FETs and photodetectors. The photodetector's pre-patterned ITO was acquired from Lumtec Ltd., while the pre-patterned ITO of FET was purchased for Ossila, with 100nm ITO thickness and 20 Ω / square roughness.

Table 3.1: Details all of the solvents employed in the thesis. They were used in their anhydrous form without any further purification.

Solvents	Properties	Manufacturer
Dimethylformamide(DMF) 	<ul style="list-style-type: none"> • anhydrous, purity>99.8% • Boiling point: 153 °C 	Sigma Aldrich
Chlorobenzene (CB) 	<ul style="list-style-type: none"> • ACS reagent, ≥99.5% • Boiling point: 132 °C 	Sigma Aldrich
Ethanol 	<ul style="list-style-type: none"> • ACS reagent, ≥99.5% • Boiling point: 78.37 °C 	HmBG
Chloroform 	<ul style="list-style-type: none"> • Boiling point: 61.2 °C 	Sigma Aldrich

3.3 Experimental procedure

3.3.1 Substrate Cleaning Procedure

In this research, two ITO substrates are used, as shown in Figure 3.6. FET will be fabricated using a pre-patterned ITO substrate (20 mm x 15 mm) with a 30 mm × 50 μm channel length, as shown in Figure 3.6(a). Figure 3.6(b) shows a pre-patterned ITO substrate (1.1 mm x 15 mm x 20 mm) purchased from Lumtec Corp, which has a thickness of 140 nm and 9~15 Ω/sq sheet resistance. The pre-patterned ITO comprises six pixels and will be used as an anode in photodiode fabrication.

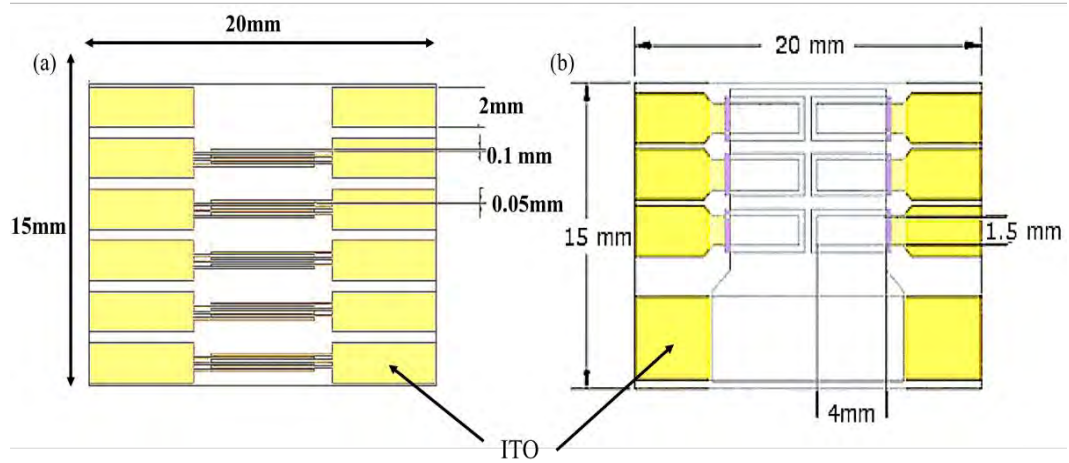


Figure 3.6: Geometry design of Pre-patterned ITO substrate of (a) FET (b) Photodiodes.

A thorough cleaning of the substrate becomes necessary because organic contaminants and dust particles from the environment may adhere to the surface of the indium tin oxide (ITO) layer during experimentation. First, the pre-patterned ITO substrates are cleaned with deionized water, acetone, and isopropyl alcohol (IPA), followed by deionized water each for 10 min with the aid of ultrasonic agitation. Lastly, inert nitrogen (N_2) gas purging removes any dust particles on the ITO surface. The cleaned substrates were baked inside the oven for 2 hours to remove any moisture residue. All the ITO substrates were treated with oxygen plasma for 5 minutes (Figure 3.7). The oxygen plasma treatment tends to eliminate the ITO surface absorbed impurities and increase the work function of ITO. This step is crucial to reduce energy offset between ITO and subsequently deposited layer and ease the charge transport (Ke et al., 2016).



Figure 3.7: Oxygen plasma parallel plate etcher (Polaron PT7170).

3.3.2 Thin film preparation and device fabrication

Spin-coating is a commonly adopted technique to deposit solution-processed materials on substrates. When the solution is spin-coated, the solution is sheared by the centripetal force and facilitates uniform distribution across the substrate to form a thin film. The spin-coating method only requires a small amount of precursor solution to form nanoscale range film thickness. Figure 3.8(a) depicts the spin-coating technique on a pre-patterned substrate. Thickness and coverage can be modified by altering rotation speed, time, steps, and acceleration ramp. The following equation illustrates the inverse relationship between thickness (t) and angular velocity (ω).

$$t \propto \frac{1}{\sqrt{\omega}} \quad (3.1)$$

Therefore, all the active layers were spin-coated using WS-650-23nppm, Laurell Technologies spin coater, as shown in Figure 3.8(b).

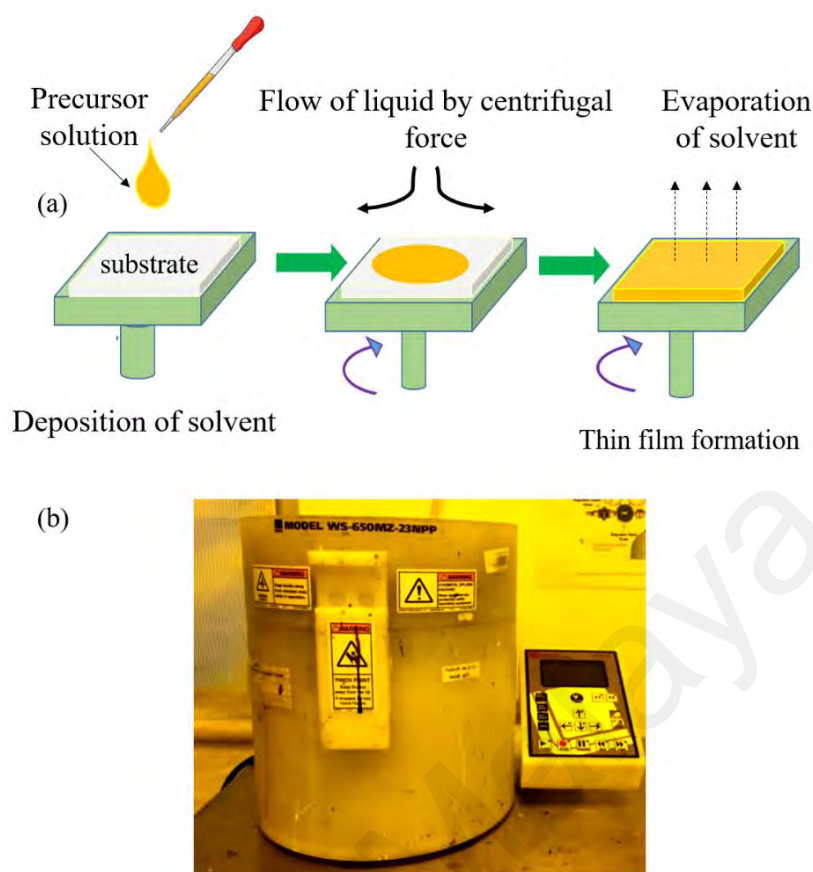


Figure 3.8: (a) Spin-coating process (b) Spin coater (WS-650-23nppm, Laurell Technologies).

Figure 3.9 illustrates the fabrication process of FET and photodiode devices. After cleaning, the pre-patterned ITO substrates were transferred into a Nitrogen gas-filled glove box (Figure 3.10a). Then perovskite precursor solution is dynamically dispensed on the spinning ITO substrate. The substrates were annealed on a hot plate at 100°C for 15min. The perovskite films were covered by spin coating with a dielectric solution in the glove box. After wiping the top and side ITO with cotton swap dampened in DMF (excludes the channel area), the substrate was heated on a hot plate for 10min. Finally, the FET device is completed by depositing 100nm Aluminum as a Gate electrode using a shadow mask, as shown in Figure 3.10(a). Physical vapour deposition (PVD) under a high vacuum ($\sim 10^{-4}$ Torr) was used to deposit aluminium electrodes.

Briefly, this technique is performed by heating a material in a vacuum chamber until its surface atoms have sufficient energy to evaporate from the surface and then condensate at the substrate surface. The structure diagram of the thermal evaporator is depicted in Figure 3.10(b).

PEDOT: PSS was filtered using 0.22 μm syringe PTFE filters and spun-coated on the pre-patterned ITO surface to form HTL for the photodiode device, as depicted in Figure 3.9(b). The PEDOT: PSS layer was heated on a hot plate at 140°C for 30min in the clean room. Subsequently, perovskite precursor was deposited as described above. Next, a layer of PCBM was spun-coated at 3000 r.p.m. for 40 seconds, followed by a 15-minute annealing period at 100°C. The unwanted spun-coated material at the Cathode and side of the ITO pixel was rubbed away using the appropriate solvent after the deposition of each active layer. This step is crucial to ensure good contact with the Aluminum electrode. Finally, a 100nm Aluminum electrode was thermally evaporated on the PCBM layer in PVD (see Figure 3.10). A large current (~ 110 A) is used to evaporate the metal Al pieces placed on the tungsten boat by the evaporator. As shown in Figure 3.11(b), a shadow mask is used to form a 0.045cm² active area.

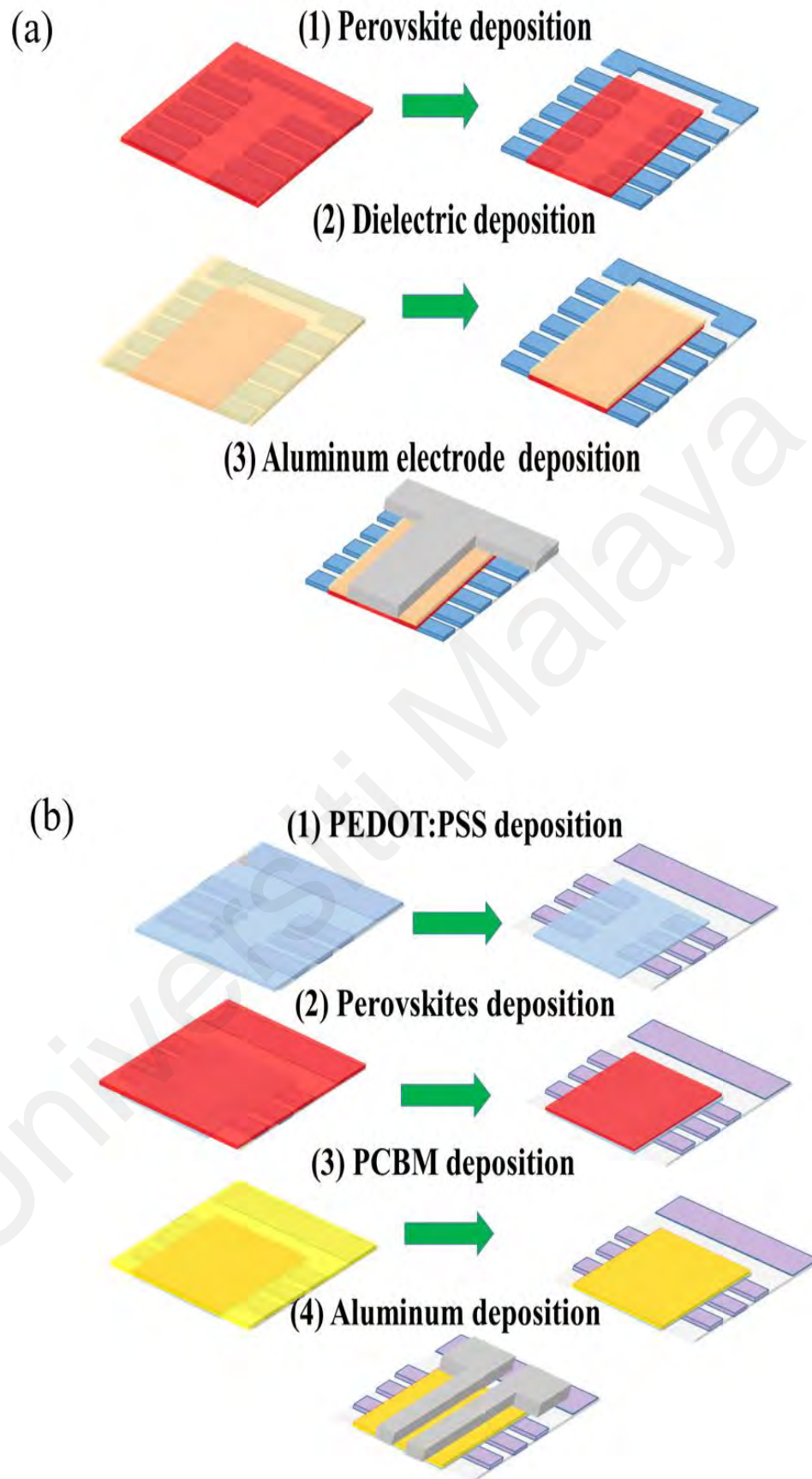


Figure 3.9: The fabrication process of (a) FET and (b) Photodiodes.

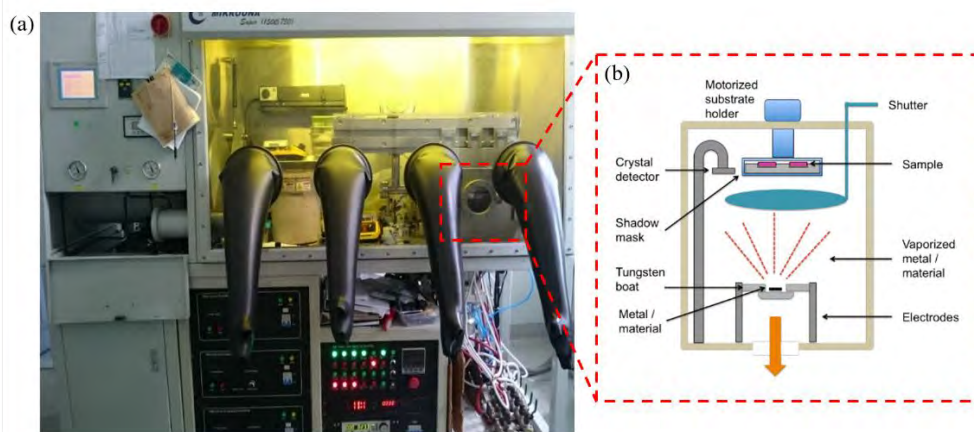


Figure 3.10: (a) Thermal Evaporation System inside Nitrogen gas-filled glove box, Low Dimensional Material Research Centre (LDMRC), (b) structure diagram of the thermal evaporator.

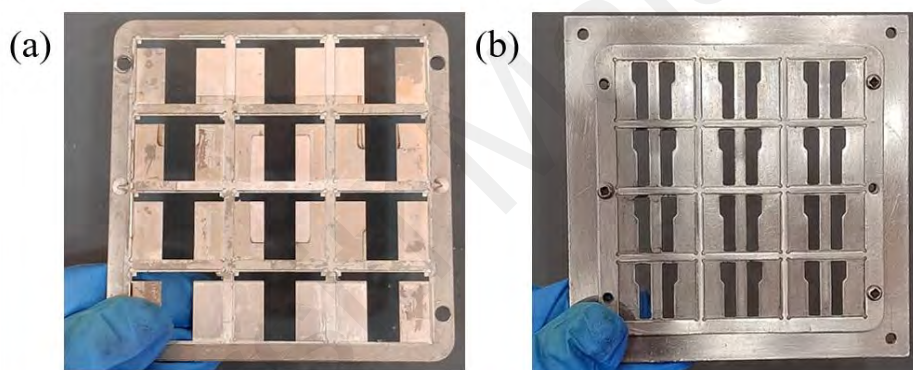


Figure 3.11: (a) FET shadow mask and (b) Photodiode shadow mask.

3.4 Thin film characterization

3.4.1 Surface Profilometer

Surface profiler KLA Tencor P-6 functions based on contact mode. It uses a probe to detect the surface, physically moving a probe along the sample surface in a vertical order to determine the surface height. Using a cantilever system with a 60° radius, this profiler's stylus tip maintains a constant force throughout the scanning process. A thin film is wiped with a sharp-tipped cotton swab soaked in a suitable solvent, creating a groove between the film and substrate surface for the stylus to measure the thickness. The stylus tip is then slid perpendicularly across the scratched trace to separate film and substrate levels.

This distance defines the thin film's thickness, as shown in the schematic diagram (Figure 3.12b). Figure 3.12 (a) shows the experimentally measured thickness of the test sample.

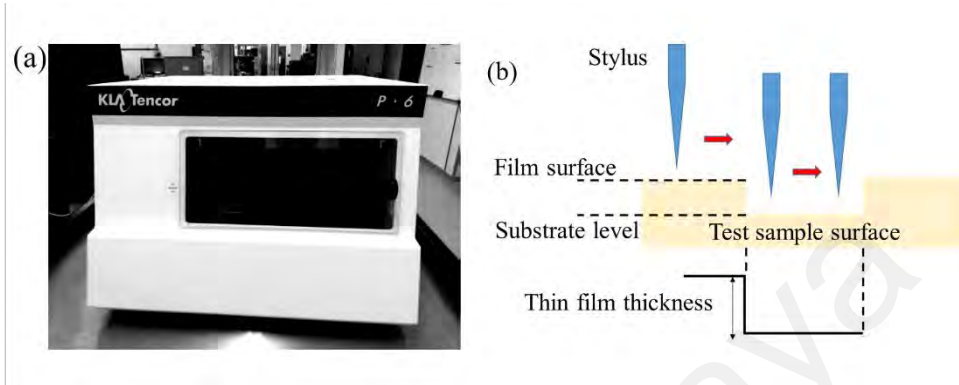


Figure 3.12: (a) The KLA Tencor P-6 Surface Profiler (b) Thickness measurements using a surface profiler.

3.4.2 Contact angle measurement

The most accessible approach to measuring a contact angle is sessile drop contact angle goniometer, which uses a direct visual measurement at the point of contact. As a drop of liquid is placed on a material surface, and the drop forms a dome shape on the surface, a contact angle is created, induced by surface tension, resulting from homogeneous molecular forces acting against one another. When a liquid comes into contact with a solid surface, a non-uniform interaction occurs between the liquid, the solid, and the gas around it. This causes the droplet's shape to be influenced by the outside forces and the surface tensions at the interfaces (Y. Yuan & Lee, 2013). The contact angle is the angle produced between the outline of the contact surface and the drop's tangent line. As demonstrated below, Young's equation defines this interaction as the mechanical equilibrium of the surface tensions.

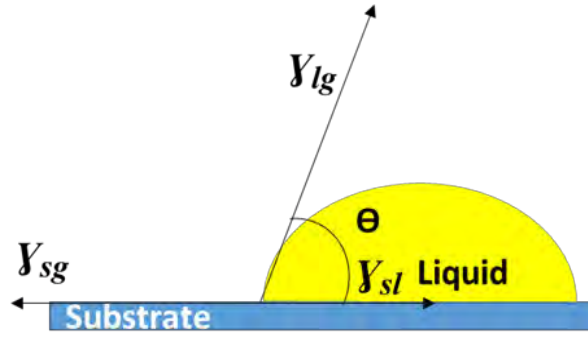


Figure 3.13: Diagram of equilibrium for droplets on a surface

$$\gamma_{lg} \cos \theta_Y = \gamma_{sg} - \gamma_{sl} \quad (3.2)$$

Surface tensions at the liquid-gas, solid-gas, and solid-liquid interfaces are denoted by γ_{lv}

, γ_{sv} , and γ_{sl} , respectively; the contact angle is denoted by θ_Y .

In this study, the wettability substrate to perovskite precursor solution was measured using Attention Theta Lite as portrayed in Figure 3.14(a). A 100 μl syringe with perovskite precursor solution was positioned above the sample and in the middle of the film on a horizontal stage. A computer-connected CCD camera was used to capture the spreading of perovskite precursor droplets. Their wetting behaviour is analyzed by OneAttension software, as illustrated in Figure 3.14(b). Higher and lower contact angles signify different levels of wettability, as shown in Figure 3.14 (c) (Tanaka et al., 2014).

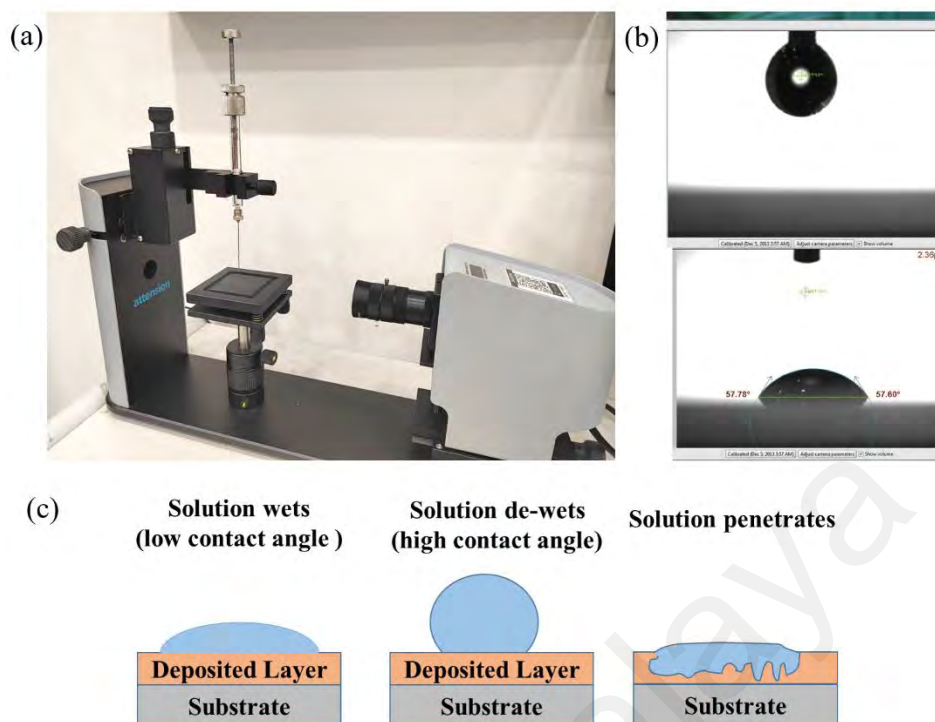


Figure 3.14: (a) Contact angle measurement set-up, (b) OneAttension software, (c) Wettability.

3.4.3 Ultraviolet/visible/infrared (UV/Vis/NIR) Spectrophotometer

Spectroscopy studies the interaction between electromagnetic radiation (UV/Vis/NIR) and materials. The sample was made by applying a spin coating or drop casting technique over a quartz substrate, which was chosen for its superior capacity to transmit ultraviolet (UV) light in comparison to glass. As illustrated in Figure 3.15, the optical characteristics of the thin films were determined using a UV/VIS/NIR spectrophotometer Perkin Elmer model Lambda 750. It has UV-Vis and NIR resolutions of 0.17 to 5.00 nm, respectively. UV-VIS-NIR spectrometers use a light source, a monochromator to pick the wavelength of required light, and a detector to read the intensity of the light. A baseline measurement is taken where the quartz substrate is placed in front of both the reference beam and the sample beam to produce a 100% transmission measurement to remove any contributions from the substrate.

The transmission spectrum of the sample is then measured by placing a substrate coated with the perovskite material in front of the sample beam. The tungsten lamp measures the visible spectrum, while a deuterium lamp measures the ultraviolet spectrum. Figure 3.15(c) depicts the measuring setup of the system. A grating in the monochromator spreads the light from the source and divides it into two separate beams, one for the thin film and one for the reference quartz substrate. The photomultiplier tube subsequently converts the count of photons into an electrical signal by illuminating these lights. Next, UV Winlab software amplifies and processes the signal to create a film's optical absorption spectrum. This study's visible range was the focus; thus, optical data were obtained from 300 to 600 nm.

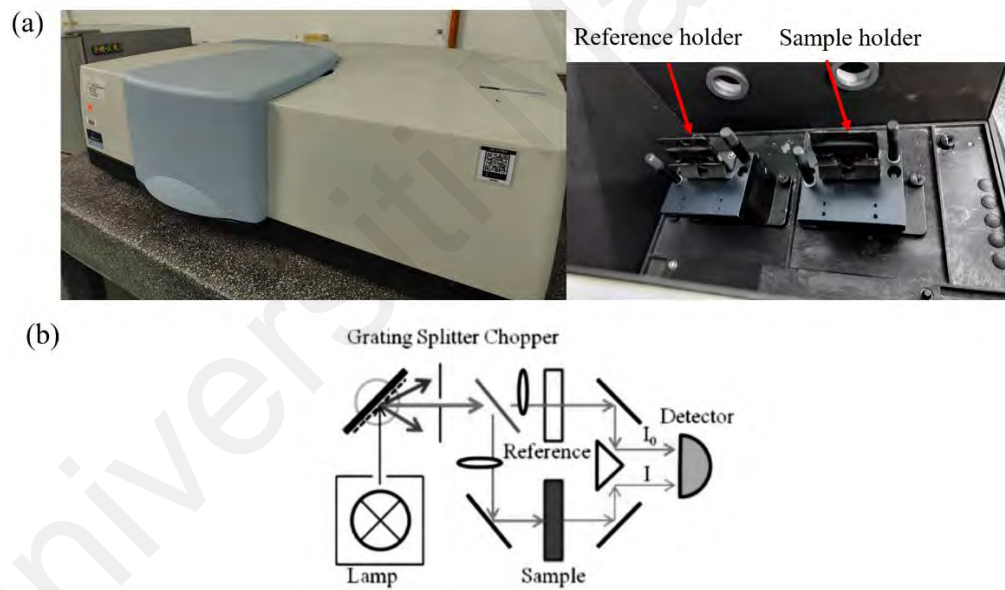


Figure 3.15: (a) Lambda 750 UV-VIS-NIR Spectrometer and (b) the optical path of the UV-VIS-NIR system.

The energy of the incident light is converted into kinetic energy as the electron in the valence band is shifted to the conduction band:

$$E = h\nu = h \frac{c}{\lambda} \quad (3.3)$$

λ is the wavelength, h is the Planck constant, ν is the frequency of light and c is the speed of light.

The material's optical bandgap can be estimated using this relationship. The optical bandgap E_G might be calculated from the Tauc plot (Figure. 3.16b) for materials with a direct allowed transition in the bandgap using the equation:

$$\alpha h\nu = A(h\nu - E_G)^{1/2} \quad (3.4)$$

An example of a UV-visible absorption spectrum obtained with a Lambda 750 spectrometer from PerkinElmer is displayed in Figure 3.16(a).

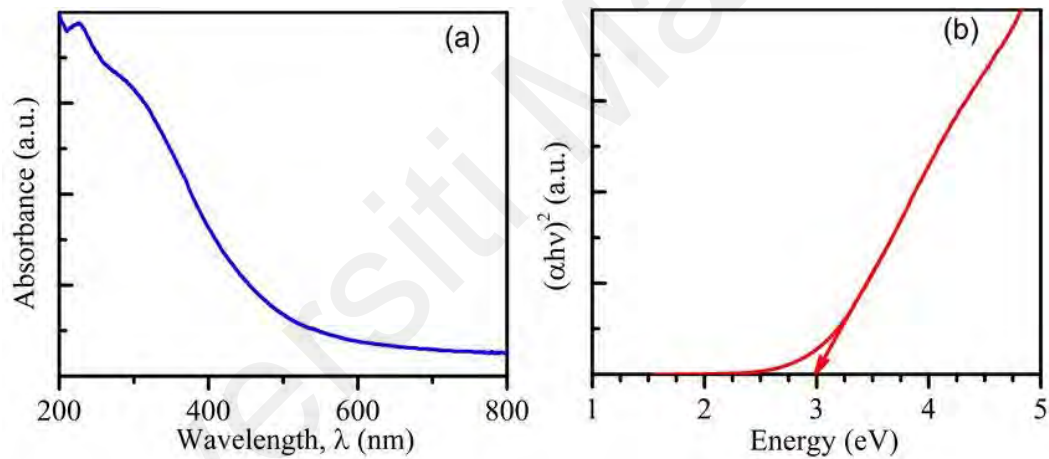


Figure 3.16: (a) UV-Vis spectra and (a) Tauc plot of perovskite with an estimated optical bandgap of 1.59 eV. [Picture source from (LI, 2022)].

3.4.4 Atomic force microscope (AFM)

The AFM measurements in this study were performed at Universiti Kebangsaan Malaysia using the NT-MDT NTEGRA-Prima system by Quasi-S Technology Sdn. Bhd. AFM analyses the surface morphology of solid materials. It examines material surfaces by detecting weak atomic interactions between the sample and the cantilever. A silicon or silicon nitride cantilever is attached to a fine microscopic tip at one end. The cantilever tip has nanometer-scale curvature.

One end of the cantilever is fixed and lit by a laser diode. Due to a weak repulsive attraction between the tip and surface atoms, the cantilever bends and undulates during sample scanning. Detecting the spot's position changes with a photodiode yields atomic-resolution surface topography data. The scan size of the AFM picture in this study was $5\mu\text{m} \times 5\mu\text{m}$. The preparation of the sample for AFM involved the deposition of perovskite precursor solution onto a pristine glass substrate using the spin-coating technique.

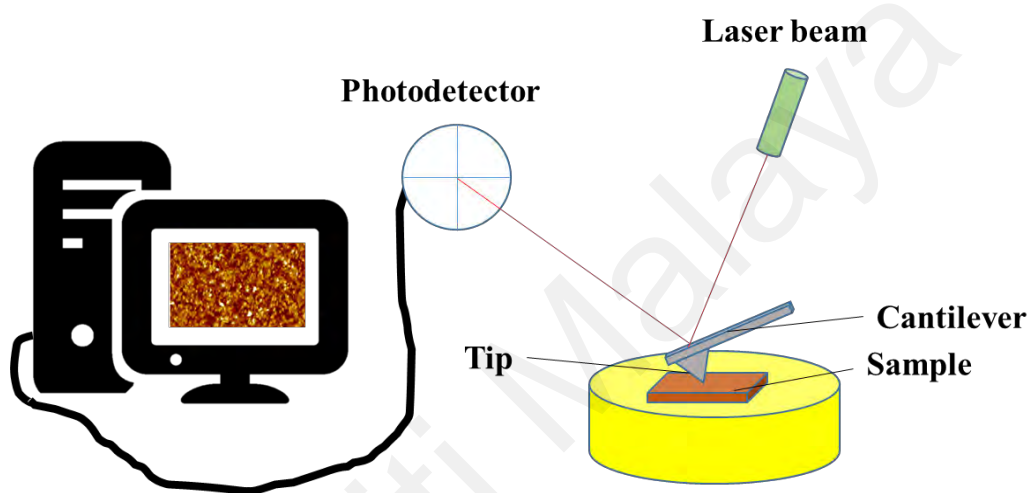


Figure 3.17: Schematic diagram of AFM

3.4.5 Field Emission Scanning Electron Microscope (FESEM) and Energy dispersive X-ray (EDX)

With an infinite depth of field, FESEM offers topographical and elemental information at magnifications ranging from 10x to 300,000x. FESEM can produce images that are more distinct, less distorted electrostatically, and have a spatial resolution of up to 1.5 nanometers. Figure 3.18 displays FESEM used in this research. In the FESEM, electrons are supplied to the sample's surface via a field-emission cathode in the electron gun. The secondary electrons with lower energies are generated close to the material's surface.

The intensity of the secondary electron is measured as a function of the position of the scanning primary electron beam to generate an image of the surface of the sample. Elements on a solid surface can be identified and quantified by the use of EDX. It is practical and easy to operate. It is done by analyzing the X-rays released by the sample's distinctive elements and their wavelength and intensity. Consequently, it determines the concentrations of various elements and compares their intensities. Excitation of the surface by a high-energy electron beam results in the emission of unique X-ray wavelengths for each element, which is detected by an energy dispersive detector.

A "fingerprint" spectrum, which can be used to identify elements by comparing them to reference spectra, has been assigned to each element. The process of preparing the thin film sample for FESEM entailed depositing a solution of perovskite precursor onto a clean glass substrate by the utilization of the spin-coating method.



Figure 3.18: Field Emission Scanning Electron Microscope (FESEM) JEOL JSM-7600F.

3.4.6 X-ray diffraction (XRD)

XRD consists of a dependable X-ray generator, a sample stage that can be adjusted as needed, a sensitive X-ray detector, and an accurate processing system. The monochromatic X-ray is represented in Figure 3.19(a), where the X-ray functions as an EM wave on the crystal. The wavelength of the X-ray beams is comparable to the distance between the atoms in the sample, and the distance between the atoms in the molecule will influence the diffraction angle. This is in contrast to the use of much longer wavelengths, resulting in the diffraction angle unaffected by the distance between the atoms. X-ray is dispersed by atoms and reflected from the centre of atoms. The scattered waves have a defined phase connection because of the periodic arrangement of these atoms.

Diffraction occurs because scattered X-rays reinforce each other in specific directions while cancelling each other out in others. The diffraction pattern of each crystal is unique, just like fingerprints. The diffraction line's intensity and the crystal's quality are revealed by the diffraction line distribution, which is determined by the unit cell's size, shape, and orientation. The diffraction behaviour of X-rays in a crystalline substance is described by Bragg's Law. As shown in Figure 3.19(a), in the unit cell, an X-ray with a wavelength (λ) near the interplanar distance (d) can be reflected so that the reflection angle (θ) is equal to the incident angle (θ). While the equation in the graph of Figure 3.19(b) expresses the difference in path length as an integer of the wavelength. Diffractogram analysis can provide both qualitative and quantitative data, such as crystal structure, crystallinity level, lattice parameters of the unit cell, and the concentration of the various phases present in the sample material. Multiple characteristic peaks corresponding to each crystal plane in the unit cell can be seen in a typical XRD crystalline material (Figure 3.19c). These peak positions are used for lattice parameter calculation and qualitative phase analysis.

Using Bragg's equation ($2d \sin \theta = n \lambda$), the unit cell's dimensions can be calculated, where d is the distance between atomic planes, λ is the wavelength that was added, and θ is the angle of diffraction (Bragg, 1913). In this dissertation, a Rigaku diffractometer with Cu $K\alpha$ radiation ($\lambda = 1.5406 \text{ \AA}$), 2θ ranging from 10° to 40° is used to analyze the structures of perovskites, including phase analysis and crystallinity determination. A typical X-ray diffraction pattern (Figure 3.19b) depicts signal intensity at different angles at two theta positions. The diffraction angle from the incident x-ray beam transmitted into the samples determines the two theta positions, which correspond to a specific spacing between the crystals or atoms in the samples. The stronger the peak, the more crystals or molecules are in that spacing. Thinner peaks indicate larger crystals. A broader peak indicates a smaller crystal, crystalline defect, or amorphous sample.

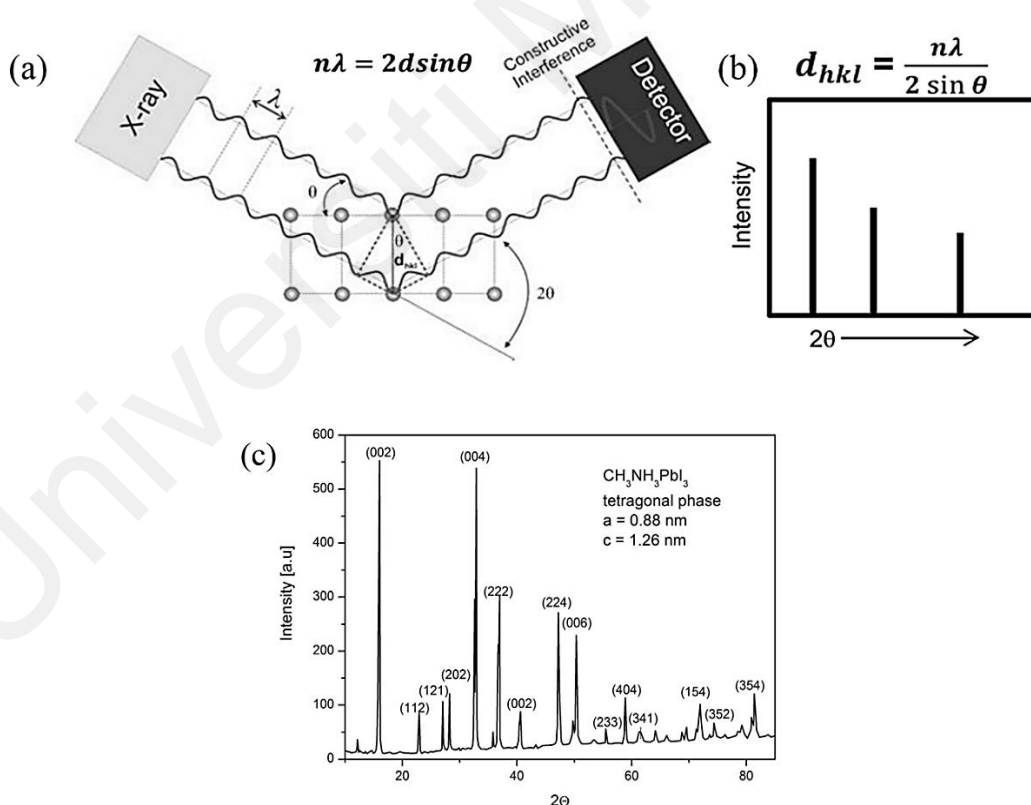


Figure 3.19: (a) A visual representation of Bragg's Law (Bragg, 1913), (b) XRD pattern, (c) Example of experimental X-ray diffraction pattern (Gawlinska et al., 2017).

3.4.7 Grazing incidence X-ray diffraction (GIXRD)

Beamline BL7.2W: MX (Figure 3.20) in SLRI, Nakhon Ratchasima, was used for the GIXRD measurement since it required high X-ray brightness and precise control of small angles. Typical Bragg-Brantano geometry is used by conventional X-ray diffractometers(Kriegner et al., 2015); the incidence angle is set between the sample surface and the incident X-ray beam, and the diffraction angle(2θ) is set between the incident beam and the reflect beam. Grazing geometry is critical for increasing the interaction between volume of X-rays and the materials in very thin films. In 1979, GIXRD measurement was originally pioneered by Marra et al. for the study of crystalline surfaces and interfaces by adjusting the X-incidence ray's angle to achieve total X-ray external reflection(Marra et al., 2008). The grazing measuring geometry improves signal yield by increasing irradiation volume.

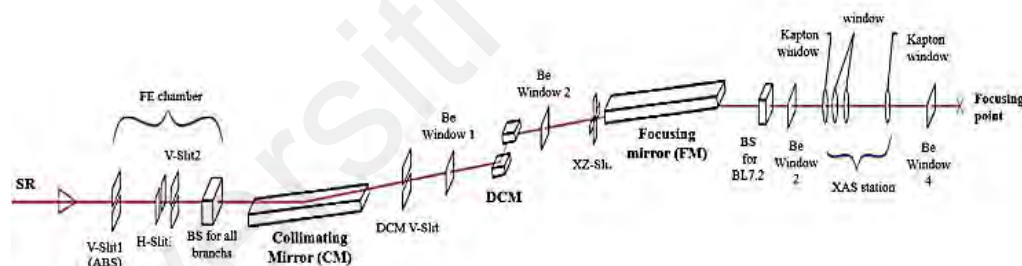


Figure 3.20: Layout of the BL7.2W: MX beamline(Sripukdee et al., 2018).

Synchrotron X-rays' narrow beam size makes it possible to do GIXRD measurements over a thin material region. Synchrotron X-rays have a substantially higher intensity than spinning anode X-rays, allowing for much less time spent collecting data. The continuous spectrum of synchrotron X-rays allows for selecting any optimal X-ray wavelength for the materials under study. Grazing incidence configurations were developed to resolve the problems with traditional XRD.

In thin film characterization, the beam penetration depth may be considerably more significant than the sample thickness, as shown in figure 3.21(a), because X-rays with fixed shallow incidence angles of incidence penetrate the material a few to several hundred micrometres. Consequently, the signals observed at high angles mostly came from the substrate, resulting in inaccuracy in transparency. Therefore, conventional XRD is inadequate for in-depth analyses of sub-micrometric layers in thin film specimens. It is, therefore, necessary to position the x-ray source at an angle of incidence ($<5^\circ$) that permits shallow penetration and so restricts only to the top-most surface of the sample.

Particularly in the case of thin film nm-scale samples, the grazing measuring geometry helps enhance signal yield by maximizing the irradiation volume. Additionally, as shown in figure 3.21(b), it has the advantage of lowering the volume of the irradiated substrate. The GIXRD method was widely used by researchers interested in the atomic structure of thin films. GIXRD studies allow for the simultaneous acquisition of surface microstructure information (strain field, preferred orientation, etc.)(A. A. Williams et al., 1991) and sample structure information (thickness, phase, etc.)(K. Wang et al., 2005).

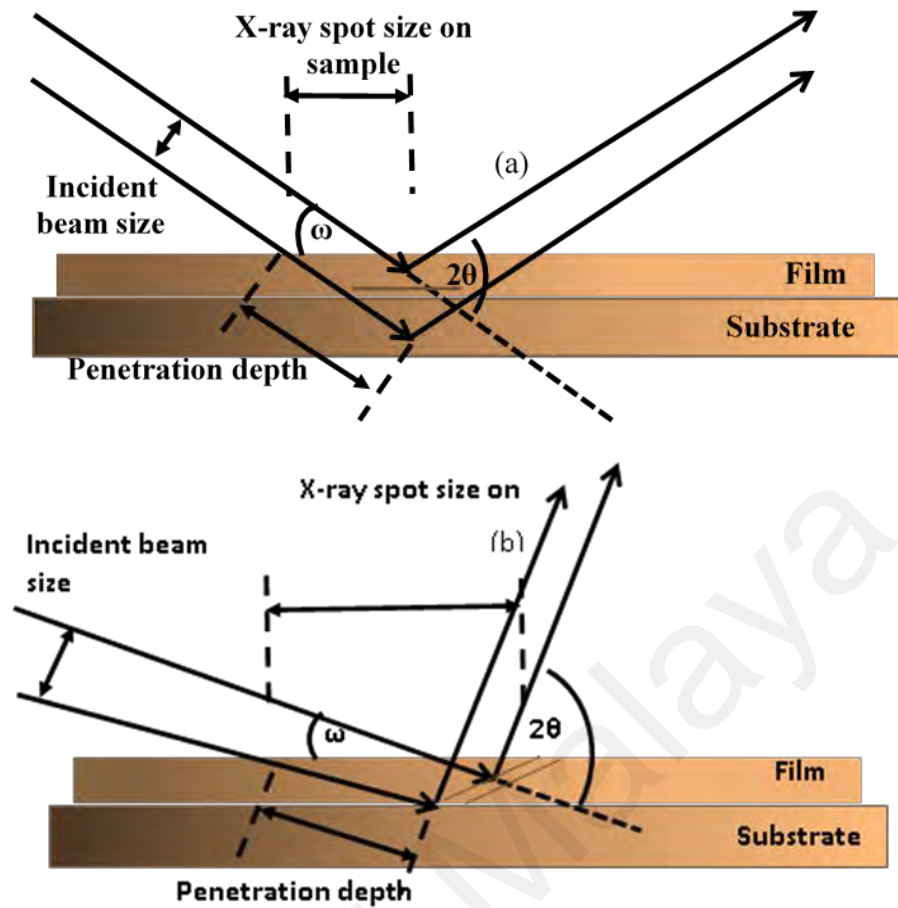


Figure 3.21: Graphical Representation of GIXRD (a) A depiction of high-incidence X-ray diffraction on a thin film. (b) The same evaluation as in (a), but with a small incident angle(Widjonarko, 2016).

The scattering vector, q , is the difference between the wave vectors of the diffracted beam and the primary beam, and it is a crucial quantity in a GIXRD experiment. If the scattering vector q is equal to a reciprocal lattice vector, then a diffraction peak should be seen, as proposed by Laue; many peaks can be used to determine the crystallographic lattice. Figure 3.22 can observe q in the three-dimensional reciprocal space, along with its in-plane component $q_{xy} = \sqrt{q_x^2 + q_y^2}$ and its out-of-plane component q_z .

In contrast to static (or integral rotational) GIXRD, which can only access two of the scattering vector's components (q_{xy} , q_z), rotating GIXRD can resolve all three of the scattering vector's components (q_x , q_y , and q_z). The total length of the scattering vector, q , is given by $q = (4\pi/\lambda) \sin \Theta$, where λ is the wavelength of the incident beam and Θ is half the scattering angle. To prepare a perovskite thin film using the spin-coating process for GIXRD measurement, the initial step involves chemically cleaning the glass substrate, followed by rinsing it with de-ionized water and subsequently drying it in ambient air.

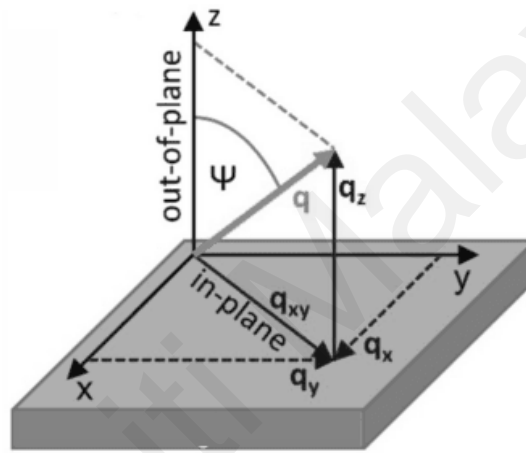


Figure 3.22: In three-dimensional reciprocal space, the scattering vector q is composed of in-plane elements (q_x , q_y , or $q_{xy} = \sqrt{(q_x^2) + (q_y^2)}$, as well as an out-of-plane component q_z .

3.4.8 Ultraviolet photoelectron spectroscopy (UPS)

Photoelectron spectroscopy (PES) is a method used to describe the material's surface. The method is known as Ultraviolet photoelectron spectroscopy (UPS) when UV excitation is utilized in PES. The low-energy bound electrons can be excited by a lower excitation source ($< 50\text{eV}$) of UV radiation, resulting in great intensity resolution at UPS's low-energy spectrum valence level. The analysis of the lower energy range of the spectra reveals details about the density of occupied states (DOS) in the valence band (VB). UPS determines a substance's surface and valence states. A fundamental UPS approach is shown in Figure 3.23.

The UPS analysis uses low-energy radiation irradiation (below 50 eV) and can only examine the ionizing electrons at the valence level of the outermost levels of atoms.

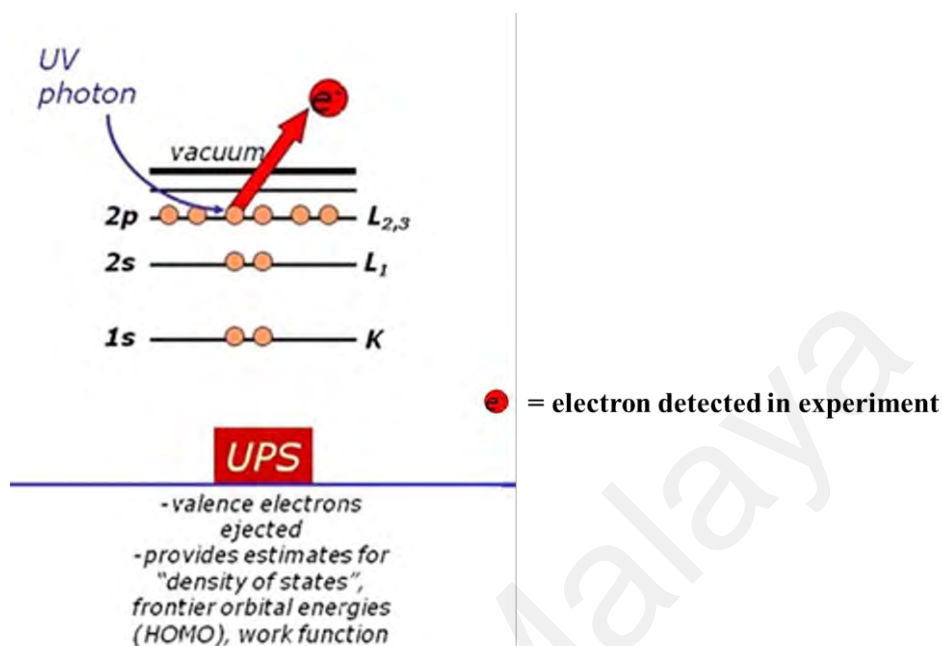


Figure 3.23: Valence electrons in UPS are excited by lower energy photons from the deep UV region.

The UPS samples were fabricated by the deposition technique of spin coating onto an indium tin oxide (ITO) substrate. Before spin-coating, the substrates underwent ultrasonic cleaning using deionized water, acetone, isopropyl alcohol, and deionized water once more, each for a duration of 10 minutes.

Following a 5-minute oxygen plasma treatment, the precursor solution was spin-coated onto a cleaned ITO substrate. In UPS, electrons are emitted from a material's valence band in response to incoming ultraviolet light, allowing the work function (ϕ) and ionization potential to be calculated (IP). Work functions characterize the difference between the sample's Fermi and vacuum levels. When referring to semiconductors, the ionization potential describes the distance between the HOMO or conduction band to the vacuum level. Figure 3.24 exhibits the energetics of UPS spectra. The photons originate from a He II lamp, with an energy of $h\nu = 39.5$ eV.

Typically UPS spectrum has two prominent elements, the secondary electron onset and HOMO level onset. The vacuum level of the sample E_{vac} is correlated with the secondary electron onset, which is the sharp onset of the spectrum at low kinetic energy. An external bias is typically given to the sample to ensure that the sample's vacuum level is higher than the level of the vacuum of the detector $E_{vac}(d)$. Lower kinetic energy increases the likelihood of the appearance of secondary electrons, which are electrons that are dispersed inelastically before being ejected from the sample.

Work function can be calculated from the location of the secondary electron onset (E_{SECO}) using the following equation:

$$\phi = h\nu + E_{SECO} - E_{KINF} \quad (3.5)$$

where E_{KINF} is the kinetic energy corresponding to the Fermi level of the sample, which can be calibrated using a metal reference's spectrum onset.

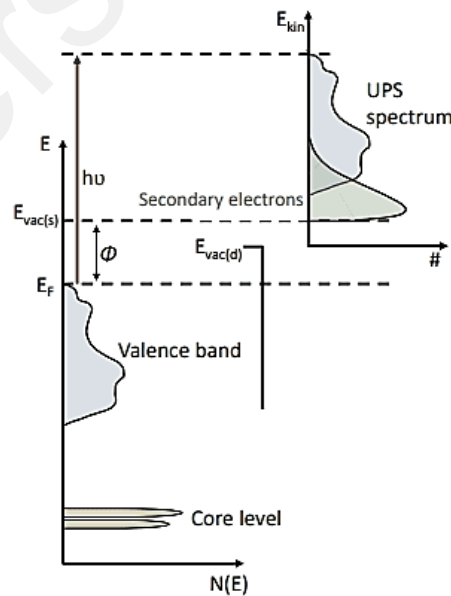


Figure 3.24: Photoelectric effect measurement of UPS.

Figure 3.25(b) illustrates the UPS spectrum of Au excited by He (I). To determine the parameters, the energy cutoff's precision is required.

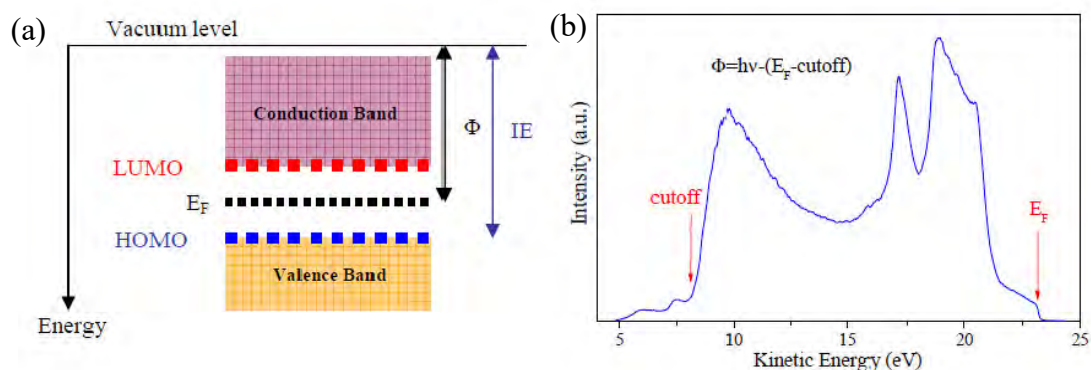


Figure 3.25: An illustration of (a) an atom's outer energy and (b) the UPS spectrum of Au.

A straight line can be fitted into the leading edge to yield the work function and valence band maximum (VBM) level, as shown in Figure 3.26.

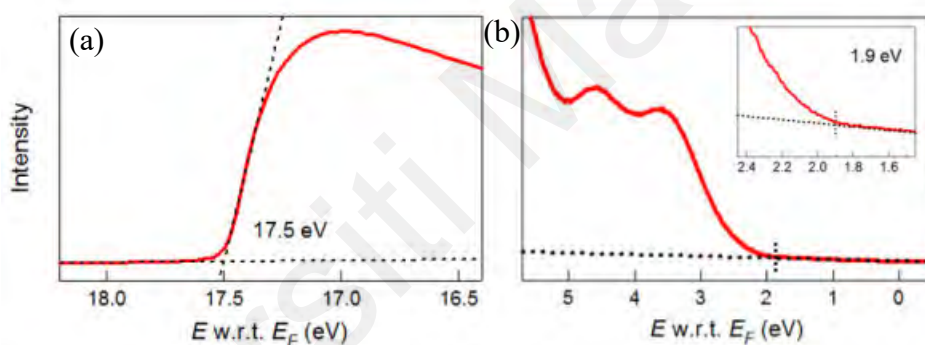


Figure 3.26: UPS spectra of the (He I) of HDABiI₅/FTO for direct determination of (a) work function and (b) valence-band maximum [picture source from (Fabian & Ardo, 2016)].

3.4.9 4-point probe analysis

The four-point probe method uses four contacts in place of two, enabling two distinct pairs of contacts to drive current and measure voltage, with the main advantage of removing intrinsic voltage drops from the measurement. This instrument uses four probes, as suggested by its name, two of which detect electric current while the other two measure voltage when placed in a substance (sample). Figure 3.27 illustrates the schematic diagram of a four-contact measurement.

The type of doping (positive and negative) and material mobility are two additional factors that can be determined from material measurement utilizing this instrument. This thesis employs a four-point probe measurement to assess the material's conductivity and resistivity on thin film samples. A steady electric current flows along the sample through the two outermost probes. When the current flows along the sample, a voltage drop will occur if the sample has resistance. Two internal probes are used to measure the voltage shift. The four-point probe method precisely measures electrical quantities indicative of a material's conductivity, such as voltage and current.

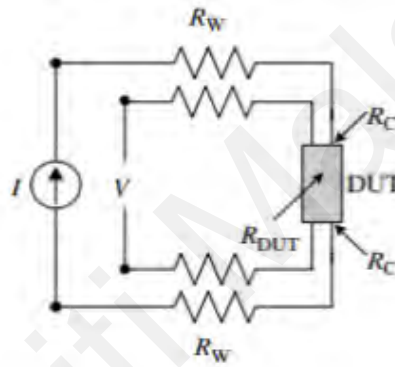


Figure 3.27: Diagram illustrating the four-point probe technique.

The samples' electrical conductivity was determined with a 4-point probe model Jandel Universal Probe connected to a Keysight B2902A source meter, as illustrated in Figure 3.28. The system consists of four functioning tungsten wires coupled to a source measure unit (SMU). Probes 1 and 4 sources current, and probes 2 and 3 measure voltage. After positioning the samples on the sample stage, the probes were brought down to make contact with the surfaces of the samples. The current source ranged from 0 to 10 mA, and the measurement was carried out three times to collect readings from various locations on the sample. Spin coating was used for the deposition process on ITO substrate to create the samples.

The substrates were ultrasonically cleaned in succession for 10 minutes with deionized water, acetone, isopropyl alcohol, and deionized water before being spun coated. The precursor solution was spin-coated onto a sterile ITO substrate after being treated with oxygen plasma for 5 minutes.

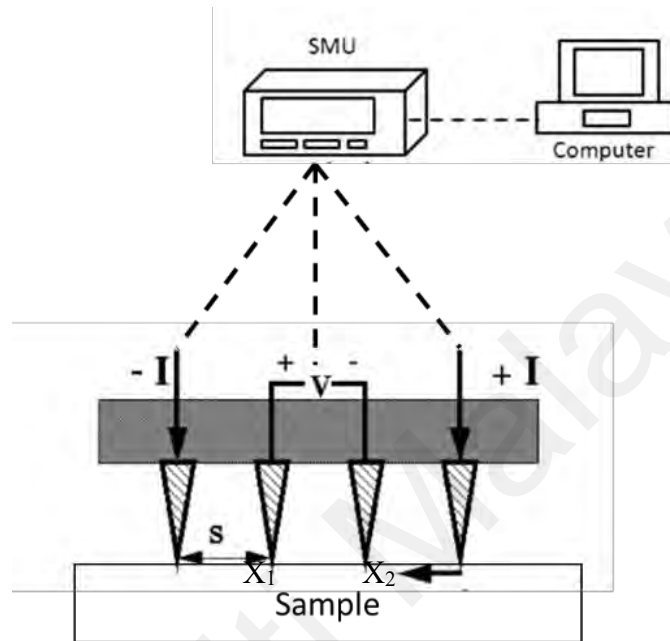


Figure 3.28: Schematic diagram of a 4-point probe set-up.

When the probe distance is larger than the film thickness, the thin film conductivity (σ) can be calculated. Assuming a thin film with the square geometry shown in Figure 3.29, rings rather than spheres are obtained for very thin layers (Brown & Jakeman, 1966).

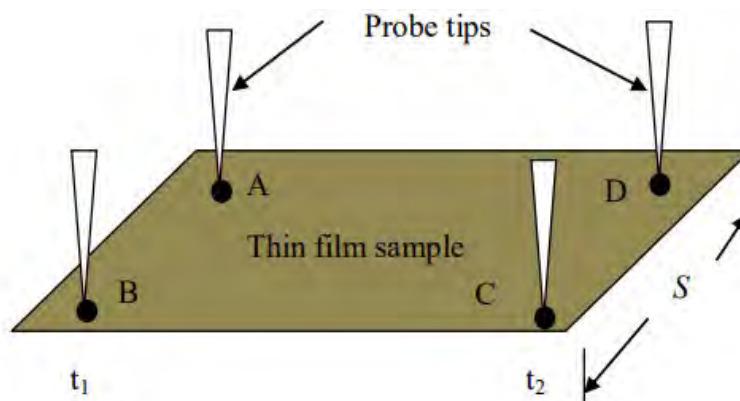


Figure 3.29: Square probe tips on a thin film sample surface.

Thus, the area,

$$A=2\pi xt \text{ where } t \text{ is the thickness of the film} \quad (3.6)$$

$$\text{Given, } R = \rho_s \left(\frac{dx}{A} \right) \quad (3.7)$$

where ρ_s is the sheet resistivity, A is the area of the film and dx is the distance between x_1 and x_2 .

$$R_s = \int_{x_1}^{x_2} \rho \frac{dx}{2\pi xt} \quad (3.8)$$

$$= \int_s^{2s} \frac{\rho}{2\pi t} \frac{dx}{x}, \text{ where } S \text{ is the probe spacing} \quad (3.9)$$

$$= \frac{\rho}{2\pi t} \ln(x) \Big|_s^{2s} \quad (3.10)$$

$$= \frac{\rho}{2\pi t} \ln 2 \quad (3.11)$$

Therefore, the thin film sheet resistivity is given by where $R = \frac{V}{I}$,

$$\rho_s = \frac{\pi t}{\ln 2} \left(\frac{V}{I} \right) \quad (3.12)$$

Therefore conductivity σ is,

$$\sigma = \frac{1}{\rho} = \frac{\ln 2}{\pi t} \left(\frac{I}{V} \right) \quad (3.13)$$

3.5 Measurement of Perovskites-Based Devices

3.5.1 I-V Characterization of FETs Devices

A two-channel Keithley 2612B source meter is used to assess the FETs' electrical performance, apply voltages and record current readings. Two standard I/V measurement sets for characterizing FET devices are output and transfer-characteristic. In both circumstances, the source contact is grounded. Figure 3.30 portrays the experimental set-up, including a FET device being tested.

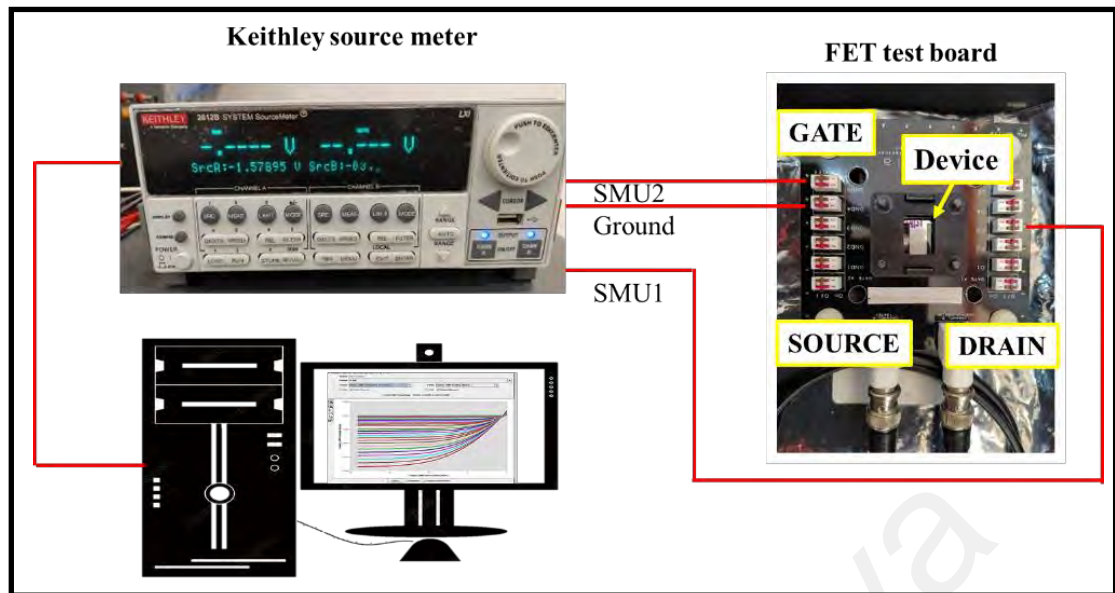


Figure 3.30: Experimental set-up and device structure of I-V characterization.

For the output I/V-characteristic, a voltage sweep is applied to the drain contact while the gate-electrode is kept at a constant potential. The measured drain current is typically plotted linearly against the drain voltage after many sweeps have been applied at various constant gate voltages. Multiple gate-voltage sweeps can be fitted with an upward-curving parabola at the linear-to-saturated transition points. Figure 3.31 shows an example of the I/V curve. In contrast to the output characteristic described above, the drain-electrode is maintained at a constant potential. At the same time, the gate contact is subjected to a voltage sweep for the transfer I/V characteristic.

Essential performance parameters, such as field effect mobility (μ) and threshold voltage (V_{TH}), can be extracted from the transfer characteristic using the I-V curves. This work prefers the transfer characteristics over the output characteristics for extracting performance parameters. Since the transfer characteristic allows for a more accurate and quantitative performance assessment, this method is frequently used for FETs. TSP Express Software, which operates on a PC linked to the Source Meter, automates all measurements and data collecting.

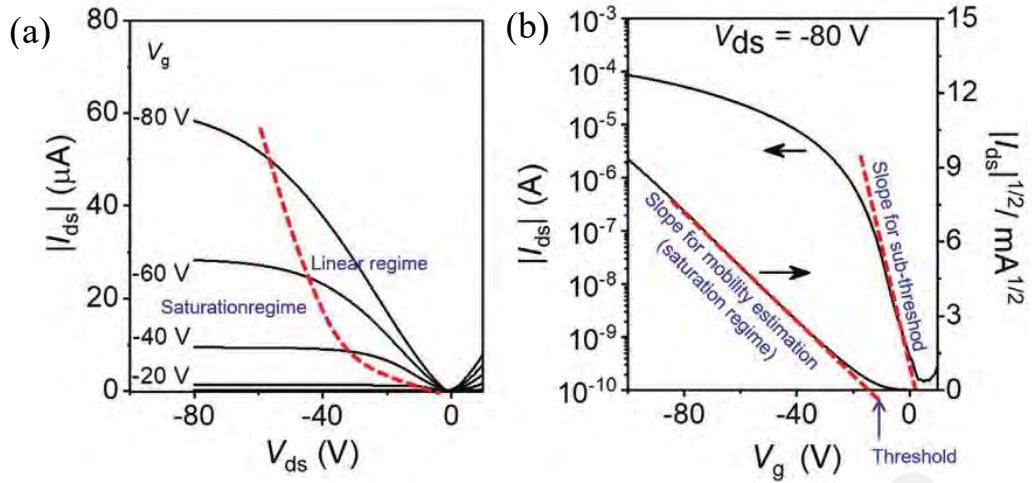


Figure 3.31: Typical FET characteristics (a) output (b) transfer curves of the p-type device [Picture source from (Blom, 2020)].

3.5.2 I-V and Characterization of PDs Devices

I-V curves are the most crucial metrics to evaluate the performance of the photodiode. Dark currents and photocurrents control the device's responsiveness and sensitivity. The devices are placed inside a black box, which keeps them from other electrical and optical disturbances, as shown in Figure 3.32. The output current is then measured using a Labview-controlled Keithley SMU after being subjected to a voltage sweep, typically from 1V to -1V. The photocurrents are quantified by shining light on the ITO electrode side to create electron-hole pairs on a perovskite photodiode. A UV light source (Warson 838) was used at a wavelength of 395 nm with an irradiation intensity of 13.5 mW/cm².

Neutral density filters with various optical densities, as shown in Figure 3.33, are employed to modulate UV light output. An optical filter will absorb light of all wavelengths to the same degree, resulting in a general dimming but not affecting the light's colour. The consistency of the device's photo response was investigated by switching the UV light input on and off at regular intervals using a mechanical optical chopper (Figure 3.34) that was set to a frequency of 0.2 hertz.

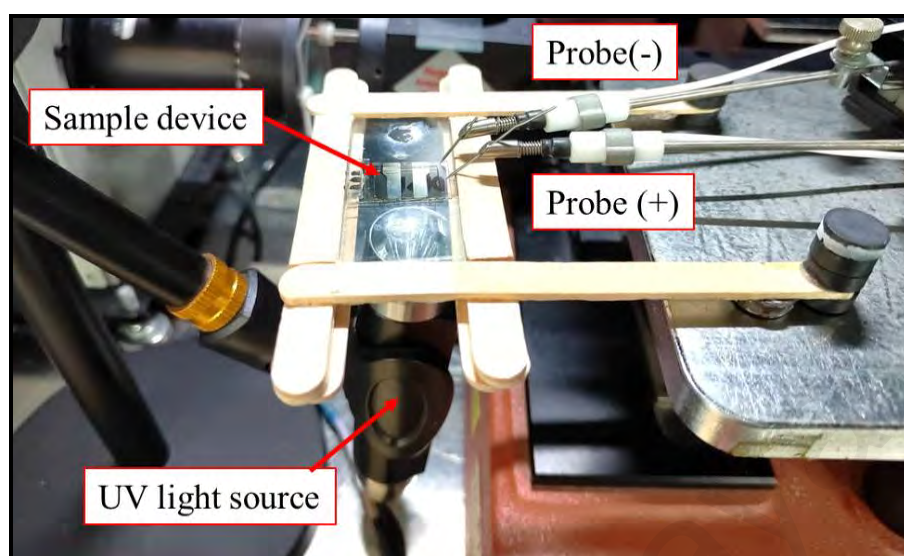


Figure 3.32: Schematic IV set-up measurement.

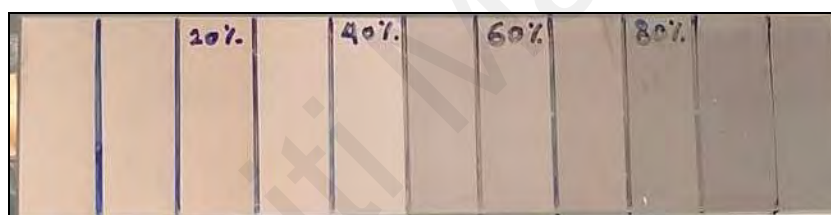


Figure 3.33: Optical density filter.

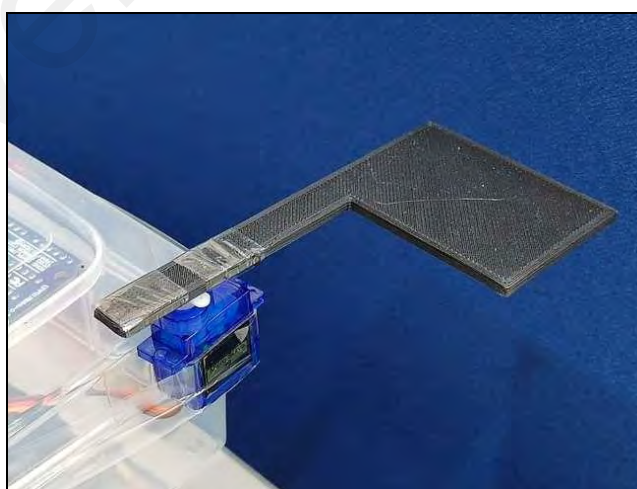


Figure 3.34: Optical chopper

The fall and rise response times were measured with a digital oscilloscope and pulsed LED light without any external supply. A square-wave signal function generator (Tektronix AFG 2021) drove a UV LED light with a 395nm wavelength to produce pulsed light. The response time of the photodiode is analyzed by displaying the electrical signal created by the photodiode on a digital oscilloscope, Agilent DSO-X 3052A. As aforementioned, the response time can be evaluated by measuring the duration between 10 % and 90 % of the maximum photocurrent. Figure 3.35 depicts the experimental arrangement of the response time setup.

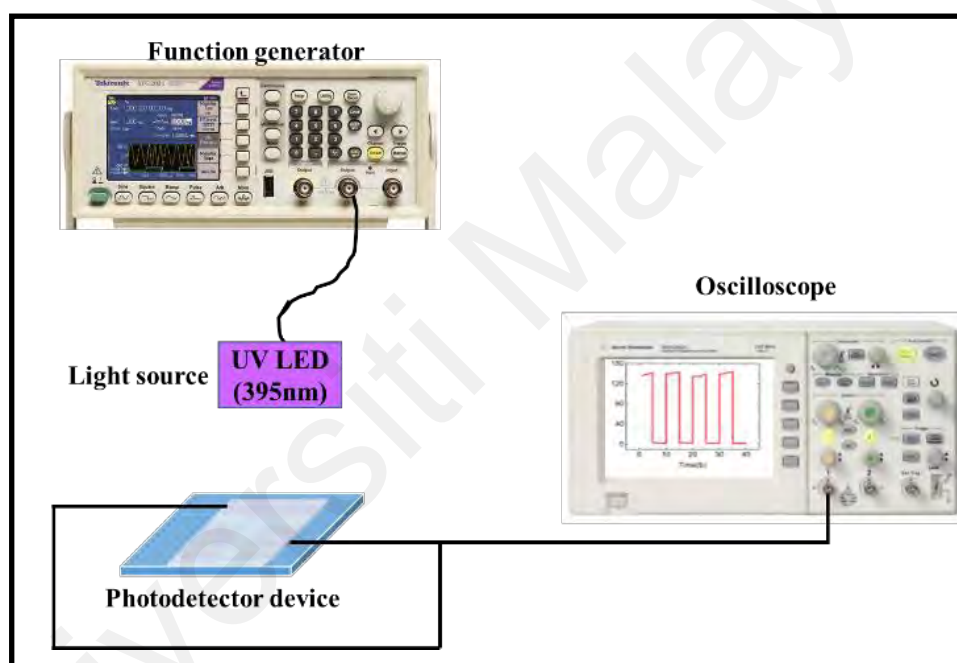


Figure 3.35: Schematic of response time measurement.

3.6 Summary

This chapter describes the study's materials and substances. This chapter also detailed the standard processing flow and techniques for fabricating perovskite-based devices. Each device's I-V and perovskite thin film characterizations are presented. Based on optimized thin film characterizations, two devices were fabricated: a FET and a photodiode. The steps involved in making these devices are described in detail in **Chapters 4 and 5.**

CHAPTER 4: PA: PVK-BASED FIELD-EFFECT TRANSISTOR (FET)

4.1 Introduction

FETs are the fundamental discrete electronic component that has advanced everyday human lives today. Thanks to advances in promising semiconducting materials and unique device designs and integration technologies, FET technologies have matured and covered nearly all typical electronic applications. High-performance of low-dimensional perovskite FETs is feasible because of the benefits of low-dimensional hybrid perovskite materials, such as excellent electronic and optoelectronic properties, particularly the high carrier mobility and adjustable growth orientation characteristics. Moreover, low-dimensional perovskite contains a longer organic cation that acts as a "barrier" to produce hydrophobicity. It is more resistant to humidity than 3D perovskite (Misra et al., 2017). Li et al. reported $(\text{BA})_2(\text{MA})_{n-1}\text{Pb}_n\text{I}_{3n+1}$ single crystal-based FET with $1.25 \text{ cm}^2\text{V}^{-1}\text{s}^{-1}$ mobility at 77 K (M. K. Li et al., 2018). After that, Wang and co-workers continued their research on the $(\text{BA})_2\text{PbI}_4$ perovskite FETs and came to the observation that the in-plane mobility of $8.2 \times 10^{-2} \text{ cm}^2\text{V}^{-1}\text{s}^{-1}$ is much more significant by more than an order of magnitude than the out-of-plane mobility of $4.7 \times 10^{-3} \text{ cm}^2\text{V}^{-1}\text{s}^{-1}$. Zhu et al. revealed a facile and speedy anti-solvent crystallization method for synthesis $(\text{PEA})_2\text{PbI}_4$ nanosheets with a few-layer thickness. The FET has a V_{TH} of 5.19 V and mobility of $1.43 \times 10^{-1} \text{ cm}^2\text{V}^{-1}\text{s}^{-1}$ at ambient temperature (L. Zhu et al., 2018). The research on FETs on low-dimensional perovskites is in its early phases and deserves more attention.

Optimal FET performance relies heavily on the interface characteristics of the electrode and the active semiconductor layer. Perovskites' valence band maximum (VBM) energy level is around 5.4–7.3 eV (P. Gao et al., 2014). For example, the VBM of methylammonium lead iodide (MAPbI_3) is 5.43 eV, near the gold electrode work function of 5.1 eV (Labram et al., 2015) and can easily match the VBM energy level of MAPbI_3 .

Thus gold is widely utilized as source and drain(S/D) electrodes in perovskite-based FETs. However, recently it has been found that thermally evaporated gold atoms tend to diffuse into perovskite materials and deteriorate the device performance(D. Li et al., 2016; Mei et al., 2015). Indium tin oxide, often known as ITO, is a transparent electrode material explored for devices such as organic light-emitting diodes and solar cells due to its high conductivity and transmittance. Fluorinated polymer modification of the drain and source electrode was proposed to enhance contact characteristics between perovskite and ITO source/drain electrodes.

This chapter explores the effect of the work function of the source/drain electrode on the performance of the PAPbBr_3 (PA) based FET. The Indium Tin Oxide (ITO) is selected as the source and drain(S/D) electrode, polytetrafluoroethylene (PTFE) as the dielectric layer, respectively. PAPbBr_3 (PA) is an interesting one-dimensional OIHP with a single-chain structure that has strong anisotropic nature (Niu et al., 2018), stronger electron-phonon interaction(Saidaminov et al., 2017), and excellent potential in optoelectronic device applications. However, high exciton binding energy, narrow light absorption range, small diffusion lengths, and limited charge carrier mobility (Kamminga et al., 2016; Z. Wu et al., 2017; Z. Yuan et al., 2017) have been observed in one-dimensional metal halides. This chapter further demonstrates the morphological effect of blending PVK and perovskite material. PVK is selected as the polymer host because of its excellent film-forming properties, high hole transport capabilities, and good solubility in DMF (J. Jeong et al., 2018; Talik et al., 2016; L. Yang et al., 2017). The last part of this chapter studies the PA: PVK-based FETs electrical performance.

4.2 Experimental Method

First, the pre-patterned ITO substrate was cleaned with deionized water, acetone, isopropyl alcohol (IPA), and deionized water each for 10 min with ultrasonic agitation followed by nitrogen (N_2) purge to get rid of dust particles before spin-coating. A Nafion solution was prepared with ethanol at a volume ratio of 1:10. Nafion solution was spin-coated on top of cleaned ITO substrates at a speed of 2500 rpm for one minute and annealed at 100 °C for 10 min to form a layer of ~6 nm thickness. PAPbBr₃ and PVK were dissolved in DMF according to a series of ratios concentration of 5 w/v% PA: PVK 0%, PA: PVK 16%, and PA: PVK 25%, and vigorously stirred on a magnetic stirring plate overnight. The blended solutions of PA and PVK in DMF are shown in Figure 4.2. After being stirred for an entire night, the solution appeared utterly transparent. For PAPbBr₃: PVK devices, the DMF solution of PAPbBr₃: PVK was spin-coated onto ITO substrate to form an active layer with a thickness of 60 nm and then annealed at 100 °C for 15 min. After that, a 200 nm dielectric layer of polytetrafluoroethylene (PTFE) was spin-coated onto the active layer and baked for 10 minutes at 100 degrees Celsius. As illustrated in Figure 4.3, the devices were completed by thermally evaporated Aluminum (Al) with a deposition rate of 0.5 Å/s to form a 100 nm top-gate electrode. The fabrication process was performed at room temperature inside a nitrogen-filled glove box. The transfer and output characteristics of the FETs were determined using a Keithley 4200 semiconductor parametric analyzer under the dark and at room temperature under ambient pressure.

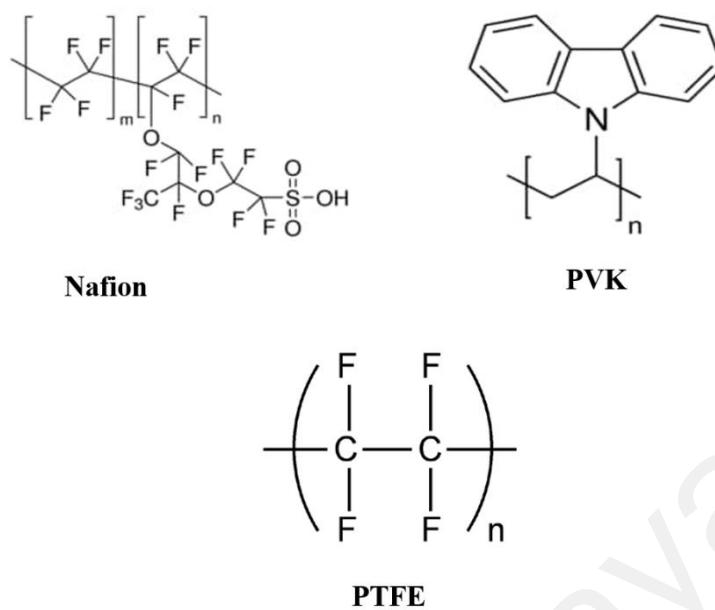


Figure 4.1: The molecular structure of materials used in this research section.

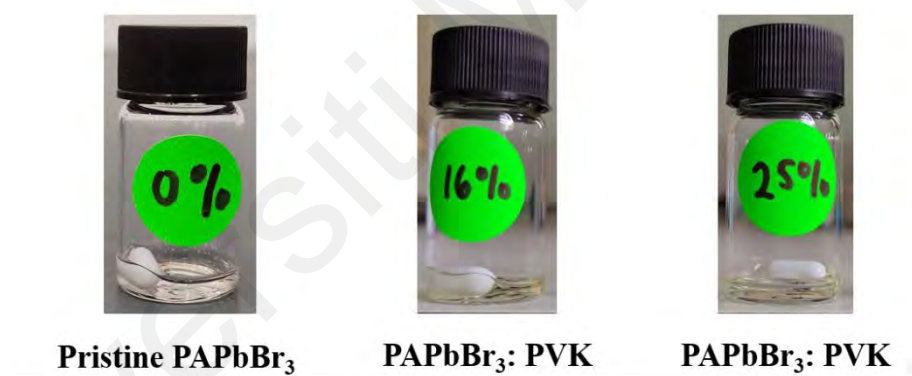


Figure 4.2: PA and PVK blended solutions in DMF

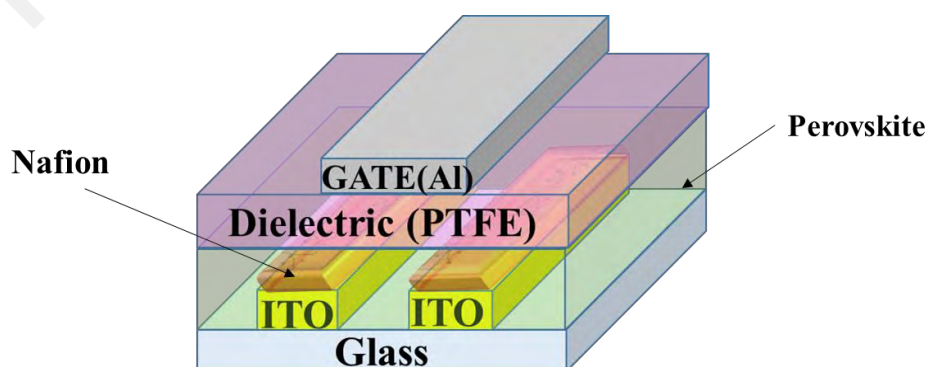


Figure 4.3: Schematic diagram of Top-gate bottom contact FET

The surface morphology of the films was studied by a Hitachi S-4800 FESEM. XRD spectra of these films were collected using a Rigaku diffractometer with Cu K α radiation ($\lambda = 1.5406 \text{ \AA}$), 2θ ranging from 10° to 40° . The transfer and output characteristics of the FETs were determined using a Keithley 4200 semiconductor parametric analyzer under the dark and at room temperature under ambient pressure. The work function measurements were carried out at the UPS system of the BL3.2U of SLRI, the Synchrotron Light Research Institute (SLRI) (Euaruksakul et al., 2013). The system's vacuum pressure is below $2.7 \times 10^{-8} \text{ Pa}$. Synchrotron radiation with 39.5 eV photon energy was used for the excitation. The photoelectron kinetic energy was measured using a Thermo VG Scientific-Alpha110 energy analyzer with a pass energy of 10 eV.

The crystal orientation of thin films was examined by the Grazing Incidence X-Ray Diffraction (GIXRD) at the BL7.2W beamline of the SLRI using X-ray with a photon energy of 8.00 keV ($\lambda = 0.15498 \text{ nm}$) and grazing incidence angle of 0.15° (Sripukdee et al., 2018). A Mar165 CCD detector system acquired 2D GIXRD patterns. The distance between the detector and the sample is $\sim 95 \text{ mm}$. The 2D GIXRD patterns were analyzed using the DAWN software (Basham et al., 2015). The spin-coated PAPbBr₃ and PAPbBr₃: PVK on glass substrates was tested for material absorbance using a PerkinElmer Lambda 750 UV-Vis-NIR.

4.3 Result and discussion

4.3.1 Effect of ITO work function modification on PA-based FET.

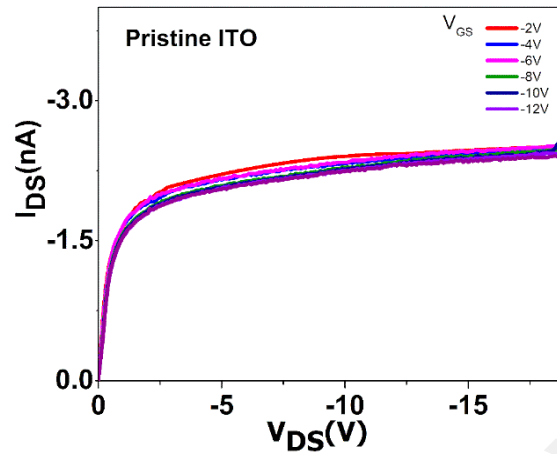


Figure 4.4: Output characteristics of FET using pristine ITO

To test whether deep VBM PAPbBr₃ can be used for a transistor, FET using pristine PAPbBr₃ as an active layer is fabricated in the bottom contact/top gate. The use of a top-gate FET geometry is especially appealing because, in this geometry, the perovskite layer is shielded from the environment while exhibiting outstanding operational and environmental stability even in moist conditions (C. Y. Wang et al., 2017). As can be seen from Figure 4.4, the device showed a poor hole injection with a current lower than 3 nA and weak field-induced current modulation. Due to the absence of transistor behavior in the device using bare ITO, it was not possible to determine the field-effect mobility. At the same time, a dramatic change in the transfer characteristics was observed after the Nafion treatment. Figure 4.5(b) displays the transfer characteristics of these devices, acquired during a continuous sweep of the gate voltage (V_{GS}) from 0 V to -18 V, while maintaining the drain-source voltage (V_{DS}) at -20 V. Under negative gate-source voltages (V_{GS}), holes collected at the PTFE/PAPbBr₃ interface form a conducting channel, demonstrating that the PAPbBr₃ FETs act as p-type devices.

The transfer characteristics of Nafion treated device are obtained in the saturation regime at $V_{DS} = -20$ V, and the mobility is calculated using the equation (4.1):

$$I_{DS} = \frac{W}{2L} C_i \mu (V_{GS} - V_{TH})^2 \quad (4.1)$$

where C_i is gate capacitance per unit area, W is the channel width, and L is the channel length. As a result, the extracted field-effect mobility (μ_{FET}) of Nafion-treated ITO FET is significantly enhanced to $8.62 \times 10^{-5} \text{ cm}^2/\text{Vs}$ with on/off current of 10^3 .

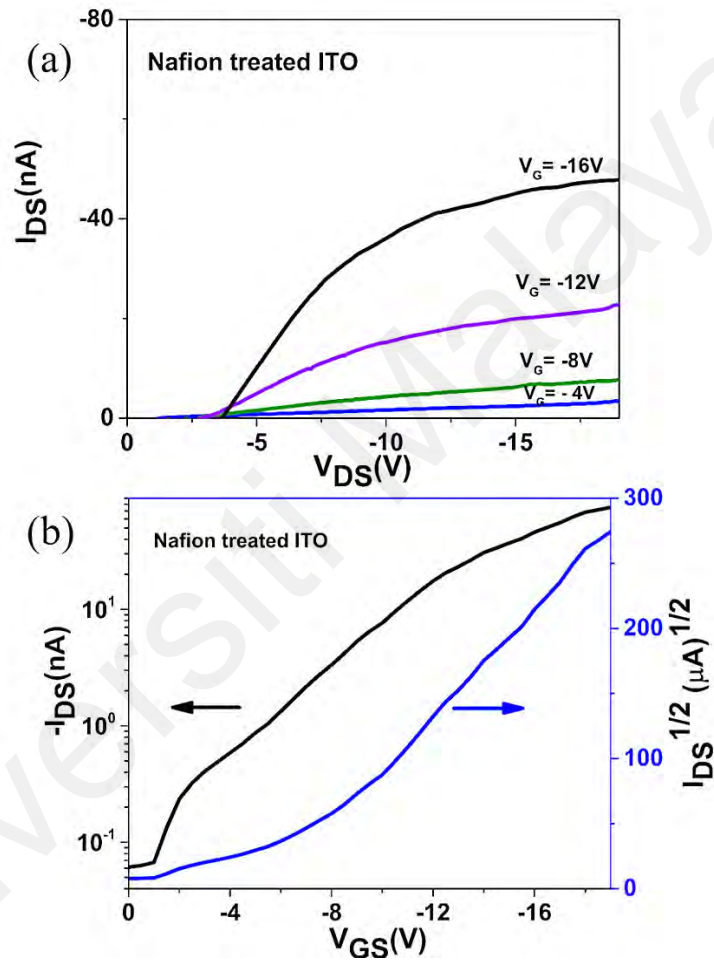


Figure 4.5: (a) Output characteristics of FET Nafion treated ITO as S/D electrode, (b) Transfer characteristics of FET using pristine ITO and Nafion treated ITO as S/D electrode.

The VBM for materials and the vacuum level at the interface can be empirically determined by using UPS to determine the outermost valence's electronic structure. UPS spectra at high-energy cut-off (HECO) and low-energy cut-off (LECO) for PAPbBr₃/ITO and PAPbBr₃/Nafion/ITO substrate are as shown in Figure 4.6(a) and (b) respectively. The HECO onset of ITO and PAPbBr₃/ITO was 35.10 eV and 34.78 eV, respectively, determined via linear extrapolation.

The work function of ITO and Nafion-treated ITO are obtained minus the HECO onset from photon energy (39.5 eV). The work function of untreated ITO is 4.4 eV which is in good agreement with literature values for untreated ITO (Michaelson, 1977). The lower HECO of PAPbBr₃ compared to ITO indicated the formation of an interfacial dipole of 0.32 eV. The injection barrier can be reduced by spin coating a thin layer of Nafion between the ITO and perovskite active layer. The decreased binding energy of the HECO indicates an increased work function of the ITO electrode because of the Nafion treatment. The effective work function of the ITO is increased up to 4.90 eV. The Nafion's C-F bonds can withdraw electrons from perovskite and accumulate holes in the perovskite layer, greatly enhancing the hole transport ability (Aragaw et al., 2013). Although it is possible to treat the ITO with oxygen or chloride plasma to increase the work function, however, the reactive species that form at the surface of the ITO that result in increased work function tend to break down within a relatively short time, limiting its practicality in devices (He et al., 2014).

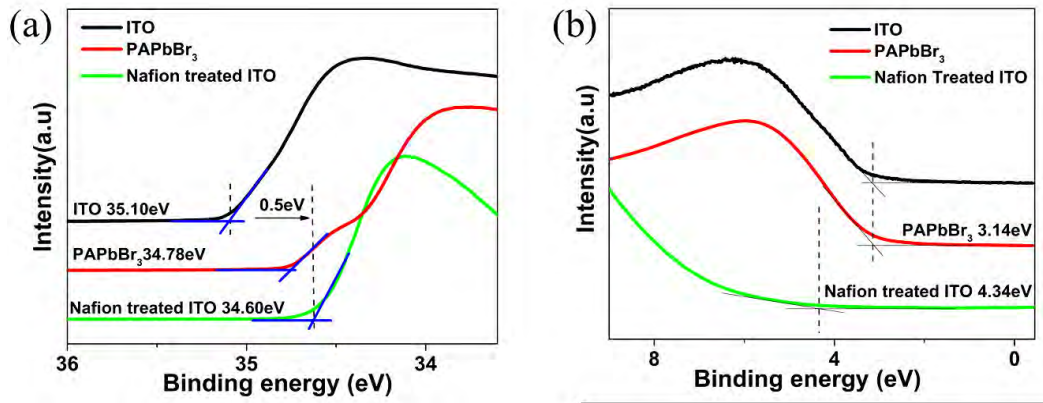


Figure 4.6: (a) UPS spectra at high-energy cut-off (HECO) and (b) low-energy cut-off (LECO) for PAPbBr₃/ITO and PAPbBr₃/Nafion/ITO.

The energy diagram of the interface is summarized in Figure 4.7. The optical bandgap (E_g) of pristine PAPbBr₃ was estimated using the absorption spectrum's onset described in **Chapter 3**(section 3.4.2). However, the charge transport may be limited by the grain boundaries in the pristine perovskite thin film. The characteristics of the FETs are expected to be highly related to the crystallinity of the PAPbBr₃.

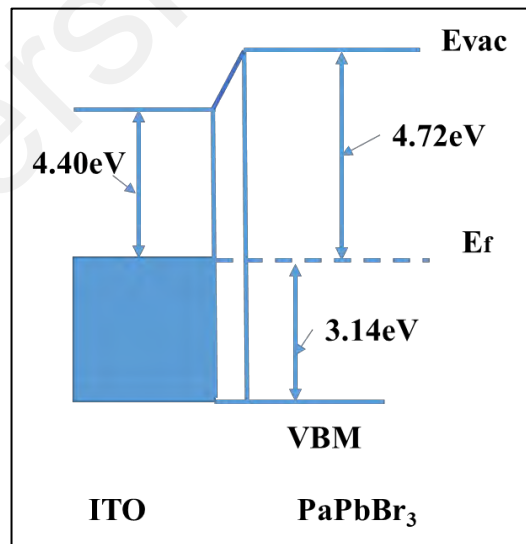


Figure 4.7: The energy diagram of the charge injection at the interface between the metal and perovskite, E_{vac} is vacuum level, and E_f is the Fermi level.

4.3.2 Effect of PVK blending on PA-based FET

Generally, the fast crystallization of perovskite materials with solvent evaporation results in uncontrollable film morphology (Q. Cao et al., 2016) and poor surface coverage (Konstantakou et al., 2017). The high average molecular weight PVK used ensures the high viscosity (Intrinsic viscosity = 52.3 ml/g) (Leon & Rodriguez, 1979) required to form good coverage thin film. Furthermore, the grain boundaries can be passivated when blending with PVK. Recently, enhancement of performance in hybrid perovskite-based solar cells has been reported when grain boundaries are passivated via blending *insulating* polymers such as polyvinylpyrrolidone and poly(acrylic acid) (Zuo et al., 2017).

(a) *Physical and optical characterization of PA: PVK blended film*

Deposition methods of solution-processed hybrid perovskite have direct effects on the thin-film morphology and may affect the charge transport properties of the materials (Cardoso et al., 2016). To investigate the behavior of pristine PA and PVK blended precursor solution on Nafion-treated ITO substrates, a wettability test measuring the contact angle was undertaken at room temperature. At room temperature, using a contact angle (CA) measurement apparatus in air, 1 μ L droplets of perovskite precursor solution were carefully put onto the surface of the thin film to investigate the wetting behavior of an ITO substrate with Nafion treatment. The contact angle of the perovskite precursor is depicted in Figure 4.8. The contact angle for pristine perovskite precursor is $\sim 52.3^\circ$, and the angle decreases with increasing PVK ratio in DMF precursor, 49.1° and 41.2° for PVK-16% and PVK-25%, respectively. As shown in Figure 4.8, the Nafion-treated ITO was highly wettable by the PVK blended precursor solution compared to the untreated film, which may result in a homogeneous perovskite layer with higher coverage.

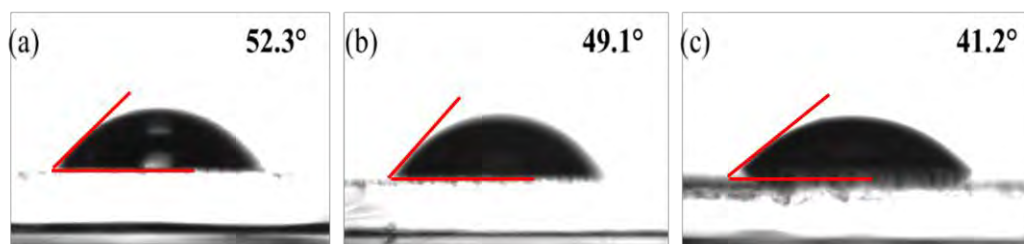


Figure 4.8: Contact angle images (average angle value of four measurements noted in the image) of (a) Pristine (PVK-0%), (b) PVK-16%, and (c) PVK-25% precursor solution, respectively, on Nafion/ITO substrates.

Figure 4.9 presents the absorption spectrum of pristine PaPbBr_3 and PaPbBr_3 -PVK blended thin films deposited on the glass substrate. To observe the effect of PVK blending on perovskite, the UV-vis absorption extends from 370 to 450 nm. The spectra of pristine PaPbBr_3 and PaPbBr_3 -PVK blends in DMF display a single absorption peak at a wavelength (λ_{max}) of 401 nm (3.1 eV). As the PVK content of the films in the PA: PVK blend increases, the intensity of the PA: PVK blend's absorption gradually increases. Increased absorption intensity in the blend films suggests a better crystalline quality and higher perovskite surface coverage. As can be seen, the intensity of the absorption peak is highest at PVK-25%. Moreover, it should be noted that the contribution of absorption from PVK would be minimal as the onset of absorption of PVK is 350 nm (3.5 eV) (S. W. Lee et al., 2016).

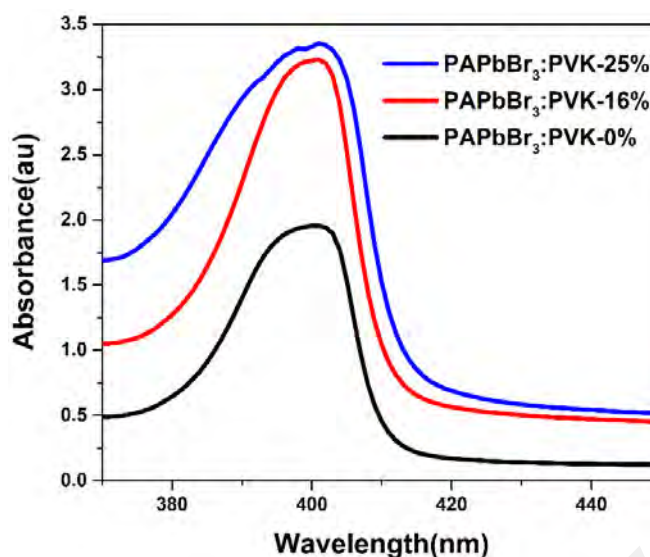


Figure 4.9: Absorption spectra of pristine PAPbBr₃ and PAPbBr₃-PVK blends films.

(b) Structural and Morphological Analysis

Thin films of the PAPbBr₃ and PAPbBr₃-PVK blends thin films were fabricated on glass substrates and then subjected to XRD analysis. Figure 4.10 displays the XRD curves of the PVK blended films mounted on glass. The figure shows the characteristic peaks of films at 14.05°, 21.18°, 28.35°, and 35.7°, where the peak spacing is all pretty much the same and could be attributed to PAPbBr₃ perovskites. These peaks correspond to the (002), (003), (004), and (005) planes of a simple cubic crystal structure with $a=b=c=12.57\text{\AA}$ (Appendix). Notably, compared to the pristine samples, the PA: PVK 25% samples display an increase in peak intensities of approximately twofold, primarily in the (002) and (003) peaks. This reveals that the addition of PVK to PAPbr₃ films increases their crystallinity.

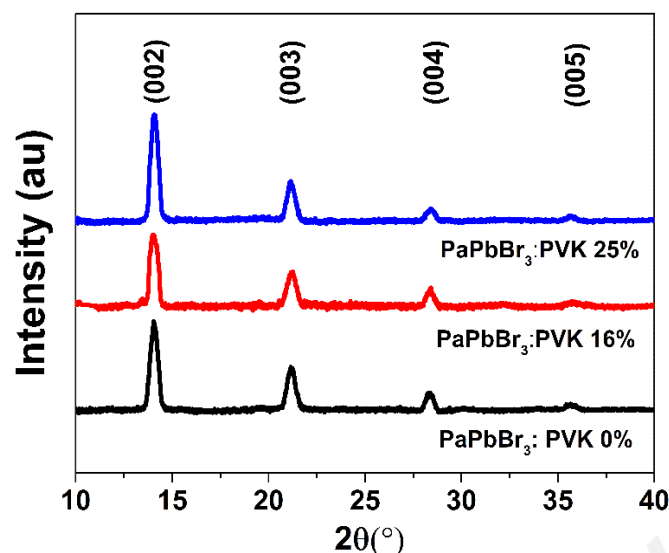


Figure 4.10: XRD pattern of Pristine PA and PA: PVK blended films.

The top-view FESEM was carried out to explore the effect of surface topography of PVK blended PAPbBr₃ films. The pristine PAPbBr₃ films in figure 4.11(a) exhibit nanopillar structures with different crystallographic orientations and a high density of deep voids (red circles). The number of deep voids is reduced when 16% PVK is added. The voids have become shallower in the polymer blend films of higher PVK content (Figure 4.11b). The size of each nanopillar (as viewed vertically) was determined from the FESEM images using ImageJ to be (73±10) nm, (74 ±1) nm, (72±9) nm for pristine, 16% and 25% -PVK blended PAPbBr₃ films respectively (refer to Figure A in Appendix B). The measurements are taken by averaging the diameters of 50 nanopillars. There is no clear distinction in the change of nanopillar sizes between the pristine PAPbBr₃ film and the PAPbBr₃-PVK blended films. This indicates that PVK polymer does not change the size of nanopillars. The gap between two nanopillars is estimated to be 7.14 nm (refer to Figure B, Appendix), unchanged with a different blending ratio.

However, in pristine PAPbBr₃, these nanopillars tend to orientate more randomly within each domain. (The domains can orientate vertically, horizontally, and tilted at various angles). Furthermore, the domain size for pristine PAPbBr₃ film is small (Figure 4.11a) compared to Figure 4.11b-c.

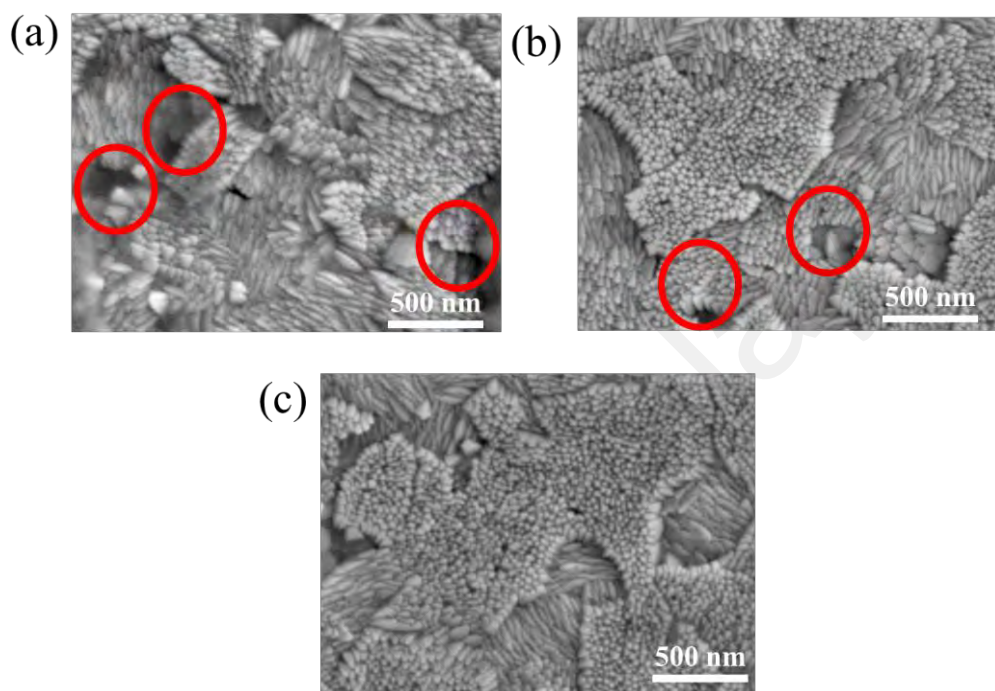


Figure 4.11: FESEM images of PAPbBr₃-PVK blend films at different ratios: (a) Pristine PAPbBr₃ (PVK-0%), (b) PVK-16%, (c) PVK-25%.

The optical microscope pictures in Figure 4.12 demonstrate that the PVK ratio substantially impacts the morphologies of the produced perovskite thin film. In Figure 4.12(a) extensive islands of PAPbBr₃ are seen on the surface of the Nafion/ITO substrate in sample 0%, which does not include PVK. A sizable substrate section is exposed without PAPbBr₃ coverage (Figure 4.12a). The film's visual appearance is drastically altered when PVK (at a concentration of 25%) is added to the PAPbBr₃ precursor solution. With PVK, coverage is significantly higher than without it, and the size of the "exposed substrate" region decreases (Figure 4.12c).

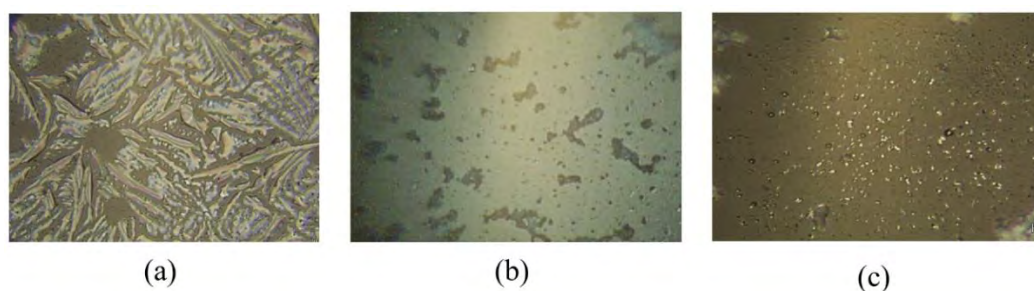


Figure 4.12: Optical microscope images of spin-coated (a) Pristine (PVK-0%), (b) PVK-16%, and (c) PVK-25% on Nafion/ITO substrates, respectively. (Scale bar= 20μm).

Moreover, the PA: PVK blended thin films were analyzed with AFM to learn more about their surface profile. The root mean square roughness of pristine perovskite, PVK 16% and 25% are 17nm, 52.64nm and 47.17nm respectively. The blend films exhibit a much higher surface roughness compared to the pristine film. The mobility of charge carriers is influenced by the aggregation behavior rather than the surface roughness, as the charge carrying channel is established on the dielectric interface (M. S. Park & Kim, 2019). Pristine perovskite showed plate-like domains with sharp grain boundary steps, as shown in Figure 4.13(a). Blending the perovskite with PVK reduced the appearance of the grain boundary steps and deep voids between them, as shown in Figure 4.13(c). The grains in PVK-blended films are seamlessly connected with lesser voids compared to pristine perovskite film, which accords with the results of the optical microscope images.

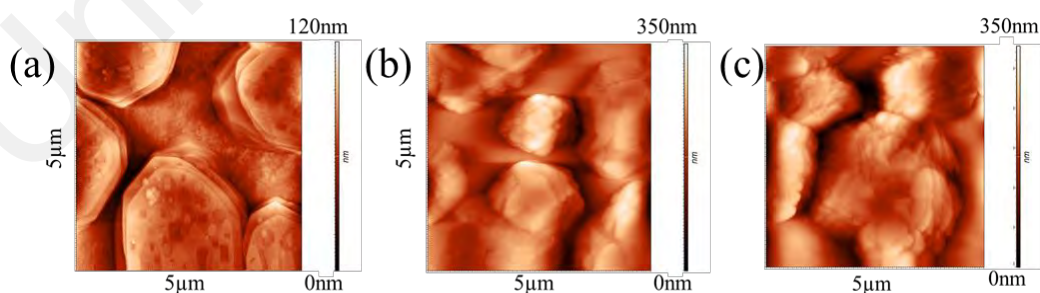


Figure 4.13: AFM images of PAPbBr₃-PVK blend films at different ratios: (a) Pristine PAPbBr₃ (PVK-0%), (b) PVK-16%, (c) PVK-25%.

2D GIXRD of perovskite and PVK blend films were carried out to study the preferred growth orientation of the nanopillars, as shown in Figure 4.14. The hkl peaks can be assigned based on a simulated XRD signal on a simple cubic structure. The strong signal of (001) along q_z , the absence along q_{xy} , and the presence of a weak signal of (111) and (210) along q_{xy} only indicated a highly preferential in-plane orientation of perovskite juxtaposed with horizontal growth. The in-plane growth is reduced when 16% of PVK is added (Figure 4.10b). Still, when 25% of PVK is added, the signal from (111) and (210) along q_{xy} becomes comparatively more substantial, indicating a preferential vertical growth along those crystallographic directions. In the past, control of crystallization has been attempted for 3D perovskite using an annealing procedure (Feng et al., 2016; Z. Wu et al., 2014), interfacial modification (K. W. Tan et al., 2015; Y. Yang et al., 2017) and recently the addition of K^+ dopant into quasi-2D perovskites (Kuai et al., 2020) with the latter achieved highly spotty Bragg like diffraction. Here, blending PVK shown can also induce highly ordered 1-D perovskite.

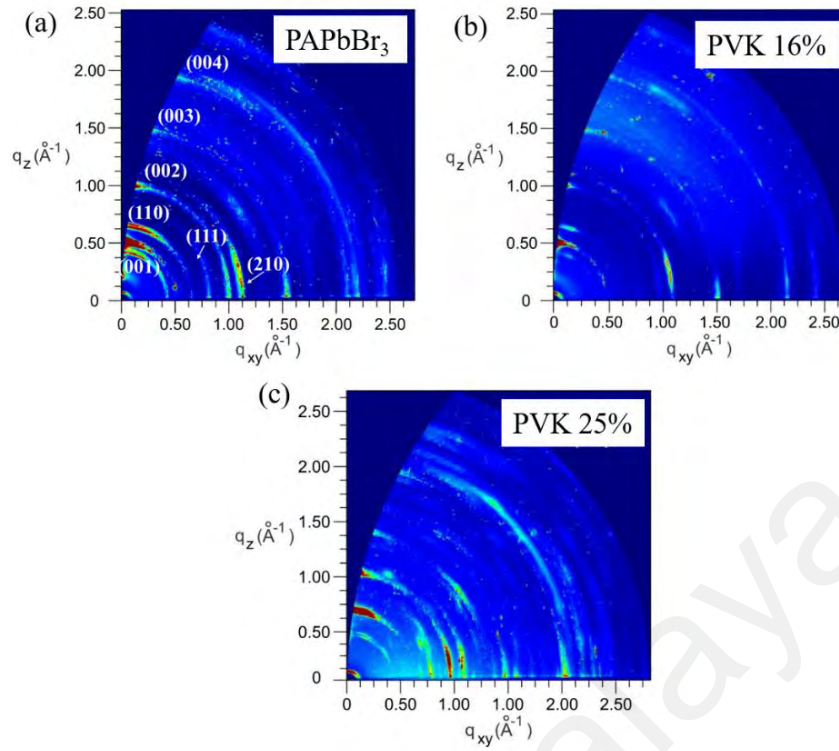


Figure 4.14: 2D-GIXRD pattern of (a) pristine PAPbBr₃, (b) PVK-16% and (c) PVK-25% blends films.

4.3.3 Electrical performance of FET based on PAPbBr₃-PVK blend system

The PAPbBr₃-PVK blend system was tested in a bottom contact/top gate FET. The output and transfer characteristics for a sweep voltage V_G range from 0 V to -18 V. The effect of the PVK blended ratio on device performance was investigated by contrasting the functionality of the FET with PVK blended ratios of 16% and 25% with a control ratio of 0%. Figure 4.15 shows the output characteristics (drain-source current I_{DS} vs. drain-source voltage V_{DS} for increasing values of gate-source voltage V_{GS}) and transfer characteristics ($|\sqrt{I_{DS}}|$ vs. V_{GS} plotted on a logarithmic scale and $|\sqrt{I_{DS}}|$ vs. V_{GS} , at $V_{DS} = -20$ V) for the two FETs. Field-effect mobilities and threshold voltages were calculated by fitting the $|\sqrt{I_{DS}}|$ vs. V_{GS} data to the square law.

The PA: PVK-25% and PA: PVK-16% transistors were found to have field-effect mobility of $0.012 \pm 0.03 \text{ cm}^2/\text{Vs}$ and $1.93 \pm 0.02 \times 10^{-3} \text{ cm}^2/\text{Vs}$, respectively. Blending PVK into PAPbBr₃ increases mobility. The enhancement in the performance is attributed to improved crystallinity (Da Silva Ozório et al., 2016; Tiwari et al., 2017) and orientation order (Chaudhary et al., 2019). As the perovskite's dimensionality reduces, the crystal domain's connection deteriorates, which results in poorer conductivity (Safdari et al., 2017). Thus the polymer's increased connectivity between PAPbBr₃ grain domains directly improves the FET mobility. The threshold voltage can be determined by extracting the x-axis intercept of the linear fit of the square root of the absolute value of drain current ($|I_{DS}|^{1/2}$) against gate voltage (V_{GS}) curve as shown in Figure 4.15(c). As previously mentioned, the existence of a barrier to hole injection can disrupt the process of hole injection from the electrode to the active layer. Consequently, holes that are unable to surmount this barrier might get trapped at the interface between the electrode and the active layer. To compensate for the immobility of trapped holes during the application of a gate-bias stress, a larger V_G is needed to inject holes from the electrode to produce conducting channels (S. H. Kim et al., 2017).

Because of this, a large V_{TH} is produced. A decrease in threshold voltage from -5.86V to -3.33V is observed in PVK blended devices. This result is likely attributable to the reduction in contact resistance at the metal/semiconductor interface (Choi et al., 2016). It has been reported in a few studies that the increase in the crystallinity of perovskite film results in a reduction of contact resistance (Giannaccini et al., 2018; Jiang et al., 2018). Moreover, the HOMO of PVK is -5.8 eV (Whitcher et al., 2018); blending PVK into pristine PAPbBr₃ can serve as a "ladder-step" energy level between the ITO/Nafion and PAPbBr₃ (Figure 4.16) further decreasing the charge-injection barrier.

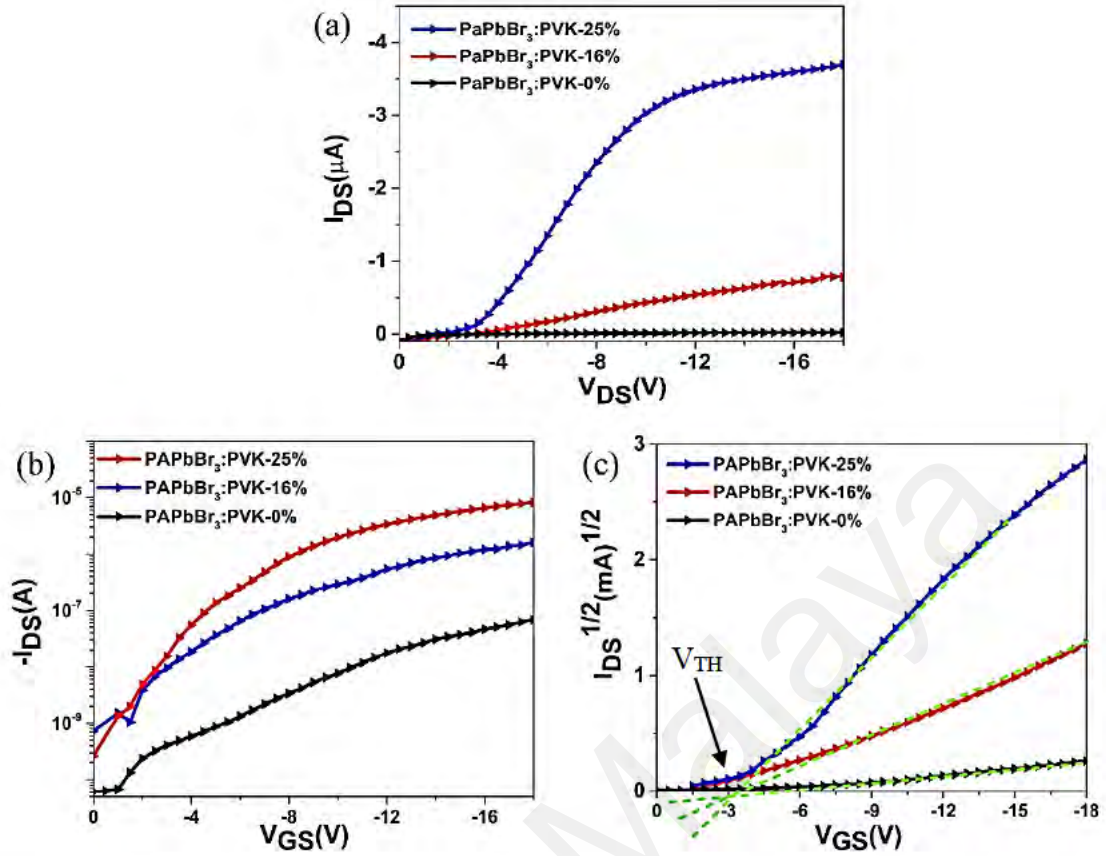


Figure 4.15: (a) Output characteristic of pristine, PVK-16% and PVK-25% blend FET (b) Semi-logarithmic curve of transfer characteristic of pristine, PVK-16% and PVK-25% blend FET, (c) Square root curve of transfer characteristic of pristine, PVK-16% and PVK-25% blend FET.

Table 4.1: Performance comparison of PAPbBr₃ FETs based on different PVK blending ratio.

Active layer	μ (cm ² /Vs)	I_{ON}/I_{OFF}	V_{TH} (V)
PAPbBr ₃ :PVK-0%	$8.62 \pm 0.04 \times 10^{-5}$	10^3	5.86
PAPbBr ₃ :PVK-16%	$1.93 \pm 0.02 \times 10^{-3}$	10^3	3.84
PAPbBr ₃ :PVK-25%	0.012 ± 0.03	10^3	3.33

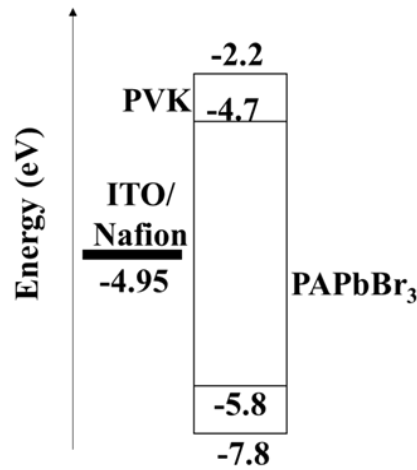


Figure 4.16: Energy level structure

Table 4.2: Comparison of mobility of low dimensional perovskites based FETs from literature.

Perovskite	S/D	Dielectric	Mobility (cm ² /V/s)	Measuring condition	Ref
PAPbBr₃	ITO	Teflon	10⁻²	RT	ambient
(BA) ₂ (MA) _{n-1} PbI _{3n+1}	Ag	SiO ₂	1.25	77K	inert
(PEA) ₂ PbBr ₄	Au	PVA	8.51×10 ⁻²	RT	ambient
(PEA) ₂ CsSn2I ₇	Cr/Au	SiO ₂	34	77K	vacuum
(PEA) ₂ SnI ₄	Au	SiO ₂	0.40	RT	vacuum
4TmSnI ₄	Au	SiO ₂	1.78	RT	vacuum
PEA ₄ BiAgBr ₈	Au	SiO ₂	1.66 × 10 ⁻⁵	RT	ambient
(TEA) ₂ SnI ₄	Au	SiO ₂	1.8	100K	-
(BA) ₂ (MA) _{n-1} PbI _{3n+1}	Cr	SiO ₂	10 ⁻²	RT	inert

However, the FET mobility decreases to 1.02 x 10⁻⁴ cm²/Vs at a higher bending ratio, PVK-50% (Figure 4.17a). At a blending ratio of PVK50%, the film exhibited enhanced continuity and uniformity. Nonetheless the PAPbBr₃ domains were observed to be smaller in size, hence limiting the performance of the device due to the presence of domain boundaries (Figure 4.17c). The transfer characteristics of a PVK-based FET using Nafion-treated ITO for the S/D electrodes are portrayed in Figure 4.17(b).

The field-effect mobilities were determined to be $1 \times 10^{-5} \text{ cm}^2/\text{Vs}$, lower than that of a pristine PAPbBr₃-based device. The extracted hole mobility of the PVK transistor corresponds to the value previously reported in the literature (D. H. Lee et al., 2010). Therefore the improvement in PA: PVK blended FET cannot be accounted for by charge hopping among PVK polymers. PVK can only facilitate the charge transfer between adjacent PAPbBr₃ domains. Thus, a larger ratio of PAPbBr₃ is critical to provide adequate distribution in the blend film. As PVK content increases, the limited hole mobility of PVK outweighs the increased crystal quality and may reduce mobility. Furthermore, PVK increased the degree of ordering of nanopillars and induced preferential orientation. Thus, PAPbBr₃-PVK 25% FET showed optimized performance.

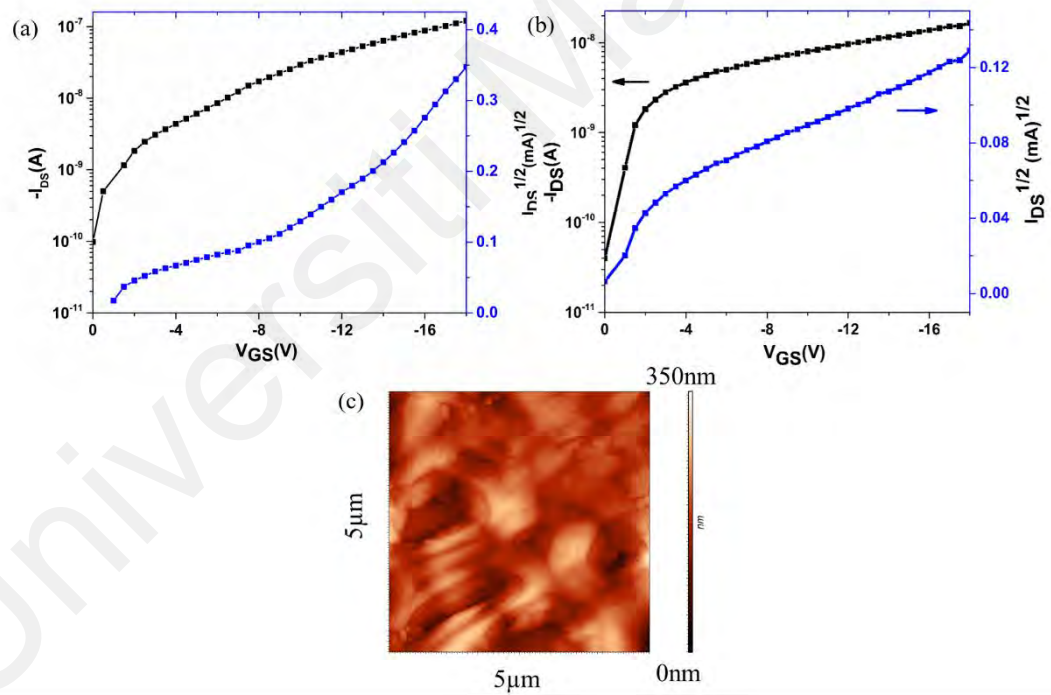


Figure 4.17: Transfer characteristics of (a) PAPbBr₃-PVK 50%, (b) Pristine PVK FET, (c) AFM image of PAPbBr₃-PVK 50% blend film.

In addition, the hysteresis behaviour of the devices was investigated, as shown in Figure 4.18. The hysteresis (ΔV_{TH}) was evaluated from the difference between the V_{TH} of the forward and backward sweeps of the transfer curve (Rajeev et al., 2015). The pristine PAPbBr₃ device Figure 4.18(a) exhibited a significant hysteresis, ΔV_{TH} of 4V. The observed hysteresis and negative voltage shift in V_{TH} may attribute to the charge carrier trap at the semiconductor/dielectric interface and ion migration (Egginger et al., 2009; Y. Liang et al., 2020; Senanayak et al., 2017; F. Wang et al., 2018). While hysteresis considerably declined to 0.95V in PAPbBr₃: PVK-25% device (Figure 4.18c), which can be ascribed to the improved crystallinity and reduced structural defect afforded by PVK blending. This finding agrees with prior research, which indicated that the passivation of perovskite film morphological defects also reduces hysteresis (Y. Liang et al., 2020; Senanayak et al., 2017; H. Yuan et al., 2016).

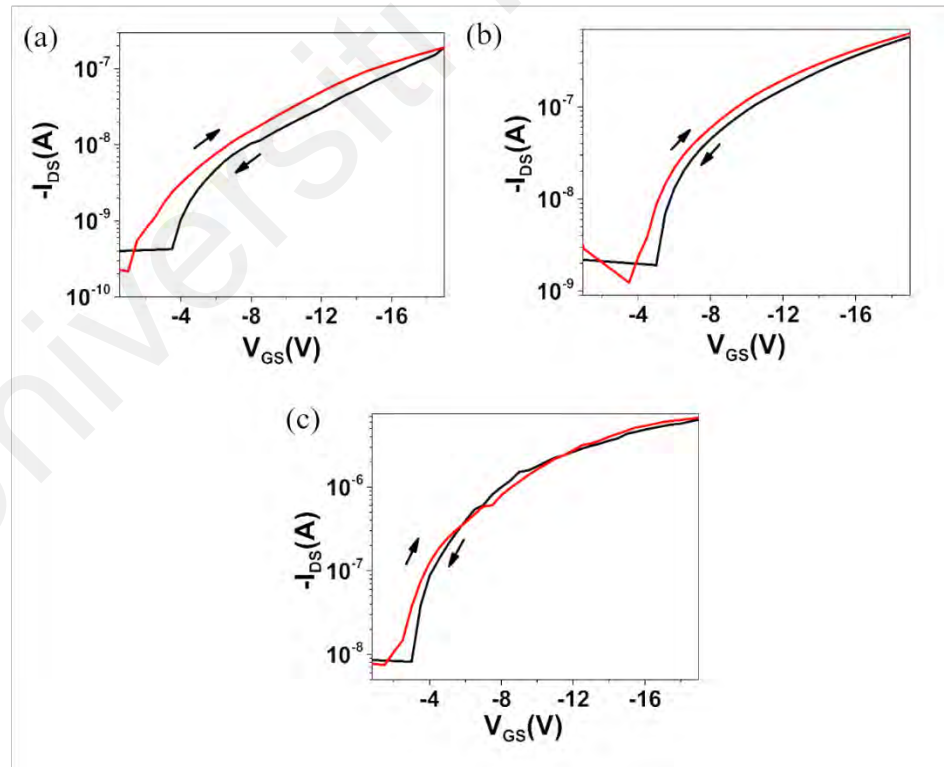


Figure 4.18: Transfer characteristics of (a) pristine PAPbBr₃, (b) PVK-16%, and (c) PVK 25%.

Moreover, the water contact angle measurements (Figure 4.19, a-c) indicate a positive correlation between the water contact angle and the PVK ratio. Pristine perovskite thin films have a smaller angle, suggesting that water molecules may be able to penetrate the film. The hydrophobic aspect of PVK polymers can be attributed to their high carbon content (S. Wang et al., 2021; Yao et al., 2022). Consequently, the introduction of these polymers into perovskite materials is expected to decrease their hydrophilic characteristics, where water contact angle of PVK 25% increased to 54.6°. This is anticipated to hinder the penetration of water and enhance the overall moisture stability of the device.

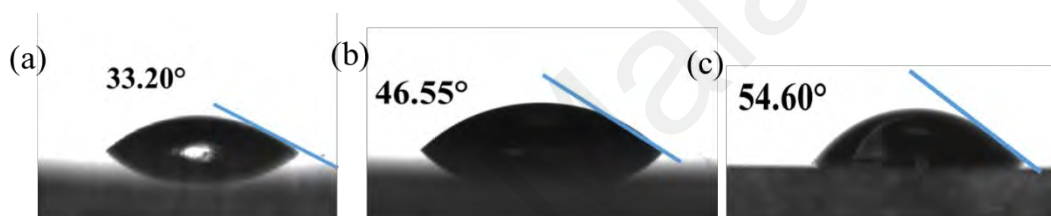


Figure 4.19: Contact angles with water of (a) Pristine (PVK-0%), (b) PVK-16%, and (c) PVK-25%.

Figure 4.20 illustrates the logarithmic scale representation of the field-effect mobility of the FETs based on the PVK blend system. The parameters of the FET were derived from at least five devices fabricated in various batches. Device PVK 25% exhibits a variation of no more than one order of magnitude. On the other hand, the mobility of pristine perovskite FET exhibited a significant range of 6×10^{-6} to $2.3 \times 10^{-3} \text{ cm}^2/\text{Vs}$, showing substantial fluctuations over 3 orders of magnitude. The PAPbBr₃: PVK blend-based FET shows excellent reproducibility considering the low variation in operating parameters. Based on these findings, a blend of perovskite and polymer can be used as the active layer in a high-performance FET made from perovskite.

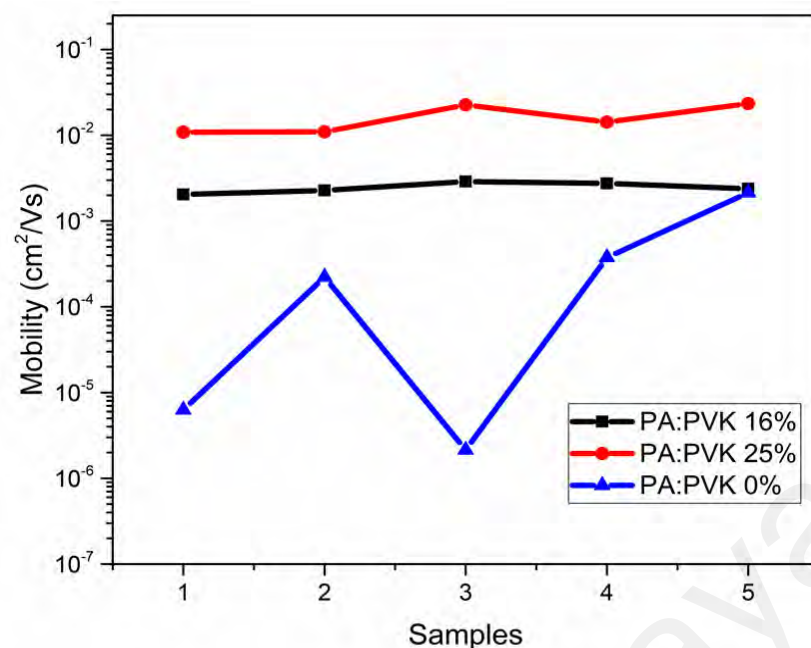


Figure 4.20: Log-scale plot of the extracted field-effect mobility from different pristine PA and PVK blend film based FETs.

In order to confirm that the observed behavior of the transistor can be attributed to the perovskite material rather than the presence of the Nafion interlayer, a control device with only the Nafion interlayer was measured. However, this device did not exhibit any transistor characteristics, thereby eliminating the possibility that the transistor behavior is solely caused by the insertion of the Nafion layer (Figure 4.21).

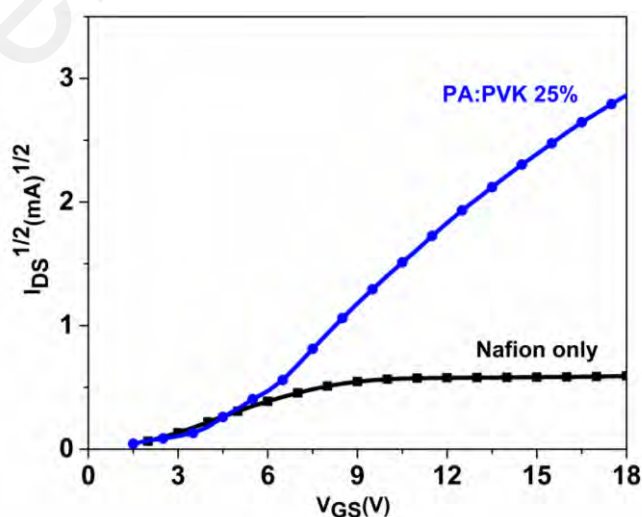


Figure 4.21: Comparison of transfer characteristics of Nafion only FET with optimized PA:PVK 25% FET device in the saturation regime at room.

4.4 Conclusion

High mobility FETs using deep valence band maximum perovskite can be fabricated using Nafion as a surface modifier, reducing the charge injection barrier. Blending the one-dimensional perovskite with PVK results in preferential vertical growth of the nanopillars. As a result of higher ordering, these nanopillars formed a more extensive domain size, thus increasing the field-effect mobility. Therefore, combining the low-cost process with these excellent transport properties and high stability features, the low-dimensional perovskite FETs hold appreciable value in future device applications and electronic industries.

CHAPTER 5: PEA₂PBBR₄-BASED SELF-POWERED ULTRA-VIOLET PHOTODIODE

5.1 Introduction

Photodiodes, a key optoelectronic component, are used in imaging, biosensing, environmental monitoring, and optical communication. Photodiodes based on 2-dimensional (2D) perovskites have made significant progress due to the rapid development of perovskites. Br⁻ is expected to provide better UV absorbers, as it will help to reduce intrinsic charge carrier density due to a broader band gap (B. Guo et al., 2020). In addition, bromide-based 2D perovskites are less susceptible to oxidation in ambient air (Tong, 2020). Therefore 2D layered phenethylammonium lead bromide (PEA₂PbBr₄) is a promising candidate for UV photodiodes. Recently, Guo's group reported PEA₂PbBr₄ photodetectors based on gravity-guided growth (GGG) with a photocurrent of 2.31×10^{-5} mA/cm² and a response time of 0.5 ms at a light intensity of 41.56 mWcm⁻² (T. Guo et al., 2021).

Furthermore, Yan Lian et al. demonstrated 0.28 s rise time and 2.4×10^{-6} mA/cm² photocurrent by employing cesium halide into the PEA₂PbBr₄ active layer (Y. Li et al., 2022). However, the photocurrent density (on the order of 10⁻⁵) and the slow response time of those devices might be enhanced to accommodate an even wider variety of practical applications. The current density of 2D perovskites is considerably lower than that of their 3D counterparts due to the suppression of out-of-plane charge transfer by the massive organic cations, which function as insulating barriers between the highly conducting inorganic slabs (H. Tsai et al., 2016). For the photo-induced carriers to be oriented toward the electrodes, a bias must be supplied in most lateral structure photodiodes (e.g., metal-semiconductor-metal). On the other hand, the zero-bias operation is simplified in vertically structured photodiodes due to the shorter carrier route to the hole injection layer (Nguyen et al., 2021).

In the p-i-n configuration photodiodes, the HTL between the perovskite and the anode plays a significant role in electron blocking and hole extraction could be further enhanced to extend the range of practical applications. Currently, the materials investigated as potential HTL include organic and inorganic materials such as NiO_x , CuI , CuSCN , CuO_x and polytriarylamine (PTAA)(Afzal et al., 2021; C. Liu et al., 2019; K. Zhao et al., 2015; Zheng et al., 2017). However, most of them have low solubility, are costly and require a high-temperature process to prepare a homogenous and compact film to achieve a better charge transport, e.g. NiO_x requires annealing at a high temperature of 300°C (You et al., 2016). PEDOT: PSS is a widely used HTL material, mainly owing to its high transparency, flexibility, low-cost material and conventional deposition techniques.

Nevertheless, the highest occupied molecular orbital (HOMO) for PEDOT: PSS is only about 5 eV, which doesn't match the valence band of most of the perovskite layer (5.4–7.3 eV)(P. Gao et al., 2014). Moreover, the surface character of PEDOT: PSS is hydrophilic and can affect the morphology of the subsequently deposited photoactive layer(Y. Li et al., 2019). Perovskite films with high-density small grains were formed on the hydrophilic surface of PEDOT: PSS, leading to a large trap density at grain boundaries, while those grown on the non-wetting surface formed large grains and lower charge recombination at the PEDOT: PSS/perovskite interface (Bi et al., 2015). Therefore interlayers between PEDOT: PSS and perovskite were employed to minimize the acidity and hydrophilicity of PEDOT: PSS. PEDOT: PSS and perovskite interface modification is one of the strategies to achieve high device performance and good stability. Koushik et al. employed Al_2O_3 (atomic-layer-deposited) as a buffer layer at the perovskite active layer and PEDOT: PSS interface, which passivated and enhanced photocurrent performance (Koushik, Verhees, Zhang, et al., 2017).

Shi et al. incorporated a poly-N-vinyl carbazole (PVK) layer to modulate the HOMO level of PEDOT: PSS to improve the hole injection (Shi et al., 2017). Moreover, sodium citrate-modified PEDOT: PSS transport holes effectively and suppressed charge recombination, thereby increasing the device's stability (Syed et al., 2019). Y. Zhou et al. reduced the energy barrier between the HTL and emissive layer by incorporating insulating MoO₃ and PEDOT: PSS as HTL (P. Zhao et al., 2017).

Poly(sulfonated tetrafluoroethylene) fluoropolymer (Nafion) comprises a fluorocarbon backbone and a perfluoro vinyl ether branch composed of sulfonic acid. Nafion has been widely explored as the proton-exchange membrane in fuel cell applications due to its high chemical stability and good proton conductivity (Heitner-Wirguin, 1996; Mauritz & Moore, 2004; Nagao, 2017; Yoshitake & Watakabe, 2008). Recently, Nafion has been employed as a dopant in poly(thienothiophene) for use in OLEDs to alter the surface energy of the charge injection layer (Engmann et al., 2019; J. K. Park et al., 2012) and as a layer for the extraction of holes in inverted structures (Manceau & Berson, 2014). In addition, Nafion-doped PEDOT: PSS structures have been reported to improve performance when used as HTL in CH₃NH₃PbI₃ perovskite solar cell fabrication (S. Ma et al., 2018). Nafion doping to PEDOT: PSS dispersions, on the other hand, are seen as less practical because it adds an acidic component to the composition (Moet et al., 2010). As a result, indium migrates from the ITO into the PEDOT: PSS layer due to corrosion by PEDOT: PSS (De Jong et al., 2000). However, the work function of the anode can be raised by applying a thin layer of Nafion. An increase of 0.5 eV in the work function of ITO was achieved by covering it with a thin coating of Nafion (Subramaniam et al., 2021).

This chapter is divided into two sections. The first section investigated the effects of the Nafion interlayer at the hole-transporting layer and perovskite interface on photodiode performance. In section two, the optimized Nafion ratio was selected to evaluate the current density characteristics under different light intensities to extract the critical parameters of the self-powered photodiode.

5.2 Experiment methods

The pre-patterned ITO substrates were pre-cleaned with ultrasonic agitation in deionized water, acetone, isopropyl alcohol (IPA) and deionized water each for 10 min, followed by nitrogen (N_2) purging before spin-coating. Next, the cleaned ITO/glass substrates were treated with oxygen plasma for 5 min before spin coating HTL. The filtered (using 0.45 PTFE filters) hole transporting material, PEDOT: PSS aqueous solution, spun onto the ITO-based substrates at a speed of 3000 rpm for 30 seconds using a spin coater. Then, the substrates were baked on a hot plate at a temperature of 120°C for 30 minutes. The Nafion solutions were prepared by diluting with ethanol at different volume ratios, Nafion/Ethanol (1:10) and Nafion/Ethanol (1:4) corresponding to 9wt% and 20wt% respectively. Nafion in ethanol solution was spin-coated on the surface of annealed PEDOT: PSS layer and heated at a temperature of 100 °C for 10 minutes. The thickness of the deposited Nafion layer 1:10 and 1:4 are 15nm and 33nm respectively. PEA_2PbBr_4 was dissolved in DMF/CB at a 3:1 ratio and vigorously stirred on a magnetic stirring plate overnight. PCBM was dissolved in chloroform at a concentration of 20 mg/ml, then spin-coated at a speed of 3000 rpm for forty seconds. At last, the aluminium (Al) electrode was thermally evaporated at 0.5 Å/s depositions to form a 100 nm thickness.

The contact angle measurement was conducted with the sessile drop method using an Attension® Theta Lite optical tensiometer. A UV–Visible spectrophotometer (Thermo Scientific EVOLUTION 201) was used to measure the absorption spectra of perovskite layers. A Rigaku diffractometer detected X-ray diffraction (XRD) patterns with Cu K α radiation, at an angle ranging from 10° to 40°. The microstructure and elementary mapping of perovskite layers were captured by a field-emission scanning electron microscope (FESEM). Moreover, the device's current density (I–V) characterization was performed using Keithley 236 source measuring unit under dark and illumination of 395 nm UV light irradiated at the ITO glass side. The intensity of the irradiated UV light was detected using a light power meter (THORLABS-s1000VC). The stability of photo response of the device was studied by periodically ON and OFF the UV light input by using a mechanical light shutter operating at 0.2 Hz. The measurement voltage bias was fixed at 0 V to represent self-powered mode. The measurements were performed under an ambient environment at room temperature. The photo response speed was acquired using a digital oscilloscope (Agilent DSO-X 3052 A) under a square-pulsed simulated UV light LED (395 nm), which was generated by a function generator (Tektronix AFG 2021).

5.3 Result and discussion

5.3.1 Effect of Nafion interlayer on PEA₂PbBr₄ morphology

The surface contact angle of DMF/CB containing PEA₂PbBr₄ on PEDOT: PSS films without and with the Nafion layer was tested to characterize the wetting capability of the films. Figure 5.1 (b-d) reflects the change in wettability of the PEDOT-PSS film after Nafion coating. The contact angle of PEA₂PbBr₄ solution on PEDOT: PSS film is 6° (Figure 5.1b), while it gradually increased with a higher Nafion ratio. This indicated that the wettability of PEDOT: PSS decreased with increasing Nafion ratio.

The dewetting property of PEDOT: PSS/Nafion film might benefit the formation of a high-quality upper photoactive layer. Which could result in enhanced charge carrier mobility and consequently boost the photocurrent of photodiodes (Upama et al., 2017).

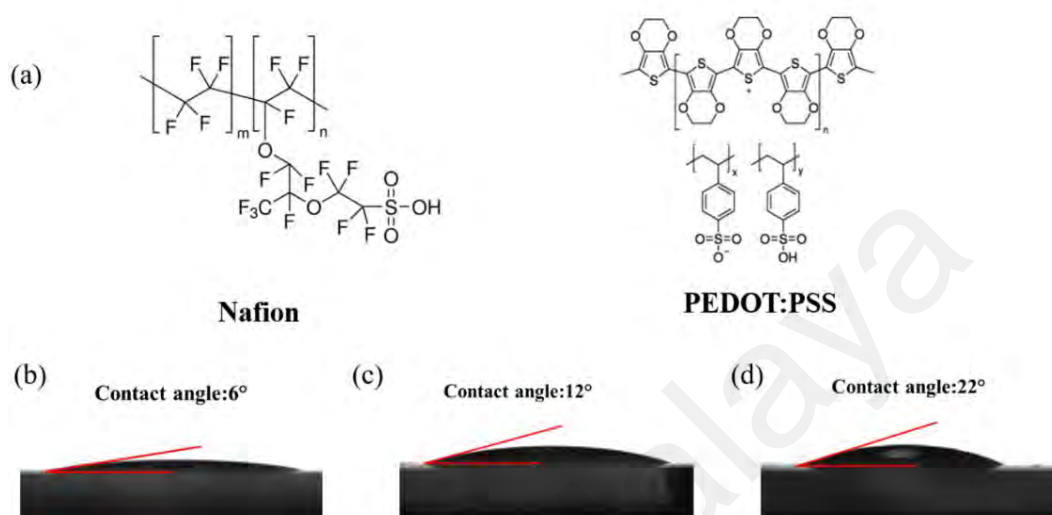


Figure 5.1: (a) Chemical structures of Nafion and PEDOT: PSS. Contact angle of DMF/CB solvent containing PEA₂PbBr₄ on top of PEDOT: PSS (b) PEDOT: PSS without Nafion layer (c) PEDOT: PSS/Nafion 1:10 (d) PEDOT: PSS/Nafion 1:4.

To verify this, FESEM was conducted to uncover the effect of the Nafion layer on the morphology of the following deposited PEA₂PbBr₄ film and their corresponding Energy dispersive X-ray spectroscopy (EDX) elemental distribution of Lead (Pb) and Bromide (Br) as shown in Figure 5.2. A significant correlation between substrate surface wettability and film morphologies was observed in Figure 5.2a-c. The PEA₂PbBr₄ film on PEDOT: PSS without Nafion exhibited island formation and discontinuous domains. In contrast, the PEA₂PbBr₄ film on Nafion 1:4 in Figure 5.2(c) displayed a more compact, homogeneous formation and higher substrate coverage. Without Nafion, Pb (Figure 5.2d) and Br (Figure 5.2e) elements were unevenly distributed. Elements are homogeneously dispersed on Nafion HTLs, confirmed by EDX results. Increasing HTL surface wettability has allowed the solute to diffuse faster on the substrate and decreased the nucleation work of PEA₂PbBr₄ domains (Di et al., 2020).

This might lead to randomly orientated $\text{PEA}_2\text{PbBr}_4$ domains on the PEDOT: PSS surface. The surface with lower wettability induces fewer $\text{PEA}_2\text{PbBr}_4$ nuclei upon spin-coating of precursor solution, hence assists in compact and homogenous perovskite growth (Y. Li et al., 2019). Perovskite grains formation is highly dependent on the wettability of the bottom layer surface (Bi et al., 2015).

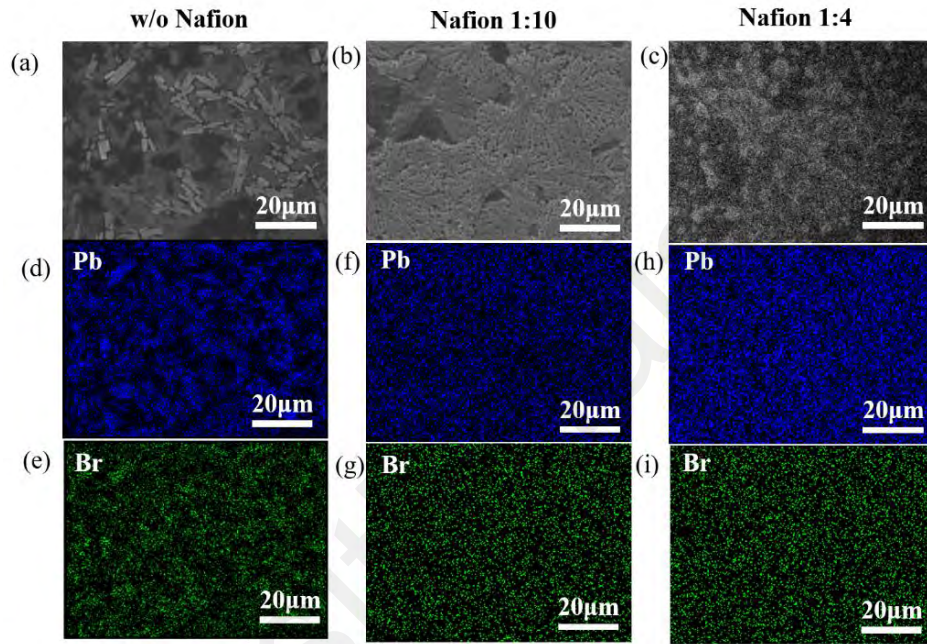


Figure 5.2: FESEM top view images (a-c) and mapping images of EDX analysis PEA layer corresponding to bromine and lead mapping on PEDOT: PSS (d-e) without Nafion layer, (f-g) Nafion 1:10 layer, (h-i) Nafion 1:4 layer.

The phase and crystallinity of the $\text{PEA}_2\text{PbBr}_4$ film spin-coated on PEDOT: PSS with and without Nafion layers was studied by X-ray diffraction (XRD) spectra, as shown in Figure 5.3(a). The significant peaks at the 2θ values: 10.5° , 15.9° , 21.2° , 26.5° , and 30.3° corresponded to the atomic planes of (004), (006), (008), (012), (014) respectively consistent with literature reported (D. Ma et al., 2017). All the thin films showed nearly identical XRD patterns indicating that the structural ordering and preferential orientation of the crystallites relative to the HTL were retained in all the films.

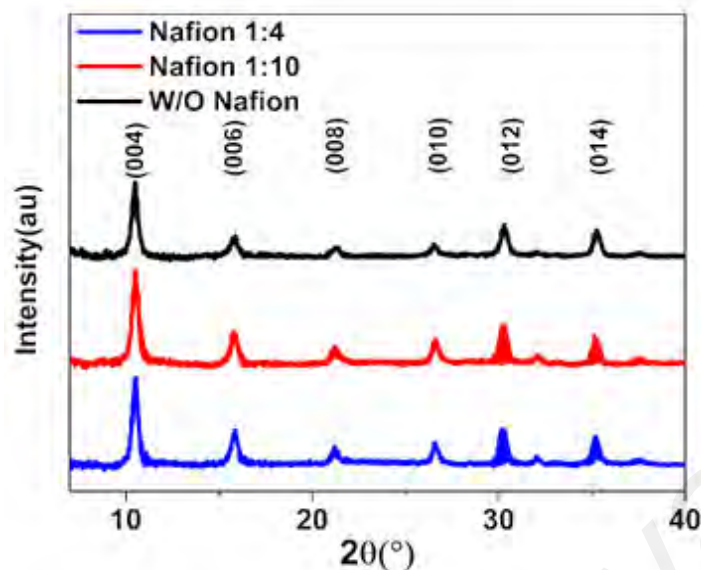


Figure 5.3: XRD spectra of the $\text{PEA}_2\text{PbBr}_4$ thin films deposited at the same concentration and speed on PEDOT: PSS without and with the Nafion layer.

The UV–vis absorption spectra presented in Figure 5.4 demonstrated the $\text{PEA}_2\text{PbBr}_4$ sample deposited on PEDOT: PSS with and without the Nafion layer. All the films showed an absorption peak at 406 nm, which can be assigned to $\text{PEA}_2\text{PbBr}_4$ (B. Guo et al., 2020). This demonstrated good light-harvesting capability over wavelength in the near UV range. As expected from FESEM data, Nafion 1:4 exhibits the highest optical absorption compared to film without Nafion. Poor coverage of $\text{PEA}_2\text{PbBr}_4$ films (without Nafion) resulted in light passing through them and hence a lower absorption despite spin-coated it at the same concentration and speed. This indicated that the hydrophobic Nafion interlayer helped organize the $\text{PEA}_2\text{PbBr}_4$ film quality.

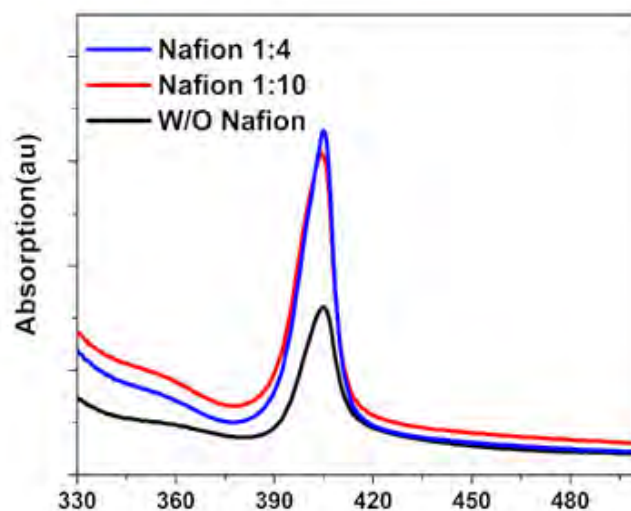


Figure 5.4 : Absorption spectra of the $\text{PEA}_2\text{PbBr}_4$ thin films deposited at the same concentration and speed on PEDOT: PSS without and with the Nafion layer.

The thicknesses of $\text{PEA}_2\text{PbBr}_4$ layers on PEDOT: PSS, Nafion 1:10, and Nafion 1:4 are 86.2 ± 7 nm, 86.6 ± 6 nm, and 87.9 ± 4 nm, respectively (Figure 5.5). Since the mean $\text{PEA}_2\text{PbBr}_4$ thicknesses are comparable, the higher surface coverage of the $\text{PEA}_2\text{PbBr}_4$ layer may be responsible for the enhanced absorption. (Figure 5.4).

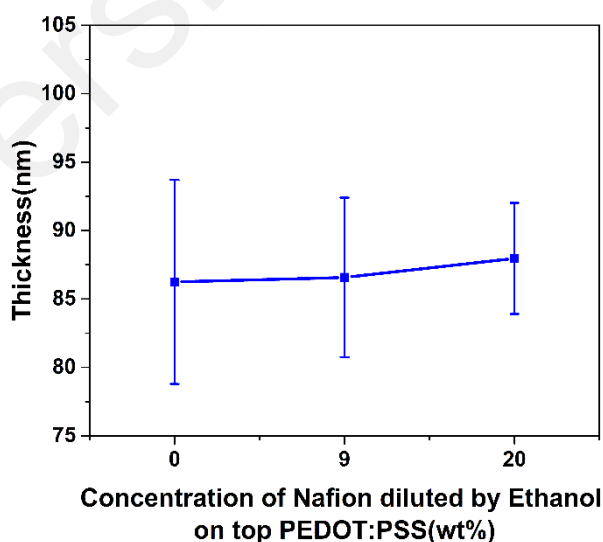


Figure 5.5: Thickness of spin-coated $\text{PEA}_2\text{PbBr}_4$ layer on PEDOT: PSS/Nafion bilayer with different Nafion dilution concentration.

5.3.2 Electrical Performance of $\text{PEA}_2\text{PbBr}_4$ Photodiode

Figure 5.6(a) shows the configuration of the $\text{PEA}_2\text{PbBr}_4$ photodiode on the ITO substrate. The PEDOT: PSS with Nafion layer as HTL and PCBM was selected as electron transporting hole blocking layer, respectively, responsible for carrier extraction and transport. Upon UV light illumination, the electron and hole pairs were generated in the perovskite layer, and the holes were transported to the ITO electrode via HTL while the electrons were extracted by ETL to the ITO electrode, thus producing the corresponding photocurrent. Figure 5.6(b) illustrates the energy level diagram of a photodiode without Nafion or with Nafion-treated PEDOT: PSS as the HTL.

HOMO of PEDOT: PSS is 5 eV (S. Ma et al., 2018). PEDOT: PSS with Nafion has a HOMO value (5.7 eV) (T. W. Lee et al., 2007; Van Reenen et al., 2014) closer to the $\text{PEA}_2\text{PbBr}_4$. Thus, the PEDOT: PSS/Nafion HTL offers a more favorable alignment of the energy band to VBM of the $\text{PEA}_2\text{PbBr}_4$ layer. The high HOMO of the PEDOT: PSS with Nafion layer HTL would decrease the interfacial barrier at HTL/Perovskite layer. This smoothed the pathway for the hole transport, which may reduce the current leakage, yielding high-performance photodiodes.

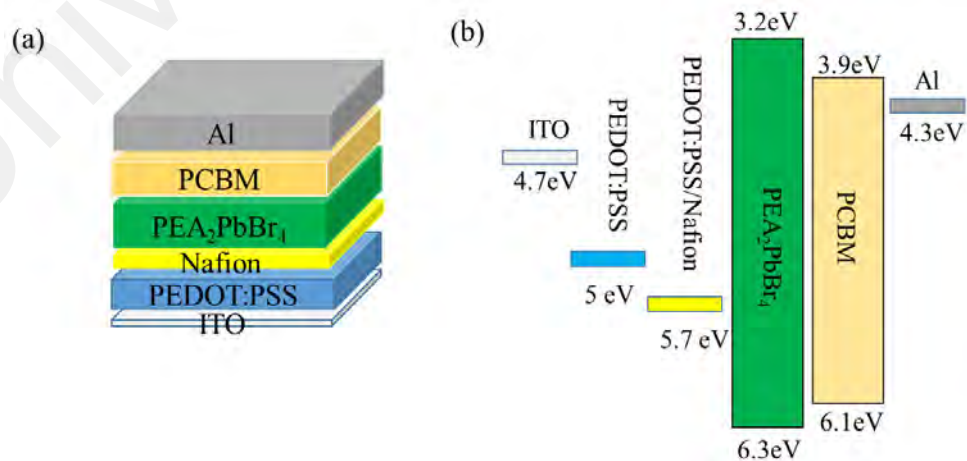


Figure 5.6: (a) Schematic structure (b) energy level diagram of the photodiodes based on $\text{PEA}_2\text{PbBr}_4$.

The device Nafion-based photodiode showed a lower dark current than the device without PEDOT: PSS under 0 V (Figure 5.7), where the dark current falls from $2.67 \times 10^{-3} \text{ mA/cm}^2$ to $4.58 \times 10^{-5} \text{ mA/cm}^2$. The improved performance was ascribed to Nafion layers minimizing the energy barrier between HTL and $\text{PEA}_2\text{PbBr}_4$ interface and reducing the dark current. Therefore, by assuring improved charge selectivity at the ITO, PEDOT: PSS with a Nafion layer can function as a better electron-blocking layer than PEDOT: PSS without Nafion.

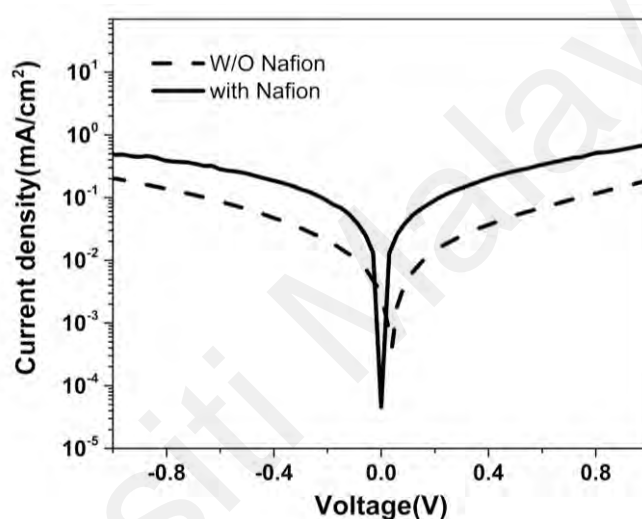


Figure 5.7: J-V curves of the devices under dark without Nafion and with Nafion layer-based photodiode.

In order to gauge the performance of the fabricated $\text{PEA}_2\text{PbBr}_4$ devices under UV light, the current density and voltage characteristics of the photodiodes were studied under the illumination of a 395 nm UV light with an intensity of 13.5 mW/cm^2 (which was irradiated on 0.045 cm^2 active area) biasing from -1.0V to 1.0V. All the measurements were taken at room temperature under ambient settings. The current density and voltage (J-V) curves without and with various Nafion ratio devices shown in Figure 5.8 (a) illustrated a noticeable photovoltaic effect, which means that the photodiode can function as a self-driven device without an external power source.

Moreover, devices using the PEDOT: PSS/Nafion showed a considerable enhancement of the V_{oc} by 0.46 V compared to the individual PEDOT: PSS with a V_{oc} of 0.04 V. The increase in V_{oc} may mainly be attributed to the energy differences at the perovskite/Nafion interface (Ali Khawaja et al., 2021). When Nafion was applied onto PEDOT: PSS, the energy difference between its PEDOT: PSS and PEA_2PbBr_4 shrank from 1.3 eV to 0.6 eV (PEDOT: PSS/Nafion/ PEA_2PbBr_4) (Figure 5.6b). As discussed previously, the HOMO of PEDOT: PSS/Nafion (5.7 eV) matches well with perovskite (6.3 eV), likely resulting in efficient charge extraction from perovskite to electrode.

The current density-voltage characteristics implied that built-in electric fields were present in PEDOT: PSS, and even a minimal bias could extract the carriers. Nafion 1:4 PD has a larger PEA_2PbBr_4 domain on top of HTL, which caused an increment in the absorption area of the device; the active layer will detect higher light under similar illumination conditions. As a result, the present photocurrent was significantly higher than without Nafion devices, indicating a strong ability to convert a light signal to an electrical signal at zero bias (Pan et al., 2021). A similar trend is also clearly shown in the time-dependent photoresponse ($I-t$) curves with repeated on/off switching cycles at zero bias, as shown in Figure 5.8(b). A maximum on/off ratio of 10800 at 13.5 mW/cm^2 was achieved under 395 nm irradiation at zero bias.

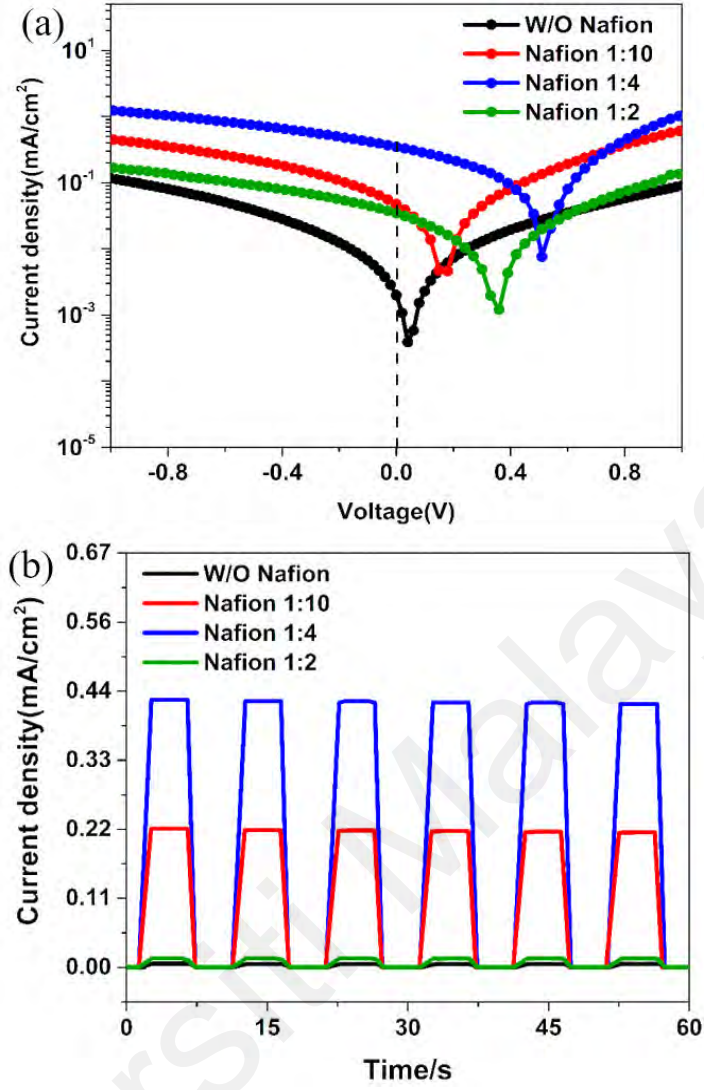


Figure 5.8: (a) Current density-voltage curves of the devices (b) time-dependent photocurrent response under periodic illumination of 395 nm UV irradiation (13.5 mW/cm²) at zero bias.

The conductivity of PEDOT: PSS film with and without Nafion layer was tested using four-point probe techniques. The electrical conductivity, denoted by the symbol (σ), which is the inverse of the resistivity (ρ), the value was calculated through the Van der Pauw method, based on the following equation:

$$\sigma = \frac{1}{\rho} = \frac{\ln 2}{\pi d} \left(\frac{I}{V} \right) \quad (5.1)$$

where d is the film thickness, V is the voltage, and I is the current.

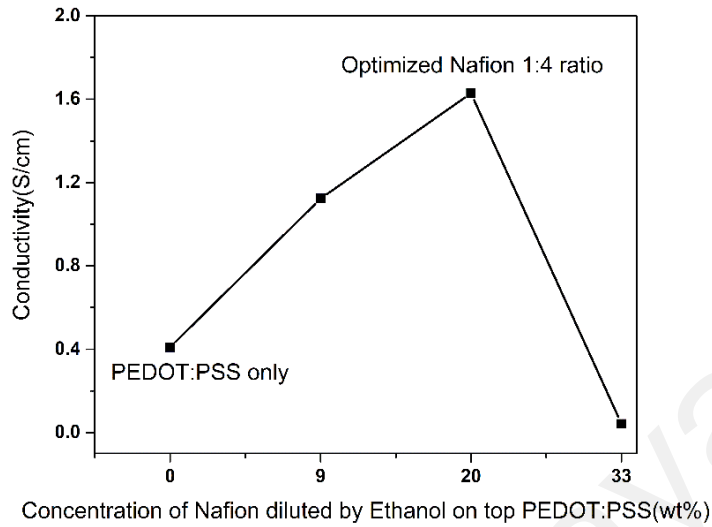


Figure 5.9: Conductivity of PEDOT: PSS/Nafion bilayer with different Nafion dilution concentrations.

The calculated conductivity of PEDOT: PSS without the Nafion layer was 0.41 S/cm(Figure 5.8), which is in the range of the previously reported value (Ph, 2012). The conductivity increased to 1.63 S/cm for PEDOT: PSS with Nafion 1:4 layer (Figure 5.9). Thus the generated charge carriers in $\text{PEA}_2\text{PbBr}_4$ film were extracted before recombination due to higher conductive HTL. The PEDOT: PSS consisted of hydrophobic conductive PEDOT and hydrophilic insulating PSS ionomers, resulting in poor conductivity(Xia et al., 2021). When Nafion in ethanol solution was spun-coated onto PEDOT: PSS, the insulating PSS component was partly washed out for the surface. A previous XPS study of PEDOT: PSS/Nafion film reported a reduction of the PSS component (S2p peak) upon Nafion coating(Hossain et al., 2016). The sulfonate group in both Nafion and PSS interacted, weakening the Columbic interaction between PEDOT and PSS(Elbohy et al., 2019). This contributed to separating PEDOT from PSS and forming a continuous percolation path for inter-domain charge transfer, thus increasing conductivity(J. K. Park et al., 2012). However, conductivity decreases at a higher Nafion layer concentration.

This may explain the reduction in photocurrent of Nafion 1:2-based PD, as depicted in Figure 5.8, where the film's increased series resistivity limited both the transmission and charge transport (Manceau & Berson, 2014; W. Qiu et al., 2015). Thus, the Nafion 1:4 photodiodes showed optimized performance. Therefore, PD with Nafion 1:4 as the HTL focused on further investigations.

The essential parameters commonly used to evaluate photodiodes' performance are photoresponsivity (R) and detectivity (D). The responsivity and detectivity of PDs can be determined using the formulas $R = J_{ph}/J_{Light}$ and $D = R\sqrt{2dj_d}$ respectively. Figure 5.10 illustrates the semi-logarithmic plot of photo responsivity and detectivity of Nafion 1:4 PD and without Nafion under 395 nm UV light. These results clearly showed that the value of R and D of Nafion 1:4 PD was higher than those with PEDOT: PSS as HTL without the Nafion layer. We found that under illumination ($\sim 13.5 \text{ mW/cm}^2$), the detectivity value for the optimized device was as high as 2.54×10^{11} Jones at zero bias due to the decreased dark current and improved responsivity. The value of responsivity was determined to be 25.8 mA/W under zero bias. The improved quality HTL/PEA₂PbBr₄ interface also contributed to the performance of Nafion 1:4.

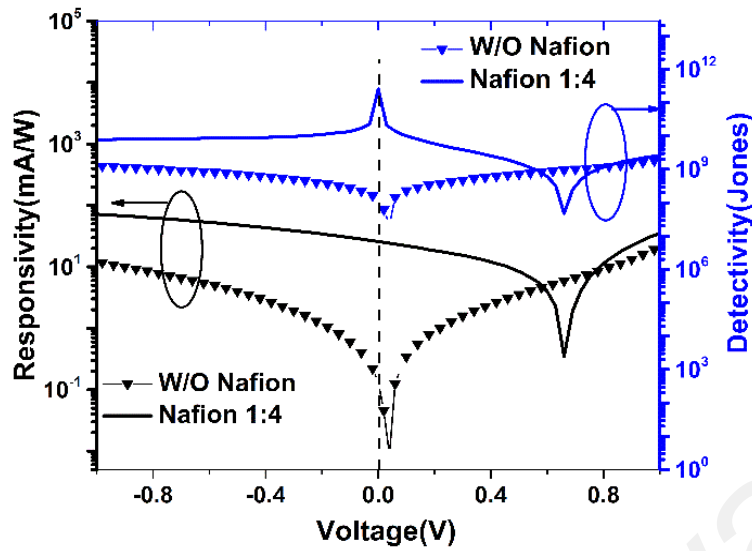


Figure 5.10: The semi-logarithmic plot of responsivity and detectivity of the optimized device Nafion 1:4 and without Nafion at bias voltage from -1 to 1 V, under 395 nm UV illumination.

Table 5.1: Performance comparison of $\text{PEA}_2\text{PbBr}_4$ UV photodiode devices based on HTL with and without Nafion at 0 V bias.

Device	J_{dark} (mA/cm ²)	J_{photo} (mA/cm ²)	R (mA/W)	D^* (10^{11} Jones)
PEDOT:PSS	0.0027	0.002	2.41	0.078
PEDOT:PSS/Nafion 1:10	4.58×10^{-5}	0.047	3.51	0.345
PEDOT:PSS/Nafion 1:4	7.06×10^{-5}	0.348	25.8	2.543

An oscilloscope detected the device's response time under 395 nm light at 100 Hz. Photodiode based on Nafion 1:4 showed no significant degradation in photocurrent even after continuous UV light illumination for 20 cycles with turning on and off. This result suggested excellent reproducibility and good stability of the Nafion 1:4 photodiode (Figure 5.11a). A similar trend was observed for the device at a repeating frequency of 1000 Hz, as shown in Figure 5.11(b). The rise time and fall times were calculated by the transition time of photocurrent from 10% to 90% (rise time) and decreasing from 90% to 10%, respectively (Z. Gao et al., 2020).

The average rise and fall times of the photodiode with Nafion 1:4 were measured to be $15.7 \pm 0.8 \mu\text{s}$ and $15.6 \pm 0.7 \mu\text{s}$ (Figure 5.11c), which was faster than previously reported self-powered perovskite PD (Beisenbayev et al., 2022; X. Wu et al., 2021; S. Xu et al., 2020). As shown in Table 5.2, the optimized device characteristics based on Nafion 1:4 achieved in this work are equivalent to those of previously published self-powered UV photodiode devices. The efficient charge extraction resulted in a shorter response time showing further enhancement in the performance of perovskite photodiodes (C. Xu et al., 2021).

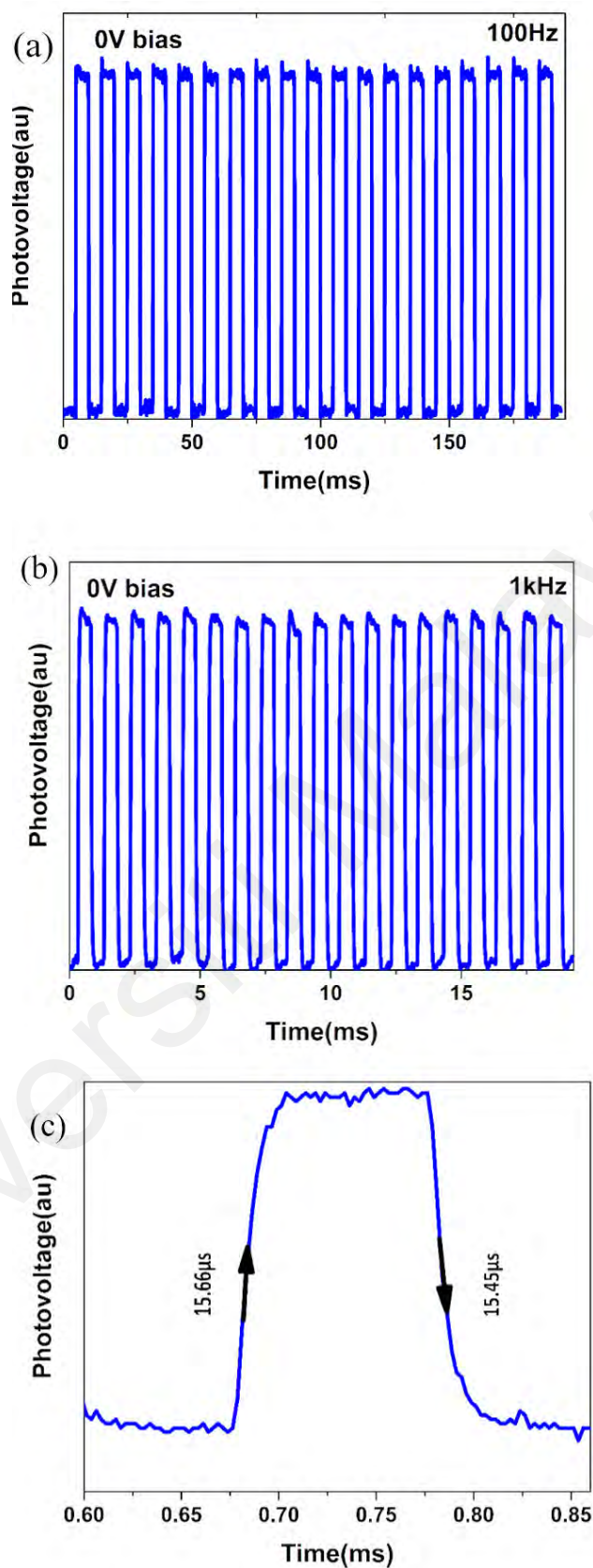


Figure 5.11: (a) On-off cycles of Nafion 1:4 photodiodes under 395 nm LED light (3 mWcm⁻²) at 100 Hz and (b) at 1000 Hz (c) Singular cycle showing the rise and decay time of the resultant perovskite PD.

Table 5.2: Comparison of the characteristic parameters of self-powered photodiodes reported in the literature with that of reported in this work. (Applied voltage = 0 V).

Device structure	Wavelength (nm)	R (mA/W)	D*(Jones)	Response time	Ref
ITO/PEDOT:PSS/Nafion/PEA ₂ PbBr ₄ /PCBM/Al	395	25.8	2.54 x 10¹¹	15.6 μs	This work
LSG/CsPbBr ₃	405		1.6 × 10 ¹¹	18 ms	(Shkir et al., 2019)
ITO/CsPbBr ₃ :ZnO/Ag	405	11.5	-	17.92 ms	(C. Li et al., 2017)
CsPbI ₃ :Ag/PEDOT:PSS	450	1.70	2.54 × 10 ⁹	-	(Weng et al., 2022)
FTO/TiO ₂ /ZrO ₂ /CsPbCl ₃ :Mn	340	7.30	-	20 ms	(S. Xu et al., 2020)
(4-AMP)(MA) ₂ Pb ₃ Br ₁₀ /MAPbBr ₃	405	11.5	10 ¹²	600 μs	(X. Zhang et al., 2020)
FTO/CH ₃ NH ₃ PbBr ₃ /Au	450	11.5	-	2.3 s	(M. Cao et al., 2016)
FTO/PEDOT:PSS:AgNPs/CH ₃ NH ₃ PbI ₃ /Al	400	250	1.53 × 10 ¹¹	110 ms	(Ghosh et al., 2019)

The stability of perovskite PD is crucial for its practical application. The stability of the two encapsulated photodiodes without Nafion and Nafion 1:4 were explored. The light-soaking stability was investigated by continuous UV light exposure to 395-nm LED ambient lighting conditions for 15 hrs. Figure 5.12 shows the time-dependent photoresponse of the Nafion 1:4 and without Nafion before and after continuous exposure. The Nafion 1:4 photodiode in Figure 5.12(b) shows good UV stability. As displayed in Figure 5.12, both I_{light} and I_{dark} show slight changes and exhibited sustaining performance of the device after continuous UV illumination. In contrast, the performance of the photodiode without the Nafion layer dropped > 50%. This could explain that the hygroscopic properties of PEDOT: PSS might cause moisture absorption from the environment, which might cause the perovskite layer to decompose (Feng et al., 2016). It is known that perovskite materials are sensitive to the moisture present in the environment (N. G. Park et al., 2016).

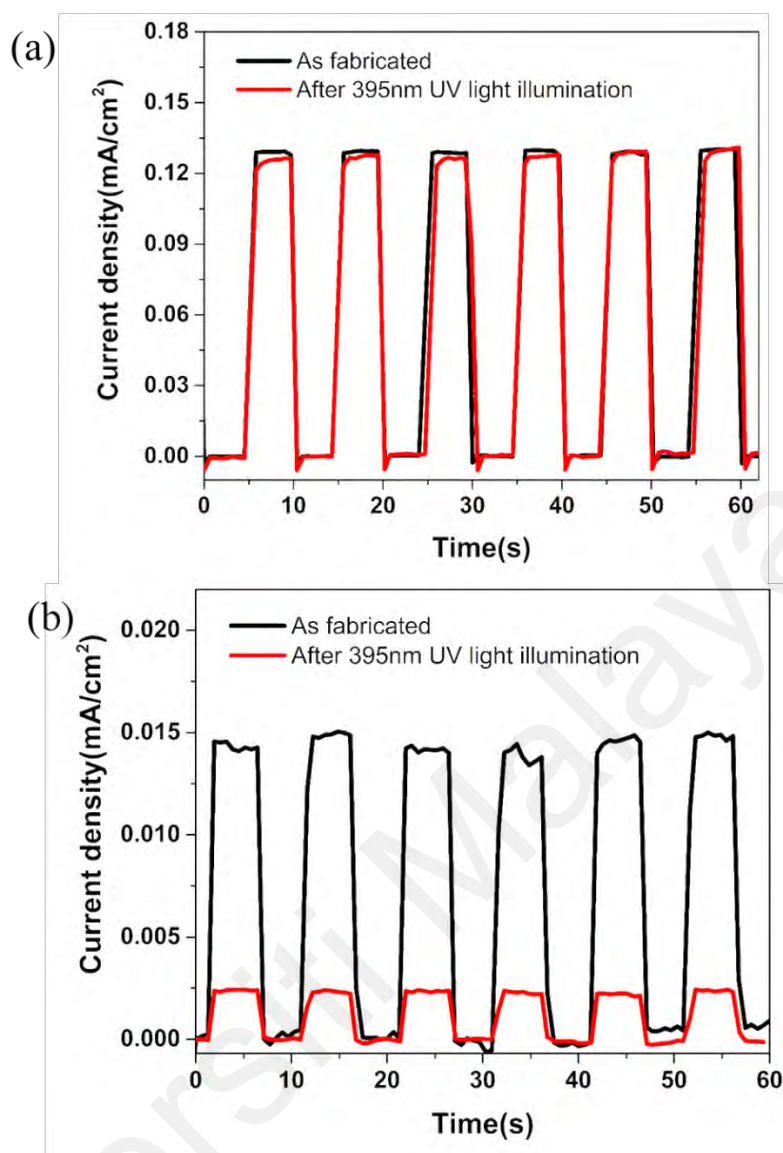


Figure 5.12: Time-dependent photoresponse of Nafion 1:4 photodiode (a) without Nafion photodiode (b) before and after continuous exposure to 395 nm LED light for 15 hrs.

The water contact angle on PEDOT: PSS film was 21.5° (Figure 5.13a) and increased to 43.1° (Figure 5.13b) with the Nafion layer. The hydrophobic Nafion layer insulated PEA₂PbBr₄ from direct contact with the PEDOT: PSS layer and acted as a moisture-proof coating, thus reducing the degradation of the PEA₂PbBr₄ layer and leading to improved Nafion stability photodiode.

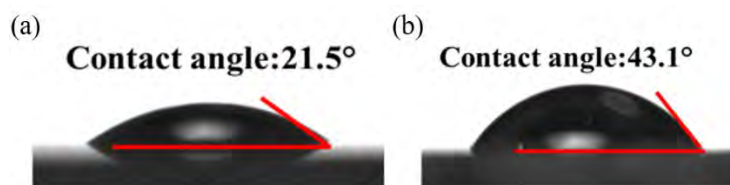


Figure 5.13: (a) Contact angle of water on PEDOT-PSS, Without Nafion, (b) Contact angle of water on PEDOT-PSS, Nafion 1:4.

(a) Electron only devices (EOD) and Hole only devices (HOD)

Electron only devices (EOD) and hole only devices (HOD) have been fabricated in order to study the charge transport characteristics of Nafion. The electron-only devices have structures of ITO/LiF/Nafion/LiF/Al and ITO/LiF/PEDOT: PSS/Nafion/LiF/Al. While hole-only devices have structures of ITO/PEDOT:PSS/Au and ITO/PEDOT:PSS/Nafion/Au. The current density of Nafion-based hole-only devices is significantly greater than that of Nafion-based electron-only devices (Figure 5.14). This suggests that the Nafion layer enhances the transport of holes and doesn't allow the flow of electrons. In addition, the device with the PEDOT: PSS/Nafion had a higher hole current density than the device with the PEDOT: PSS only, indicating that the Nafion layer enhances hole transport in the photodiodes (Figure 5.14b). Therefore, by assuring improved charge selectivity at the ITO, PEDOT: PSS with Nafion layer can function as a better electron blocking layer than PEDOT: PSS without Nafion.

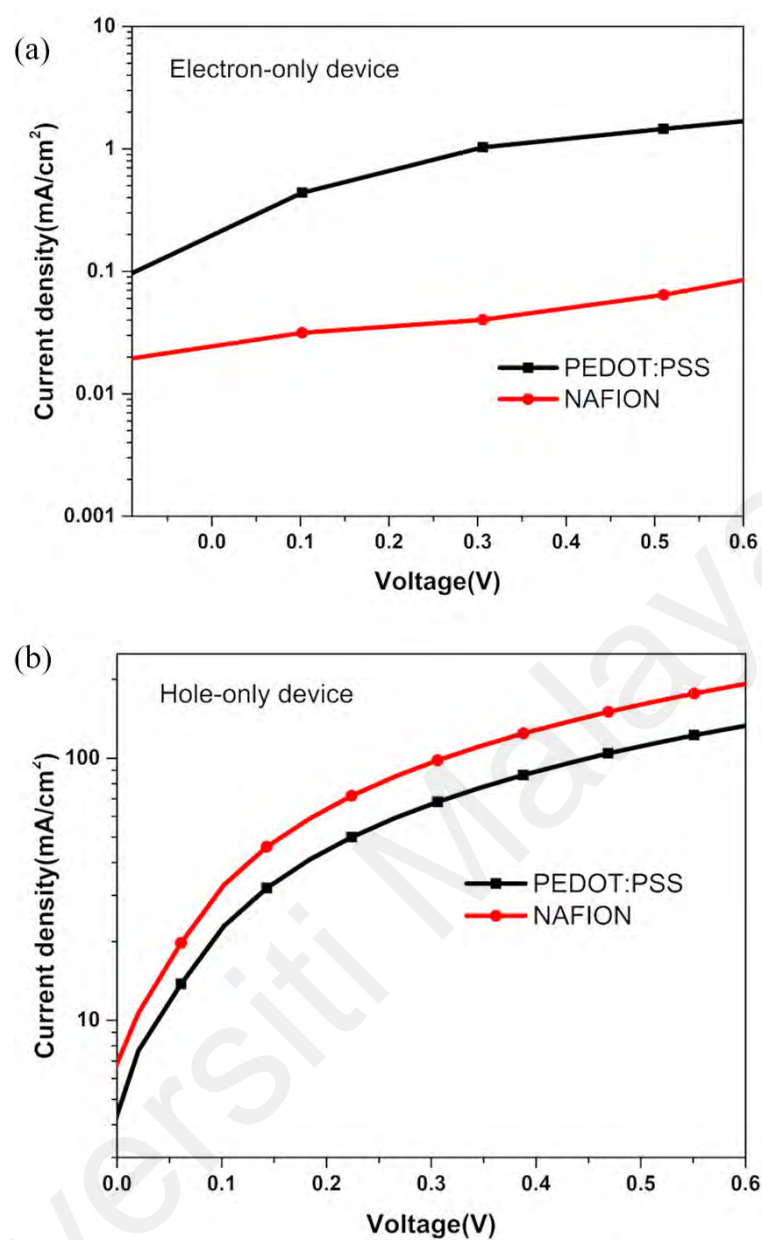


Figure 5.14: (a) Electron-only device (ITO/LiF/PEDOT:PSS or Nafion/LiF/Al) and (b) Hole-only device (ITO/PEDOT:PSS or PEDOT:PSS/Nafion/Au).

5.3.3 Effect of illumination intensity on the performance of optimized self-powered PEA₂PbBr₄ Photodiode

As the Nafion 1:4 photodiodes showed optimized performance, PD with Nafion 1:4 as the HTL focused on the further investigation with different UV light intensities. Figure 5.15 reveals a typical J–V characterization of the Nafion 1:4 device under various illumination intensities of UV light with wavelength $\lambda=395\text{nm}$. Clearly, the photocurrent of the photodiode shows a direct correlation with light intensity. This is because the photodiode absorbs more photons due to the higher photon flow. As a result, more electron-hole pairs are created, and charge carriers are separated at the HTL and ETL interfaces respectively. This causes a greater photocurrent production as the free charge carriers are redirected toward the electrodes. Interestingly a maximum self-powered photocurrent is generated when the bias is at 0 V, which is characterized as the short-circuit current density (J_{sc}). The J_{sc} increases from $0.022\text{mA}/\text{cm}^2$ to $0.42\text{mA}/\text{cm}^2$ as the UV light intensity increases from $0.08\text{mW}/\text{cm}^2$ to $32.5\text{mW}/\text{cm}^2$ at 0V bias. Figure 5.15(b) indicates that the J_{sc} increases linearly with light intensity, and the open-circuit voltage (V_{oc}) increases logarithmically.

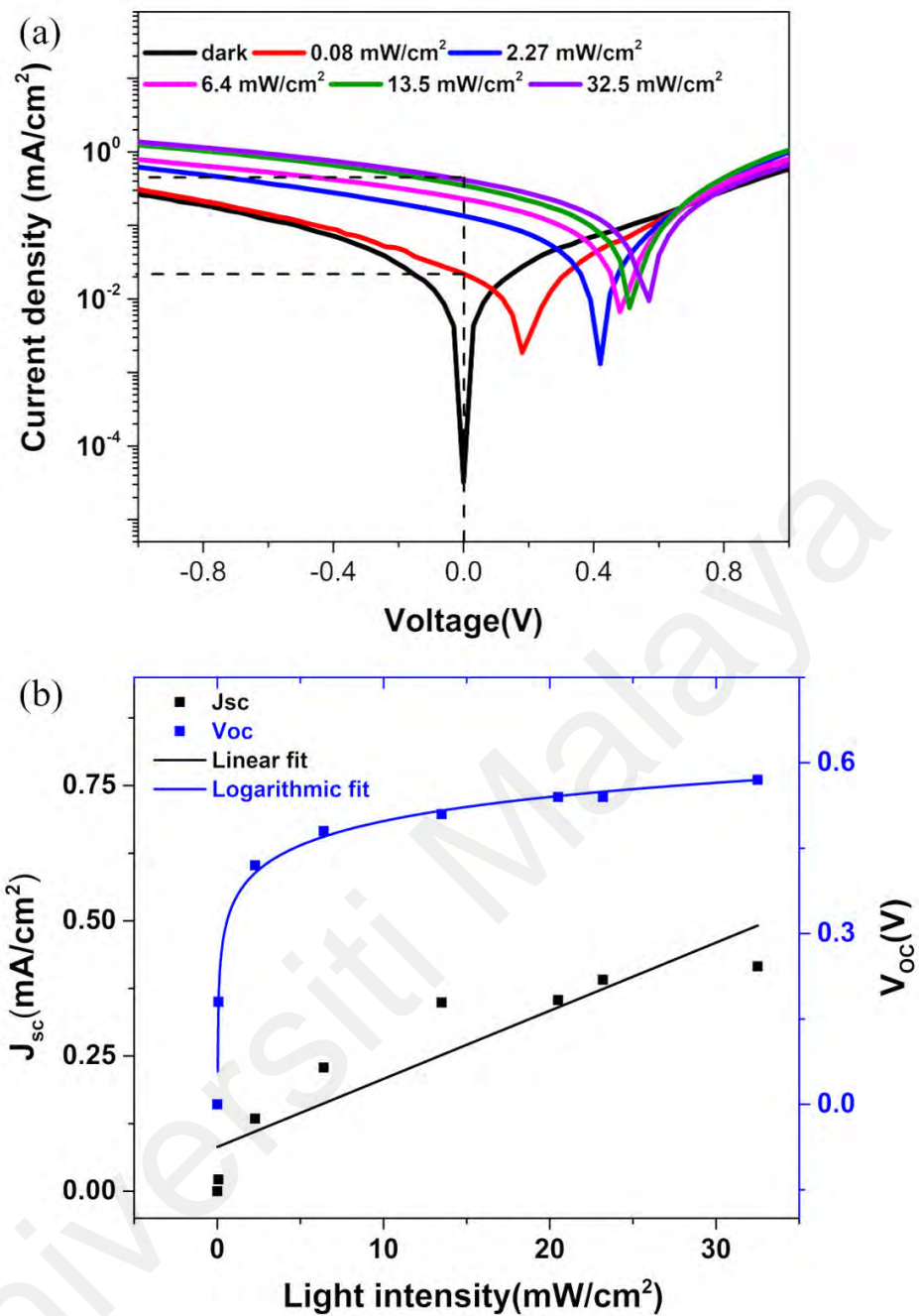


Figure 5.15 : (a) Semi-log J–V curve of photodiode based on Nafion 1:4 HTL under different UV light intensity, (b) The relationship of J_{sc} and V_{oc} parameters of self-powered Nafion 1:4 based photodiode with various UV light intensity.

As illustrated in Figure 5.16, the influence of illumination intensity on the produced photocurrent was examined further at various bias voltages. Figure 5.16(a) depicts a linear dependency of photocurrent on incident power at low illumination intensity (13.5mW/cm^2). However, at a higher light intensity, the photodiode saturates and became independent of light intensity. In the region of saturation, a nonlinear behavior is observed. This behavior may result from the presence of a large number of electron-hole pairs. (Abdel-Khalek et al., 2018). This occurrence might have happened because of the carrier-screening effect and high carrier concentrations that could have reduced the carrier's mean free path. Since the carrier's mean free path is inversely correlated with its concentration, a greater carrier distribution concentration will result in a lower mean free path(Jishi Cui et al., 2018). Due to the uneven distribution of electron-hole pairs, a substantial electric field was generated that resisted the external bias(Giboney et al., 1996). These results show that the constructed photodiode may be employed at small biasing voltages (-0.5 to 0 Volt) and detect low-intensity signals, presenting a new photodiode for optoelectronic applications.

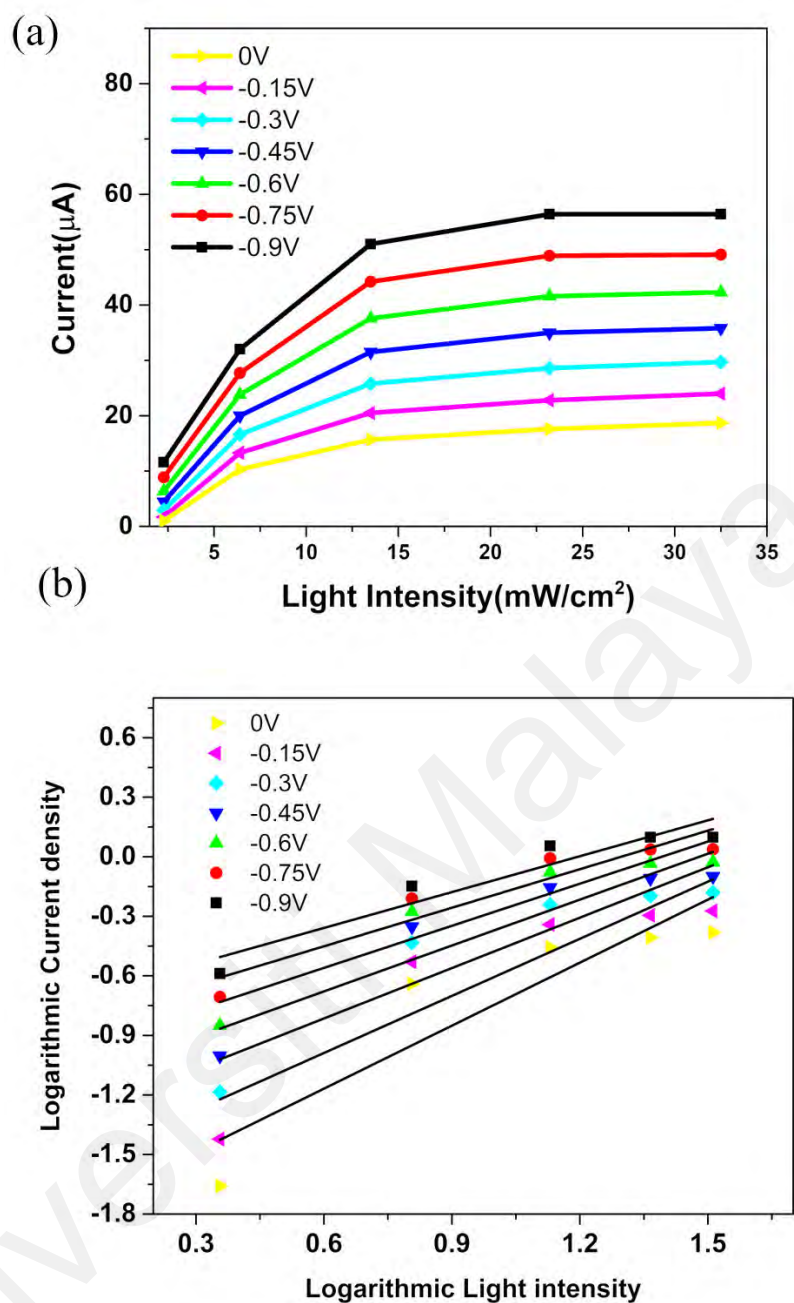


Figure 5.16 : The relation between (a) photocurrent and light intensity and (b) log of photocurrent vs log of light intensity at different reverse biasing voltages of Nafion 1:4 photodiodes.

Photosensitivity is calculated as the ratio of photocurrent to dark current. Figure 5.17(a) depicts the results of a self-powered mode measurement of the photosensitivity of a Nafion 1:4-based photodiode exposed to varying levels of ultraviolet radiation. At light intensity of 32.5 mW/cm^2 , photodiode exhibits maximum sensitivity of 1.2×10^4 at 0V bias. According to Figure 5.17, (b) the linear rise in sensitivity with increasing light intensity was observed at 0 V bias. The high illumination intensities cause the perovskite active layer to experience higher photo absorption.

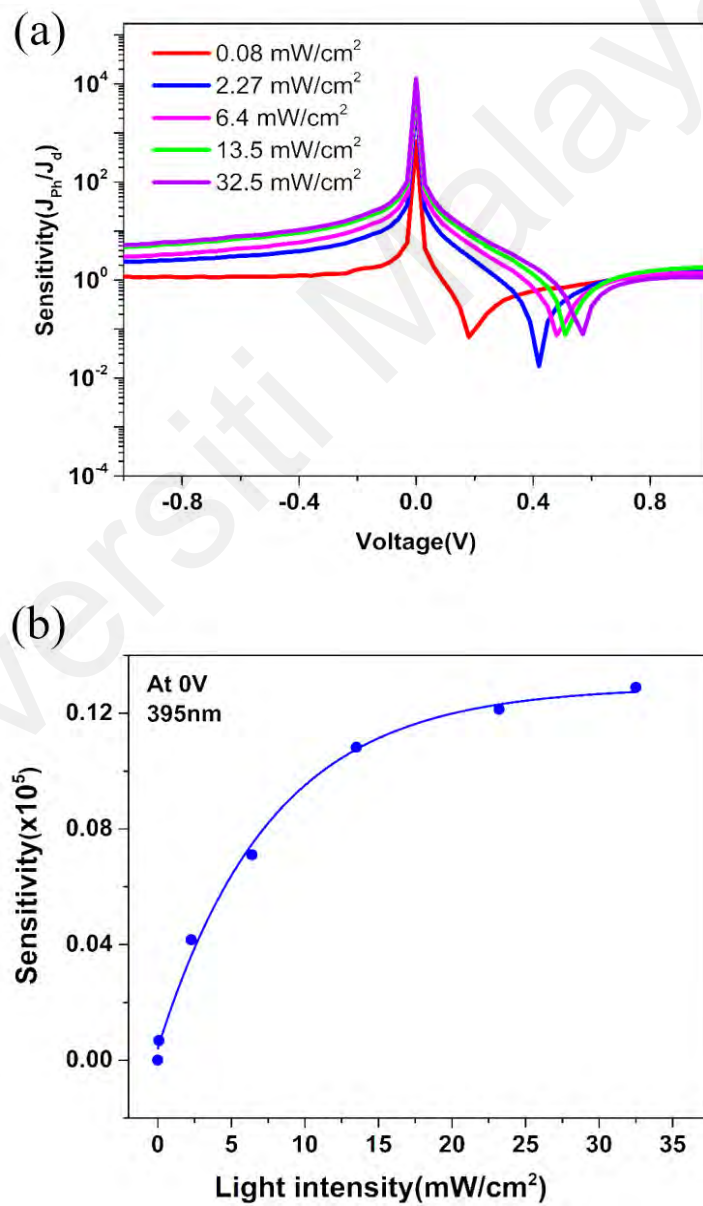


Figure 5.17 : (a) Semi-log photosensitivity of self-powered based Nafion 1:4 under different UV light intensity (b) Sensitivity versus light intensity at 0 V bias.

Figure 5.18 illustrates that photodiode responsivity and detectivity decline exponentially with light intensity. Remarkably, the responsivity, R and detectivity, D were found to be high at low lighting intensities, allowing the self-powered photodiode to detect low-intensity lights efficiently.

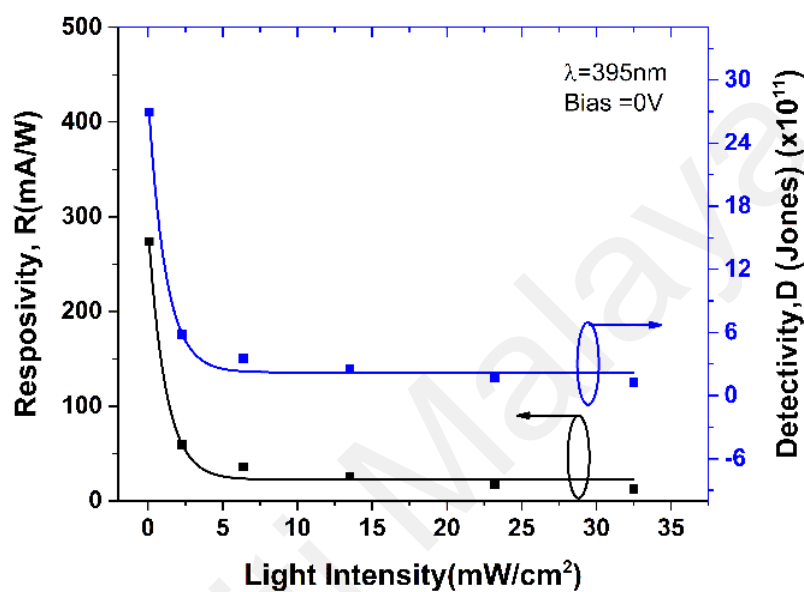


Figure 5.18 : The change of responsivity and detectivity of self- powered Nafion 1:4 based photodiode with illumination intensity.

Figure 5.19 illustrates the ON/OFF switching behaviors of Nafion 1:4 photodiodes under the impact of varying light intensity at 0V bias using the transit current–time method. As the plot maintained an almost constant square form across the allotted period, it was clear that the photodiode responded quite well to UV light.

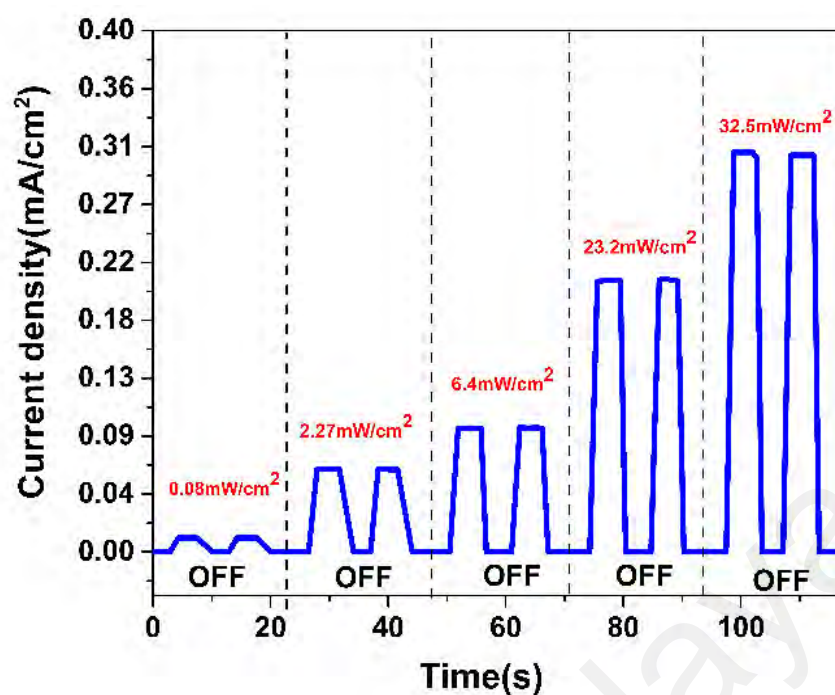


Figure 5.19 : ON/OFF switching behavior of Nafion 1:4 photodiode under the influence of various illumination intensities.

5.4 Conclusion

Coating hydrophobic Nafion onto PEDOT: PSS films acting as an efficient hole transport layer for solution-processed self-powered photodiodes based on 2-dimensional perovskites enhanced the photocurrent to 0.35 mA/cm^2 . This simple solution-processed method exhibited uniform perovskite polycrystalline thin films with high surface coverage, high detectivity, efficient charge mobilities and fast response time. In addition, the photodiode based on the Nafion modification layer has higher stability than the pristine PEDOT: PSS under UV light exposure.

CHAPTER 6: CONCLUSION AND FUTURE WORKS

6.1 Conclusion

Solution-processable low dimensional perovskites-based field-effect transistors and photodiode have been successfully fabricated. A field-effect transistor (FET) was fabricated by employing deep VBM PAPbBr₃ as an active layer. Nafion is employed as a surface modifier to increase the work function of ITO. The charge injection barrier is reduced by spin coating a thin layer of Nafion between the ITO and perovskite active layer. The effective work function of the ITO is modified from 4.40 eV to 4.90 eV. After the Nafion treatment, FET shows p-type transport characteristics.

Further, PVK was chosen as the polymer host due to its good film-forming characteristics, good hole transport capability, and solubility in DMF. Blending PVK with PAPbBr₃ induces preferential vertical orientation of one-dimensional nanopillars and improved single-crystal quality. As a result of higher ordering, these nanopillars formed a larger domain size with the maximum field-effect mobility improved to 0.012 cm²/Vs for a blend ratio of PAPbBr₃: PVK-25%. Moreover, pristine PAPbBr₃ FET devices exhibited a significant hysteresis, ΔV_{th} of 4 V. The observed hysteresis and negative voltage shift in V_{th} may be attributed to the charge carrier trap at the semiconductor/dielectric interface and ion migration. Blending PVK into pristine PAPbBr₃ reduced the hysteresis to 0.95 V (in PAPbBr₃: PVK-25% device), which can be due to the improved crystallinity and reduced structural defect.

In the second section of this thesis, photodiodes based on 2-dimensional PEA₂PbBr₄ perovskite were fabricated. A simple interface engineering technique is adapted by sandwiching a thin layer of Nafion between PEDOT: PSS (HTL) and PEA₂PbBr₄ (active layer).

Different ratios of highly diluted Nafion in ethanol solvent were spin-coated onto PEDOT: PSS layer and systematically investigated how the concentration of Nafion impacted both the performance of the UV photodiode and its resistance to degradation when exposed to UV light. It was found that the optimized Nafion 1:4 dilution ratio concentration in ethanol obtained more homogenous and compact $\text{PEA}_2\text{PbBr}_4$ domains. The optimized Nafion 1:4 based UV photodiode demonstrated evidence of a photovoltaic effect, which indicates that the photodiode is capable of operating as a self-powered device, independent of the need for an additional power source. Through the implementation of this technique, the efficiency of charge extraction was increased, resulting in a photocurrent of 0.34 mA/cm^2 at zero bias.

Additionally, devices using the PEDOT: PSS/Nafion 1:4 demonstrated a notable improvement in the V_{oc} of 0.46 V compared to 0.04 V in the device without Nafion. Photoresponsivity (R) and detectivity (D^*) are two of the essential metrics that are typically considered when evaluating the performance of photodiodes. Under zero bias, the responsivity value was 25.8 mA/W . Due to the reduced dark current and enhanced responsivity, the optimized device's detectivity value was as high as $2.54 \times 10^{11} \text{ Jones}$ at zero bias under illumination (13.5 mW/cm^2). Moreover, the device's photodiode based on Nafion 1:4 displayed a smaller dark current than the one using PEDOT: PSS only when operating at zero volts. Coating hydrophobic Nafion onto PEDOT: PSS films acts as an efficient hole transport layer and has higher stability than the pristine PEDOT: PSS under UV light exposure. The improved quality HTL/ $\text{PEA}_2\text{PbBr}_4$ interface also contributed to the performance of Nafion 1:4, resulting in a fast response time of $15.7 \mu\text{s}$. These results may open up new opportunities for developing self-powered UV sensing systems in health and safety applications.

6.2 Future Works

Low-dimensional perovskites have promising properties and are suitable for use as active layers in the manufacture of optoelectronic devices. However, there are still some research gaps that can be addressed in the future, and the following strategies were not feasible within the parameters of this study's time range.

- 1) Examining the effects of environmental factors like humidity on a FET's performance can be used to test a device's stability and reliability. Experiments like this would bring perovskite devices one step closer to practical use in the real world.
- 2) It is suggested that more characterization techniques be performed, such as GIXRD measurement, to investigate the mechanism behind how spin-coated perovskite orients itself on top of a layer of hydrophobic Nafion. This will give further insight into the correlation between microstructure and charge transport in solution-processed UV photodiodes.
- 3) Using an ultra-thin layer of conjugated polymer with deep HOMO as an interfacial layer between PCBM and the Al electrode may further minimize the dark current in perovskites photodiodes. For example, conjugated polymers such as 2,9-dimethyl-4,7-diphenyl-1,10-phenanthroline (BCP) can create a significant hole injection barrier between the Al electrodes and PCBM because of deep HOMO level [BCP (7eV)], which may inhibit hole injection but promote electron injection, resulting in a significant reduction in interface leakage current.

REFERENCES

- Abdel-Khalek, H., Shalaan, E., Abd-El Salam, M., & El-Mahalawy, A. M. (2018). Effect of illumination intensity on the characteristics of Cu(acac)₂/n-Si photodiode. *Synthetic Metals*, 245(May), 223–236.
- Afzal, A. M., Bae, I. G., Aggarwal, Y., Park, J., Jeong, H. R., Choi, E. H., & Park, B. (2021). Highly efficient self-powered perovskite photodiode with an electron-blocking hole-transport NiO_x layer. *Scientific Reports*, 11(1), 1–14.
- Agranovich, V. M., Gartstein, Y. N., & Litinskaya, M. (2011). Hybrid resonant organic-inorganic nanostructures for optoelectronic applications. *Chemical Reviews*, 111(9), 5179–5214.
- Ahmad, S., Kanaujia, P. K., Beeson, H. J., Abate, A., Deschler, F., Credgington, D., Steiner, U., Prakash, G. V., & Baumberg, J. J. (2015). Strong Photocurrent from Two-Dimensional Excitons in Solution-Processed Stacked Perovskite Semiconductor Sheets. *ACS Applied Materials and Interfaces*, 7(45), 25227–25236.
- Ali Khawaja, K., Khan, Y., Park, Y. J., Lee, J. H., Kang, J. H., Kim, K., Yi, Y., Seo, J. H., & Walker, B. (2021). Lithium Polystyrene Sulfonate as a Hole Transport Material in Inverted Perovskite Solar Cells. *Chemistry - An Asian Journal*, 16(20), 3151–3161.
- Ansari, M. I. H., Qurashi, A., & Nazeeruddin, M. K. (2018). Frontiers, opportunities, and challenges in perovskite solar cells: A critical review. *Journal of Photochemistry and Photobiology C: Photochemistry Reviews*, 35, 1–24.
- Antonietta Loi, M., & Hummelen, J. C. (2013). Hybrid solar cells: Perovskites under the Sun. In *Nature Materials* (Vol. 12, Issue 12, pp. 1087–1089).
- Aragaw, B. A., Su, W. N., Rick, J., & Hwang, B. J. (2013). Highly efficient synthesis of reduced graphene oxide-Nafion nanocomposites with strong coupling for enhanced proton and electron conduction. *RSC Advances*, 3(45), 23212–23221.
- Báez-Lópe, D., & Guerrero-Castro, F. E. (2011). Semiconductor Devices. In *Circuit Analysis with Multisim*.
- Bald, T., Quast, T., Landsberg, J., Rogava, M., Glodde, N., Lopez-Ramos, D., Kohlmeyer, J., Riesenberger, S., Van Den Boorn-Konijnenberg, D., Hömig-Hölzel, C., Reuten, R., Schadow, B., Weighardt, H., Wenzel, D., Helfrich, I., Schadendorf, D., Bloch, W., Bianchi, M. E., Lugassy, C., ... Tüting, T. (2014). Ultraviolet-radiation-induced inflammation promotes angiogenesis and metastasis in melanoma. *Nature*, 507(7490), 109–113.
- Bandakkanavar, R. (2017). *Wearable Biosensors and recent advancements - Krazytech*. <https://krazytech.com/technical-papers/wearable-biosensors>
- Bardeen, J., & Brattain, W. H. (1949). Physical Principles Involved in Transistor Action. *Bell System Technical Journal*, 28(2), 239–277.

- Basham, M., Filik, J., Wharmby, M. T., Chang, P. C. Y., El Kassaby, B., Gerring, M., Aishima, J., Levik, K., Pulford, B. C. A., Sikharulidze, I., Sneddon, D., Webber, M., Dhesi, S. S., Maccherozzi, F., Svensson, O., Brockhauser, S., Náray, G., & Ashton, A. W. (2015). Data Analysis Workbench (DAWN). *Journal of Synchrotron Radiation*, 22(May), 853–858.
- Baumbauer, C. L., Anderson, M. G., Ting, J., Sreekumar, A., Rabaey, J. M., Arias, A. C., & Thielens, A. (2020). Printed, flexible, compact UHF-RFID sensor tags enabled by hybrid electronics. *Scientific Reports*, 10(1), 1–12.
- Beisenbayev, A. R., Sadirkhanov, Z. T., Yerlanuly, Y., Kaikanov, M. I., & Jumabekov, A. N. (2022). Self-Powered Organometal Halide Perovskite Photodetector with Embedded Silver Nanowires. *Nanomaterials*, 12(7), 1034.
- Bi, C., Wang, Q., Shao, Y., Yuan, Y., Xiao, Z., & Huang, J. (2015). Non-wetting surface-driven high-aspect-ratio crystalline grain growth for efficient hybrid perovskite solar cells. *Nature Communications*, 6, 1–7.
- Billing, D. G., & Lemmerer, A. (2007). Inorganic-organic hybrid materials incorporating primary cyclic ammonium cations: The lead iodide series. *CrystEngComm*, 9(3), 236–244.
- Billing, D. G., & Lemmerer, A. (2009). Inorganic-organic hybrid materials incorporating primary cyclic ammonium cations: The lead bromide and chloride series. *CrystEngComm*, 11(8), 1549–1562.
- Blom, P. W. M. (2020). Polymer Electronics: To Be or Not to Be? *Advanced Materials Technologies*, 5. <https://api.semanticscholar.org/CorpusID:219416011>
- Boix, P. P., Agarwala, S., Koh, T. M., Mathews, N., & Mhaisalkar, S. G. (2015). Perovskite solar cells: Beyond methylammonium lead iodide. In *Journal of Physical Chemistry Letters* (Vol. 6, Issue 5, pp. 898–907). American Chemical Society.
- Borriello, I., Cantele, G., & Ninno, D. (2008). Ab initio investigation of hybrid organic-inorganic perovskites based on tin halides. *Physical Review B - Condensed Matter and Materials Physics*, 77(23), 235214.
- Bouilly-Gauthier, D., Jeannes, C., Maubert, Y., Duteil, L., Queille-Roussel, C., Piccardi, N., Montastier, C., Manissier, P., Piérard, G., & Ortonne, J. P. (2010). Clinical evidence of benefits of a dietary supplement containing probiotic and carotenoids on ultraviolet-induced skin damage. *British Journal of Dermatology*, 163(3), 536–543.
- Braga, J. P., Lima, G. R. De, Gozzi, G., & Santos, L. F. (2018). Electrical Characterization of Thin-Film Transistors Based on Solution-Processed Metal Oxides. *Design, Simulation and Construction of Field Effect Transistors*.
- Bragg, W. H. (1913). The Reflection of X-Rays by Crystals. *Nature*, 91(2280), 477.
- Bretos, I., Jiménez, R., Ricote, J., & Calzada, M. L. (2018). Low-temperature crystallization of solution-derived metal oxide thin films assisted by chemical processes. In *Chemical Society Reviews* (Vol. 47, Issue 2, pp. 291–308).

- Brown, M. A. C. S., & Jakeman, E. (1966). Theory of the four-point probe technique as applied to the measurement of the conductivity of thin layers on conducting substrates. *British Journal of Applied Physics*, 17(9), 1143.
- Burschka, J., Pellet, N., Moon, S. J., Humphry-Baker, R., Gao, P., Nazeeruddin, M. K., & Grätzel, M. (2013). Sequential deposition as a route to high-performance perovskite-sensitized solar cells. *Nature* 2013 499:7458, 499(7458), 316–319.
- Cao, D. H., Stoumpos, C. C., Farha, O. K., Hupp, J. T., & Kanatzidis, M. G. (2015). 2D Homologous Perovskites as Light-Absorbing Materials for Solar Cell Applications. *Journal of the American Chemical Society*, 137(24), 7843–7850.
- Cao, M., Tian, J., Cai, Z., Peng, L., Yang, L., & Wei, D. (2016). Perovskite heterojunction based on CH₃NH₃PbBr₃ single crystal for high-sensitive self-powered photodetector. *Applied Physics Letters*, 109(23), 3–7.
- Cao, Q., Yang, S., Gao, Q., Lei, L., Yu, Y., Shao, J., & Liu, Y. (2016). Fast and Controllable Crystallization of Perovskite Films by Microwave Irradiation Process. *ACS Applied Materials and Interfaces*, 8(12), 7854–7861.
- Cardoso, L. S., Stefanelo, J. C., & Faria, R. M. (2016). Induced characteristics of n- and p-channel OFETs by the choice of solvent for the dielectric layer towards the fabrication of an organic complementary circuit. *Synthetic Metals*, 220, 286–291.
- Chaudhary, V., Pandey, R. K., Prakash, R., Kumar, N., & Singh, A. K. (2019). Highly aligned and crystalline poly(3-hexylthiophene) thin films by off-center spin coating for high performance organic field-effect transistors. *Synthetic Metals*, 258(August), 116221.
- Chen, J., & Park, N. G. (2019). Causes and Solutions of Recombination in Perovskite Solar Cells. *Advanced Materials*, 31(47), 1803019.
- Chen, P., Bai, Y., Lyu, M., Yun, J. H., Hao, M., & Wang, L. (2018). Progress and Perspective in Low-Dimensional Metal Halide Perovskites for Optoelectronic Applications. *Solar RRL*, 2(3).
- Chen, S., Song, L., Tao, Z., Shao, X., Huang, Y., Cui, Q., & Guo, X. (2014). Neutral-pH PEDOT:PSS as over-coating layer for stable silver nanowire flexible transparent conductive films. *Organic Electronics*, 15(12), 3654–3659.
- Chen, W. H., Qiu, L., Zhang, P., Jiang, P. C., Du, P., Song, L., Xiong, J., & Ko, F. (2019). Simple fabrication of a highly conductive and passivated PEDOT:PSS film via cryo-controlled quasi-congealing spin-coating for flexible perovskite solar cells. *Journal of Materials Chemistry C*, 7(33), 10247–10256.
- Chen, Y., Sun, Y., Peng, J., Zhang, W., Su, X., Zheng, K., Pullerits, T., & Liang, Z. (2017). Tailoring Organic Cation of 2D Air-Stable Organometal Halide Perovskites for Highly Efficient Planar Solar Cells. *Advanced Energy Materials*, 7(18), 1700162.
- Cho, H., Kim, J. S., Wolf, C., Kim, Y. H., Yun, H. J., Jeong, S. H., Sadhanala, A., Venugopalan, V., Choi, J. W., Lee, C. L., Friend, R. H., & Lee, T. W. (2018). High-Efficiency Polycrystalline Perovskite Light-Emitting Diodes Based on Mixed

Cations. *ACS Nano*, 12(3), 2883–2892.

- Choi, S., Fuentes-Hernandez, C., Wang, C. Y., Khan, T. M., Larrain, F. A., Zhang, Y., Barlow, S., Marder, S. R., & Kippelen, B. (2016). A Study on Reducing Contact Resistance in Solution-Processed Organic Field-Effect Transistors. *ACS Applied Materials and Interfaces*, 8(37), 24744–24752.
- Christians, J. A., Fung, R. C. M., & Kamat, P. V. (2014). An inorganic hole conductor for Organo-lead halide perovskite solar cells. improved hole conductivity with copper iodide. *Journal of the American Chemical Society*, 136(2), 758–764.
- Christians, J. A., Miranda Herrera, P. A., & Kamat, P. V. (2015). Transformation of the excited state and photovoltaic efficiency of CH₃NH₃PbI₃ perovskite upon controlled exposure to humidified air. *Journal of the American Chemical Society*, 137(4), 1530–1538.
- Cohen, B. El, Wierzbowska, M., & Etgar, L. (2017). High Efficiency and High Open Circuit Voltage in Quasi 2D Perovskite Based Solar Cells. *Advanced Functional Materials*, 27(5), 1604733.
- Da Silva Ozório, M., Nogueira, G. L., Morais, R. M., Da Silva Martin, C., Constantino, C. J. L., & Alves, N. (2016). Poly(3-hexylthiophene): TIPS-pentacene blends aiming transistor applications. *Thin Solid Films*, 608, 97–101.
- Das, D., Gopikrishna, P., Barman, D., Yathirajula, R. B., & Iyer, P. K. (2019). White light emitting diode based on purely organic fluorescent to modern thermally activated delayed fluorescence (TADF) and perovskite materials. *Nano Convergence*, 6(1), 31.
- Davidovich, R. L., Stavila, V., Marinin, D. V., Voit, E. I., & Whitmire, K. H. (2009). Stereochemistry of lead(II) complexes with oxygen donor ligands. *Coordination Chemistry Reviews*, 253(9), 1316–1352.
- De Jong, M. P., Van Ijzendoorn, L. J., & De Voigt, M. J. A. (2000). Stability of the interface between indium-tin-oxide and poly(3,4-ethylenedioxythiophene)/poly(styrenesulfonate) in polymer light-emitting diodes. *Applied Physics Letters*, 77(14), 2255–2257.
- Dequilettes, D. W., Frohna, K., Emin, D., Kirchartz, T., Bulovic, V., Ginger, D. S., & Stranks, S. D. (2019). Charge-Carrier Recombination in Halide Perovskites. *Chemical Reviews*, 119(20), 11007–11019.
- Di, H., Jiang, W., Sun, H., Zhao, C., Liao, F., & Zhao, Y. (2020). Effects of ITO substrate hydrophobicity on crystallization and properties of MAPbBr₃ single-crystal thin films. *ACS Omega*, 5(36), 23111–23117.
- Dinelli, F., Murgia, M., Levy, P., Cavallini, M., Biscarini, F., & De Leeuw, D. M. (2004). Spatially correlated charge transport in organic thin film transistors. *Physical Review Letters*, 92(11).
- Ding, B., Gao, L., Liang, L., Chu, Q., Song, X., Li, Y., Yang, G., Fan, B., Wang, M., Li, C., & Li, C. (2016). Facile and Scalable Fabrication of Highly Efficient Lead Iodide

- Perovskite Thin-Film Solar Cells in Air Using Gas Pump Method. *ACS Applied Materials and Interfaces*, 8(31), 20067–20073.
- Dodabalapur, A., Torsi, L., & Katz, H. E. (1995). Organic Transistors: Two-Dimensional Transport and Improved Electrical Characteristics. *Science*, 268(5208), 270–271.
- Dong, Q., Fang, Y., Shao, Y., Mulligan, P., Qiu, J., Cao, L., & Huang, J. (2015). Electron-hole diffusion lengths > 175 μm in solution-grown $\text{CH}_3\text{NH}_3\text{PbI}_3$ single crystals. *Science*, 347(6225), 967–970.
- Du, F. P., Cao, N. N., Zhang, Y. F., Fu, P., Wu, Y. G., Lin, Z. D., Shi, R., Amini, A., & Cheng, C. (2018). PEDOT:PSS/graphene quantum dots films with enhanced thermoelectric properties via strong interfacial interaction and phase separation. *Scientific Reports*, 8(1), 1–12.
- Duan, C., Liu, Z., Yuan, L., Zhu, H., Luo, H., & Yan, K. (2020). PEDOT:PSS-Metal Oxide Composite Electrode with Regulated Wettability and Work Function for High-Performance Inverted Perovskite Solar Cells. *Advanced Optical Materials*, 8(17), 1–11.
- Egginger, M., Bauer, S., Schwödiauer, R., Neugebauer, H., & Sariciftci, N. S. (2009). Current versus gate voltage hysteresis in organic field effect transistors. *Monatshefte Fur Chemie*, 140(7), 735–750.
- El Gemayel, M., Börjesson, K., Herder, M., Duong, D. T., Hutchison, J. A., Ruzié, C., Schweicher, G., Salleo, A., Geerts, Y., Hecht, S., Orgiu, E., & Samori, P. (2015). Optically switchable transistors by simple incorporation of photochromic systems into small-molecule semiconducting matrices. *Nature Communications* 2015 6:1, 6(1), 1–8.
- Elbohy, H., Bahrami, B., Mabrouk, S., Reza, K. M., Gurung, A., Pathak, R., Liang, M., Qiao, Q., & Zhu, K. (2019). Tuning Hole Transport Layer Using Urea for High-Performance Perovskite Solar Cells. *Advanced Functional Materials*, 29(47), 1–9.
- Engmann, S., Barito, A. J., Bittle, E. G., Giebink, N. C., Richter, L. J., & Gundlach, D. J. (2019). Higher order effects in organic LEDs with sub-bandgap turn-on. *Nature Communications*, 10(1).
- Era, M., & Yamada, T. (2001). PbBr-based layered perovskite organic-inorganic superlattice with photochromic chromophore-linked ammonium molecules as an organic layer. *Molecular Crystals and Liquid Crystals Science and Technology Section A: Molecular Crystals and Liquid Crystals*, 371, 183–186.
- Euaruksakul, C., Jearanaikoon, N., Bussayaporn, W., Kamonsutthipaijit, N., Photongkam, P., Tunmee, S., & Songsiriritthigul, P. (2013). Photoemission electron microscopy beamline at the Synchrotron Light Research Institute. *Journal of Physics: Conference Series*, 425(PART 18).
- Fabian, D. M., & Ardo, S. (2016). Hybrid organic–inorganic solar cells based on bismuth iodide and 1{,}6-hexanediammonium dication. *J. Mater. Chem. A*, 4(18), 6837–6841.

- Feng, S., Yang, Y., Li, M., Wang, J., Cheng, Z., Li, J., Ji, G., Yin, G., Song, F., Wang, Z., Li, J., & Gao, X. (2016). High-Performance Perovskite Solar Cells Engineered by an Ammonia Modified Graphene Oxide Interfacial Layer. *ACS Applied Materials and Interfaces*, 8(23), 14503–14512.
- Forrest, S. R. (2020). Introduction to organic electronics. In *Organic Electronics* (pp. 3–30). Oxford University Press.
- Frohna, K., & Stranks, S. D. (2019). 7 - Hybrid perovskites for device applications. In O. Ostroverkhova (Ed.), *Handbook of Organic Materials for Electronic and Photonic Devices (Second Edition)* (Second Edi, pp. 211–256). Woodhead Publishing.
- Frost, J. M., Butler, K. T., Brivio, F., Hendon, C. H., Van Schilfgaarde, M., & Walsh, A. (2014). Atomistic origins of high-performance in hybrid halide perovskite solar cells. *Nano Letters*, 14(5), 2584–2590.
- Gao, L. L., Liang, L. S., Song, X. X., Ding, B., Yang, G. J., Fan, B., Li, C. X., & Li, C. J. (2016). Preparation of flexible perovskite solar cells by a gas pump drying method on a plastic substrate. *Journal of Materials Chemistry A*, 4(10), 3704–3710.
- Gao, L., & Yang, G. (2020). Organic-Inorganic Halide Perovskites: From Crystallization of Polycrystalline Films to Solar Cell Applications. *Solar RRL*, 4(2).
- Gao, P., Grätzel, M., & Nazeeruddin, M. K. (2014). Organohalide lead perovskites for photovoltaic applications. *Energy and Environmental Science*, 7(8), 2448–2463.
- Gao, Y., Wei, Z., Yoo, P., Shi, E., Zeller, M., Zhu, C., Liao, P., & Dou, L. (2019). Highly Stable Lead-Free Perovskite Field-Effect Transistors Incorporating Linear Π -Conjugated Organic Ligands. *Journal of the American Chemical Society*, 141(39), 15577–15585.
- Gao, Z., Zheng, Y., Huang, G., Yang, G., Yu, X., & Yu, J. (2020). Additive modulated perovskite microstructures for high performance photodetectors. *Micromachines*, 11(12), 1–12.
- Gawlinska, K., Iwan, A., Starowicz, Z., Kulesza-Matlak, G., Stan-Glowinska, K., Janusz, M., Lipinski, M., Boharewicz, B., Tazbir, I., & Sikora, A. (2017). Searching of new, cheap, air- and thermally stable hole transporting materials for perovskite solar cells. *Opto-Electronics Review*, 25(4), 274–284.
- Gedamu, D., Asuo, I. M., Benetti, D., Basti, M., Ka, I., Cloutier, S. G., Rosei, F., & Nechache, R. (2018). Solvent-Antisolvent Ambient Processed Large Grain Size Perovskite Thin Films for High-Performance Solar Cells. *Scientific Reports* 2018 8:1, 8(1), 1–11.
- Ghosh, J., Natu, G., & Giri, P. K. (2019). Plasmonic hole-transport-layer enabled self-powered hybrid perovskite photodetector using a modified perovskite deposition method in ambient air. *Organic Electronics*, 71(March), 175–184.
- Giannaccini, M. E., Georgilas, I., Horsfield, I., Peiris, B. H. P. M., Lenz, A., Pipe, A. G., Dogramadzi, S., Kim, B. S., Song, J. B., Al, P. L. et, Ham, K. B., Han, J., Park, Y. J., Li, X., Chen, W., Lin, W., Low, K. H., Brown, J., Bruni, S., ... Woodward, B.

- (2018). The roles of acetylacetone additives in enhancing perovskite solar cell performance. *Materials Research Express*, 36(3), 4620–4625.
- Giboney, K. S., Rodwell, M. J. W., & Bowers, J. E. (1996). Traveling-wave photodetector design and measurements. *IEEE Journal on Selected Topics in Quantum Electronics*, 2(3), 622–629.
- Giuliano, G., Bonasera, A., Scopelliti, M., Chillura Martino, D., Fiore, T., & Pignataro, B. (2021). Boosting the Performance of One-Step Solution-Processed Perovskite Solar Cells Using a Natural Monoterpene Alcohol as a Green Solvent Additive. *ACS Applied Electronic Materials*, 3(4), 1813–1825.
- Gong, X., Tong, M., Xia, Y., Cai, W., Moon, J. S., Cao, Y., Yu, G., Shieh, C. L., Nilsson, B., & Heeger, A. J. (2009). High-detectivity polymer photodetectors with spectral response from 300 nm to 1450 nm. *Science*, 325(5948), 1665–1667.
- Groenendaal, B., Jonas, F., Freitag, D., Pielartzik, H., & Reynolds, J. (2000). Poly(3,4-ethylenedioxythiophene) and Its Derivatives: Past, Present, and Future. *Advanced Materials*, 12(7), 481–494. [https://doi.org/10.1002/\(SICI\)1521-4095\(200004\)12:7%3C481::AID-ADMA481%3E3.0.CO;2-C](https://doi.org/10.1002/(SICI)1521-4095(200004)12:7%3C481::AID-ADMA481%3E3.0.CO;2-C)
- Guo, B., Luo, C., Yan, C., Sun, B., Li, W., & Yang, W. (2020). Understanding Excitonic Behavior in Light Absorption and Recombination Process. *Journal of Physical Chemistry C*, 124(47), 26076–26082.
- Guo, T., Tian, C., Zhao, S., Chu, Z., Ma, J., Li, Y., Shi, Z., & Ran, G. (2021). Gravity-Guided Growth of Large-Area High-Quality Two-Dimensional Ruddlesden-Popper Perovskite Thin Films for Stable Ultraviolet Photodetectors. *Journal of Physical Chemistry C*, 125(25), 13909–13916.
- Harwell, J. R. (2018). *Optoelectronic Applications of Lead Halide Perovskites*.
- He, K., Yang, X., Yan, H., Wu, Z., Li, Z., Zhong, S., Ou, Q., & Liang, R. (2014). Work function changes of plasma treated indium tin oxide. *Organic Electronics*, 15(8), 1731–1737.
- Heitner-Wirguin, C. (1996). Recent advances in perfluorinated ionomer membranes: structure, properties and applications. *Journal of Membrane Science*, 2016-Augus, 1–33.
- Hori, T. (1997). *MIS Structure* (pp. 23–74). Springer, Berlin, Heidelberg.
- Horowitz, G. (1998). Organic Field-Effect Transistors. *Advanced Materials*, 10(5). https://www.researchgate.net/publication/273256487_Organic_Field-Effect_Transistors
- Horowitz, G., Hajlaoui, R., Bourguiga, R., & Hajlaoui, M. (1999). Theory of the organic field-effect transistor. *Synthetic Metals*, 101(1–3), 401–404.
- Hossain, J., Liu, Q., Miura, T., Kasahara, K., Harada, D., Ishikawa, R., Ueno, K., & Shirai, H. (2016). Nafion-modified PEDOT:PSS as a transparent hole-transporting layer for high-performance crystalline-Si/organic heterojunction solar cells with

- improved light soaking stability. *ACS Applied Materials and Interfaces*, 8(46), 31926–31934.
- Hu, L., Sun, K., Wang, M., Chen, W., Yang, B., Fu, J., Xiong, Z., Li, X., Tang, X., Zang, Z., Zhang, S., Sun, L., & Li, M. (2017). Inverted Planar Perovskite Solar Cells with a High Fill Factor and Negligible Hysteresis by the Dual Effect of NaCl-Doped PEDOT:PSS. *ACS Applied Materials and Interfaces*, 9(50), 43902–43909.
- Hua, J., Li, Z., Lam, J. W. Y., Xu, H., Sun, J., Dong, Y., Dong, Y., Qin, A., Yuan, W., Chen, H., Wang, M., & Tang, B. Z. (2005). Induced chain alignment, efficient energy transfer, and enhanced light emission in functional poly acetylene-perovskite hybrids. In *Macromolecules* (Vol. 38, Issue 20, pp. 8127–8130). American Chemical Society.
- Huang, J., Tan, S., Lund, P. D., & Zhou, H. (2017). Impact of H₂O on organic–inorganic hybrid perovskite solar cells. *Energy & Environmental Science*, 10(11), 2284–2311.
- Im, J. H., Chung, J., Kim, S. J., & Park, N. G. (2012). Synthesis, structure, and photovoltaic property of a nanocrystalline 2H perovskite-type novel sensitizer (CH₃CH₂NH₃)PbI₃. *Nanoscale Research Letters*, 7(1), 1–7.
- Jansen-van Vuuren, R. D., Armin, A., Pandey, A. K., Burn, P. L., & Meredith, P. (2016). Organic Photodiodes: The Future of Full Color Detection and Image Sensing. *Advanced Materials*, 28(24), 4766–4802.
- Jeong, B., Gkoupidenis, P., Asadi, K., Jeong, B., Gkoupidenis, P., & Asadi, K. (2021). Solution-Processed Perovskite Field-Effect Transistor Artificial Synapses. *Advanced Materials*, 33(52), 2104034.
- Jeong, J., Lee, J., Lee, H., Hyun, G., Park, S., Yi, Y., Cho, S. W., & Lee, H. (2018). Energy level alignment and hole injection property of poly(9-vinylcarbazole)/indium tin oxide interface. *Chemical Physics Letters*, 706, 317–322.
- Jiang, L. L., Wang, Z. K., Li, M., Zhang, C. C., Ye, Q. Q., Hu, K. H., Lu, D. Z., Fang, P. F., & Liao, L. S. (2018). Passivated Perovskite Crystallization via g-C₃N₄ for High-Performance Solar Cells. *Advanced Functional Materials*, 28(7), 1–8.
- Jishi Cui, J. C., Bowen Bai, B. B., Fenghe Yang, F. Y., & Zhiping Zhou, Z. Z. (2018). Optical saturation characteristics of dual- and single-injection Ge-on-Si photodetectors. *Chinese Optics Letters*, 16(7), 072502.
- Jørgensen, M., Norrman, K., & Krebs, F. C. (2008). Stability/degradation of polymer solar cells. *Solar Energy Materials and Solar Cells*, 92(7), 686–714.
- Kamminga, M. E., Fang, H. H., Filip, M. R., Giustino, F., Baas, J., Blake, G. R., Loi, M. A., & Palstra, T. T. M. (2016). Confinement Effects in Low-Dimensional Lead Iodide Perovskite Hybrids. *Chemistry of Materials*, 28(13), 4554–4562.
- Kang, R., Kim, J.-E., Yeo, J.-S., Lee, S., Jeon, Y.-J., & Kim, D.-Y. (2014). Optimized Organometal Halide Perovskite Planar Hybrid Solar Cells via Control of Solvent Evaporation Rate. *The Journal of Physical Chemistry C*, 118(46), 26513–26520.

- Kawabata, Y., Yoshizawa-Fujita, M., Takeoka, Y., & Rikukawa, M. (2009). Relationship between structure and optoelectrical properties of organic–inorganic hybrid materials containing fullerene derivatives. *Synthetic Metals*, 159(9–10), 776–779.
- Ke, J. C., Wang, Y. H., Chen, K. L., & Huang, C. J. (2016). Effect of organic solar cells using various power O₂ plasma treatments on the indium tin oxide substrate. *Journal of Colloid and Interface Science*, 465, 311–315.
- Kielar, M., Dhez, O., Pecastaings, G., Curutchet, A., & Hirsch, L. (2016). Long-Term Stable Organic Photodetectors with Ultra Low Dark Currents for High Detectivity Applications. *Scientific Reports* 2016 6:1, 6(1), 1–11.
- Kieslich, G., Sun, S., & Cheetham, A. K. (2015). An extended Tolerance Factor approach for organic–inorganic perovskites. *Chemical Science*, 6(6), 3430–3433.
- Kim, C. S., Yang, H. M., Lee, J., Lee, G. S., Choi, H., Kim, Y. J., Lim, S. H., Cho, S. H., & Cho, B. J. (2018). Self-Powered Wearable Electrocardiography Using a Wearable Thermoelectric Power Generator. *ACS Energy Letters*, 3(3), 501–507.
- Kim, H.-B., Choi, H., Jeong, J., Kim, S., Walker, B., Song, S., & Kim, J. Y. (2014). Mixed solvents for the optimization of morphology in solution-processed, inverted-type perovskite/fullerene hybrid solar cells. *Nanoscale*, 6(12), 6679–6683.
- Kim, H. S., Im, S. H., & Park, N. G. (2014). Organolead halide perovskite: New horizons in solar cell research. *Journal of Physical Chemistry C*, 118(11), 5615–5625.
- Kim, S. H., Kim, J., Nam, S., Lee, H. S., Lee, S. W., & Jang, J. (2017). Tuning the Work Function of Printed Polymer Electrodes by Introducing a Fluorinated Polymer to Enhance the Operational Stability in Bottom-Contact Organic Field-Effect Transistors. *ACS Applied Materials and Interfaces*, 9(14), 12637–12646.
- Kim, S., Márquez, J. A., Unold, T., & Walsh, A. (2020). Upper limit to the photovoltaic efficiency of imperfect crystals from first principles. *Energy & Environmental Science*, 13(5), 1481–1491.
- Kittel, C. (2004). Introduction to Solid State Physics Solution Manual, 8th Edition. In *Wiley* (p. 704). <https://www.wiley.com/en-us/Introduction+to+Solid+State+Physics%2C+8th+Edition-p-9780471415268>
- Klauk, H. (2006). Organic Electronics: Materials, Manufacturing and Applications. In *Organic Electronics: Materials, Manufacturing and Applications*. Wiley-VCH.
- Kojima, A., Teshima, K., Shirai, Y., & Miyasaka, T. (2009). Organometal halide perovskites as visible-light sensitizers for photovoltaic cells. *Journal of the American Chemical Society*, 131(17), 6050–6051.
- Konstantakou, M., Perganti, D., Falaras, P., & Stergiopoulos, T. (2017). Anti-solvent crystallization strategies for highly efficient perovskite solar cells. *Crystals*, 7(10), 1–21.
- Konstantatos, G., & Sargent, E. H. (2010). Nanostructured materials for photon detection. *Nature Nanotechnology*, 5(6), 391–400.

- Konstantatos, G., & Sargent, E. H. (2011). Colloidal quantum dot photodetectors. *Infrared Physics and Technology*, 54(3), 278–282.
- Koushik, D., Verhees, W. J. H., Kuang, Y., Veenstra, S., Zhang, D., Verheijen, M. A., Creatore, M., & Schropp, R. E. I. (2017). High-efficiency humidity-stable planar perovskite solar cells based on atomic layer architecture. *Energy & Environmental Science*, 10(1), 91–100.
- Koushik, D., Verhees, W. J. H., Zhang, D., Kuang, Y., Veenstra, S., Creatore, M., & Schropp, R. E. I. (2017). Atomic Layer Deposition Enabled Perovskite/PEDOT Solar Cells in a Regular n–i–p Architectural Design. *Advanced Materials Interfaces*, 4(18).
- Kriegner, D., Matěj, Z., Kužel, R., & Holý, V. (2015). Powder diffraction in Bragg–Brentano geometry with straight linear detectors. *Journal of Applied Crystallography*, 48(Pt 2), 613.
- Krishna, A., & Grimsdale, A. C. (2017). Hole transporting materials for mesoscopic perovskite solar cells – towards a rational design? *Journal of Materials Chemistry A*, 5(32), 16446–16466.
- Kuai, L., Li, J., Li, Y., Wang, Y., Li, P., Qin, Y., Song, T., Yang, Y., Chen, Z., Gao, X., & Sun, B. (2020). Revealing Crystallization Dynamics and the Compositional Control Mechanism of 2D Perovskite Film Growth by in Situ Synchrotron-Based GIXRD. *ACS Energy Letters*, 5(1), 8–16.
- Labram, J. G. (2011). *Ambipolar Organic Transistors for Opto-Electronic Applications*. <https://spiral.imperial.ac.uk/handle/10044/1/9036%5Cnhttps://spiral.imperial.ac.uk/bitstream/10044/1/9036/1/Labram-JG-2011-PhD-Thesis.pdf>
- Labram, J. G., Fabini, D. H., Perry, E. E., Lehner, A. J., Wang, H., Glaudell, A. M., Wu, G., Evans, H., Buck, D., Cotta, R., Echegoyen, L., Wudl, F., Seshadri, R., & Chabiniyc, M. L. (2015). Temperature-Dependent Polarization in Field-Effect Transport and Photovoltaic Measurements of Methylammonium Lead Iodide. *Journal of Physical Chemistry Letters*, 6(18), 3565–3571.
- Lee, D. H., Liu, Y. P., Lee, K. H., Chae, H., & Cho, S. M. (2010). Effect of hole transporting materials in phosphorescent white polymer light-emitting diodes. *Organic Electronics*, 11(3), 427–433.
- Lee, S. W., Cha, S. H., Choi, K. J., Kang, B. H., Lee, J. S., Kim, S. W., Kim, J. S., Jeong, H. M., Gopalan, S. A., Kwon, D. H., & Kang, S. W. (2016). Low dark-current, high current-gain of PVK/ZnO nanoparticles composite-based UV photodetector by PN-heterojunction control. *Sensors (Switzerland)*, 16(1).
- Lee, T. W., Chung, Y., Kwon, O., & Park, J. J. (2007). Self-organized gradient hole injection to improve the performance of polymer electroluminescent devices. *Advanced Functional Materials*, 17(3), 390–396.
- Leguy, A. M. A., Hu, Y., Campoy-Quiles, M., Alonso, M. I., Weber, O. J., Azarhoosh, P., Van Schilfgaarde, M., Weller, M. T., Bein, T., Nelson, J., Docampo, P., & Barnes, P. R. F. (2015). Reversible hydration of CH₃NH₃PbI₃ in films, single

crystals, and solar cells. *Chemistry of Materials*, 27(9), 3397–3407.

Leijtens, T., Bush, K., Cheacharoen, R., Beal, R., Bowring, A., & McGehee, M. D. (2017). Towards enabling stable lead halide perovskite solar cells; interplay between structural, environmental, and thermal stability. *Journal of Materials Chemistry A*, 5(23), 11483–11500.

Lekina, Y., & Shen, Z. X. (2019). Excitonic states and structural stability in two-dimensional hybrid organic-inorganic perovskites. *Journal of Science: Advanced Materials and Devices*, 4(2), 189–200.

Leon, L. M., & Rodriguez, M. (1979). Solution Properties of Poly (N-Vinyl Solvents. *Analysis*, 15, 29–34.

Lerner, C., Birkhold, S. T., Moudrakovski, I. L., Mayer, P., Schoop, L. M., Schmidt-Mende, L., & Lotsch, B. V. (2016). Toward fluorinated spacers for MAPI-derived hybrid perovskites: Synthesis, characterization, and phase transitions of (FC₂H₄NH₃)₂PbCl₄. *Chemistry of Materials*, 28(18), 6560–6566.

Li, C., Han, C., Zhang, Y., Zang, Z., Wang, M., Tang, X., & Du, J. (2017). Enhanced photoresponse of self-powered perovskite photodetector based on ZnO nanoparticles decorated CsPbBr₃ films. *Solar Energy Materials and Solar Cells*, 172(June), 341–346.

Li, D., Wang, G., Cheng, H. C., Chen, C. Y., Wu, H., Liu, Y., Huang, Y., & Duan, X. (2016). Size-dependent phase transition in methylammonium lead iodide perovskite microplate crystals. *Nature Communications*, 7(1), 1–8.

Li, L., Sun, Z., Wang, P., Hu, W., Wang, S., Ji, C., Hong, M., & Luo, J. (2017). Tailored Engineering of an Unusual (C₄H₉NH₃)₂(CH₃NH₃)₂Pb₃Br₁₀ Two-Dimensional Multilayered Perovskite Ferroelectric for a High-Performance Photodetector. *Angewandte Chemie (International Ed. in English)*, 56(40), 12150–12154.

Li, M. K., Chen, T. P., Lin, Y. F., Raghavan, C. M., Chen, W. L., Yang, S. H., Sankar, R., Luo, C. W., Chang, Y. M., & Chen, C. W. (2018). Intrinsic Carrier Transport of Phase-Pure Homologous 2D Organolead Halide Hybrid Perovskite Single Crystals. *Small*, 14(52), 1–8.

Li, Y., Kuang, D., Guo, J., Liu, B., Zhang, Y., Xu, S., Liu, X., Li, X., & Yu, Z. (2022). Wavelength selective and cesium halides additive photodetectors based on two-dimensional perovskite: (C₈H₉NH₃)₂PbBr₄. *Journal of Alloys and Compounds*, 904.

Li, Y., Xu, Z., Zhao, S., Song, D., Qiao, B., Zhu, Y., & Meng, J. (2019). Benefits of the hydrophobic surface for CH₃NH₃PbI₃ crystalline growth towards highly efficient inverted perovskite solar cells. *Molecules*, 24(10), 1–12.

Li, Y. Y., Lin, C. K., Zheng, G. L., Cheng, Z. Y., You, H., Wang, W. D., & Lin, J. (2006). Novel <110>-oriented organic-inorganic perovskite compound stabilized by N-(3-aminopropyl)imidazole with improved optical properties. *Chemistry of Materials*, 18(15), 3463–3469.

- Liang, D., Peng, Y., Fu, Y., Shearer, M. J., Zhang, J., Zhai, J., Zhang, Y., Hamers, R. J., Andrew, T. L., & Jin, S. (2016). Color-Pure Violet-Light-Emitting Diodes Based on Layered Lead Halide Perovskite Nanoplates. *ACS Nano*, 10(7), 6897–6904.
- Liang, Y., Li, F., & Zheng, R. (2020). Low-Dimensional Hybrid Perovskites for Field-Effect Transistors with Improved Stability: Progress and Challenges. *Advanced Electronic Materials*, 6(9), 1–29.
- Liao, Y., Liu, H., Zhou, W., Yang, D., Shang, Y., Shi, Z., Li, B., Jiang, X., Zhang, L., Quan, L. N., Quintero-Bermudez, R., Sutherland, B. R., Mi, Q., Sargent, E. H., & Ning, Z. (2017). Highly Oriented Low-Dimensional Tin Halide Perovskites with Enhanced Stability and Photovoltaic Performance. *Journal of the American Chemical Society*, 139(19), 6693–6699.
- Lilienfeld, J. E. (1930). Method and apparatus for controlling electric currents. In *US Patent 1,745,175* (pp. 1–4). <http://www.google.com/patents?hl=en&lr=&vid=USPAT1745175&id=uBFMAA-AAEBAJ&oi=fnd&dq=Method+and+apparatus+for+controlling+electric+currents&printsec=abstract>
- Lin, Y., Bai, Y., Fang, Y., Wang, Q., Deng, Y., & Huang, J. (2017). Suppressed Ion Migration in Low-Dimensional Perovskites. *ACS Energy Letters*, 2(7), 1571–1572.
- Liu, C., Zhou, X., Chen, S., Zhao, X., Dai, S., & Xu, B. (2019). Hydrophobic Cu₂O Quantum Dots Enabled by Surfactant Modification as Top Hole-Transport Materials for Efficient Perovskite Solar Cells. *Advanced Science*, 6(7), 1–9.
- Liu, D., Wu, L., Li, C., Ren, S., Zhang, J., Li, W., & Feng, L. (2015). Controlling CH₃NH₃PbI₃-xCl_x Film Morphology with Two-Step Annealing Method for Efficient Hybrid Perovskite Solar Cells. *ACS Applied Materials and Interfaces*, 7(30), 16330–16337.
- Liu, M., Johnston, M. B., & Snaith, H. J. (2013). Efficient planar heterojunction perovskite solar cells by vapour deposition. *Nature*, 501(7467), 395–398.
- Liu, X., Xu, C., & Lee, E. C. (2020). Chlorobenzene-Mediated Control of Crystallization in Perovskite Films for High-Performance Solar Cells. *ACS Applied Energy Materials*, 3(12), 12291–12297.
- Liu, Y., Ye, H., Zhang, Y., Zhao, K., Yang, Z., Yuan, Y., Wu, H., Zhao, G., Yang, Z., Tang, J., Xu, Z., & Liu, S. (Frank). (2019). Surface-Tension-Controlled Crystallization for High-Quality 2D Perovskite Single Crystals for Ultrahigh Photodetection. *Matter*, 1(2), 465–480.
- Ll, J. (2022). *Hybrid perovskite materials : characterization of their electrical properties and stability at the nanoscale* Jaume Llàcer Martínez To cite this version : HAL Id : tel-03622471 Matériaux Pérovskites Hybrides : Caractérisation des Propriétés Électroniques e.
- Lu, J., Jiang, L., Li, W., Li, F., Pai, N. K., Scully, A. D., Tsai, C. M., Bach, U., Simonov, A. N., Cheng, Y. B., & Spiccia, L. (2017). Diammonium and Monoammonium Mixed-Organic-Cation Perovskites for High Performance Solar Cells with Improved

- Stability. *Advanced Energy Materials*, 7(18), 1700444.
- Luo, P., Zhou, S., Xia, W., Cheng, J., Xu, C., & Lu, Y. (2017). Chemical Vapor Deposition of Perovskites for Photovoltaic Application. *Advanced Materials Interfaces*, 4(8).
- Ma, D., Fu, Y., Dang, L., Zhai, J., Guzei, I. A., & Jin, S. (2017). Single-crystal microplates of two-dimensional organic–inorganic lead halide layered perovskites for optoelectronics. *Nano Research*, 10(6), 2117–2129.
- Ma, S., Qiao, W., Cheng, T., Zhang, B., Yao, J., Alsaedi, A., Hayat, T., Ding, Y., Tan, Z., & Dai, S. (2018). Optical-Electrical-Chemical Engineering of PEDOT:PSS by Incorporation of Hydrophobic Nafion for Efficient and Stable Perovskite Solar Cells. *ACS Applied Materials and Interfaces*, 10(4), 3902–3911.
- Manceau, M., & Berson, S. (2014). Inverted polymer solar cells with Nafion® as the hole extraction layer: Efficiency and lifetime studies. *Nanotechnology*, 25(1).
- Manser, J. S., Christians, J. A., & Kamat, P. V. (2016). Intriguing Optoelectronic Properties of Metal Halide Perovskites. In *Chemical Reviews* (Vol. 116, Issue 21, pp. 12956–13008). American Chemical Society.
- Marra, W. C., Eisenberger, P., & Cho, A. Y. (2008). X-ray total-external-reflection–Bragg diffraction: A structural study of the GaAs–Al interface. *Journal of Applied Physics*, 50(11), 6927.
- Marshall, C. J. (2017). Photonic Devices. In *Extreme Environment Electronics* (pp. 275–286). Cambridge University Press.
- Matsushima, T., Terakawa, S., Leyden, M. R., Fujihara, T., Qin, C., & Adachi, C. (2019). Toward air-stable field-effect transistors with a tin iodide-based hybrid perovskite semiconductor. *Journal of Applied Physics*, 125(23), 0–7.
- Mauritz, K. A., & Moore, R. B. (2004). State of understanding of Nafion. *Chemical Reviews*, 104(10), 4535–4585.
- Mei, Y., Zhang, C., Vardeny, Z. V., & Jurchescu, O. D. (2015). Electrostatic gating of hybrid halide perovskite field-effect transistors: Balanced ambipolar transport at room-temperature. *MRS Communications*, 5(2), 297–301.
- Meijer, E. J., Detcherry, C., Baesjou, P. J., Van Veenendaal, E., De Leeuw, D. M., & Klapwijk, T. M. (2003). Dopant density determination in disordered organic field-effect transistors. *Journal of Applied Physics*, 93(8), 4831–4835.
- Mercier, N., & Riou, A. (2004). An organic–inorganic hybrid perovskite containing copper paddle-wheel clusters linking perovskite layers: $[\text{Cu}(\text{O}_2\text{C}-(\text{CH}_2)_3-\text{NH}_2)_2]\text{PbBr}_4$. *Chemical Communications*, 4(7), 844–845.
- Michaelson, H. B. (1977). The work function of the elements and its periodicity. *Journal of Applied Physics*, 48(11), 4729–4733.
- Milot, R. L., Sutton, R. J., Eperon, G. E., Haghighirad, A. A., Martinez Hardigree, J.,

- Miranda, L., Snaith, H. J., Johnston, M. B., & Herz, L. M. (2016). Charge-Carrier Dynamics in 2D Hybrid Metal-Halide Perovskites. *Nano Letters*, 16(11), 7001–7007.
- Min, H., Lee, D. Y., Kim, J., Kim, G., Lee, K. S., Kim, J., Paik, M. J., Kim, Y. K., Kim, K. S., Kim, M. G., Shin, T. J., & Il Seok, S. (2021). Perovskite solar cells with atomically coherent interlayers on SnO(2) electrodes. *Nature*, 598(7881), 444–450.
- Misra, R. K., Cohen, B. El, Iagher, L., & Etgar, L. (2017). Low-Dimensional Organic–Inorganic Halide Perovskite: Structure, Properties, and Applications. *ChemSusChem*, 10(19), 3712–3721.
- Mitzi, D. B. (2001). Templating and structural engineering in organic-inorganic perovskites. *Journal of the Chemical Society, Dalton Transactions*, 1, 1–12.
- Mitzi, D. B., Chondroudis, K., & Kagan, C. R. (1999). Design, structure, and optical properties of organic-inorganic perovskites containing an oligothiophene chromophore. *Inorganic Chemistry*, 38(26), 6246–6256.
- Mitzi, D. B., Wang, S., Feild, C. A., Chess, C. A., & Guloy, A. M. (1995). Conducting Layered Organic-inorganic Halides Containing -Oriented Perovskite Sheets. *Science (New York, N.Y.)*, 267(5203), 1473–1476.
- Moet, D. J. D., De Bruyn, P., & Blom, P. W. M. (2010). High work function transparent middle electrode for organic tandem solar cells. *Applied Physics Letters*, 96(15), 1–4.
- Monroy, E., Omnès, F., & Calle, F. (2003). Wide-bandgap semiconductor ultraviolet photodetectors. In *Semiconductor Science and Technology* (Vol. 18, Issue 4, p. R33). IOP Publishing.
- Mousdis, G. A., Gionis, V., Papavassiliou, G. C., Raptopoulou, C. P., & Terzis, A. (1998). Preparation, structure and optical properties of [CH₃SC(NH₂)NH₂]₃PbI₅, [CH₃SC(NH₂)NH₂]₄Pb₂Br₈ and [CH₃SC(NH₂)NH₂]₃PbCl₅·CH₃SC(NH₂)NH₂Cl. *Journal of Materials Chemistry*, 8(10), 2259–2262.
- Muñoz, E., Monroy, E., Garrido, J. A., Izpura, I., Sánchez, F. J., Sánchez-García, M. A., Calleja, E., Beaumont, B., & Gibart, P. (1998). Photoconductor gain mechanisms in GaN ultraviolet detectors. *Applied Physics Letters*, 71(7), 870.
- Nagao, Y. (2017). Proton-Conductivity Enhancement in Polymer Thin Films. *Langmuir*, 33(44), 12547–12558.
- Nguyen, T. M. H., Kim, S., & Bark, C. W. (2021). Solution-processed and self-powered photodetector in vertical architecture using mixed-halide perovskite for highly sensitive UVC detection. *Journal of Materials Chemistry A*, 9(2), 1269–1276.
- Niu, S., Joe, G., Zhao, H., Zhou, Y., Orvis, T., Huyan, H., Salman, J., Mahalingam, K., Urwin, B., Wu, J., Liu, Y., Tiwald, T. E., Cronin, S. B., Howe, B. M., Mecklenburg, M., Haiges, R., Singh, D. J., Wang, H., Kats, M. A., & Ravichandran, J. (2018). Giant optical anisotropy in a quasi-one-dimensional crystal. *Nature Photonics*,

- Noh, J. H., Im, S. H., Heo, J. H., Mandal, T. N., & Seok, S. Il. (2013). Chemical management for colorful, efficient, and stable inorganic-organic hybrid nanostructured solar cells. *Nano Letters*, 13(4), 1764–1769.
- NREL. (2021). *Best Research-Cell Efficiencies*. <https://www.nrel.gov/pv/cell-efficiency.html>
- Palik, E. D. (2012). Handbook of optical constants of solids. In *Handbook of Optical Constants of Solids* (Vol. 1). Elsevier Inc.
- Pan, X., Zhang, J., Zhou, H., Liu, R., Wu, D., Wang, R., Shen, L., Tao, L., Zhang, J., & Wang, H. (2021). Single-Layer ZnO Hollow Hemispheres Enable High-Performance Self-Powered Perovskite Photodetector for Optical Communication. *Nano-Micro Letters*, 13(1).
- Pang, S., Hu, H., Zhang, J., Lv, S., Yu, Y., Wei, F., Qin, T., Xu, H., Liu, Z., & Cui, G. (2014). NH₂CH=NH₂PbI₃: An alternative organolead iodide perovskite sensitizer for mesoscopic solar cells. *Chemistry of Materials*, 26(3), 1485–1491.
- Park, J. K., Hwang, G. S., Chin, B. D., Kang, N. S., & Lee, T. W. (2012). Electrophosphorescent devices with solution processible emitter and hole transport layer stack. *Current Applied Physics*, 12(SUPPL. 1), e38–e41.
- Park, M. S., & Kim, F. S. (2019). Synergistic effects of processing additives and thermal annealing on nanomorphology and hole mobility of Poly(3-hexylthiophene) thin films. *Polymers*, 11(1), 1–11.
- Park, N. G., Grätzel, M., Miyasaka, T., Zhu, K., & Emery, K. (2016). Towards stable and commercially available perovskite solar cells. *Nature Energy*, 1(11).
- Patterson, J. D., & Bailey, B. C. (2009). Solid state physics: Introduction to the theory. In *Solid State Physics: Introduction to the Theory*. Springer Berlin Heidelberg.
- Petriz, R. L. (1956). Theory of photoconductivity in semiconductor films. *Physical Review*, 104(6), 1508–1516.
- Petty, M. C. (2007). Molecular Electronics: From Principles to Practice. In *Molecular Electronics: From Principles to Practice*.
- Ph, C. (2012). *Signi fi cant Di fferent Conductivities of the Two Grades of Poly(3,4-ethylenedioxythiophene):Poly(styrenesulfonate), Clevios P and Clevios PH1000, Arising from Di fferent Molecular Weights*.
- Qiu, W., Muller, R., Voroshazi, E., Conings, B., Carleer, R., Boyen, G., Turbiez, M., Froyen, L., Heremans, P., & Hadipour, A. (2015). *Nafion Modified MoOx as Effective Room Temperature Hole Injection Layer for High Performance and Stable Inverted Organic Solar Cells Nafion Modified MoO x as Effective Room Temperature Hole Injection Layer for High Performance and Stable Inverted Organic*.

- Qiu, X., Liu, Y., Xia, J., Guo, J., Chen, P. A., Wei, H., Shi, X., Chen, C., Zeng, Z., Chen, H., Jiang, L., Liao, L., & Hu, Y. (2023). Room temperature two-dimensional lead halide perovskite thin-film transistors with high stability. *Cell Reports Physical Science*, 4(1), 101217.
- Quan, L. N., Yuan, M., Comin, R., Voznyy, O., Beauregard, E. M., Hoogland, S., Buin, A., Kirmani, A. R., Zhao, K., Amassian, A., Kim, D. H., & Sargent, E. H. (2016). Ligand-Stabilized Reduced-Dimensionality Perovskites. *Journal of the American Chemical Society*, 138(8), 2649–2655.
- Rahaq, Y., Moussa, M., Mohammad, A., Wang, H., & Hassan, A. (2018). Highly reproducible perovskite solar cells via controlling the morphologies of the perovskite thin films by the solution-processed two-step method. *Journal of Materials Science: Materials in Electronics*, 29(19), 16426–16436.
- Rajeev, K. P., Opoku, C., Stolojan, V., Constantinou, M., & Shkunov, M. (2015). *Electrical analysis of hysteresis in solution processed silicon nanowire field effect transistors*. 1–17. <http://arxiv.org/abs/1507.04719>
- Ren, X., Yan, X., Ahmad, A. S., Cheng, H., Li, Y., Zhao, Y., Wang, L., & Wang, S. (2019). Pressure-induced phase transition and band gap engineering in propylammonium lead bromide perovskite [Research-article]. *Journal of Physical Chemistry C*, 123(24), 15204–15208.
- Reza, K. M., Gurung, A., Bahrami, B., Mabrouk, S., Elbohy, H., Pathak, R., Chen, K., Chowdhury, A. H., Rahman, M. T., Letourneau, S., Yang, H. C., Saianand, G., Elam, J. W., Darling, S. B., & Qiao, Q. (2020). Tailored PEDOT:PSS hole transport layer for higher performance in perovskite solar cells: Enhancement of electrical and optical properties with improved morphology. *Journal of Energy Chemistry*, 44, 41–50.
- Rondiya, S. R., Jagt, R. A., Macmanus-Driscoll, J. L., Walsh, A., & Hoyer, R. L. Z. (2021). Self-trapping in bismuth-based semiconductors: Opportunities and challenges from optoelectronic devices to quantum technologies. *Applied Physics Letters*, 119(22), 220501.
- Safdari, M., Phuyal, D., Philippe, B., Svensson, P. H., Butorin, S. M., Kvashnina, K. O., Rensmo, H., Kloo, L., & Gardner, J. M. (2017). Impact of synthetic routes on the structural and physical properties of butyl-1,4-diammonium lead iodide semiconductors. *Journal of Materials Chemistry A*, 5(23), 11730–11738.
- Saidaminov, M. I., Mohammed, O. F., & Bakr, O. M. (2017). Low-dimensional-networked metal halide perovskites: The next big thing. *ACS Energy Letters*, 2(4), 889–896.
- Saparov, B., & Mitzi, D. B. (2016). Organic-Inorganic Perovskites: Structural Versatility for Functional Materials Design. In *Chemical Reviews* (Vol. 116, Issue 7, pp. 4558–4596). American Chemical Society.
- Sasaki, S., Prewitt, C. T., Bass, J. D., & Schulze, W. A. (1987). Orthorhombic perovskite CaTiO₃ and CdTiO₃: structure and space group. *Acta Crystallographica Section C*, 43(9), 1668–1674.

- Senanayak, S. P., Yang, B., Thomas, T. H., Giesbrecht, N., Huang, W., Gann, E., Nair, B., Goedel, K., Guha, S., Moya, X., McNeill, C. R., Docampo, P., Sadhanala, A., Friend, R. H., & Sirringhaus, H. (2017). Understanding charge transport in lead iodide perovskite thin-film field-effect transistors. *Science Advances*, 3(1), 1–11.
- Shao, D., Zhu, W., Liu, X., Li, M., Chen, J., Sun, Y. Y., Xin, G., Lian, J., & Sawyer, S. (2020). Ultrasensitive UV Photodetector Based on Interfacial Charge-Controlled Inorganic Perovskite-Polymer Hybrid Structure. *ACS Applied Materials and Interfaces*, 12(38), 43106–43114.
- Shen, H., Li, J., Wang, H., Ma, J., Wang, J., Luo, H., & Li, D. (2019). Two-Dimensional Lead-Free Perovskite (C₆H₅C₂H₄NH₃)₂CsSn₂I₇ with High Hole Mobility. *The Journal of Physical Chemistry Letters*, 10(1), 7–12.
- Shi, Y. L., Liang, F., Hu, Y., Wang, X. D., Wang, Z. K., & Liao, L. S. (2017). High-efficiency quantum dot light-emitting diodes employing lithium salt doped poly(9-vinylcarbazole) as a hole-transporting layer. *Journal of Materials Chemistry C*, 5(22), 5372–5377.
- Shkir, M., Khan, M. T., Ashraf, I. M., Almohammed, A., Dieguez, E., & AlFaify, S. (2019). High-performance visible light photodetectors based on inorganic CZT and InCZT single crystals. *Scientific Reports*, 9(1), 1–9.
- Shockley, W., Pearson, G. L., & Haynes, J. R. (1949). Hole Injection in Germanium—Quantitative Studies and Filamentary Transistors. *Bell System Technical Journal*, 28(3), 344–366.
- Shor Peled, S., Perez, M., Meron, D., Osherov, A., Bulovic, V., Katz, E. A., & Golan, Y. (2021). Morphology control of perovskite films: a two-step, all solution process for conversion of lead selenide into methylammonium lead iodide. *Materials Chemistry Frontiers*, 5(3), 1410–1417.
- Simone, G., Dyson, M. J., L Weijtens, C. H., J Meskers, S. C., Coehoorn, R., J Janssen, R. A., Gelinck, G. H., Simone, G., Dyson, M. J., L Weijtens, C. H., J Meskers, S. C., Coehoorn, R., J Janssen, R. A., & Gelinck, G. H. (2020). On the Origin of Dark Current in Organic Photodiodes. *Advanced Optical Materials*, 8(1), 1901568.
- Smith, I. C., Hoke, E. T., Solis-Ibarra, D., McGehee, M. D., & Karunadasa, H. I. (2014). A layered hybrid perovskite solar-cell absorber with enhanced moisture stability. *Angewandte Chemie (International Ed. in English)*, 53(42), 11232–11235.
- Song, Z., Abate, A., Wathage, S. C., Liyanage, G. K., Phillips, A. B., Steiner, U., Graetzel, M., & Heben, M. J. (2016). Perovskite Solar Cell Stability in Humid Air: Partially Reversible Phase Transitions in the PbI₂-CH₃NH₃I-H₂O System. *Advanced Energy Materials*, 6(19), 1600846.
- Sparnacci, K., Antonioli, D., Deregibus, S., Laus, M., Poggio, T., Kapeliouchko, V., Palamone, G., Zuccheri, G., & Passeri, R. (2009). PTFE-Based Core-Soft Shell Nanospheres and Soft Matrix Nanocomposites. *Macromolecules*, 42(10), 3518–3524.
- Sripukdee, M., Songsiriritthigul, C., Mothong, N., Seawsakul, K., Saisopa, T.,

- Horprathum, M., & Songsiriritthigul, P. (2018). Grazing Incidence X-Ray Diffraction using Synchrotron Light at SLRI. *Journal of Physics: Conference Series*, 1144(1).
- Steve Kelly. (2013, June). *Organic Semiconductors for Flexible Displays*. <https://www.azom.com/article.aspx?ArticleID=9210>
- Stoumpos, C. C., Cao, D. H., Clark, D. J., Young, J., Rondinelli, J. M., Jang, J. I., Hupp, J. T., & Kanatzidis, M. G. (2016). Ruddlesden-Popper Hybrid Lead Iodide Perovskite 2D Homologous Semiconductors. *Chemistry of Materials*, 28(8), 2852–2867.
- Stoumpos, C. C., Frazer, L., Clark, D. J., Kim, Y. S., Rhim, S. H., Freeman, A. J., Ketterson, J. B., Jang, J. I., & Kanatzidis, M. G. (2015). Hybrid germanium iodide perovskite semiconductors: Active lone pairs, structural distortions, direct and indirect energy gaps, and strong nonlinear optical properties. *Journal of the American Chemical Society*, 137(21), 6804–6819.
- Stranks, S. D., Burlakov, V. M., Leijtens, T., Ball, J. M., Goriely, A., & Snaith, H. J. (2014). Recombination Kinetics in Organic-Inorganic Perovskites: Excitons, Free Charge, and Subgap States. *Physical Review Applied*, 2(3), 1–8.
- Strickley, J. D., Messerschmidt, J. L., Awad, M. E., Li, T., Hasegawa, T., Ha, D. T., Nabeta, H. W., Bevins, P. A., Ngo, K. H., Asgari, M. M., Nazarian, R. M., Neel, V. A., Jenson, A. B., Joh, J., & Demehri, S. (2019). Immunity to commensal papillomaviruses protects against skin cancer. *Nature*, 575(7783), 519–522.
- Subramaniam, Y., Woon, K. L., Nakajima, H., Chaiprapa, J., & Songsiriritthigul, P. (2021). Preferential vertically oriented nanopillar perovskite induced by poly(9-vinylcarbazole) field-effect transistor. *Synthetic Metals*, 281(August), 116901.
- Sun, K., Li, P., Xia, Y., Chang, J., & Ouyang, J. (2015). Transparent Conductive Oxide-Free Perovskite Solar Cells with PEDOT:PSS as Transparent Electrode. *ACS Applied Materials and Interfaces*, 7(28), 15314–15320.
- Syed, A. A., Poon, C. Y., Li, H. W., & Zhu, F. (2019). A sodium citrate-modified-PEDOT:PSS hole transporting layer for performance enhancement in inverted planar perovskite solar cells. *Journal of Materials Chemistry C*, 7(18), 5260–5266.
- Sze, S. M., & Ng, K. K. (2006). Physics of Semiconductor Devices. In *Physics of Semiconductor Devices*. John Wiley & Sons, Inc.
- Talik, N. A., Woon, K. L., & Yap, B. K. (2016). Effect of mixed hole transporting host on the mobility, Gaussian density of states and efficiencies of a heterojunction phosphorescent organic light emitting diode. *Journal of Physics D: Applied Physics*, 49(15), 155103.
- Tan, K. W., Moore, D. T., Saliba, M., Sai, H., Estroff, L. A., Hanrath, T., Snaith, H. J., & Wiesner, U. (2015). Thermally Induced Structural Evolution and Performance of Mesoporous Block Copolymer-Directed Alumina Perovskite Solar Cells. *ACS Nano*, 8(5), 4730–4739. <https://doi.org/10.1021/nn500526t>

- Tan, Z. K., Moghaddam, R. S., Lai, M. L., Docampo, P., Higler, R., Deschler, F., Price, M., Sadhanala, A., Pazos, L. M., Credgington, D., Hanusch, F., Bein, T., Snaith, H. J., & Friend, R. H. (2014). Bright light-emitting diodes based on organometal halide perovskite. *Nature Nanotechnology*, 9(9), 687–692.
- Tan, Z., Wu, Y., Hong, H., Yin, J., Zhang, J., Lin, L., Wang, M., Sun, X., Sun, L., Huang, Y., Liu, K., Liu, Z., & Peng, H. (2016). Two-Dimensional (C₄H₉NH₃)₂PbBr₄ Perovskite Crystals for High-Performance Photodetector. *Journal of the American Chemical Society*, 138(51), 16612–16615.
- Tanaka, T., Lee, J., & Scheller, P. R. (2014). Chapter 1.5 - Interfacial Free Energy and Wettability. In S. Seetharaman (Ed.), *Treatise on Process Metallurgy* (pp. 61–77). Elsevier.
- Tieke, B., & Chapuis, G. (1984). Solid-State Polymerization of Butadienes. Crystal Structure and Solution Properties of a Stereoregular Amphoteric 1,4-Trans-Polybutadiene. *Journal of Polymer Science: Polymer Chemistry Edition*, 22(11 pt 1), 2895–2921.
- Tiwari, S. P., Verma, R., Alam, M. B., Kumari, R., Sinha, O. P., & Srivastava, R. (2017). Charge transport study of P3HT blended MoS₂. *Vacuum*, 146, 474–477.
- Tong, Y. (2020). The exploration and outlook of two-dimensional perovskites. *Journal of Physics: Conference Series*, 1653(1).
- Tsai, H., Nie, W., Blancon, J. C., Stoumpos, C. C., Asadpour, R., Harutyunyan, B., Neukirch, A. J., Verduzco, R., Crochet, J. J., Tretiak, S., Pedesseau, L., Even, J., Alam, M. A., Gupta, G., Lou, J., Ajayan, P. M., Bedzyk, M. J., Kanatzidis, M. G., & Mohite, A. D. (2016). High-efficiency two-dimensional ruddlesden-popper perovskite solar cells. *Nature*, 536(7616), 312–317.
- Tsai, T. C., Chang, H. C., Chen, C. H., Huang, Y. C., & Whang, W. T. (2014). A facile dedoping approach for effectively tuning thermoelectricity and acidity of PEDOT:PSS films. *Organic Electronics*, 15(3), 641–645.
- Upama, M. B., Elumalai, N. K., Mahmud, M. A., Wang, D., Haque, F., Gonçalves, V. R., Gooding, J. J., Wright, M., Xu, C., & Uddin, A. (2017). Role of fullerene electron transport layer on the morphology and optoelectronic properties of perovskite solar cells. *Organic Electronics*, 50, 279–289.
- Urieta-Mora, J., García-Benito, I., Molina-Ontoria, A., & Martín, N. (2018). Hole transporting materials for perovskite solar cells: a chemical approach. *Chemical Society Reviews*, 47(23), 8541–8571.
- Van Reenen, S., Kouijzer, S., Janssen, R. A. J., Wienk, M. M., & Kemerink, M. (2014). Origin of Work Function Modification by Ionic and Amine-Based Interface Layers. *Advanced Materials Interfaces*, 1(8).
- Wakamiya, A., Endo, M., Sasamori, T., Tokitoh, N., Ogomi, Y., Hayase, S., & Murata, Y. (2014). Reproducible Fabrication of Efficient Perovskite-based Solar Cells: X-ray Crystallographic Studies on the Formation of CH₃NH₃PbI₃ Layers. *Chemistry Letters*, 43, 711–713.

- Waldauf, C., Schilinsky, P., Perisutti, M., Hauch, J., & Brabec, C. J. (2003). Solution-Processed Organic n-Type Thin-Film Transistors. *Advanced Materials*, 15(24), 2084–2088.
- Waleed, A., Tavakoli, M. M., Gu, L., Hussain, S., Zhang, D., Poddar, S., Wang, Z., Zhang, R., & Fan, Z. (2017). All Inorganic Cesium Lead Iodide Perovskite Nanowires with Stabilized Cubic Phase at Room Temperature and Nanowire Array-Based Photodetectors. *Nano Letters*, 17(8), 4951–4957.
- Walsh, A. (2015). Principles of chemical bonding and band gap engineering in hybrid organic-inorganic halide perovskites. *Journal of Physical Chemistry C*, 119(11), 5755–5760.
- Wang, C. Y., Fuentes-Hernandez, C., Chou, W. F., & Kippelen, B. (2017). Top-gate organic field-effect transistors fabricated on paper with high operational stability. *Organic Electronics*, 41, 340–344.
- Wang, F., Bai, S., Tress, W., Hagfeldt, A., & Gao, F. (2018). Defects engineering for high-performance perovskite solar cells. *Npj Flexible Electronics*, 2(1).
- Wang, F., Geng, W., Zhou, Y., Fang, H. H., Tong, C. J., Loi, M. A., Liu, L. M., & Zhao, N. (2016). Phenylalkylamine Passivation of Organolead Halide Perovskites Enabling High-Efficiency and Air-Stable Photovoltaic Cells. *Advanced Materials (Deerfield Beach, Fla.)*, 28(45), 9986–9992.
- Wang, J., Wang, N., Jin, Y., Si, J., Tan, Z.-K., Du, H., Cheng, L., Dai, X., Bai, S., He, H., Ye, Z., Lai, M. L., Friend, R. H., & Huang, W. (2015). Interfacial control toward efficient and low-voltage perovskite light-emitting diodes. *Advanced Materials (Deerfield Beach, Fla.)*, 27(14), 2311–2316.
- Wang, K., Steimer, C., Wamwangi, D., Ziegler, S., & Wuttig, M. (2005). Effect of indium doping on Ge₂Sb₂Te₅ thin films for phase-change optical storage. *Applied Physics A* 2005 80:8, 80(8), 1611–1616.
- Wang, K., Wu, C., Hou, Y., Yang, D., & Priya, S. (2019). Monocrystalline perovskite wafers/thin films for photovoltaic and transistor applications. *Journal of Materials Chemistry A*, 7(43), 24661–24690.
- Wang, S., Frisch, S., Zhang, H., Yildiz, O., Mandal, M., Ugur, N., Jeong, B., Ramanan, C., Andrienko, D., Wang, H. I., Bonn, M., Blom, P. W. M., Kivala, M., Pisula, W., & Marszalek, T. (2022). Grain engineering for improved charge carrier transport in two-dimensional lead-free perovskite field-effect transistors. *Materials Horizons*, 9(10), 2633–2643.
- Wang, S. Q., Setlow, R., Berwick, M., Polsky, D., Marghoob, A. A., Kopf, A. W., & Bart, R. S. (2001). Ultraviolet A and melanoma: A review. *Journal of the American Academy of Dermatology*, 44(5), 837–846.
- Wang, S., Zhang, Z., Tang, Z., Su, C., Huang, W., Li, Y., & Xing, G. (2021). Polymer strategies for high-efficiency and stable perovskite solar cells. *Nano Energy*, 82(December 2020), 105712.

- Wang, X., Li, K., Xu, H., Ali, N., Wang, Y., Shen, Q., & Wu, H. (2020). Synthesis of large two-dimensional lead-free bismuth–silver double perovskite microplatelets and their application for field-effect transistors. *Chemical Communications*, 56(57), 7917–7920.
- Wang, Z., Lin, Q., Chmiel, F. P., Sakai, N., Herz, L. M., & Snaith, H. J. (2017). Efficient ambient-air-stable solar cells with 2D-3D heterostructured butylammonium-caesium-formamidinium lead halide perovskites. *Nature Energy*, 2(9), 1–10.
- Weng, J., Xu, M., Wang, X., Wang, F., & Zhang, B. O. (2022). Self-powered, ultraviolet-to-near infrared broadband photodetector based on Ag-doped CsPbI₃/PEDOT:PSS heterojunction. *Optics Express*, 30(21).
- Whitcher, T. J., Wong, W. S., Talik, A. N., Woon, K. L., Rusydi, A., Chanlek, N., Nakajima, H., Saisopa, T., & Songsiriritthigul, P. (2018). Energy level alignment of blended organic semiconductors and electrodes at the interface. *Current Applied Physics*, 18(9), 982–992.
- Widjonarko, N. (2016). Introduction to Advanced X-ray Diffraction Techniques for Polymeric Thin Films. *Coatings*, 6(4), 54.
- Williams, A. A., Thornton, J. M. C., MacDonald, J. E., Van Silfhout, R. G., Van Der Veen, J. F., Finney, M. S., Johnson, A. D., & Norris, C. (1991). Strain relaxation during the initial stages of growth in Ge/Si(001). *Physical Review B*, 43(6), 5001.
- Williams, R. T., & Song, K. S. (1990). The self-trapped exciton. *Journal of Physics and Chemistry of Solids*, 51(7), 679–716.
- Wu, X., Sun, J., Shao, H., Zhai, Y., Li, L., Chen, W., Zhu, J., Dong, B., Xu, L., Zhou, D., Xu, W., Song, H., & Bai, X. (2021). Self-powered UV photodetectors based on CsPbCl₃ nanowires enabled by the synergistic effect of acetate and lanthanide ion passivation. *Chemical Engineering Journal*, 426(June), 131310.
- Wu, Y., Islam, A., Yang, X., Qin, C., Liu, J., Zhang, K., Peng, W., & Han, L. (2014). Retarding the crystallization of PbI₂ for highly reproducible planar-structured perovskite solar cells via sequential deposition. *Energy Environ. Sci.*, 7(9), 2934–2938.
- Wu, Z., Bai, S., Xiang, J., Yuan, Z., Yang, Y., Cui, W., Gao, X., Liu, Z., Jin, Y., & Sun, B. (2014). Efficient planar heterojunction perovskite solar cells employing graphene oxide as hole conductor. *Nanoscale*, 6(18), 10505–10510.
- Wu, Z., Ji, C., Wang, S., Zhang, W., Wang, Y., Li, L., Zhao, S., Sun, Z., & Luo, J. (2017). (2-Methylpiperidine)PbI₃: An ABX₃-type organic-inorganic hybrid chain compound and its semiconducting nanowires with photoconductive properties. *Journal of Materials Chemistry C*, 5(44), 11466–11471.
- Xia, Y., Yan, G., & Lin, J. (2021). Review on tailoring pedot:Pss layer for improved device stability of perovskite solar cells. *Nanomaterials*, 11(11), 1–16.
- Xiao, Z., Kerner, R. A., Zhao, L., Tran, N. L., Lee, K. M., Koh, T. W., Scholes, G. D., & Rand, B. P. (2017). Efficient perovskite light-emitting diodes featuring nanometre-

sized crystallites. *Nature Photonics*, 11(2), 108–115.

- Xu, C., Liu, Z., & Lee, E. C. (2021). Stability and efficiency improved perovskite solar cells through tuning the hydrophobicity of the hole transport layer with an organic semiconductor. *Journal of Materials Chemistry C*, 9(2), 679–686.
- Xu, S., Huang, G., Wang, C., Shao, H., & Cui, Y. (2020). Carbon-based fully printable self-powered ultraviolet perovskite photodetector: Manganese-assisted electron transfer and enhanced photocurrent. *Nanomaterials and Nanotechnology*, 10, 1–8.
- Yan, K., Long, M., Zhang, T., Wei, Z., Chen, H., Yang, S., & Xu, J. (2015). Hybrid Halide Perovskite Solar Cell Precursors: Colloidal Chemistry and Coordination Engineering behind Device Processing for High Efficiency. *Journal of the American Chemical Society*, 137(13), 4460–4468.
- Yang, L., Yan, Y., Cai, F., Li, J., & Wang, T. (2017). Poly(9-vinylcarbazole) as a hole transport material for efficient and stable inverted planar heterojunction perovskite solar cells. *Solar Energy Materials and Solar Cells*, 163(December 2016), 210–217.
- Yang, Y., Feng, S., Li, M., Xu, W., Yin, G., Wang, Z., Sun, B., & Gao, X. (2017). Annealing induced re-crystallization in $\text{CH}_3\text{NH}_3\text{PbI}_3\text{-xCl}_x$ for high performance perovskite solar cells. *Scientific Reports*, 7(April), 19–20.
- Yang, Y., You, J., Hong, Z., Chen, Q., Cai, M., Song, T. Bin, Chen, C. C., Lu, S., Liu, Y., & Zhou, H. (2014). Low-temperature solution-processed perovskite solar cells with high efficiency and flexibility. *ACS Nano*, 8(2), 1674–1680.
- Yao, J., Kong, J., Shi, W., & Lu, C. (2022). The Insolubility Problem of Organic Hole-Transport Materials Solved by Solvothermal Technology: Toward Solution-Processable Perovskite Solar Cells. *ACS Applied Materials and Interfaces*, 14(5), 7493–7503.
- Ye, S., Sun, W., Li, Y., Yan, W., Peng, H., Bian, Z., Liu, Z., & Huang, C. (2015). CuSCN-Based Inverted Planar Perovskite Solar Cell with an Average PCE of 15.6%. *Nano Letters*, 15(6), 3723–3728.
- Yin, W. J., Shi, T., & Yan, Y. (2014). Unusual defect physics in $\text{CH}_3\text{NH}_3\text{PbI}_3$ perovskite solar cell absorber. *Applied Physics Letters*, 104(6).
- Yoshitake, M., & Watakabe, A. (2008). Perfluorinated ionic polymers for PEFCs (including supported PFSA). In *Advances in Polymer Science* (Vol. 215, Issue 1, pp. 127–155). Springer, Berlin, Heidelberg.
- You, J., Meng, L., Song, T. Bin, Guo, T. F., Chang, W. H., Hong, Z., Chen, H., Zhou, H., Chen, Q., Liu, Y., De Marco, N., & Yang, Y. (2016). Improved air stability of perovskite solar cells via solution-processed metal oxide transport layers. *Nature Nanotechnology*, 11(1), 75–81.
- Yuan, H., Debroye, E., Janssen, K., Naiki, H., Steuwe, C., Lu, G., Moris, M., Orgiu, E., Uji-I, H., De Schryver, F., Samorì, P., Hofkens, J., & Roeffaers, M. (2016). Degradation of Methylammonium Lead Iodide Perovskite Structures through Light and Electron Beam Driven Ion Migration. *Journal of Physical Chemistry Letters*,

- Yuan, M., Quan, L. N., Comin, R., Walters, G., Sabatini, R., Voznyy, O., Hoogland, S., Zhao, Y., Beauregard, E. M., Kanjanaboos, P., Lu, Z., Kim, D. H., & Sargent, E. H. (2016). Perovskite energy funnels for efficient light-emitting diodes. *Nature Nanotechnology*, 11(10), 872–877.
- Yuan, S., Wang, Z. K., Zhuo, M. P., Tian, Q. S., Jin, Y., & Liao, L. S. (2018). Self-Assembled High Quality CsPbBr₃ Quantum Dot Films toward Highly Efficient Light-Emitting Diodes. *ACS Nano*, 12(9), 9541–9548.
- Yuan, Y., & Lee, T. R. (2013). Contact angle and wetting properties. *Springer Series in Surface Sciences*, 51(1), 3–34.
- Yuan, Z., Zhou, C., Tian, Y., Shu, Y., Messier, J., Wang, J. C., Van De Burgt, L. J., Kountouriotis, K., Xin, Y., Holt, E., Schanze, K., Clark, R., Siegrist, T., & Ma, B. (2017). One-dimensional organic lead halide perovskites with efficient bluish white-light emission. *Nature Communications*, 8, 1–7.
- Zhang, B., Liu, D., Chen, P., Liu, W., Zhao, J., Li, H., & Liu, H. (2021). Improved perovskite crystallization via antisolvent-assisted processed using additive engineering for efficient perovskite solar cells. *Journal of Alloys and Compounds*, 855, 157396.
- Zhang, F., Zhang, H., Zhu, L., Qin, L., Wang, Y., Hu, Y., Lou, Z., Hou, Y., & Teng, F. (2019). Two-dimensional organic-inorganic hybrid perovskite field-effect transistors with polymers as bottom-gate dielectrics. *Journal of Materials Chemistry C*, 7(14), 4004–4012.
- Zhang, Q., Su, R., Du, W., Liu, X., Zhao, L., Ha, S. T., & Xiong, Q. (2017). Advances in Small Perovskite-Based Lasers. *Small Methods*, 1(9), 1700163.
- Zhang, X., Ji, C., Liu, X., Wang, S., Li, L., Peng, Y., Yao, Y., Hong, M., & Luo, J. (2020). Solution-Grown Large-Sized Single-Crystalline 2D/3D Perovskite Heterostructure for Self-Powered Photodetection. *Advanced Optical Materials*, 8(19), 1–9.
- Zhao, K., Munir, R., Yan, B., Yang, Y., Kim, T., & Amassian, A. (2015). Solution-processed inorganic copper(i) thiocyanate (CuSCN) hole transporting layers for efficient p-i-n perovskite solar cells. *Journal of Materials Chemistry A*, 3(41), 20554–20559.
- Zhao, P., Soin, N., Prashanthi, K., Chen, J., Dong, S., Zhou, E., Zhu, Z., Narasimulu, A. A., Montemagno, C. D., Yu, L., & Luo, J. (2018). Emulsion Electrospinning of Polytetrafluoroethylene (PTFE) Nanofibrous Membranes for High-Performance Triboelectric Nanogenerators. *ACS Applied Materials & Interfaces*, 10(6), 5880–5891.
- Zhao, P., Yin, W., Kim, M., Han, M., Song, Y. J., Ahn, T. K., & Jung, H. S. (2017). Improved carriers injection capacity in perovskite solar cells by introducing A-site interstitial defects. *Journal of Materials Chemistry A*, 5(17), 7905–7911.
- Zhao, T., Shi, W., Xi, J., Wang, D., & Shuai, Z. (2016). Intrinsic and Extrinsic Charge

Transport in CH₃ NH₃ PbI₃ Perovskites Predicted from First-Principles. *Scientific Reports*, 7.

- Zheng, E., Yuh, B., Tosado, G. A., & Yu, Q. (2017). Solution-processed visible-blind UV-A photodetectors based on CH₃NH₃PbCl₃ perovskite thin films. *Journal of Materials Chemistry C*, 5(15), 3796–3806.
- Zhou, C., Lin, H., He, Q., Xu, L., Worku, M., Chaaban, M., Lee, S., Shi, X., Du, M. H., & Ma, B. (2019). Low dimensional metal halide perovskites and hybrids. *Materials Science and Engineering R: Reports*, 137, 38–65.
- Zhu, B. S., He, Z., Yao, J. S., Chen, C., Wang, K. H., Yao, H. Bin, Liu, J. W., & Yu, S. H. (2018). Potassium Ion Assisted Synthesis of Organic–Inorganic Hybrid Perovskite Nanobelts for Stable and Flexible Photodetectors. *Advanced Optical Materials*, 6(3), 1701029.
- Zhu, L., Zhang, H., Lu, Q., Wang, Y., Deng, Z., Hu, Y., Lou, Z., Cui, Q., Hou, Y., & Teng, F. (2018). Synthesis of ultrathin two-dimensional organic-inorganic hybrid perovskite nanosheets for polymer field-effect transistors. *Journal of Materials Chemistry C*, 6(15), 3945–3950.
- Zschieschang, U., Yamamoto, T., Takimiya, K., Kuwabara, H., Ikeda, M., Sekitani, T., Someya, T., & Klauk, H. (2011). Organic Electronics on Banknotes. *Advanced Materials*, 23(5), 654–658.
- Zuo, L., Guo, H., DeQuilettes, D. W., Jariwala, S., De Marco, N., Dong, S., DeBlock, R., Ginger, D. S., Dunn, B., Wang, M., & Yang, Y. (2017). Polymer-modified halide perovskite films for efficient and stable planar heterojunction solar cells. *Science Advances*, 3(8), 1–12.